

Propagation and Scattering of Guided Waves in Composite Plates with Defects

A dissertation submitted for the degree of

Doctor of Philosophy

April 2015

Bibi Intan Suraya Murat

University College London

DECLARATION

I, Bibi Intan Suraya Murat, confirm that the work presented in this thesis is my own. Where information has been derived from other sources, I confirm that this has been indicated in the thesis.

Faithfully yours,

Bibi Intan Suraya Murat

ACKNOWLEDGEMENT

I would like to thank my supervisor, Dr. Paul Fromme, who has provided invaluable guidance throughout this study. Without his guidance, understanding and persistent support, this PhD thesis would not have been possible. I would also like to thank Prof. Nader Saffari and Dr William Suen for their expertise and encouragement extended to me.

My sincere appreciation also extends to my sponsor, Ministry of Science, Technology and Innovation (MOSTI) Malaysia and Universiti Teknologi MARA (UiTM) Malaysia for funding this study.

I am eternally grateful to my husband and my daughter whose love and support pulled me through every obstacle that appeared in the course of my work and for always having faith in me when I did not believe in myself. My sincere gratitude should also be accorded to my family in Malaysia for their support and understanding throughout my study.

Last but not least, I am very indebted to every individual that helped even with the smallest things throughout this journey. Throughout this PhD study, I was lucky enough to have met many people and gained new experiences. It is impossible to list each and every one that I owe a favor to. Nonetheless, I really appreciate whatever help I have received through it all. Thank you.

ABSTRACT

Failure in composite structures due to low-velocity impact damage raises a significant maintenance concern because it can lead to a barely visible and difficult-to-detect damage. Depending on the severity of the impact, fiber and matrix breakage or delaminations can occur, reducing the load carrying capacity of the structure. Efficient structural health monitoring (SHM) of composite structures can be achieved by using low-frequency guided ultrasonic waves as they have advantages of propagating over large structure and being sensitive to defects located at any thickness position. This work focuses on the use of first antisymmetric guided wave mode (A_0) for health monitoring in laminated composite plates.

The first part of this work is to investigate the propagation of A_0 mode in undamaged composite plates experimentally and compare the results to Finite Element simulations and semi-analytical analysis. This study is essential in order to improve understanding of the guided waves behavior in composite plates and would benefit the interpretation of received signals particularly for defect characterization. To gain a good understanding of the A_0 mode interaction with defects in composites, a full three-dimensional (3D) Finite Element (FE) analysis is used. A systematic study of the influence of defect geometry and range of situations on guided wave scattering is demonstrated. Combined delamination with material degradation to simulate mixed-modes defect is shown. Two dimensional FE simulations used for analysis of large delamination are also presented. The final part of this thesis presents the scattering of guided waves at the impact damage using a non-contact laser interferometer. In this study, the results were quantified and compared to baseline measurements on undamaged composite panels. Significant scattering activities were observed, allowing for the detection of impact damage in composite plates. The impact damage was further characterized using standard ultrasonic C-scans. Good agreement between experiments and predictions was found.

TABLE OF CONTENTS

ACKNOWLEDGEMENT	2
ABSTRACT.....	3
CHAPTER 1 INTRODUCTION	12
1.1 Motivation.....	12
1.2 Thesis overview.....	14
CHAPTER 2 LITERATURE REVIEW	17
2.1 Low-velocity impact damage of composites.....	17
2.2 Non-destructive evaluation (NDE) of composites	20
2.3 Guided ultrasonic waves.....	22
2.4 Guided waves in composite plates	28
2.5 Guided wave scattering at defects	30
2.6 Conclusions	37
CHAPTER 3 EXPERIMENTAL MEASUREMENTS.....	38
3.1 Specimens	38
3.2 Experimental setup	42
3.3 Experimental measurements.....	49
3.4 Immersion ultrasonic C-scan.....	52
3.5 Conclusions	55
CHAPTER 4 3D FINITE ELEMENT MODELING	56
4.1 Finite element modeling using ABAQUS.....	56
4.2 Creating the input file in MATLAB.....	58
4.3 Modeling undamaged composite plates	62
4.4 Modeling composite plates with defects.....	65
4.5 Signal monitoring points and evaluation	72
4.6 Long delamination in 2D plate model.....	74
4.7 Conclusions	76
CHAPTER 5 A_0 MODE WAVE PROPAGATION IN UNDAMAGED COMPOSITE PLATES	77
5.1 Accuracy of the FE modeling approaches	77
5.2 Estimation of attenuation coefficient	86
5.3 Estimation of wave velocities	92
5.4 Angular dependency of the A_0 mode.....	97

5.5	Conclusions	106
CHAPTER 6	FE ANALYSIS OF GUIDED WAVES INTERACTION WITH DEFECTS	107
6.1	Verifications of the FE modeling approaches	109
6.2	Interaction of A_0 guided waves at large delamination.....	116
6.3	Influence of delamination size on wave scattering	130
6.4	Influence of delamination depth on wave scattering.....	137
6.5	Influence of reduction in stiffness properties.....	141
6.6	Conclusions	148
CHAPTER 7	IMPACT DAMAGE CHARACTERIZATION IN COMPOSITE PLATES	150
7.1	Impact damage detection in cross-ply composite plates	151
7.2	Scattering of A_0 wave mode by impact damage	165
7.3	Comparison with FE simulations.....	169
7.4	Conclusions	176
CHAPTER 8	CONCLUSIONS.....	178
8.1	Summary of findings	178
8.2	Recommendation for future works	183
8.3	Concluding remarks	183
REFERENCES	185

Figure 2-1: Typical pattern of impact damage modes observed in cross-ply composite panels; matrix cracks and delamination [8]. 19

Figure 2-2: Metallographic image showing matrix cracks inclined about 45° and interconnected with the delamination [10]. 19

Figure 2-3: Schematic illustration of guided waves in plates; (a) S_0 mode, and (b) A_0 mode..... 23

Figure 2-4: Phase velocity (V_{ph}) dispersion curves for homogeneous model of cross-ply composite plate; propagation direction is 0°; the blue and red lines represent the anti-symmetric and symmetric modes respectively; region of study at 0.36 MHz-mm shown. 24

Figure 2-5: Mode shape of fundamental modes (a) S_0 mode, and (b) A_0 mode; out-of-plane displacement (red line); in-plane displacement (blue line); 100 kHz-mm, cross-ply composite plate; 3.6 mm thickness. 26

Figure 3-1: (a) Large cross-ply plate; 24 plies of $[0^\circ/90^\circ]$; symmetry at the mid plane; 1140 mm x 940 mm; (b) Unidirectional plate; 24 plies of $[0^\circ]$; 245 mm x 200 mm; undamaged plate..... 40

Figure 3-2: Small cross-ply plate; 8 plies of $[0^\circ/90^\circ]$; symmetry at the mid plane; 990 mm x 110 mm; approximate impact damage of 10 mm length, 20 mm width..... 40

Figure 3-3: Coordinate system of the plate geometry and the direction of the material properties. 42

Figure 3-4: Schematic diagram of guided ultrasonic wave experimental setup..... 43

Figure 3-5: Guided wave monitoring system with the defective composite plate..... 43

Figure 3-6: Transducer locations on the small cross-ply plates..... 43

Figure 3-7: Schematic and photo of piezoelectric transducer made of Ferroperm disc and brass baking mass..... 44

Figure 3-8: (a) Typical measured time signal (blue line) and its Hilbert envelope (dashed red line), (b) frequency domain transform of the time signal; 5-cycle excitation frequency at 100 kHz in the large cross-ply composite plate; measured 50 mm from the excitation point. 45

Figure 3-9: Position of the laser monitoring; 100 mm line scans in 0° to 90° directions with 15° step size for the unidirectional plates; 200 mm line scans in 0° to 90° directions with 15° step size for the large cross-ply plate; 30 mm radius of circular scan around the excitation; 48

Figure 3-10: Geometry of the small cross-ply plate and laser monitoring positions for monitoring the impact damage; 200 mm line scans (left and rightward from transducer); 30 mm radius circular scan around transducer; 30 mm radius circular scans around impact damage and symmetric to the impact location; raster scan of 40 mm x 40 mm square with 1 mm step size. 48

Figure 3-11: Immersion ultrasonic C-scan system with defective composite plate. 53

Figure 3-11: Time-gating for the C-scan image acquisition; first time-gating to capture surface reflection; second time gating to capture reflection within plate thickness; measured from the front surface of the 2mm cross-ply plate. 54

Figure 4-1: Illustration of the plate geometry; the excitation and monitoring points are placed in the middle of plate for the generation and detection of the A_0 mode; corner nodes number identified as nb_i ($i=1, 2, 3...n$); Edge 1, 2, 3, 4 were set as the boundaries of the plate..... 60

Figure 4-2: Mesh using 8 separate layers of C3D8R brick elements with individual properties. 64

Figure 4-3: Orientation of individual unidirectional properties in a symmetric 8-crossply $[0/90]$ layered model. 64

Figure 4-4: Plate geometry for FE modeling of composite plate with rectangular shaped delamination.	66
Figure 4-5: (a) Typical FE plate model with rectangular shaped delamination; (b) Tie constraint applied to the delamination border; 8-elements in thickness direction.	66
Figure 4-6: Layered plate with rectangular shaped delamination; set of nodes across delamination surface (in green color); two master elements were defined.	69
Figure 4-7: Modeling a circular delamination by approximating the circular shape with Cartesian grid.	70
Figure 4-8: Various delamination sizes; distance between excitation point to the central delamination was 100 mm; 200 mm line scan in 0° direction; 30 mm radius circular scan around delamination.	70
Figure 4-9: Modeling three types of defects with material degradation for the FE models.	71
Figure 4-10: Typical plate geometry and monitoring scan locations; unit for dimension is mm.	73
Figure 4-11: Configuration of the 2D model with delamination located at different depths; delamination length is 200 mm; four monitoring nodes were placed at different locations; sub-laminates with different thickness labeled; material orientation above and below delamination shown.	75
Figure 5-1: Maximum amplitude of signal envelope in intact composite plates; (a) and (b) for the 24-ply cross ply plate; (c) and (d) for the 8-ply cross ply plate; (e) and (f) for the 24-ply unidirectional composite plate; line scan measured every 1 mm step along line in 0° direction; polar plot of amplitude every 5° at 30 mm radius around excitation point; 100 kHz excitation frequency.	79
Figure 5-2: Maximum amplitude of signal envelope in intact composite plates; (a) and (b) for the 24-ply cross ply plate; (c) and (d) for the 8-ply cross ply plate (only 4 and 8 elements investigated); (e) and (f) for the 24-ply unidirectional composite plate; line scan measured every 1 mm step along line in 0° direction; polar plot of amplitude every 5° at 30 mm radius around excitation point; 100 kHz excitation frequency.	82
Figure 5-3: Comparison between FE models with different Rayleigh damping values; amplitude profiles (a) and (b) for the 3.6 mm cross-ply plate, (c) and (d) for the 2 mm cross-ply plate, and (e) and (f) for the 3.6 mm UD plate; 100 kHz; homogenized model.	84
Figure 5-4: Geometrical beam spreading and the measured exponential reduction of the propagating A ₀ mode amplitude in (a) 24-cross ply; (b) 8-cross ply; (c) 24-unidirectional composite plates; Blue dashed line corresponds to the corrected amplitude pattern due to material damping and beam spreading; 100 kHz excitation frequency.	87
Figure 5-5: Measured frequency-dependent attenuation coefficient together with DISPERSE predictions; corrected for geometrical beam spreading; excitation frequency 50 – 150 kHz; measured in 0° direction; (a) 24-cross ply; (b) 8-cross ply; (c) 24-unidirectional composite plates.	90
Figure 5-6: Measured and predicted velocities for the A ₀ mode propagation in the composite plates; a) and (b) for the 3.6 mm cross-ply plate, (c) and (d) for the 2 mm cross-ply plate, and (e) and (f) for the 3.6 mm UD plate; 100 kHz; measured in 0° direction.	94

Figure 5-7: (a) Experimental measurement and (b) FE simulations of maximum amplitude of signal envelope (Hilbert transform) of propagating A_0 guided wave pulse in 24-crossply plate; measured every 1 mm step; every 15° in directions of 0° to 90° directions; 100 kHz. 101

Figure 5-8: Experimental, FE and DISPERSE values for angular dependency of the A_0 guided wave properties in a 24-crossply plate; (a) attenuation coefficient, (b) group velocity, (c) phase velocity and (d) phase slowness; measured within 100 mm distance every 15° step..... 102

Figure 5-9: (a) Experimental measurement and (b) FE simulations of maximum amplitude of signal envelope (Hilbert transform) of propagating A_0 guided wave pulse in 3.6 mm UD plate; measured every 1 mm step; every 15° in directions of 0° to 90° directions. 104

Figure 5-10: Experimental, FE and DISPERSE data of angular dependency of the A_0 guided wave properties in a 3.6 mm UD plate; (a) attenuation coefficient, (b) group velocity, (c) phase velocity, and (d) phase slowness; measured within 50 mm distance in every 15° step. 105

Figure 6-1: Amplitude of propagating guided wave over defective area of composite plate (0° direction) modeled using homogenized (black line) and layered material properties (red line); delamination was placed at different depth: (a) 0.25 mm, (b) 0.50 mm, (c) 0.75 mm and (d) 1 mm; blue and green dashed lines correspond to the baseline wave propagation over undamaged area. 110

Figure 6-2: Plot of amplitude variation measured every 5° at 30 mm radius around center of the delamination; modeled using homogenized (black line) and layered material properties (red line); delamination was placed at different depth: (a) 0.25 mm, (b) 0.50 mm, (c) 0.75 mm and (d) 1 mm; blue and green dashed line correspond to the baseline wave propagation over undamaged area. 111

Figure 6-3: Comparison between layered models with and without additional damping; delamination at 1 mm: (a) 200 mm line scan (b) 30 mm radius circular scan..... 113

Figure 6-4: Line scans for a comparison between layered models with 20 mm x 20 mm rectangular-shaped and 20 mm diameter circular-shaped delamination; delamination depths: (a) 0.25 mm, (b) 0.50 mm, (c) 0.75 mm and (d) 1 mm. 114

Figure 6-5: Circular scans for a comparison between layered models with 20 mm x 20 mm rectangular-shaped and 20 mm diameter circular-shaped delamination; delamination depths: (a) 0.25 mm, (b) 0.50 mm, (c) 0.75 mm and (d) 1 mm..... 115

Figure 6-6: Exact stress fields at different time instants; (a) 120 μ s, (b) 160 μ s, (c) 200 μ s, (d) 240 μ s, (e) 280 μ s, (f) 320 μ s; 200 mm x 200 mm rectangular delamination positioned at symmetrical layer (1 mm depth); excitation point at 100 mm from center of delamination..... 118

Figure 6-7: The predicted guided wave time signals for a 200 mm x 200 mm delamination; 1 mm depth; (a) points before delamination, (b) points behind delamination..... 120

Figure 6-8: Snapshots of displacement fields at 110 μ s time instant; 200 mm long delamination positioned at different depth; 2D FE. 122

Figure 6-9: Received signals monitored at 100 mm before delamination; delamination depth is varied from 0.25 mm to 1 mm; left side corresponding to the A_0 mode signals; right side corresponding to S_0 mode signals..... 123

Figure 6-10: Illustration of the guided wave interaction with a delamination; possible mode conversion between the A_0 and S_0 mode reflected waves (dashed blue line); delamination located

through the plate thickness (in pink area); travel times are included for each mode that travels in undamaged and damaged areas.....	124
Figure 6-11: Received signals monitored at 100 mm within delamination; delamination depth is varied from 0.25 mm to 1 mm; left side corresponding to the A_0 mode signals; right side corresponding to S_0 mode signals.....	125
Figure 6-12: Received signals monitored at 100 mm behind delamination; delamination depth is varied from 0.25 mm to 1 mm; left side corresponding to the A_0 mode signals; right side corresponding to S_0 mode signals.....	126
Figure 6-13: Maxima of signal envelope of guided wave for different delamination sizes; unit in mm; symmetric delamination ($z_d = 1$ mm); FE layered model of 2 mm cross-ply composite plate.	132
Figure 6-14: Maxima of signal envelope around various sizes of delamination; unit in mm; symmetric delamination ($z_d = 1$ mm); measured every 5° at 30 mm radius around center of the delamination; FE layered model of 2 mm cross-ply composite plate.	133
Figure 6-15: Scattered amplitude (using baseline subtraction method) around various sizes of delamination; unit in mm; symmetric delamination ($z_d = 1$ mm); measured every 5° at 30 mm radius around center of the delamination; FE layered model of 2 mm cross-ply composite plate.	133
Figure 6-16: Scattered amplitudes (using baseline subtraction method) around delamination with different length; unit in mm; symmetric delamination ($z_d = 1$ mm); measured every 5° at 30 mm radius around center of the delamination; FE layered model of 2 mm cross-ply composite plate.	135
Figure 6-17: Scattered amplitudes (using baseline subtraction method) around delamination with different width; unit in mm; symmetric delamination ($z_d = 1$ mm); measured every 5° at 30 mm radius around center of the delamination; FE layered model of 2 mm cross-ply composite plate.	135
Figure 6-18: Schematic illustration of trapped wave energy in plate with delamination size of (a) 40 mm x 20 mm, and (b) 20 mm x 40 mm; excitation point to the center of delamination = 100 mm.	136
Figure 6-19: Maxima of signal envelope across various delamination sizes; (a) 10 mm x 10 mm, (b) 20 mm x 20 mm, (c) 30 mm x 30 mm, (d) 40 mm x 40 mm, (e) 50 mm x 50 mm and (f) 60 mm x 60 mm; at different delamination depths; FE layered model of 2 mm cross-ply composite plate.....	138
Figure 6-20: Scattered amplitudes (using baseline subtraction method) around various delamination sizes; (a) 10 mm x 10 mm, (b) 20 mm x 20 mm, (c) 30 mm x 30 mm, (d) 40 mm x 40 mm, (e) 50 mm x 50 mm and (f) 60 mm x 60 mm; at different delamination depths; measured every 5° at 30 mm radius around center of the delamination; FE layered model of 2 mm cross-ply composite plate.	139
Figure 6-21: (a) Maximum amplitude of signal envelope propagating through and (b) 30 mm radius of scattered amplitudes (using baseline subtraction method) around region with reduced properties in cross-ply composite plate; stiffness properties reduced by 25%, 50% and 75%; baseline results correspond to the undamaged model; FE layered model of 2 mm cross-ply composite plate.	144

Figure 6-22: (a) Maximum amplitude of signal envelope propagating through and (b) 30 mm radius of scattered amplitudes (using baseline subtraction method) around multiple defects in cross-ply composite plate; stiffness properties reduced by 25%, 50% and 75%; no reduction results correspond to case of 20 mm x 20 mm delamination; monitoring points in mid-plane; FE layered model of 2 mm cross-ply composite plate. 146

Figure 6-23: (a) Maximum amplitude of signal envelope propagating through and (b) 30 mm radius of scattered amplitudes (using baseline subtraction method) around multiple defects in cross-ply composite plate; stiffness properties are reduced by 25%, 50% and 75%; no reduction results correspond to case of 20 mm x 20 mm delamination; monitoring points in mid-plane; FE layered model of 2 mm cross-ply composite plate. 147

Figure 7-1: X-ray images of composite plate impacted at 7.4 J with impact damage; provided by collaborator in Composite Systems Innovation Centre, University of Sheffield. 152

Figure 7-2: X-ray images of composite plate impacted at 7.4 J with impact damage; (a) vertical scattering (b) horizontal scattering; performed by collaborator in Department of Medical Physics and Biomedical Engineering, UCL. 152

Figure 7-3: Comparison of response signals at various locations; signal at location $x=5$ mm, $y=20$ mm corresponds to the undamaged signal; pulse-echo mode; focused; 5 MHz frequency. 155

Figure 7-4: C-scan image of the front surface of the 2 mm cross-ply specimen; 40 mm x 40 mm scanned area; 5 MHz frequency; 76.2 mm transducer focal length..... 156

Figure 7-5: C-scan image of negative peak amplitude measured from the frontal surface of the 2 mm cross-ply panel; 40 mm x 40 mm scanned area; 5 MHz frequency; 76.2 mm transducer focal length. 157

Figure 7-6: C-scan image of negative peak amplitude measured from the back-wall surface of the 2 mm cross-ply panel; 40 mm x 40 mm scanned area; 5 MHz frequency; 76.2 mm transducer focal length. 157

Figure 7-7: Guided wave displacement fields in two composite plates; Plate No. 1, snapshot time (a) 20 μ s and (b) 30 μ s; Plate No. 2, snapshot time (c) 20 μ s and (d) 30 μ s; 7.4 J impact; 40 mm x 40 mm scanned area..... 160

Figure 7-8: Maximum amplitudes of guided wave pulse across damaged area of composite plate: a) plate 1; b) plate 2; frequency 100 kHz; 40 mm x 40 mm area with impact location at center ($x = 20$ mm, $y = 20$ mm). 163

Figure 7-9: Wave energy distribution across damaged area of composite plate: a) plate 1; b) plate 2; frequency 100 kHz; 40 mm x 40 mm area with impact location at center ($x = 20$ mm, $y = 20$ mm). 164

Figure 7-10: Experimental time traces monitored at 25 mm from transducer (undamaged area); a) plate 1; c) plate 2; and 50 mm (damaged area): b) plate 1; d) plate 2; excitation frequency 100 kHz, time trace (solid, blue), and envelope (dashed, red)..... 165

Figure 7-11: Amplitude of propagating guided wave pulse over damaged part; excitation frequency 100 kHz, transducer placed 50 mm from the impact damage area; measured every 1 mm step. 167

Figure 7-12: Amplitude of propagating guided wave pulse over damaged part; excitation frequency 100 kHz, transducer placed 100 mm from the impact damage area; measured every 1 mm step. 167

Figure 7-13: a) Plot of amplitude variation measured every 5° at 30 mm radius around (a) impact damage; b) undamaged plate, symmetric to damage location; 100 kHz; excitation 50 mm from impact damage. 169

Figure 7-14: a) Plot of amplitude variation measured every 5° at 30 mm radius around (a) impact damage; b) undamaged plate, symmetric to damage location; 100 kHz; excitation 100 mm from impact damage. 169

Figure 7-15: Comparison between experimental and FE simulations results for the amplitude of guided wave pulse over damaged area; FE delamination size 10 mm x 30 mm; FE combined delamination and full depth material degradation; excitation 100 mm from impact area; 100 kHz. 173

Figure 7-16: Comparison between experimental and FE simulations results of amplitude variation measured every 5° at 30 mm radius around (a) impact damage; b) undamaged plate (symmetric to damage location); excitation 100 mm from impact damage; 100 kHz..... 173

Figure 7-17: Comparison between experimental and FE simulations results for the amplitude of propagating guided wave pulse over damaged area; FE delamination size 30 mm x 30 mm; FE combined delamination (0.50 mm depth) and full depth material degradation (75%); transducer placed 100 mm from the impact area; 100 kHz..... 174

Figure 7-18: Comparison between experimental and FE simulations results of amplitude variation measured every 5° at 30 mm radius around (a) impact damage; b) undamaged plate (symmetric to damage location); excitation 100 mm from impact damage; 100 kHz..... 174

CHAPTER 1 INTRODUCTION

1.1 Motivation

This PhD thesis is motivated by the goal to improve the understanding of guided ultrasonic wave propagation and scattering in composites and of developing an efficient technique for the inspection of large aerospace composite structures using guided ultrasonic waves. The use of composite materials has grown from the occasional application for a nonstructural part, i.e., baggage compartment door, to the construction of complete airframes. Carbon fiber laminate, fiberglass and Kevlar mats are among the composite materials that are used in the construction of fuselage, wing, tail, and interior of the aircraft. In the latest models, the Airbus A350 and Boeing 787, the use of composite materials is estimated to account for more than 50% of their total weight. This shows that composites can offer many advantages for aerospace applications, such as excellent strength to weight capacity and assembly simplification. These factors play an important role in reducing operating costs of aircraft in the long term.

In general, carbon fiber laminates consist of layers of polymer matrix reinforced with high strength carbon fibers. The combination of these two materials produces a material with characteristics different from the individual constituents. A composite laminate is typically made up of several plies with different fiber orientation. This laminate is weak when subjected to impact loading. The impact loading on a composite laminate can lead to barely visible impact damage that could potentially result in a catastrophic failure if exposed to repetitive loading. Cracks in the polymer matrix, debonding between fibers and separation of laminae (called delamination) are the common damage modes observed in composite structures. Among those damage modes, attention is focused on the delamination, as it reduces the load-carrying capacity of a structure and can lead to dangerous failure phenomena. Therefore, there is a demand for efficient monitoring of composite structures during their service life.

In order to maintain the quality and reliability of a composite structure, non-destructive testing (NDT) is usually used. Visual inspection, ultrasonic testing, acoustic emission, X-ray radiography, liquid penetrant and eddy-current are amongst the NDE methods employed in aerospace inspection. In the present trend for aircraft maintenance, the maintenance of aircraft must be accomplished within a scheduled time. However, for the large aircraft structures most methods are very time consuming, costly and interrupt the service of the aircraft. This indicates a need for rapid inspection and cost-effective methods for monitoring large composite structures. One possible method, the guided ultrasonic waves NDE method, is chosen to be further explored in this PhD study.

Using low excitation frequency, guided waves can propagate over long distance with limited energy loss. From a single location, the guided wave can cover large areas, which can help to reduce the inspection time. The reflection of the propagating wave at defects enables rapid detection of defects in large structures. This method has been used successfully for the detection of defects in large metal plates and long pipes, i.e., corrosion and crack detection. However, the behavior of the guided waves is somewhat more complicated in composite structures due to the physical properties of composites that are generally inhomogeneous and anisotropic in nature. The capability of the guided waves for the Structural Health Monitoring (SHM) of aerospace structures is under investigation. Therefore, the objective of this research is to investigate the use of guided ultrasonic waves for detecting typical impact damage, such as delaminations and material degradation that can occur on aerospace composite structures. This PhD study aims to achieve a better understanding of the guided wave propagation in composite plates and the interaction with impact damage. The outcome of this research will hopefully benefit the NDE field of study and help to establish an efficient technique for SHM of composite materials.

1.2 Thesis overview

This thesis investigates the propagation of guided ultrasonic waves and the interaction with impact damage in composite plates. This research intends to improve the understanding of the application of guided wave mode to composite materials. Chapter 2 presents a general introduction to impact damage of composites and other NDE methods in composites. Guided waves in plates are described and the behavior of different wave modes explained. The motivation for the choice of the A_0 guided wave mode is discussed. Previous studies on guided wave propagation and scattering at different types of defects in composite plates are discussed.

Chapter 3 presents the experimental approach used in this study. The first antisymmetrical (A_0) mode was chosen to be excited at typically 100 kHz. The three types of composite plates used in this study are described: two cross-ply laminates with different thickness and one unidirectional plate. The first section of this chapter details the experimental setup for the measurement of the A_0 mode in composite plates. Fixed piezoelectric transducers are used for the excitation and the out-of-plane signal is measured using a laser vibrometer. In order to obtain wave propagation characteristics such as velocities and attenuation and the directivity pattern, measurements on several undamaged composite plates were first performed. The second part of this chapter explains the methodology for guided wave measurement on defective composite plates. The characterization of impact damage using an ultrasonic immersion C-scan is described.

Chapter 4 introduces the 3D Finite Element (FE) modeling that has been used to model the propagation of the A_0 mode in undamaged and damaged composite plates. The input files for the FE models were programmed in MATLAB. Two types of composite models have been used: (1) composite plates with homogenized material properties, and (2) layered composite with individual ply properties. The modeling of delaminations in both types of composite models is explained, where rectangular and circular shaped delaminations were introduced. Defects in the composite plates are as well modeled as a

localized reduction in the material properties and as a combination of the delamination and reduced materials properties. In order to better understand the interaction of guided waves with impact damage, 2D FE modeling of long delaminations has been performed.

Chapter 5 deals with the guided wave propagation in undamaged composite plates. The first part of this chapter presents the verification of the FE modeling. The reliability of both homogenized and layered FE models and the influence of the FE parameters are discussed. Then, the experimental and FE analysis wave attenuation and velocities are compared, and validated against DISPERSSE. DISPERSSE is a computer code for the calculation of guided wave dispersion based on an analytical model. The final part of this chapter discusses the dependency of the A_0 wave properties on the direction of propagation.

Chapter 6 concentrates on the FE results for a composite plate with a delamination. The predicted guided wave scattering for defective composite models is discussed in this chapter. The first section of this chapter deals with the verification of the FE models and the influence of the FE parameters. The second part presents the interaction of guided waves at large delaminations based on 3D and 2D FE simulations. Then, a systematic study of the influence of the delamination parameters on the wave scattering was discussed. The delamination was placed at different depths and modelled with different sizes. In order to provide guidelines for extending the modeling of realistic multimode impact damage, the final section of this chapter discusses wave scattering by mixed defects in composite plates.

Chapter 7 examines the potential of the A_0 wave mode for the detection and characterization of barely visible impact damage in composite specimens. The first section of this chapter presents the characterization of the impact damage using X-ray radiography, ultrasonic C-scan and guided ultrasonic waves. The information obtained from these methods was compared to the measured guided wave displacements fields

around the damage area. The final part compares the wave scattering of the experimental and FE simulations results. The wave characteristics such as amplitude variations and scattering by the impact damage are discussed to validate the FE simulations results in Chapter 6.

Finally, Chapter 8 summarizes the work, highlighting the main objectives and achievements from of each chapter of this PhD thesis. Conclusions on the interaction of guided waves with defects in composite plates are drawn and future works are proposed.

CHAPTER 2 LITERATURE REVIEW

2.1 Low-velocity impact damage of composites

Composites are engineered materials that are made by combining two or more constituent materials. They are usually built up of separate thin layers consisting of polymer matrix reinforced with high strength fibers. The primary function of the fibers is to carry load along the direction of the fibers, while the polymer matrix transfers stresses between the fibers and acts as a glue to hold them together [1]. Often composites are in the form of laminates, made of layers of different fiber orientations that are bonded together. A single lamina with only one orientation of the fiber is called a unidirectional (UD) laminate (typically referred to as the 0° direction), while laminas arranged with alternate fiber orientation are called a cross-ply laminate (fibers arranged in 0° and 90° directions). The physical properties of composites generally are anisotropic in nature with the stiffness of a composite laminate depending on the orientation of the fibers, relative to the direction of the applied load [1]. Composites are widely used in various applications such as aircraft because of their unique properties that can be tailored to meet specific requirements. For the aerospace industry, the high strength to weight ratio could help to reduce aircraft fuel consumption.

One major concern related to composite structural integrity is the susceptibility of composite materials to incur low-velocity impact damage. Low-velocity impacts are often caused by bird strikes, tool drop during manufacturing and servicing, or runway debris. Such impacts may result in various forms of damage modes that can lead to a severe reduction in strength and integrity of composite structures. The brittleness of the polymer matrix and the interlayer spacing between fibers and matrix could lead to the impact damage spreading to the entire structure [2, 3]. The severity of the different damage modes depends on a variety of parameters such as the velocity and mass of the impactor and the material orientation of the composite structure [4, 5]. Several patterns of impact damages in composite laminates have been reported [4–6]: oval shape for a circular impactor shape or approximately rhombus or triangular shape for a diamond shape

impactor. The problem with the low-velocity impact damage is that it is often not visible or barely visible for typical visual inspection [3]. Visible damage can be clearly detected and remedial action could be taken immediately to maintain the structural integrity. But this is often not the case for impact damage in composites. A major concern is the growth of hidden, undetected defects caused by low-velocity impact and fatigue [7]. Failure to detect this internal damage at an early stage may result in a catastrophic failure of the composite structure. This concern provided the motivation for this PhD study.

The failure process caused by low-velocity impact in composites is a complex phenomenon. Different failure modes and mixed damage modes may occur. Matrix cracking, delamination, fiber debonding and fiber breakage are examples of various failure modes [3]. Figure 2-1 illustrates the matrix cracking and delamination in a laminate composite plate [8]. A crack in the polymer matrix typically starts under the impacted area and propagates with an inclination of 45° towards the interface between plies, where delamination then takes place. There have been several studies on the mechanism of damage initiation and propagation of composite laminates [9]. It has been established that the damage first initiates by the matrix cracks directly under the impacted area due to the large stress concentration. After initiation, the cracks usually propagate between fibers, primarily along the fiber–matrix interface, as shown in Figure 2-2 [10]. Cracks are generally perpendicular to the direction of load and extend over the entire thickness of a ply. For a cross-ply plate, the cracks propagate through the entire thickness of the ply but are unable to propagate into the adjacent ply that has fibers aligned in a different orientation [1]. Thus, the cracks terminate at the interface of two plies. However, the resulting high interlaminar stresses produce favorable conditions for starting a delamination along the ply interface. Additional delamination starts and propagates as a result of fatigue. At the time when more delaminations appear, another type of damage is also observed [11]. The presence of cracks or delaminations prevents load distribution between plies, and a composite is essentially reduced to individual plies to support the applied load. When the

weakest ply fails, it will trigger failure in the fibers; fibers may start debonding and fracturing begins to appear [1], [11].

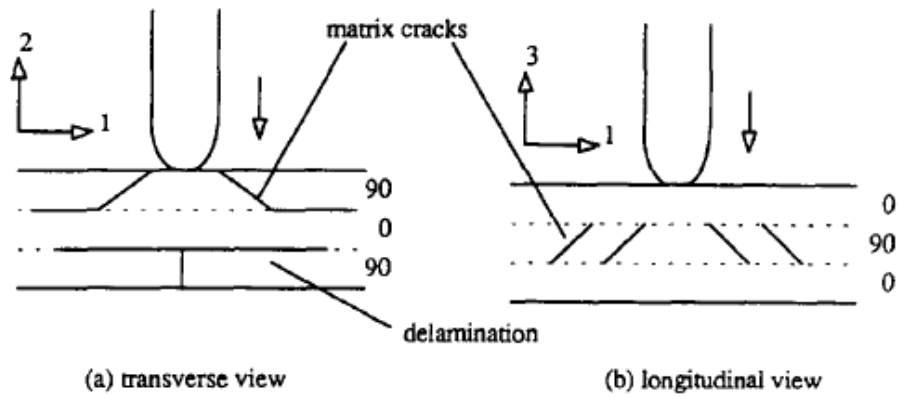


Figure 2-1: Typical pattern of impact damage modes observed in cross-ply composite panels; matrix cracks and delamination [8].

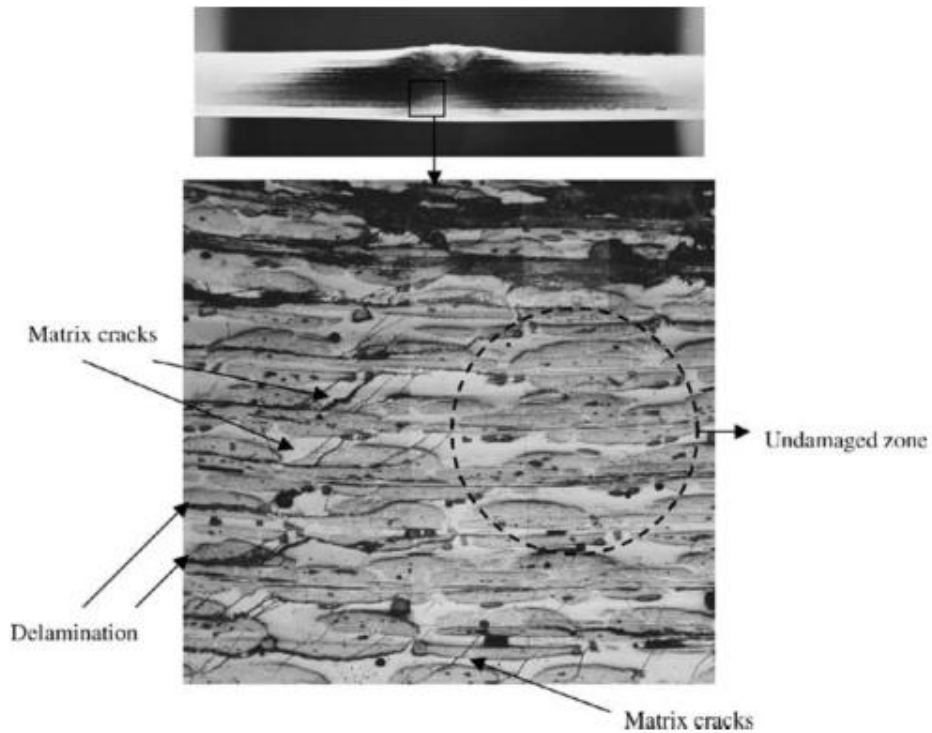


Figure 2-2: Metallographic image showing matrix cracks inclined about 45° and interconnected with the delamination [10].

Interface delamination in cross-ply composites is of particular interest because it can lead to a significant loss of load carrying capacity. Evidence of extensive delamination in the region adjacent to the failure zone has been shown in several studies [11, 12]. It was found that delamination extension could reduce the overall load bearing capacity by up to 80%, depending on the type of composite plates [12]. In contrast to matrix cracks or fiber breakage, delamination can occur in the absence of any visible damage, making it difficult to detect by a visual inspection as it normally does not appear on the surface [3]. Hence, it can be concluded that delaminations developed at the initial stage of an impact event are more dangerous to the structural integrity, as they could continue to expand and spread to the entire structure. For the aerospace industry, such defects pose a potential danger to the structural integrity of aircraft. This in turn jeopardizes passenger safety and incurs high repair costs. Therefore, it is important to efficiently monitor composite structures during the service life.

2.2 Non-destructive evaluation (NDE) of composites

Currently, the aerospace industry utilizes a variety of NDE methods for post-fabrication and in-service inspection. An overview of NDE methods can be found in [13, 14] and the main ones are as follows: visual inspection, eddy current, magnetic particle, radiography, thermography and ultrasonic inspection. Most of the methods are limited to the detection of flaws that lie near the surface such as surface cracks, corrosion and other structural defects [15, 16]. The use of liquid penetrants and magnetic particles are some of the techniques developed to enhance the sensitivity and resolution of the inspection [17]. Radiography inspection is especially suited for the inspection of internal defects that cannot be detected by visual inspection. However, it requires parts to be detached or dismantled first, hence consuming significant inspection time. Acoustic emission technique [18], electromagnetic-induction method [15], electrical resistance method [19] and embedded sensors in composites for online monitoring [20] are some of the advanced NDE methods that are able to provide damage information. However, some of these methods might be less suited for the inspection of an aircraft in noisy environments.

Conventional ultrasonic inspection normally uses high frequency waves to identify flaws and determine defect geometries. Ultrasonic C-scans can produce very sensitive measurements of the location and size of damage [13, 14]. This is an established technique but requires removal of test-parts from the structure and the test part needs to be immersed in a water tank. This causes significance disruption to service operation. The condition of the monitored structure can be easily obtained using ultrasonic double through-transmission, but it is rather impractical for inspecting large structures when access is limited. Ultrasonic inspection techniques where air-coupling is used are an alternative, but known to be less sensitive to defects [21]. High wave attenuation associated with the composite properties and high frequency transducers limits the inspection on large complex structures. Ultrasonic phased array [22] and tomography [23], [24] have recently been utilized more in aircraft SHM as they can produce high resolution images. However the biggest problem with these methods is the requirement of good coupling and a constant angle of incidence for reproducible inspection results [22].

In general, in-service NDE inspection of aerospace composite faces many challenges than defects associated with post-fabrication inspection. This is due to the access to the composite parts being limited, and the composite part generally attached to different structures or other hardware [25]. In the present trend of NDE applications for aircraft, the maintenance of aircraft normally has to be accomplished within a scheduled time and released on time for commercial operation. The shortcomings of current methods indicate a need for rapid inspection, online monitoring and cost-effective methods for the inspection of large composite structures. One possible method, the guided ultrasonic wave method, has been chosen to be further explored in this PhD study.

The principal advantages of guided ultrasonic waves in NDE are explained in more detail in [26], summarized as follows: (1) efficient for long range inspection since they can travel over long distances using low excitation frequency, (2) lower signal attenuation compared to ultrasonic bulk waves, (3) complete coverage of the waveguide cross-section,

and (4) good defect detection sensitivity. The ability to inspect a structure from a single transducer position results in a simple and fast inspection. The potential of guided wave inspection has been summarized by Rose [27]. The capacity for material characterization [28, 29] has been shown. The characteristics of guided waves have been used to determine the anisotropic elastic constants, damping parameters and dimensional properties. Guided waves have also been proven to be effective in characterizing critical defects in composites like cracks [30, 31], delaminations [32, 33], and the quality of bonding [34]. Preliminary studies for the in-situ sensing of impact force [35] have also been demonstrated.

However, a successful guided waves method for SHM can be described by this four step process: (1) detecting damage, (2) locating the damage, (3) characterizing the type and severity of the damage, and (4) evaluating the remaining life of the structure [26]. For the realization of reliable guided waves NDE techniques in composites, it is very important to understand the behavior and the characteristic of guided waves in composites.

2.3 Guided ultrasonic waves

2.3.1 Introduction to guided waves

The term guided wave is used to describe waves that require a structural boundary for their existence. Structural components such as plates, beams, rods and cylinders are commonly referred to as waveguides. In general, guided waves are generated when bulk ultrasonic waves travel inside a waveguide [36, 37]. Multiple reflections and mode conversions are constantly taking place at each boundary, resulting in constructive interferences of bulk waves that are guided by the boundaries of the waveguide. The superimposed wave packet travelling along the waveguide is known as the guided ultrasonic wave. Their amplitude and phase information is a sum of all travelling waves along the waveguide and they are strongly dependent on frequency and wave angles of propagation inside the waveguide structure [36].

Multiple reflections can form an infinite number of wave modes through the thickness. The modes can be either symmetric, noted as S_n ($S_0, S_1, S_2, \dots, S_n$), or antisymmetric noted as A_n ($A_0, A_1, A_2, \dots, S_n$), and these modes are generally dispersive [38]. Each wave mode has a different speed, a different wavelength and a different wave pattern (mode shape) across the thickness. These variations are due to the fact that the properties of guided waves are a function of the waveguide, material properties and the frequency of excitation [26]. As can be seen in Figure 2-3, the in-plane motion of the S_n wave modes is symmetrical about the mid-thickness plane. At low frequencies, the fundamental S_0 approaches the bulk longitudinal waves as the wave is expanding and compressing the plate in the same direction as the wave motion. Meanwhile, the fundamental A_0 mode at low frequencies is comparable to a flexural or bending wave. This is because of the large motion in the normal direction to the plate, resulting in the two plate surfaces moving in the same direction [39].

Guided waves in plates propagate with different velocities depending on the plate thickness and the excitation frequency. This is known as wave dispersion. There will be an increase in the pulse width and decrease in amplitude with propagation distance due to the broadening distribution of wave energy [38, 40]. The reduction in amplitude limits the propagation distance, and the increase in signal duration worsens the resolution that can be obtained.

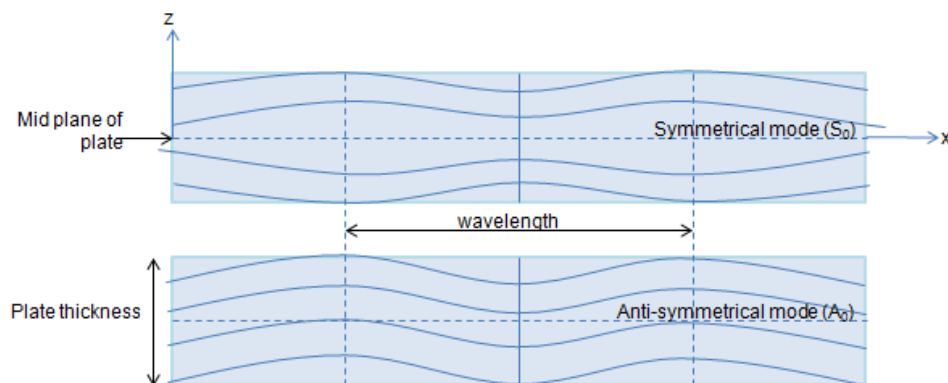


Figure 2-3: Schematic illustration of guided waves in plates; (a) S_0 mode, and (b) A_0 mode.

It is important to note that the phase velocity, that is the speed of propagation of each individual wave crest of the excited waveform, is generally different from the speed of the wave packet as a whole. The speed at which a wave packet propagates is called the group velocity [39]. The direction of propagation of the wave packet can differ from the phase front direction for anisotropic media [41]. The difference between both propagation angles is known as the steering angle [42]. A large steering angle can be found in a unidirectional plate when the composite fibers are all aligned in the 0° direction [39, 42]. The obvious implication for structural monitoring is that ignorance of the steering angle and group velocity could lead to significant errors in the calculation of defect location.

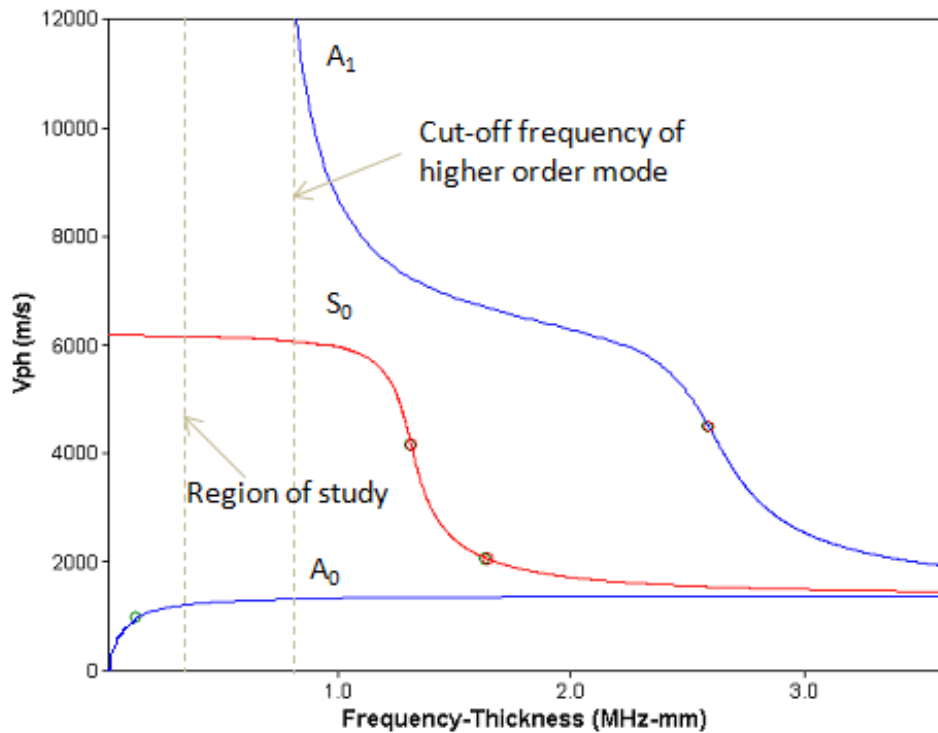


Figure 2-4: Phase velocity (V_{ph}) dispersion curves for homogeneous model of cross-ply composite plate; propagation direction is 0° ; the blue and red lines represent the anti-symmetric and symmetric modes respectively; region of study at 0.36 MHz-mm shown.

Figure 2-4 shows the phase velocity dispersion curves for guided waves in a cross-ply composite plate, plotted using DISPERSE, a software package that is based on an analytical model developed at Imperial College London [43]. It can be observed that there are three modes that can occur at a frequency-thickness product of 1 MHz.mm: A_0 , S_0 , and A_1 . This feature is undesirable in NDE monitoring as it could complicate the received signals. In term of practical NDE testing, it is advantageous to operate with a single guided mode only [38]. This can be obtained when lower excitation frequency (below the cut-off frequency of higher modes) is used. At a frequency-thickness below 0.8 MHz.mm for example, only two fundamental modes (A_0 and S_0) occur as they can exist at all frequencies.

2.3.2 Guided wave mode selection

A comprehensive guideline on wave mode selection has been discussed in [44, 45]. In brief, the main criteria for selecting a wave mode for NDE inspection are: (1) limited dispersion, (2) low attenuation, (3) good sensitivity to defect, (4) simple excitation, (5) detectability and (5) selectivity. Mode dispersion, as mentioned before, is undesirable in an inspection system. Higher excitation frequency will contribute to the generation of complex wave modes and produce higher wave attenuation [45]. Hence, less dispersive modes excited at low frequency are preferred. The A_0 and S_0 modes are less dispersive at frequency-thickness between 0.2 MHz-mm and 1 MHz-mm. The question which then arises is which mode to use and over what frequency range. At 0.36 MHz-mm for example (excitation frequency of 100 kHz, plate thickness 3.6 mm), the phase velocity of the A_0 mode is observed to be slower than for the S_0 mode, thus the response signal is more distinguishable in term of time separation between the sent and received signals. Comparing their sensitivity, the A_0 mode is more sensitive to small defects than the S_0 mode because the wavelength of A_0 mode is shorter (16 mm) than for the S_0 mode (60 mm). This recognizes the fact that typically the wavelength of the selected mode should be smaller or equal to the size of damage for good detection sensitivity [7].

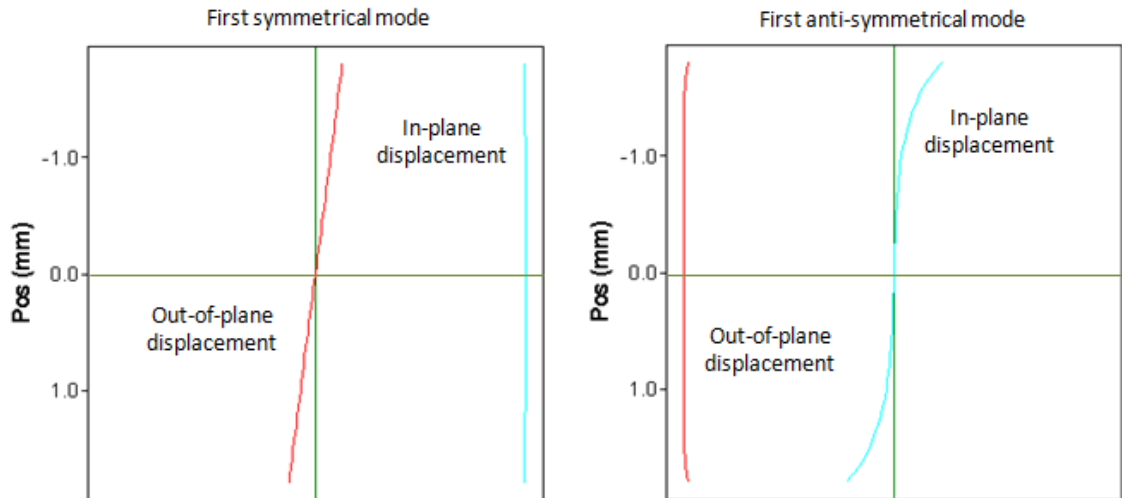


Figure 2-5: Mode shape of fundamental modes (a) S_0 mode, and (b) A_0 mode; out-of-plane displacement (red line); in-plane displacement (blue line); 100 kHz-mm, cross-ply composite plate; 3.6 mm thickness.

Another important consideration for choosing a suitable wave mode for an inspection is the defect detectability of the mode. An approximate way to obtain this information is by observing mode shapes of both fundamental modes, as can be seen in Figure 2-5. At low frequency, the S_0 mode has almost uniform in-plane displacement throughout the plate thickness, whereas the A_0 mode has almost uniform out-of-plane displacement. So in principle, both modes could demonstrate reasonable sensitivity to defects anywhere in the thickness. However, this is not the case for the S_0 mode. It has been shown that the S_0 mode cannot detect delaminations at certain locations through thickness because the reflected wave is strongly dependent on the position of the delamination [46]. This limits the application of the S_0 mode for detecting delamination in composites.

Guided wave modes can be excited and measured using various types of transducers. Wedge transducers [34], phased array transducers [47], piezoelectric ceramics [48], and piezoelectric polymers [49] are among the used contact transducers. Several non-contact transducers are the air-coupled transducer [50], optical fibre [57],

laser [58] and electromagnetic acoustic transducers (EMATs) [53]. From literature, each transducer has its advantages, limitations and use for specific application [21] and few are readily applied to composite material. For monitoring structures with access restricted to one side of the panels, the use of an air-coupled transducer or a single contact transducer is more favourable [50]. However, loss of information was observed when using air-coupled transducers due to energy leakage into the air [54]. The use of EMAT transducers is particularly effective for generating shear horizontal wave, although its application is normally restricted to metallic structures [55]. The use of contact piezoelectric elements to excite the guided waves seems to be attractive as it is cheaper than other types of transducers. The piezoelectric elements could be utilized online to record dynamic signals, such as foreign object impact [56]. To allow a rapid and automated scanning, laser monitoring can be used to monitor the guided wave propagation [57–59].

In a number of studies the symmetric mode was chosen as there is basically no dispersion for frequency-thickness products up to 1 MHz-mm. However, the problem associated with this mode is that a tricky transducer setup has to be employed in order to obtain the single symmetric mode signal [50, 60, 61]. Based on the mode conversion from longitudinal or shear waves, the S_0 mode can be generated if it is excited at particular frequencies with proper incident angles [44]. Piezoelectric transducers bonded on both surfaces of a plate are often used to generate the S_0 mode. Meanwhile, the A_0 mode can be excited rather easily by means of a single piezoelectric transducer [48]. When voltage is applied to the piezoelectric element polarized in direction of its thickness it expands and contracts. This generates a vertical force on the plate surface and excites primarily the A_0 mode as the resulting normal stress is antisymmetric [44, 62]. Although the transducer is optimized for a particular mode, the S_0 mode is also excited due to the finite transducer size. However, small amplitude of the S_0 mode was typically found, about 10% or less of the amplitude of A_0 pulse, hence the energy transferred to the S_0 mode can be neglected [56, 63].

2.4 Guided waves in composite plates

Knowledge of the properties of guided wave propagation in composites is important for the successful implementation in NDE and SHM systems. The properties of guided waves in anisotropic plates are more complicated than those in isotropic plates [27, 42]. For waves propagating in composite laminates, the wave interaction depends on many factors such as the excitation frequency, geometry of the structure, material properties, direction of propagation, and interlaminar conditions [64–66]. The key topics to understand guided wave propagation in composite plates are direction-dependent velocity, beam steering and wave attenuation [42].

Direction-dependent velocity is one of the interesting features of guided waves in anisotropic media. Knowledge of the group velocity and its direction is needed when considering the propagation path of a wave packet for calculating the arrival time, defect location and area coverage of the inspection. For a unidirectional plate for example, it is observed that the S_0 mode at low frequency with a predominantly in-plane mode shape has a phase velocity along the fiber direction about three times higher than perpendicular to the fibers, in line with the higher modulus along the fibers. For a cross-ply plate, significant direction-dependent velocity of the S_0 mode can also be observed [36, 67], but the predominantly flexural (out-of-plane) A_0 mode propagates at almost constant group velocity in all directions [67].

It has been shown [68] that the energy of a guided wave in an anisotropic plate travels normal to the phase slowness surface. The slowness is defined as the inverse of the phase velocity. Naturally, the energy is transported at the speed of the travel of wave packet, which can be assumed to be equal to the group velocity. However, such a relationship does not always hold in absorbing plates such as composites or if a highly attenuative wave is described. In the case of an absorbing plate in vacuum, it has been shown numerically that the energy velocity can differ substantially from the group velocity, especially at locations on the dispersion curves where the attenuation is high. In

such cases, the group velocity can show discontinuities and produce high velocity values. Therefore, the energy velocity should be preferred as the correct measure of velocity when predicting a wave packet in composite plates. However, the group velocity is much quicker to calculate and is likely to be acceptably accurate unless the attenuation is strong [69].

Another feature of the wave propagation in anisotropic media is the effect of elastic properties that concentrates the energy of waves in specific directions while decreasing the energy in other directions [60, 70]. This is called the beam steering. It has been shown that the anisotropy of the composite materials will steer the guided waves into the direction of the fiber instead of propagating uniformly in all directions. The complexity of the wave characteristic being dependent on the fiber arrangement is significantly related to the composite layup sequence [67, 70]. Hence, the direction of fiber alignment must be taken into account as this is important for a transducer design, i.e., phase arrays and wedge transducers [21]. Such devices would need to perform their wavelength-matching in an angular-dependent manner. Furthermore, an increase in elastic properties will increase the speed of the guided waves and an increase in density would have the opposite effect [41]. These are some of the variations in the wave properties that could complicate the process of monitoring composites. For successful SHM of composite structures, the accuracy of these wave parameters is vital for sizing and localizing defects.

Finally, a brief introduction to the attenuation of guided waves in composite plates is presented here. In composite materials, the fibers act as scatterers for the acoustic waves. The composite matrix material is responsible for the viscous damping that causes the absorption of some wave energy [71, 72]. On top of these phenomena, beam spreading occurs [72]. The attenuation of the guided wave in composite plates is significant and affects their detectability after propagation over a long distance. Results shown in [42] illustrate the large differences between the level of attenuation of the

different modes. It has been seen that the attenuation is dependent on both frequency and the phase direction [42, 67]. The attenuation is strongly related to the phase velocity dispersion, where greater frequency dispersion leads to larger attenuation. Attenuation of guided wave does not follow any well-known explicit mathematical function; instead it is dependent on mode shape and frequency [39, 42]. Large and sudden increases in attenuation are connected to the mode shape changing with frequency. It has been shown that the attenuation of the S_0 mode in a unidirectional plate changes drastically as the frequency increases [42]. For a quasi-isotropic plate, it has been shown that the attenuation of the A_0 mode is steadily increasing with frequency and the other modes (S_0 and SH_0) show a more complicated behavior [42]. But the most notable difference between the S_0 and A_0 modes is that the attenuation is much lower for the S_0 mode because the strain energy of the S_0 mode is dominated by the fibers whereas that of the A_0 mode involves the matrix, in which the viscoelastic damping occurs [42]. From a practical point of view, knowledge of the attenuation is crucial for determining the possible inspection range of any chosen mode or which modes are likely to be detected and which are likely to be attenuated

2.5 Guided wave scattering at defects

In general, when a guided wave is incident on a structural discontinuity, it is scattered in all directions. The structural discontinuity could be damage (cracks, delamination, etc.), structural features (stiffener) or a structural boundary. Scattering of guided waves by defects in a composite structure is a complex problem for NDE [64, 73, 74]. Scattering characteristics such as arrival time, amplitude, frequency content, attenuation, reflected and transmitted waves are normally used to explain the wave propagation in the defective area [74–77]. There have been several studies to investigate the scattering and mode conversion of guided waves from various types of defects [78, 79]. Strong interaction between the incident wave and defect is important for sizing and localizing the defect [46]. However, the interactions are strongly dependent on the mode of the incident wave and the size of the damage [74, 80]. The most important key in using guided waves

successfully is to understand the relationship between the characteristic of a defect and the scattered waves.

The increasing use of guided waves in NDE has led to studies on guided wave scattering at defects using numerical methods such as Finite Element Modeling (FEM). Commercial finite element software packages such as ABAQUS and ANSYS are normally used for the simulation [81]. A comprehensive two-dimensional (2D) finite element analysis of wave propagation and scattering in composite can be found in [46, 79, 82]. Limited publications were found for the analysis using three-dimensional (3D) FE models [74, 83–85]. The combination of several damage mechanisms for realistic impact damage using 3D FE analysis makes the accurate modeling more challenging, which limits the studies employing full 3D analysis.

2.5.1 Scattering at cracks

The investigation of the scattering of guided waves by cracks is necessary in order to develop an ability to characterize cracks and predict the reliability of guided wave NDE. The scattering of guided waves by cracks in a composite plate has been studied by several investigators. In general, the studies have shown the occurrences of mode conversions, a relation between signal parameters and crack size, a directivity pattern and the ability to characterize cracks.

A parametric 2D FE was used for sizing a cracked zone caused by a linear and uniform impact on a composite plate [85]. It was found that assessing the relationship between crack parameters and the scattered wave is rather difficult for anisotropic laminates [64, 85]. Bratton and Datta [87] combined analytical and FE techniques to predict scattered fields from arbitrary shaped cracks. They found no simple relationship between the reduction of the amplitude of the S_0 mode and the depth of a symmetric crack, but the results clearly show the influence of increasing crack depth on the scattered signal. Using Strip Element Method (SEM), Liu et al. [88] found that the intervals of the

time-harmonic responses in the region between two crack tips are dependent on the crack depth and less dependent on the crack length. Experimental validation by Toyoma et al. [89] reveals that the stiffness modulus in cross-ply composite laminates and the velocity of the S_0 mode decreased as the transverse crack density increased. This finding has led them to propose a rapid measurement to detect cracks using the S_0 wave speed [90].

The reflection and transmission of an incident wave mode after scattering from cracks in a composite plate have been considered by several investigators. Karunasena et al. [73] have shown that the numerical reflection coefficients of the S_0 incident mode behave significantly different from those of the A_0 incident wave with crack length. Wang and Rose [91] have provided further insight into this reflection problem using a 1D FE approach. It was found that the reflection and transmission ratios depend strongly on the frequency of the incident flexural waves, as well as the size of the damage. Karim and Kundu [67] studied scattering of the A_0 mode in a layered composite plate by interface cracks using a boundary integral formulation. It was found that the reflection coefficient approaches zero as the length of the crack becomes the same as the thickness of the plate.

It was found that the crack length can be approximately determined from a pattern change of the wave signal response [88]. Ju and Datta [65] quantitatively characterized cracks using a hybrid method combining boundary integral and FE techniques to investigate the time domain response in transversely isotropic plates. A 2D finite element-based inverse technique for sizing a cracked zone inside a composite plate was developed and applied to quantify width and depth, representing the dimension of a triangular-shaped crack [86].

An analytical study on graphite-epoxy composite plates has shown that an incident S_0 wave mode on a single surface crack can be scattered and mode converted into three

propagating modes (S_0 , A_0 and A_1) [67]. An experimental observation by Willberg et al. [78] showed that the symmetric S_0 mode continuously converts into the A_0 mode without passing a discontinuity in a multi-layer composite plate. This effect causes a considerably more complex wave field and makes the detection and localization of failures more complicated.

The directivity pattern of the scattered A_0 wave mode around a defect representing cracking in the composite material, modeled as a 3D conical shape with decayed material properties, has been predicted [84]. A general solution to the dynamic interaction problem of a matrix crack with an imperfectly bonded inhomogeneity was discussed [92]. The analytical study shows that the anti-plane stress field at the matrix crack attains a value mostly lower than the dynamic single crack solution. Some of the work presented here has successfully shown a reasonable match between experimental measurements and FE predictions using a defect implementation in three-dimensional (3D) FE simulations as a square delamination with a layer of reduced stiffness [93, 94].

2.5.2 Scattering at delaminations

Delamination is a critical failure mode in composite laminates. It may lead directly to through-thickness failure owing to interlaminar stresses, which can greatly reduce the residual compressive strength. The scattering of guided waves by delaminations in a composite plate has been investigated by many researchers. Scattering evaluation by means of reflection, transmission, mode conversions, and scattering patterns at a delamination were reported.

From 2D FE simulations, it was demonstrated that the reflected wave of the incident S_0 mode is strongly dependent on the position of the delamination through the thickness, and no wave reflection takes place when the shear stress is zero at that interface [46, 95]. The A_0 mode was found to be more sensitive to a delamination than the S_0 mode [32, 95]. From a 1D analytical solution, the reflection and transmission ratios

were found to depend strongly on the frequency of the A_0 mode, as well as the size of the damage [91]. An analytical model using flexural wave scattering analysis has shown that the reflections from the first and the second edge of a delamination appear when the delamination length increases [96]. Hu et al. [97] confirmed this via an experimental study, and also showed that the reflected wave from the entrance of a delamination is slightly higher than that from the exit of the delamination. It was also shown that the amplitude of reflection from short delamination is higher than that from long delaminations due to overlapping of reflections from the ends of short delaminations. An increase in magnitude of the reflected signals as well as a decrease in the arrival time with the extent of the defect was demonstrated [99].

Mode conversion caused by the scattering at symmetrical and anti-symmetrical delaminations has been studied comprehensively through 2D FE simulations [79, 82]. Mode conversion from the A_0 mode to the S_0 mode was observed when the guide wave propagates across the delamination [100]. Kazys et al. [54] confirmed this phenomenon through experimental works. No mode conversion can be observed when the S_0 mode passed through delaminations in a unidirectional plate [101]. Using 3D FE, it was also observed that there is little or no converted S_0 mode when the A_0 mode encounters delaminations located at a symmetric interface [80]. It was also found that guided waves propagate independently in the sub-laminates. From numerical and experimental investigations of the A_0 mode, it was concluded that modes with high amplitude within the delamination transmit most of the energy to the undamaged side [102].

Using numerical simulations, it was found that the amplitudes around a circular delamination showed a large forward scattered wave relative to the reflected pulse [74], [103]. The behavior of the backward scattered amplitude is generally more complicated than that of the forward scattered amplitude, and is generally smaller in magnitude particularly for larger delamination diameter to wavelength ratio [74]. The amplitude of the A_0 mode at the delamination can be seen to decrease [104], due to more incident

waves being scattered at the delamination site, contributing to greater dissipation of wave energy [96]. Both 2D FE and experimental studies show comparable results. The interaction of the A_0 wave mode with various sizes of rectangular delamination has been shown in a 2D configuration [95]. Ng et al. [74] have demonstrated that 3D simulations can accurately predict the scattering characteristics of guided waves at a circular-shaped delamination. The experimental approach for studying scattering patterns has shown good agreement with the results obtained by the Strip Element Method [97].

Delaminations can be located by estimating the propagation speed and travelling time from the reflected signal [105]. It was found that the size of a delamination can be predicted using time of flight of mode converted waves, and the findings were in good agreement with experimental values [100]. It has been found that this technique using the A_0 mode is more effective than that using the S_0 mode for delaminations with short lengths or located near the mid-plane of laminates. The A_0 mode has been employed to detect the delamination in composite structures [98]. Kang et al. [96] also showed satisfactory detection of a delamination (placed at mid plane) using a wavelet transform technique of the S_0 mode signal. Through-thickness delamination can be located and sized by capturing the reflected waves at both ends of the delamination [95]. Distinct zones and the size of a delamination in quasi-isotropic composite laminates were identified in B-scan images employing the A_0 mode [106]. From an experimental approach, Toyama et al. [89] investigated delaminations that developed from crack tips and found that the stiffness decreased, but claimed that the velocity increased as the delamination length increased. This research demonstrates a promising SHM system for detecting and quantifying delamination length in composite laminates.

2.5.3 Scattering at impact damage

In the previous section, typically artificial damages were investigated. This includes three-point bending, four-point bending and Teflon insertion to replicate delaminations. Limited studies were found for the monitoring of real impacted composite plates [35, 54, 107]. It

appears that every composite material has unique scattered wave patterns after being impacted. For example, the scattering at a crack in a $[0^\circ/90^\circ]$ plate will be completely different to a similar crack in unidirectional composite plates. Several patterns of impact damage in composite plates were reported [4, 8, 108]. It was concluded that the impact is a simple event, but results in complex damage modes, where the complexity is significant.

The sensitivity of the A_0 mode to real impact damage was studied experimentally in quasi-isotropic composite plates, excited at 20 kHz [107]. It was observed that even though the aspect ratio of the transmitter was high and the longitudinal mode dominant, significant wave propagation was generated across the width of the plate producing unwanted signals between excitation and reflection. From an experimental approach using indentation technique to create an impact damage, the attenuation of the A_0 wave signal was found to increase when monitored at the impacted region technique [109]. Increased amplitude of the A_0 at the impact location and a repeatable scattering pattern with significant amplitude reduction of the guided wave propagating past the damage location was observed experimentally [93, 110]. An experiment to locate a point of impact on a $[0/90]$ composite plate was carried out [35]. It was shown that the point of impact can be correctly predicted if the correct wave velocity is known [35]. Significant errors are introduced in the impact point prediction if the guided wave velocity in the plate is assumed to be constant. Real impact damage was characterized using a X-ray computed tomography (CT) scan of a damaged composite sample and used as the basis for a numerical model implementing the complex delamination geometry [83]. The incorporation of the CT scan into FE simulation was accomplished by turning the CT scan images into an image stack. The image stack was converted into a matrix containing 3D locations of the complex geometry. This helps future FE modeling of realistic impact damage.

From the literature, the potential for the detection of cracks, delaminations, and impact in composites has been demonstrated, but the interaction of the guided waves

with the complex and multi-mode impact damage requires improved understanding. Varieties of factors affect the propagation and scattering of guided waves in composite structures and could lead to inaccurate monitoring and defect detection results.

2.6 Conclusions

From the literature review, it has been shown that impact damage in composite plates is complex. Guided waves offer an effective method to detect and characterize different kinds of impact damages but the scattered waves are complicated. Many factors could affect the wave propagation and scattering. The plate geometry, material properties, fiber arrangement, fiber orientation, transducer frequency, excitation mode and type of impact damage are among the factors. Building on the literature, the A_0 mode was chosen to be explored in this study. Although the attenuation of the A_0 mode is higher than for the S_0 mode, the A_0 mode was selected for this study because of its known detection capability for delaminations at any depths, limited direction-dependency of its wave velocity, and the selective excitation by means of a piezoelectric transducer with single-sided access. Limited studies were found on monitoring real impact damage in composite plates. This motivates the author to study the interaction of guided waves with real impact damage in composite plate. This study could then provide an insight for the SHM of composites.

CHAPTER 3 EXPERIMENTAL MEASUREMENTS

This chapter presents the details of the experimental part of this study. Experimental studies were conducted to investigate the guided wave propagation and scattering by impact damage. As mentioned previously in Chapter 2, the first anti-symmetric guided wave (A_0) mode was used in this study. Two sets of guided wave experiments were performed. The first set of experiments was performed on four undamaged composite plates with different thicknesses and material properties. The aim was to measure wave propagation characteristics for comparison with the FE analysis and analytical predictions. This later served as baseline data for the damage characterization. The second set of experiments was performed on two defective composite plates for the detection and characterization of impact damage. A conventional ultrasonic C-scan technique for estimating the size and shape of the impact damage was performed.

3.1 Specimens

Four composite plates were used in this study. The first two specimens were supplied by Imperial College London. Another two specimens were supplied by the Composite System Innovation Centre, University of Sheffield. Details of the specimens can be found in Table 3-1.

The first plate was a large cross-ply carbon fiber plate, shown in Figure 3-1 (a). The plate was constructed from 24-prepreg plies in alternating $[0^\circ/90^\circ]$ orientations, with symmetry at the mid-plane. The material of the prepregs was HEC fiber (60%) / SE84 HT epoxy (40%). Each ply has a nominal thickness of 0.15 mm, giving the total plate thickness of 3.6 mm. The second plate was a small unidirectional plate, shown in Figure 3-1 (b). Due to manufacturing problems, this unidirectional (UD) plate was produced with small dimensions. The plate was constructed from 24-prepreg plies in parallel alignment. The material of the prepregs was the same as that used for the cross-ply carbon fiber plate. Nominal thickness of each ply was 0.15 mm and the thickness of the plate was 3.6 mm. The material properties of these specimens were characterized at the University of

Bordeaux in France using air-coupled ultrasonic bulk waves. Measurements of the cross-ply plates were performed at 0.5 MHz and 1 MHz, while the unidirectional plate was measured at 2 MHz. Details of the measurement can be found here [111]. Due to the difficulty in the measurements, the uncertainty in the complex stiffness constants (C_{ij}) varies significantly. Resulting stiffness components, real and imaginary parts, are presented in Table 3-2 and Table 3-3, respectively for the cross-ply and unidirectional plates. The corresponding coordinate system of the plate geometry is presented in Figure 3-3.

The final two plates were small cross-ply plates, consisted of 8-prepreg layers with a symmetric layup sequence of $[0/90]$. The plates were manufactured using carbon-fiber Tenax HTS (65%) pre-impregnated with Cytec 977-2 epoxy resin (35%). Ply thickness was 0.25 mm and 8 plies were used, giving the plate thickness of 2 mm. These plates also contained two additional layers of flexible printed circuit boards made of a 18 μm thick layer of copper and 25 μm thick polyimide film, which had been used for electrical resistance measurements at the University of Sheffield [19]. The additional layers were neglected for the simulations as they were too thin to significantly influence the wave propagation characteristics. As shown in Figure 3-2, the center of the plates were subjected to a 7.4 J impact using a hemispherical 15 mm impactor head, following standard drop weight impact procedures. In order to reveal the extent of the impact damage, an X-ray imaging was performed on a different plate from the same lot after the impact. A small degree of fiber fracture and indentation was just about visible on the surface of the plates, as shown in Figure 3-6. Based on the X-ray image, the size of impact damage can be estimated to be about 10 mm length, 20 mm width. Additional impacts were also performed in one of the plate, creating impact damage close to the edge. However, the measured ultrasonic signals were quite complicated because of the multiple reflections from the plate edges that cannot be separated. Hence, these measurements were not continued.

Table 3-1: Composite specimens.

Test plates	Fiber arrangement	Plate size (mm)	Thickness (mm)	Density (kg/m ³)
Large cross-ply	24-ply; [0°/90°] _{6s}	1140 x 940	3.6	1550 [42]
Small cross-ply	8-ply; [0°/90°] _{2s}	990 x 110	2	1350
UD plate	24-ply; [0°] ₂₄	245 x 200	3.6	1550 [42]

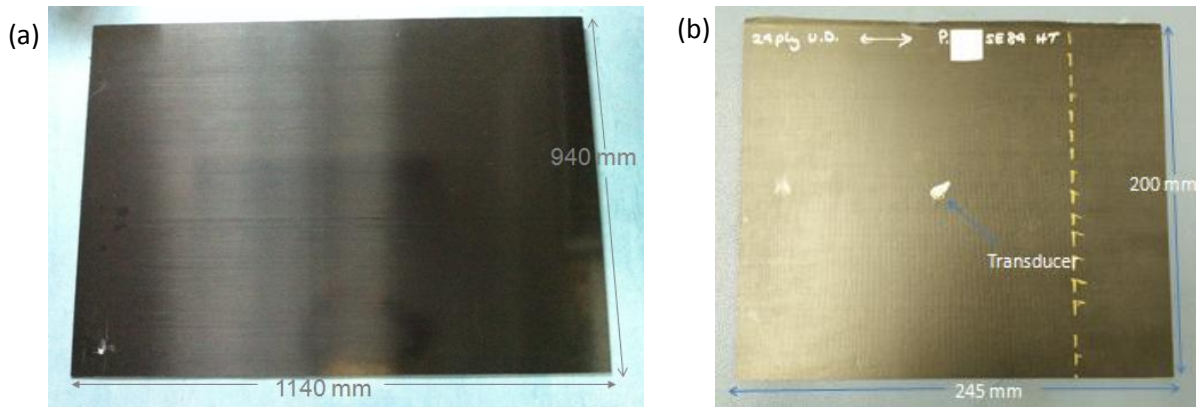


Figure 3-1: (a) Large cross-ply plate; 24 plies of [0°/90°]; symmetry at the mid plane; 1140 mm x 940 mm; (b) Unidirectional plate; 24 plies of [0°]; 245 mm x 200 mm; undamaged plate.

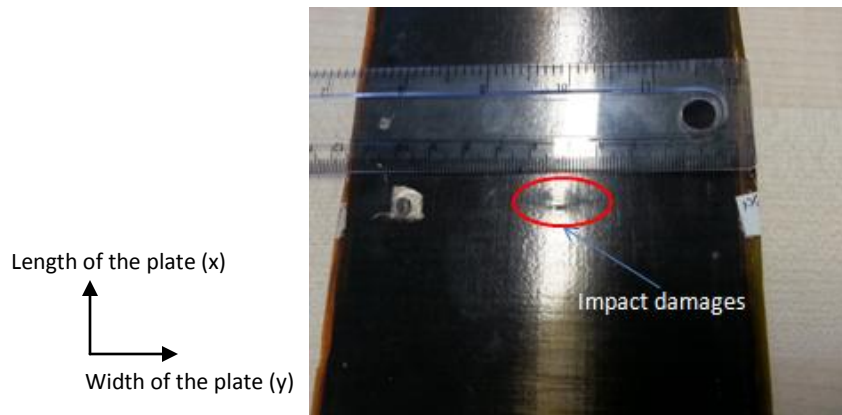


Figure 3-2: Small cross-ply plate; 8 plies of [0°/90°]; symmetry at the mid plane; 990 mm x 110 mm; approximate impact damage of 10 mm length, 20 mm width.

Table 3-2: Measured material properties of the large cross-ply plate $[0^\circ/90^\circ]_{6S}$; characterization frequencies: 0.5 MHz and 1 MHz; obtained at University of Bordeaux, France [69, 126].

Stiffness constants of Carbon epoxy $[0/90]$ (GPa)	
C_{11}	$12.15 + i0.34$
C_{12}	$8.39 + i0.88$
C_{13}	$7.73 + i0.65$
C_{22}	$70.87 + i9.19$
C_{23}	$5.6 + i0.60$
C_{33}	$64.24 + i10.1$
C_{44}	$4.7 + i0.28$
C_{55}	$3.06 + i0.19$
C_{66}	$2.97 + i0.20$

Table 3-3: Measured material properties of the unidirectional plate; characterization frequency: 2 MHz; obtained at University of Bordeaux, France [69, 126].

Stiffness constants of Carbon epoxy UD (GPa)	
C_{11}	$12.56 + i0.34$
C_{12}	$6.87 + i0.25$
C_{13}	$6.47 + i0.65$
C_{22}	$13.15 + i0.65$
C_{23}	$5.6 + i0.60$
C_{33}	$109.9 + i8.23$
C_{44}	$4.7 + i0.28$
C_{55}	$4 + i0.25$
C_{66}	$2.27 + i0.25$

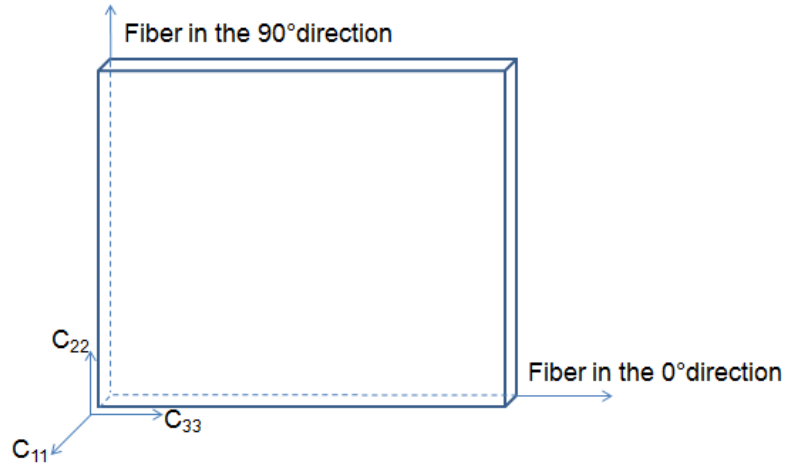


Figure 3-3: Coordinate system of the plate geometry and the direction of the material properties.

3.2 Experimental setup

3.2.1 General setup

The setup for the guided wave measurements consists of an existing modular scanning rig controlled via LabView from a computer. Figure 3-4 illustrates the general setup for guided wave testing. Figure 3-5 shows the guided wave monitoring system for composite plates. The excitation signal is generated by a function generator (Agilent 33220A) as a voltage signal, amplified by a wide band amplifier (Krohn-Hite 7602M) and then applied to a piezoelectric transducer. A laboratory-made piezoelectric transducer was used to excite the A_0 wave mode as in Figure 3-6. The displacement field in the specimen is measured using a commercially available heterodyne laser vibrometer (Polytec OVF 5000), controlled by the scanning rig that moves parallel to the specimen. The time traces (voltage signal) of the received signals were filtered using a bandpass filter (Krohn-Hite 3945). The cut-off frequencies were set as $\pm 25\%$ of the pulse center frequency. The signals were recorded and averaged (20 averages) using a digital storage oscilloscope (Le Croy 9304) to improve the signal-to-noise ratio. The function generator triggers the oscilloscope so that the excitation and measurement start at the same time. The measured time traces were then transferred to the computer and further analyzed using MATLAB. Different types of signal processing techniques were used to extract information from the time domain signal, further described in the following sub-chapters.

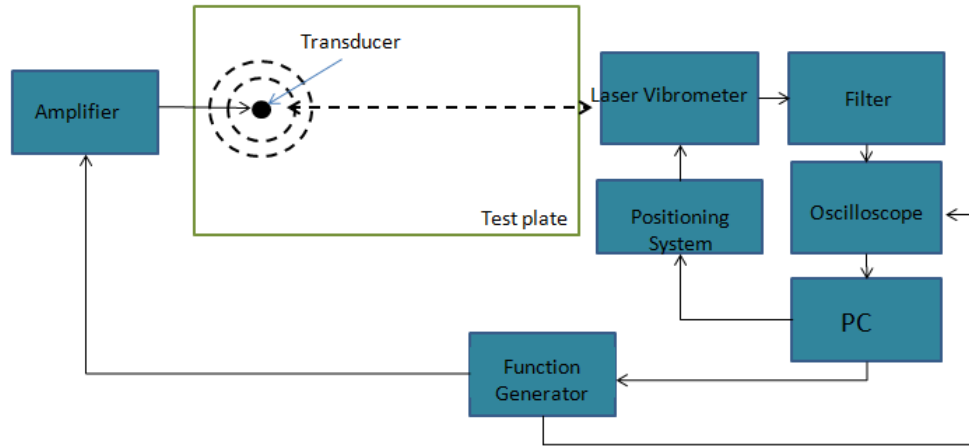


Figure 3-4: Schematic diagram of guided ultrasonic wave experimental setup.



Figure 3-5: Guided wave monitoring system with the defective composite plate.

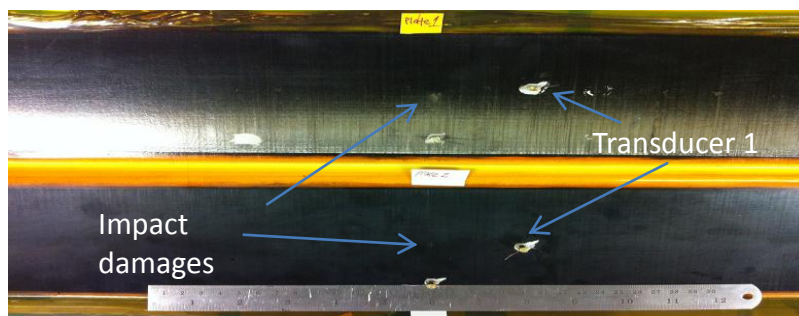


Figure 3-6: Transducer locations on the small cross-ply plates.

3.2.2 Signal excitation

As discussed in Chapter 2, it was decided to use the first antisymmetrical (A_0) guided wave mode below the cut-off frequencies of the higher order modes. The A_0 mode can be easily excited and received using a simple piezoelectric element [112] as it has a significant out-of plane displacement. Figure 3-7 shows the piezoelectric transducer consisting of a piezoelectric disc and a backing mass that was constructed in the lab. A Ferroperm ceramics Pz27 disc (diameter: 5 mm; thickness: 2 mm) was used as the material of the piezoelectric transducer, polarized through the thickness. The disc acts in good approximation as a point source and the waves propagate radially outwards. Referring to [112], it was found that the signal performance was not significantly affected by disc size. A brass backing mass (diameter: 5 mm; thickness: 6 mm) was carefully bonded to the piezoelectric disc using Loctite 2-part epoxy glue. Experiments with different heights of brass backing materials have shown that the brass backing mass improved the transducer performance [112]. Electrical voltage is applied via a copper wire that was soldered to the backing mass. The piezoelectric transducer was directly bonded onto a thin layer of silver coated paint (Electrolube SCP03B) on the composite plate using epoxy glue. The use of silver paint acts as ground connection for the transducer. When the voltage is applied to the piezoelectric transducer, the piezoelectric disc contracts and expands. This generates a vertical force to the plate surface and excites primarily the A_0 mode. Good and repeatable signals were obtained.

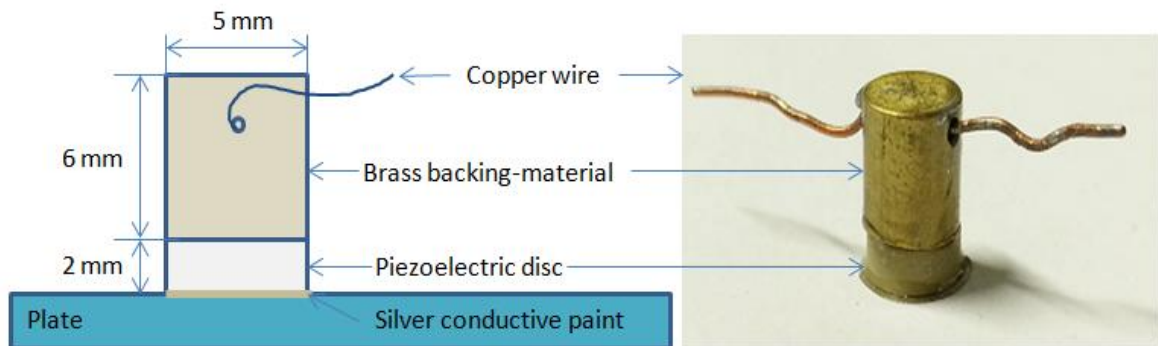


Figure 3-7: Schematic and photo of piezoelectric transducer made of Ferroperm disc and brass backing mass.

In order to avoid the complication of multiple wave modes, the maximum excitation frequency is often chosen well below the lowest cut-off frequency of the higher modes. For composite plates with a thickness of 3.6 mm for example, this limits the maximum frequency range to about 270 kHz, and gives a minimum wavelength of 17 mm. The typical excitation frequency was chosen to be 100 kHz, where there was a good tradeoff between lower wave attenuation and good transducer sensitivity.

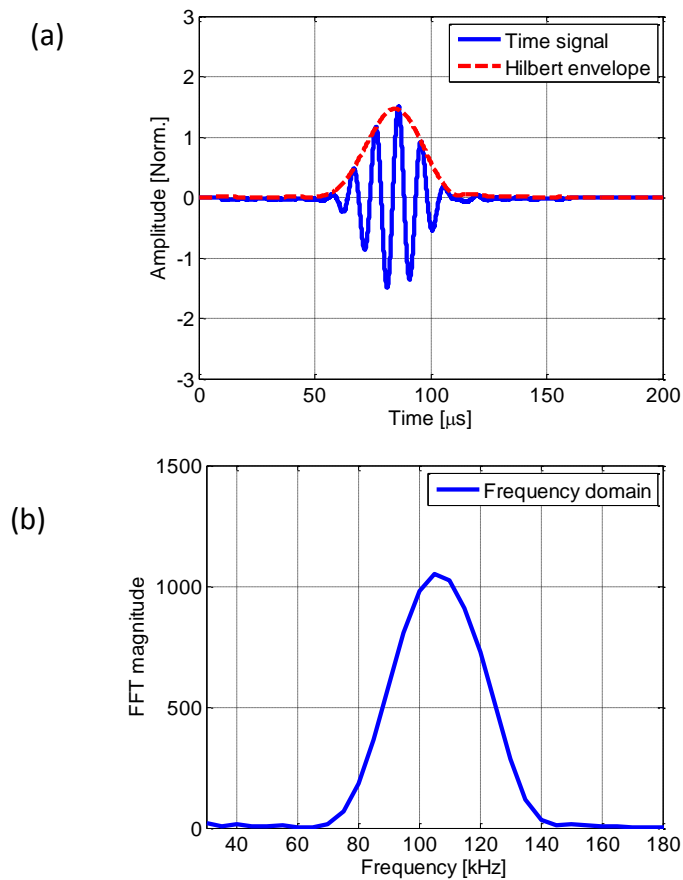


Figure 3-8: (a) Typical measured time signal (blue line) and its Hilbert envelope (dashed red line), (b) frequency domain transform of the time signal; 5-cycle excitation frequency at 100 kHz in the large cross-ply composite plate; measured 50 mm from the excitation point.

The excitation signal was a 5-cycle Hanning windowed toneburst generated by a programmable function generator and then amplified to 200 V peak to peak. The Hanning windowed function produces a short pulse and narrowband signal with energy concentrated around the center frequency. Short pulse allows a time separation between different pulses [113]. A narrowband signal is required to avoid signal distortion due to the dispersive character of the A_0 mode. The pulse width of the signal can be controlled by the number of cycles and center frequency as per Eq. 3-1:

$$Pulse\ width = \frac{no.of\ cycles}{center\ frequency} \quad Eq. 3-1$$

Figure 3-8 shows a typical measured signal. A good signal to noise ratio was achieved as can be seen from the time signal. The energy of the pulse was concentrated close to the center frequency.

3.2.3 Laser monitoring

The wave propagation and scattering around defects is measured using a commercially available heterodyne laser vibrometer fixed to a scanning rig, which permits the non-contact and remote sensing of the guided waves. The voltage signal corresponds to the velocity of the out-of-plane-displacement of the specimen surface [58]. The laser beam diameter is well below 0.1 mm. This allows an accurate point measurement of the wave propagation on a test structure. The movement of the laser interferometer for various monitoring approaches is controlled using a positioning system.

Figure 3-9 shows the position for the laser monitoring on the undamaged unidirectional specimen. The laser interferometer was moved parallel to the plate to perform line scans (in 0° direction) over a length of 100 mm from the excitation transducer with 1 mm step size. For the large cross-ply plate, the line scans were performed over 200 mm distance due to bigger plate size. Circular scans were performed at 30 mm radius every 5° around the transducer in order to obtain the wave profile

around the excitation. These measurements on the undamaged part of the specimens served as the baseline measurement and the results are discussed in Chapter 5. For the purpose of observing the directionality pattern of the wave propagation, 100 mm line scans were performed in different directions (from 0° to 90° with 15° step size). Due to the smaller width specimen size, the directivity scans were not performed on the small cross-ply plate.

The wave scattering by the impact damage was measured on the small cross-ply plates, where the plates had barely visible impact damage from the impact test. Two sets of measurements on damaged composite plates were performed. For the first set, the transducer was initially placed at 50 mm distance to the impact damage in order to get high incident wave amplitude. Then, the transducer was moved to 100 mm from the impact damage to observe reflections by the impact damage. Figure 3-10 illustrates the geometry of the composite plate specimens, with the impact damage approximately in the center, as well as the laser measurement locations. Three types of scans were used; (i) 200 mm horizontal scans in (0° direction) over the impact damage from the transducer location with 1 mm step size, and 200 mm symmetrical horizontal scans over the undamaged plate part; (ii) circular scans with 30 mm radius measured every 5° around the impact damage, and 30 mm symmetrical circular scan on the undamaged part; and (iii) raster scans of the 40 mm x 40 mm area containing the impact damage with a step size of 1 mm in both directions. The time traces of the received signals were collected and further processed as described in the section below.

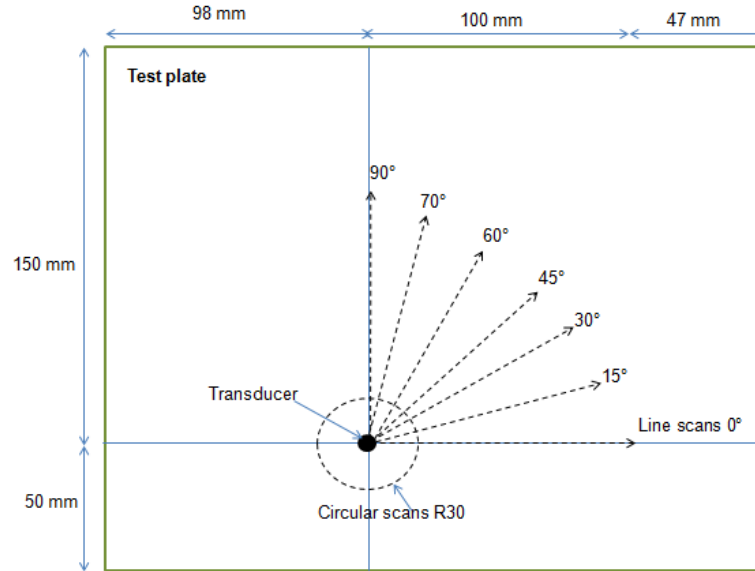


Figure 3-9: Position of the laser monitoring; 100 mm line scans in 0° to 90° directions with 15° step size for the unidirectional plates; 200 mm line scans in 0° to 90° directions with 15° step size for the large cross-ply plate; 30 mm radius of circular scan around the excitation;

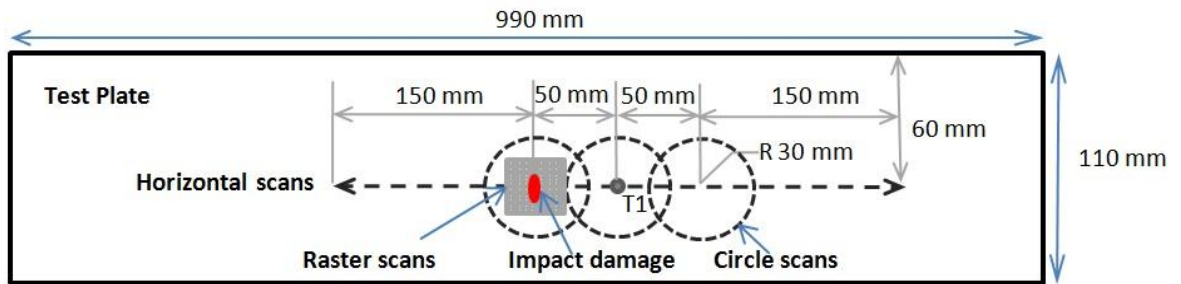


Figure 3-10: Geometry of the small cross-ply plate and laser monitoring positions for monitoring the impact damage; 200 mm line scans (left and rightward from transducer); 30 mm radius circular scan around transducer; 30 mm radius circular scans around impact damage and symmetric to the impact location; raster scan of 40 mm x 40 mm square with 1 mm step size.

3.2.4 Data processing

The measured signals were further processed in MATLAB for evaluation. Initially it was necessary to eliminate unwanted signals due to background noise. The signals were initially filtered using a Butterworth band pass filter to improve the signal quality. The 5th order Butterworth band pass filter was applied to the acquired signals and they were filtered at $\pm 50\%$ pass band of the center frequency. However, further improvements to the transducer led to significantly improved signal quality, and removed the need for the additional filter for all results presented in this thesis. For the line and circular measurements, Hilbert transform was applied to the received time traces and the peak amplitude was extracted. The arrival time of the peak of the signal envelope was used for group velocity measurement. Fast Fourier transform (FFT) was applied on the time-gated signal for the phase velocity measurements, and the amplitude and phase values at the center frequency were extracted. The next section details the measurements of the received signals.

3.3 Experimental measurements

3.3.1 Attenuation

In general, ultrasonic wave signals in any material will experience decay in amplitude with propagation distance due to the material damping. The wave attenuation coefficient is normally used to describe the reduction in the signal amplitude. For guided waves that are propagating from a point source, the reduction in its amplitude not only represents the material damping but is also affected by the geometrical wave spreading [72]. Wave spreading is described as the loss of amplitude due to the growing length of the wave front departing into all directions from a source. Without damping the energy radiated outward from a point source would be the same at any radial distance r , with the amplitude A equal to the square root of the energy (Eq. 3-2). By rearranging the equation, the reduction in signal amplitude is then inversely proportional to the square root of the radial distance from the source, as defined in Eq. 3-3. Meanwhile, the wave attenuation

due to material absorption is assumed to result in exponential decay of the amplitude with distance of propagation, as defined in Eq. 3-4.

$$A_1^2(2\pi r_1) = A_2^2(2\pi r_2) \quad \text{Eq. 3-2}$$

$$A_2 = A_1 \frac{1}{\sqrt{\frac{r_2}{r_1}}} \quad \text{Eq. 3-3}$$

$$A_2 = A_1 e^{-\alpha(r_2-r_1)} \quad \text{Eq. 3-4}$$

$$A_2 = \frac{A_1}{\sqrt{\frac{r_2}{r_1}}} e^{-\alpha(r_2-r_1)} \quad \text{Eq. 3-5}$$

$$\alpha = \frac{1}{r_2-r_1} \ln \left(\frac{A_2 \sqrt{\frac{r_2}{r_1}}}{A_1} \right) \quad \text{Eq. 3-6}$$

where A_1 , A_2 , r_1 and r_2 are respectively the amplitudes and radial distances at two measured locations and α is the attenuation coefficient due to the material damping. Combining these two effects, the amplitude of the signal at distance r_2 is given by Eq. 3-5. Rearranging this equation, the attenuation coefficient can be determined using Eq. 3-6, corrected for the geometrical spreading. Using the experimental signals obtained from the line scans, the amplitude curve can be fitted to Eq. 3-5, and the attenuation coefficient can be estimated using Eq. 3-6. It should be noted that this equation is strictly valid for isotropic plates only and there could be another factor affecting the attenuation measurement in the non-principal directions of a composite plate, which is the effect of the anisotropic beam steering. However, this effect has not been investigated in this thesis.

3.3.2 Phase and group velocities

As discussed in Chapter 2, the phase velocity (C_p) is described as the velocity of propagation of a wave crest along the plate. In experimental measurements, the phase velocity can be determined by using Eq. 3-6. Fast Fourier Transform (FFT) was applied to the signal time traces to obtain the phase change at a given frequency (f .) The phase angle (φ) difference between two points spaced 1 mm apart was calculated and the values were then used in the Eq. 3-7 to calculate the phase velocity. The phase velocities were plotted against the frequency thickness product ($f.d$).

The group velocity (C_g) can be thought of as describing the propagation of group of waves of similar frequency along the plate. To calculate the group velocity, the arrival time of the signal envelopes obtained using Hilbert transform were used to estimate the propagating time between two measurement points spaced 100 mm apart. Then, the group velocity was calculated using Eq. 3-8, where x and t are respectively the distance and arrival time between two readings. It is understood that for a highly attenuative plate such as composites the correct practice is to calculate the energy velocity instead of calculating the group velocity [114]. However, it is acceptable to use the group velocity as the method is much quicker and the wave attenuation is not very strong. The measured phase and group velocities was then compared to the finite element and semi-analytical predictions.

$$C_p = 2\pi f \left(\frac{x_2 - x_1}{\varphi_2 - \varphi_1} \right) \quad \text{Eq. 3-7}$$

$$C_g = \frac{x_2 - x_1}{t_2 - t_1} \quad \text{Eq. 3-8}$$

A slowness value is defined for each wave mode by taking the reciprocal of the phase velocity according to Eq. 3-7. For a given frequency and mode, the value of phase velocity varies with the wave propagation direction. Therefore the slowness curve varies with direction as well.

3.3.3 Complex scattering and baseline subtraction

To obtain the wave scattering, the received signals from the circular scans around the impact damage and a location symmetrically to the impact damage were processed. FFT was applied to the time-gated signals and the complex magnitudes (amplitude and phase) at the center frequency were extracted. Taking the difference between the complex magnitude for each point with and without the defect, the amplitude of the scattered waves at the impact damage can be isolated. Polar plots can then be created for the scattered waves around the impact damage. However, there were inconsistencies in the resulting scattered fields using the FFT extracted information. Therefore the amplitudes of the signal envelopes (Hilbert transform) were used for plotting the scattered field. Consistent and repeatable results were then obtained.

3.3.4 Wave propagation field

As described earlier, an area of 40 mm x 40 mm around the impact damage was monitored using a raster scan with step size 1 mm. Hilbert transform was applied to the received signals and the amplitudes of the signal envelope were used to plot the scattered wave field. No baseline data was required for this purpose. In order to understand the behavior of the propagating wave field in the composite plate with impact damage, a visualization based on the arrival time of each monitored signals was constructed in MATLAB. From this visualization, the wave propagation and wave scattering can be observed.

3.4 Immersion ultrasonic C-scan

In order to obtain an approximation of the size, shape and depth of the impact damage in the defective composite plates, an immersion ultrasonic C-scan method was performed. The method involved the detection of echoes produced when an ultrasonic pulse was reflected from a discontinuity or an interface in the plates. The C-scan inspection was performed on one small cross-ply plate due to the requirement of cutting the plate into a

small piece for immersion in the water tank. The plate was cut to 200 mm length, keeping the 110 mm width. The plate thickness was 2 mm. The impact was located approximately at the middle of the cut-out plate.

A 5 MHz focused ultrasonic transducer was used, where the focal length was 3 inch (76.2 mm). A focused immersion transducer was used because it increases the sensitivity to small defects or other reflectors. For longitudinal wave travelling in thickness direction of the small cross-ply plate at 2700 m/s speed, the wavelength was estimated to be 0.54 mm. The transducer was mounted perpendicular to the surface of the small cross-ply plate. The water path distance between the transducer and the test plate was set to be about 3 inch. The reason was to match the focal length of the transducer, where the signal with the maximum amplitude was located. The scanned area was 40 mm x 40 mm. The inspection resolution was 1 mm in both the x- and y-direction for the amplitude C-scan images.



Figure 3-11: Immersion ultrasonic C-scan system with defective composite plate.

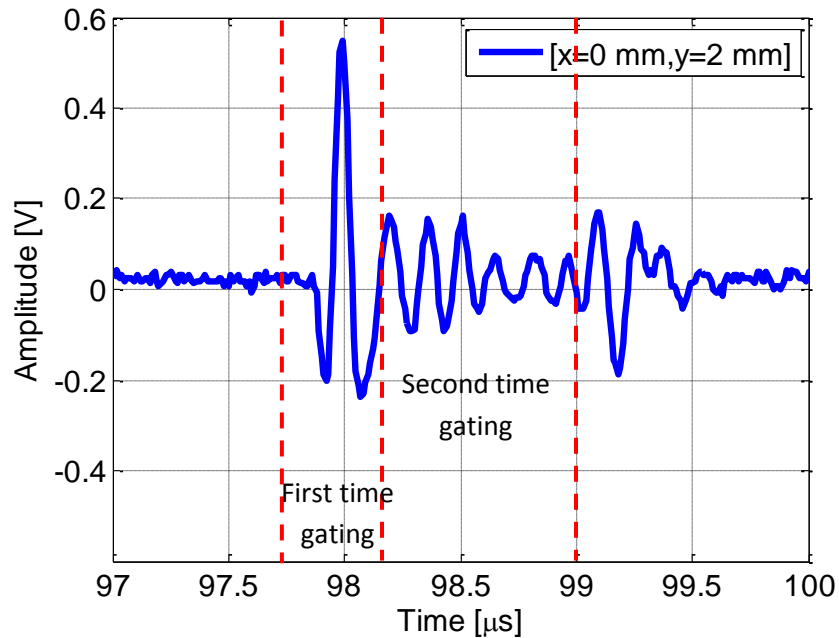


Figure 3-12: Time-gating for the C-scan image acquisition; first time-gating to capture surface reflection; second time gating to capture reflection within plate thickness; measured from the front surface of the 2mm cross-ply plate.

Figure 3-11 shows the immersion C-scan system used for the characterization of impact damage in the small cross-ply plate. The transducer was attached to an automated system that was equipped with a computer-controlled stepped motor driver. Pulse-echo mode was selected in the pulser-receiver unit (Panametric 5601T), where the transducer acted as the signal transmitter and receiver. The acquisition of the scanned area was defined in a Labview program. Two different time gating settings were used as shown in Figure 3-12. The first time gate was set to capture the positive maximum of reflections from the surface. This was performed to obtain the signal variations on the impacted surface. The second time gate was set to capture the negative minimum amplitude. This corresponds to the signal propagated and reflected within the plate thickness. Two scans were performed on the front surface of the specimen to collect the front wall echo and echo through the thickness. For data comparison, another two scans were performed on

the back wall of the plate from the opposite direction. However, the back wall surface was quite rough. Therefore, the investigation on the back surface was eliminated as the results were quite poor and showed significant variation. All the received reflected waves were recorded using an oscilloscope (Le Croy 9304 Quad 175 MHz) and saved in the computer for further analysis in MATLAB. A 100 MHz sampling rate was used during data acquisition. The amplitudes of the received time traces were time-gated and extracted to plot the plan view of the scanned area. Based on the total time of flight in a round trip distance, the depth of the defect location can be estimated.

3.5 Conclusions

This chapter presented the experimental measurements throughout the thesis. A piezoelectric transducer was bonded to the surface of the test plate and generated the A_0 mode in the investigated 4 composite plates. The first part of the work includes the investigation of the wave propagation of the A_0 mode in undamaged composite plates. The aim was to obtain the wave characteristics and the baseline data for damage characterization. The second part of the work investigated the wave scattering in composite plates with real impact damage. Line and circular type of scans were carried out for the purpose of the study. Two methods for imaging the impact damage were performed: guided wave laser monitoring in a square region (raster scan) and a conventional ultrasonic C-scan of the impact damage. All results described in this chapter are presented in Chapter 5 and Chapter 7.

CHAPTER 4 3D FINITE ELEMENT MODELING

This chapter presents the procedure for the 3D finite element modeling of composite plates. The input files for the FE models were created in MATLAB, and then imported into ABAQUS for the simulation and analysis. The composite plate was initially modeled without defect using two different sets of material properties (for the homogenized and individual layer models). Rayleigh damping was added to the model for a comparison between FE models with and without damping. Defects such as delamination and material degradation were introduced in the model for a systematic study. Delamination depth and size were varied to investigate their influence on the scattered guided wave.

4.1 Finite element modeling using ABAQUS

Guided wave propagation problems were modeled using the finite element (FE) method. The commercial software package ABAQUS/Explicit was used to simulate the wave propagation in composite plates. Wave propagation is introduced when the initial equilibrium is disturbed by the application of forces or displacement on nodes. The displacement in elements, which can be obtained by integrating the accelerations twice, is then used to solve the wave propagation problem. The accelerations at the beginning of the time step are completely determined by the mass and force acting on the elements. With the explicit method, the state of the elements is advanced through an increment of time using known values from the previous time step [115].

However, if the time increment (Δt) is larger than the amount of time that the state can be advanced, the increment is said to have exceeded the stability limit. This may cause a numerical instability and lead to unbounded solutions. For computational stability, the time increment must be smaller than the critical time step. In wave propagation modeling, the critical time step (Δt_{cr}) can be defined as the transit time at the highest wave speed through the smallest element in the model. Eq. 4-1 is used to satisfy the stability requirement, where l_e and C_l are respectively the smallest element length and the fastest wave speed of the material. The length of the element (l_e) is typically calculated

from the shortest wavelength (λ_{min}) to be analyzed, as shown in Eq. 4-2. For the accuracy of the simulation, typically at least 10 elements per shortest wavelength are defined [45]. The chosen time increment must be below the stability limit. These criteria lead to a large computational memory demand.

$$\Delta t \leq \Delta t_{cr} = \frac{l_e}{c_l} \quad \text{Eq. 4-1}$$

$$l_e = \frac{\lambda_{min}}{10 \text{ elements}} \quad \text{Eq. 4-2}$$

Concerns related to the FE simulation of wave propagation are the model size and the type of element. The model must be large enough to separate unwanted signals that come from plate boundaries or other geometrical features, and leave only the required signal. A very large number of elements are needed to model the entire plate size. There are a number of ways to reduce the number of elements for meshing necessary waveguides [116], such as using a 2D FE approach or using efficient absorbing regions. However, the large computational demand can be fulfilled at UCL, where the FE simulations were run on a shared-memory Linux machine with 94 GB physical memory. Therefore, it was decided to initially use a large plate model size of 1m x 1m in this study. One of the specimens (large cross-ply) used in the experiments has a similar size.

In order to provide a realistic wave model, the full 3D element structure was incorporated in the model. The element type was chosen as an 8-node linear brick with reduced integration (C3D8R). These hexahedral elements provide a good and regular mesh within a model of a plate and been used extensively for the guided ultrasonic wave propagation simulation. In MATLAB, the location of the excitation and the monitoring points or any required points can be controlled and changed easily due to the pre-labeled Cartesian coordinate grid.

4.2 Creating the input file in MATLAB

ABAQUS models are generally created using ABAQUS/CAE that provides a graphical user interface for creating a model and submitting the model for simulations. However, this is a rather slow process when some model parameters need to be changed or when defining new node numbers and elements for different analysis purposes. Although ABAQUS allows users to apply routines to their particular analysis requirement (via subroutines), the process is more complicated and longer than using a programmable input file. In this project, the FE models were generated from MATLAB as an input file, which was then imported into the ABAQUS/Explicit solver for the simulations.

The MATLAB program was originally written by a master student, Robert Watson [117], to simulate guided wave propagation in isotropic aluminum plates with cracks. For the present study, this program was modified for composite plates with defects. With these modifications, anisotropic homogenized and layered plates could be modeled. The material properties and their local orientation were assigned by either individual properties or homogenized properties. Additional damping was also added, where the feature can be optionally added. Defects such as delamination and material degradation were programmed, where more options of defect geometries can be changed by altering or adding few lines in MATLAB codes of the input file program.

Similarly as in ABAQUS CAE, the required steps to create a model for a simulation are as the following: (1) define dimensions of the model, (2) set sections and assembly of the model, (3) mesh the structure with elements, (4) assign material properties on the elements, (5) apply load to the structure, (6) set the time step and total propagation time, (7) submit simulation job and (8) request output history of the simulations. The parameters of the FE model and analysis can be generated from MATLAB using specific syntax that is readable by ABAQUS. The written input file was then exported into ABAQUS/Explicit.

For a rectangular plate with dimension of L_x , L_y and L_z (length of the plate in x-, y- z- axes), the number of nodes (N_{nx} , N_{ny} , N_{nz}) and elements (N_{ex} , N_{ey} , N_{ez}) needed in each direction can be calculated using Eq. 4-3 and Eq. 4-4 respectively. Hence, the product of number of nodes in x- and y- axes was the total numbers of nodes in each layer (plane direction), as shown in Eq. 4-5. Similarly, the total number of elements in each layer was the product of number of elements in x- and y- axes, Eq. 4-6.

$$\begin{aligned} \text{Number of nodes, } Nn(x, y, z) & \quad \text{Eq. 4-3} \\ & = \frac{\text{Length } (x, y, z)}{\text{Size of element } (x, y, z)} + 1 \end{aligned}$$

$$\begin{aligned} \text{Number of element, } Ne(x, y, z) & \quad \text{Eq. 4-4} \\ & = \frac{\text{Length } (x, y, z)}{\text{Size of element } (x, y, z)} \end{aligned}$$

$$\begin{aligned} \text{Total nodes in a layer of elements} & \quad \text{Eq. 4-5} \\ & = N_{nx} * N_{ny} \end{aligned}$$

$$\begin{aligned} \text{Total element in a layer of elements} & \quad \text{Eq. 4-6} \\ & = N_{ex} * N_{ey} \end{aligned}$$

Figure 4-1 illustrates the plate geometry and points for the signal monitoring. In general, the borders of the plate surfaces were formed based on the defined number of corner nodes. As can be seen in Figure 4-1 the corner nodes were identified by nb_i (i=1, 2, 3....n). These nodes were connected to form the edges of the plate surfaces. Edge 1 and 2, for example, were set as two boundaries of the top layer. Similarly, Edge 3 and 4 were set as the boundaries of the bottom layer. Once the edges were defined, the incremental node numbers on the top layer and bottom layer (for a single layer plate) were generated. This process was repeated on every layer up to the final layer (for the layered model) until layer was filled with nodes. 8 nodes are required to form a single C3D8R brick element.

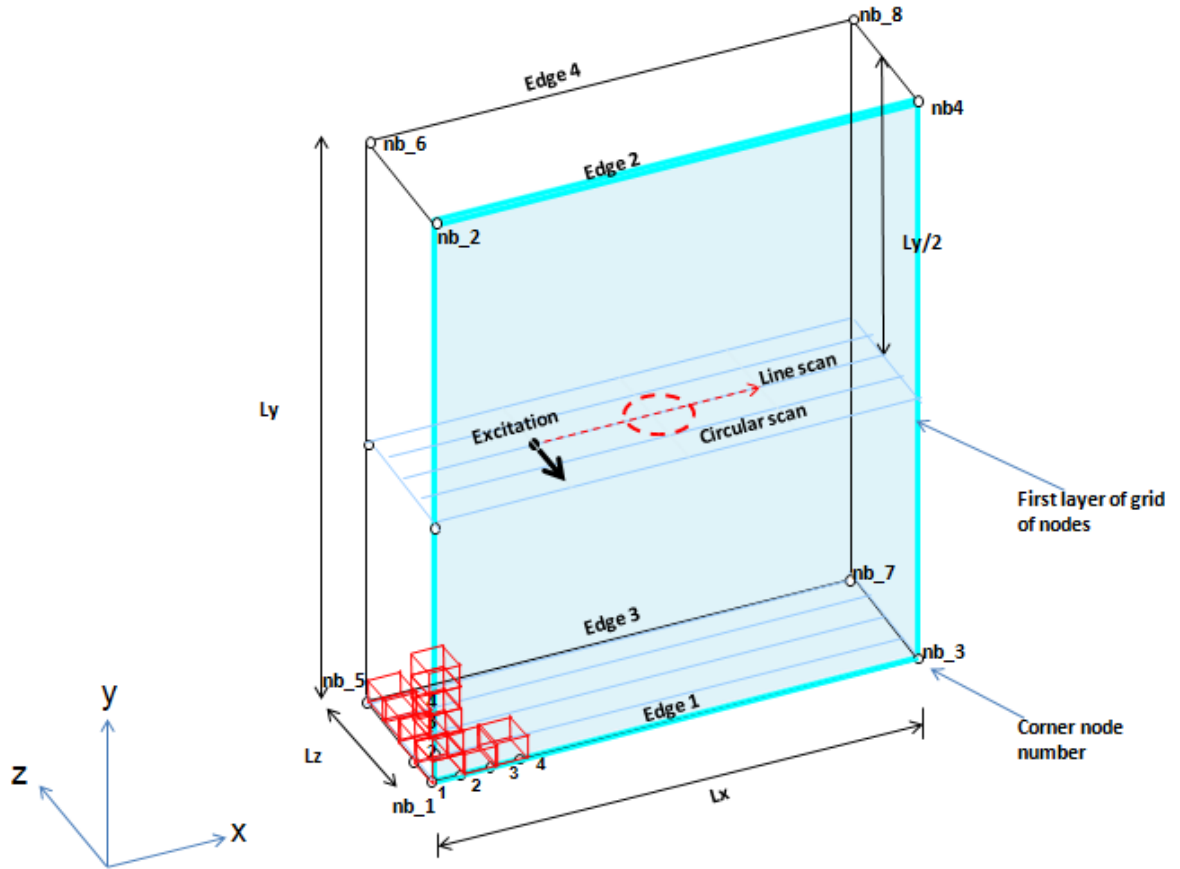


Figure 4-1: Illustration of the plate geometry; the excitation and monitoring points are placed in the middle of plate for the generation and detection of the A_0 mode; corner nodes number identified as nb_i ($i=1, 2, 3...n$); Edge 1, 2, 3, 4 were set as the boundaries of the plate.

Elements were generated by connecting all the nodes throughout the plate; however, a master element and its node numbers were assigned first. The material properties for each elements were defined when the plate was filled with elements. Nine orthotropic stiffness values (real part C_{ij}), as listed in Table 3-2 and 3-3, were assigned for all elements. The input for the linear anisotropic material assigned to the meshed elements was made by using the option *Elastic , Type = Orthotropic. Due to the fact that the direction "1" and "3" of the measured properties correspond to the direction normal to the plate and the direction of the fibers (0°), the material properties require a

rearrangement in the C_{ij} 's orthotropic definition based on the orientation defined in ABAQUS.

Furthermore, an additional local material direction is compulsory to be defined in ABAQUS when defining the anisotropic properties. The local direction is specified with respect to the ortho-normal system at the material point resulting from the current orientation definition. However, the stress and strain of the materials are affected by the rotation of the material matrix with respect to the global coordinate system of the object. Therefore, an additional local direction is needed, where the rotation is used to relate the local orientation of the material to the global coordinate system of the object as a whole. This was carried out with the creation of local co-ordinates by using the option *Orientation in the middle of the plate, and followed by an additional rotation of 90° about the y-axis.

The final step for the element generation was to set the damping terms. The damping terms was defined to be either zero (no damping condition) or using Rayleigh damping. Rayleigh linear damping is one of the damping mechanisms available in ABAQUS/Explicit, where it can introduce either mass-proportional damping (Alpha, α) or stiffness- proportional damping (Beta, β). In this study, the stiffness-proportional damping was defined in each element in the plate model to introduce damping that is proportional to the strain rate and elastic material stiffness [115]. However, it should be noted that introducing damping to the solution reduces the stable time increment; hence, the step time should be carefully defined.

For the excitation of the A_0 wave mode, an out-of-plane concentrated force (*CFORCE option) was applied at the middle of the plate thickness. The excitation was located at the mid-plane of the plate for a selective A_0 mode excitation. At the mid-plane, the S_0 mode has no out-of-plane displacement component and is thus not excited, while the A_0 mode has no in-plane displacement. The excitation signal was a 5-cycle signal in a

Hanning window; chosen to achieve a short-time, narrow-band signal in order to avoid extensive signal distortion due to the dispersive nature of the A_0 mode. The pulse was generated with arbitrary low amplitude based on Eq. 4-7, as used in the experiments.

$$Amp = 0.5 * (1 - \cos\left(\frac{2\pi f * t}{no.of\ cycles}\right)) * (\sin(2\pi f * t)) \quad \text{Eq. 4-7}$$

For the detection of the A_0 mode, the monitoring points were also placed in the middle of the plate thickness. This is to obtain a single guided wave mode signal and to avoid the detection of the S_0 mode. The S_0 mode has no out-of-plane displacement at the middle of the plate thickness and thus the monitoring is selective for the A_0 mode. For this specific reason, an even number of elements in the thickness direction was chosen in order to create a proper separation between the A_0 and S_0 mode. For further post-simulation analysis, the out-of-plane displacements of the A_0 mode (in the thickness direction) at each monitoring points were collected via history output request.

4.3 Modeling undamaged composite plates

4.3.1 Single homogenized model

Similar to the experimental specimens, three types of composite plates were modeled. Their dimensions and properties are provided in Table 3.1 and 3.2. However, all plates were modeled with a large size of 1 m x 1 m in order to reduce any unwanted edge reflections to allow simpler analysis of the main guided wave propagation and scattering properties. Element size of 1 mm in the x- and y- directions was employed. Twenty four, eight or four elements through the thickness direction were used, resulting in 24, 8 or 4 million elements respectively. The element variations were performed in order to investigate the influence of mesh size on the accuracy of the simulations of the A_0 mode propagation. A general procedure for the generation of a solid homogenous plate can be seen in section 4.2. For a plate without a defect, a master element for the whole plate was defined. Then elements were generated within the plate by connecting the pre-assigned node numbers. The orthotropic homogenized $[0^\circ/90^\circ]$ material properties (Table 3.2) were assigned for both cross-ply models. Meanwhile, the orthotropic unidirectional

properties (Table 3-3) were assigned for the unidirectional plate model. The damping terms were set to zero initially, and later the Rayleigh damping (Beta) term was added for a comparison with the experimental results. The employed largest element size (1 mm) and time step (0.01 μ s) fulfilled the stability criteria. The out-of-plane displacement was monitored at locations similar to the line and circular scans performed experimentally.

Initial simulations were performed for the undamaged composite plates in order to predict the guided wave propagation and to capture the incident wave field at the delamination location separately. A simulation of a large homogenized composite model with plate dimensions of 1000 mm x 1000 mm x 3.6 mm and element size of 1 mm x 1 mm x 0.45 mm (8 elements through thickness), using 6 parallel CPUs took about 2 hours.

4. 3. 2 Layered model

In order to obtain a realistic model of laminate composite plates, a layered model was used. A plate consisting of several layers was programmed in MATLAB due to the fact that the 'Composite Layups' user-interface cannot be used in ABAQUS/Explicit. Twenty four or eight elements through the thickness direction were used for the generation of the layers. All plates were modeled with a large size of 1 m x 1 m and element size of 1 mm in the x- and y- directions. For a layered model, each layer of elements (across the plate thickness) needs to be defined with their individual properties. Hence, each layer has to be assigned as different sections but connected as one plate. Therefore, the master elements and the boundaries of each layer were calculated, and the solid brick elements (C3D8R) were generated within the specified boundaries. As shown in Figure 4-2, the orthotropic unidirectional properties (Table 3-3) were assigned to the individual layer. For the cross-ply model, the unidirectional properties were assigned alternately based on the ply orientation of the real specimens. For the example of the 8-crossply plate (Figure 4-3), the properties were orientated symmetrically in 0° and 90° directions. For the unidirectional plate, the stiffness coefficients were arranged only in the 0° direction in every layer. The damping terms were set to either zero or Rayleigh (Beta) damping was added. Similar

excitation and monitoring points as described in section 4.3.1 were set. A simulation of a large layered composite model with dimension of 1000 mm x 1000 mm x 3.6 mm with elements size of 1 mm x 1mm x 0.15 mm (24 elements through thickness), using 6 parallel CPUs took more than 15 hours. A comparison study between homogenized and layered models was performed to investigate their efficiency and accuracy.

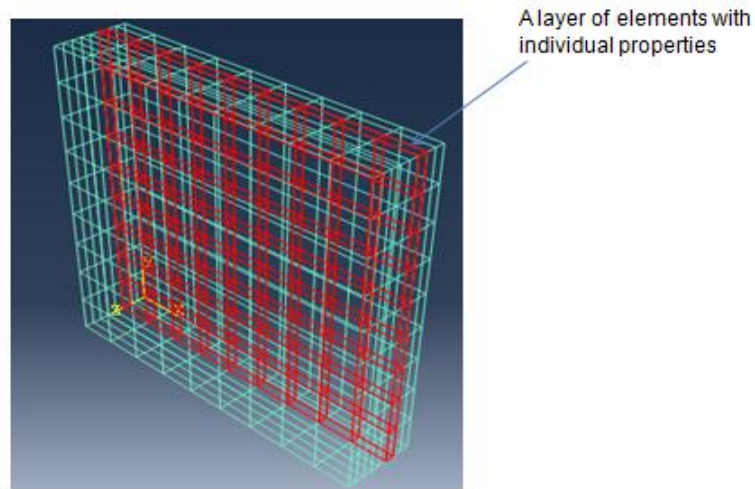


Figure 4-2: Mesh using 8 separate layers of C3D8R brick elements with individual properties.

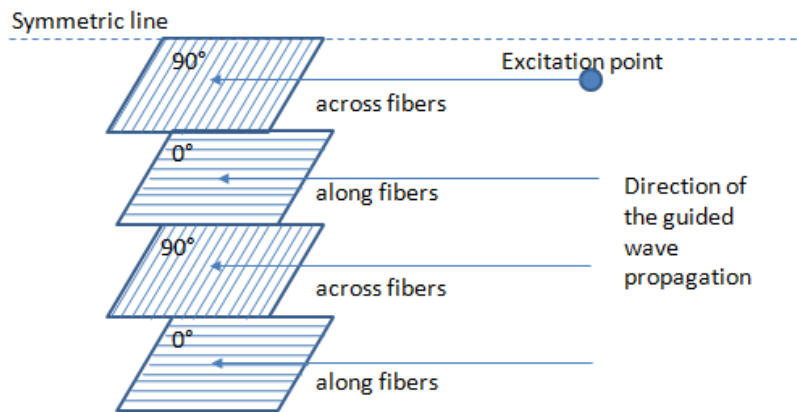


Figure 4-3: Orientation of individual unidirectional properties in a symmetric 8-crossply [0/90] layered model.

4. 4 Modeling composite plates with defects

4. 4. 1 Single homogenized model

The second set of simulations was run with a delamination present in the composite plate. The plate thickness was set to 2 mm thickness (8 elements through the thickness), similar to the damaged specimen. The plate size and element size in the x- and y- directions was kept similar to the undamaged model. A single layer with homogenized [0/90] properties was used with the addition of a delamination at the center of the plate. The defect was initially created as a 20 mm × 20 mm square-shaped delamination. The through-thickness location was varied to 0.25 mm, 0.50 mm, 0.75 mm and 1 mm.

The MATLAB program for creating the input file was designed to be conveniently changed for different types of defects. The general procedure described in section 4.2 and 4.3.1 was applied. The user can choose either to model the undamaged plate or the plate with delamination or with a notch. In order to have this kind of input file, the input data for the MATLAB program was created based on Figure 4-4. The plate was divided into seven sub-plates (shown as plates with different colors). The sizes of each sub-plate were defined based on the plate and delamination sizes. For example, the width and the length of sub-plate A is L_y , and $L_x - L_d$ – delamination length (L_d) – length of plate D respectively. To form the plates, the master elements and the node numbers of each sub-plate were calculated and defined. By connecting the nodes, the C3D8R elements were generated within the specified border of each plate. Similarly as described in section 4.3, material properties listed in Table 3.2 and Table 3.3 were assigned for the elements of cross-ply and the unidirectional models respectively. The damping terms were set to zero initially, and later Rayleigh damping (Beta) was added for a comparison with the experimental results.

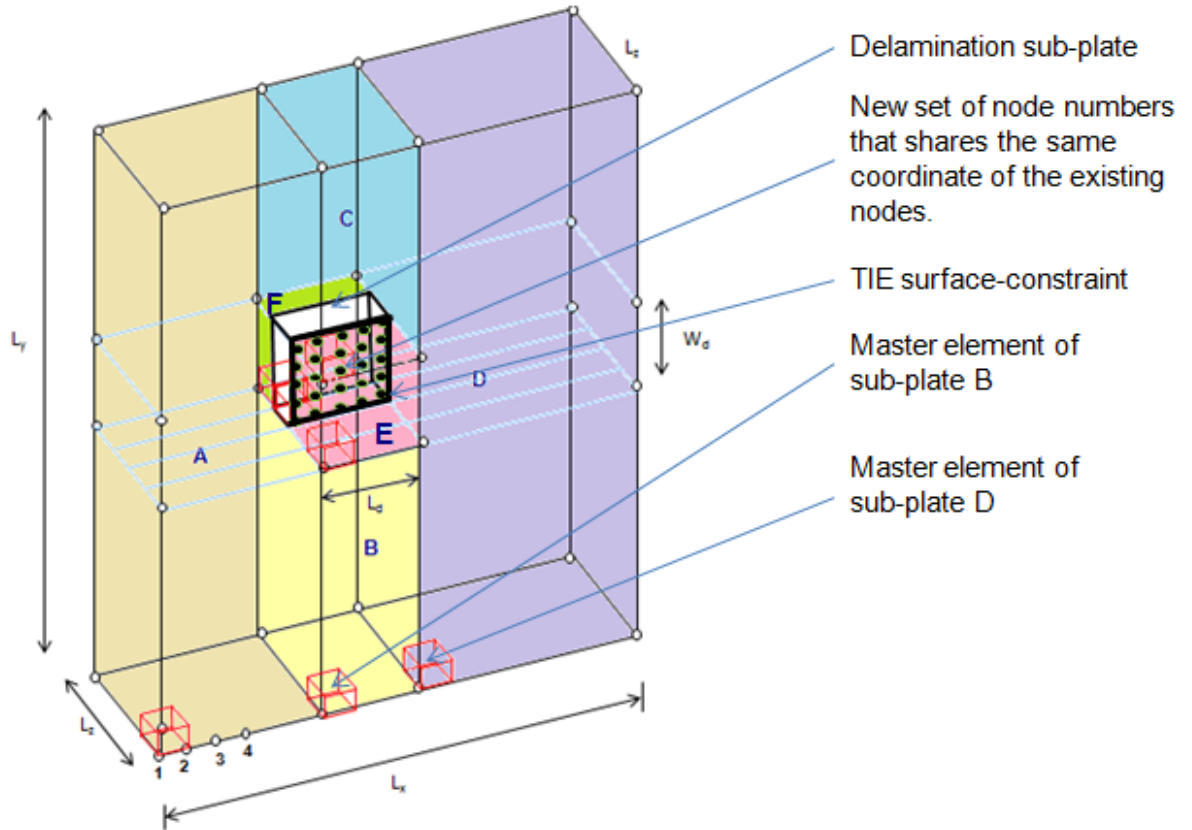


Figure 4-4: Plate geometry for FE modeling of composite plate with rectangular shaped delamination.

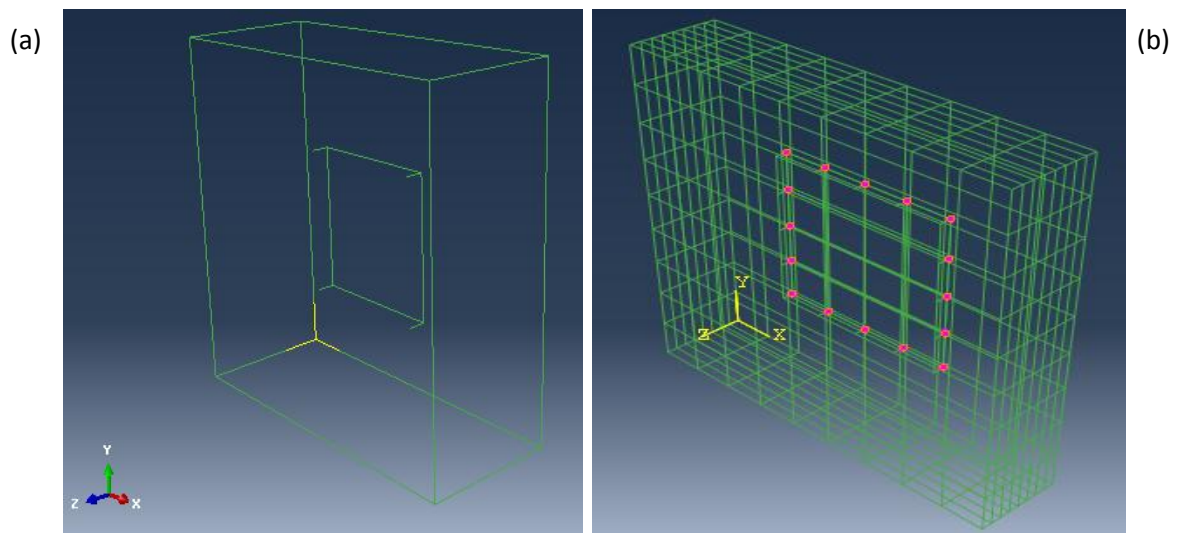


Figure 4-5: (a) Typical FE plate model with rectangular shaped delamination; (b) Tie constraint applied to the delamination border; 8-elements in thickness direction.

The plate without color (Figure 4-4) shows the sub-plate for the delamination area (one element size in thickness direction). The size of the delamination sub-plate was defined in the MATLAB program with length of L_d and width of W_d . The sub-plate was then generated using the similar incremental element generation as described in the previous sections. In order to model a delamination between elements, a new set of node numbers was introduced. The new set has the same coordinate values as the existing nodes. In ABAQUS, two nodes with the same coordinates can generate a split or ripped surface to simulate a delamination or crack on a surface [115]. Therefore, the delamination surface was created between the delamination and sub-plate E. Then, the delamination borders were tied to the existing nodes using a surface-based TIE constraint (*TIE option). Figure 4-5 shows the applied square-shaped delamination the middle of the plate, where the TIE constraint was applied on the nodes that formed the delamination borders. The excitation point was positioned 100 mm from the center of the defect.

4. 4. 2 Layered model with delamination

A similar procedure for creating a layered plate described in section 4.3.2 was repeated, where every layer of elements through the thickness is assigned individual properties. The layup arrangement followed the cross-ply $[0/90]_{2s}$ plate with thickness of 2 mm, as used for the experimental study. The plate size and element size in the x-, y- and z- directions were kept similar to the homogenized model with delamination. The defect was initially created as a 20 mm × 20 mm square-shaped delamination located at 1 mm depth (symmetric location through the plate thickness), and then the size was changed.

In order to create a sub-plate for the delamination in between the layers, a similar procedure as described in section 4.4.1 was used. The plate was divided into 7 sub-plates as can be seen in Figure 4-4. Using the layered model, the material properties for the delamination sub-plate changed accordingly based on the orientation of each layer. For the delamination positioned at 1 mm, 0.75 mm, 0.50 mm and 0.25 mm, the unidirectional properties at the delamination sub-plate were assigned with properties orientated in 90°,

0°, 90° and 0° respectively. It is important to note that the properties of the two surfaces that form the delamination at different depth position varied. However, this procedure is quite complicated due to the need of the generation of the seven sub-plates; much more if an arbitrary shaped-delamination is required. The formation of the sub-plates and the calculation of their master elements and node numbers are going to be complex and difficult if a multi-level or an arbitrary-shaped delamination has to be implemented.

Alternatively, the delamination sub-plate can be created without forming the other six plates. As can be seen in Figure 4-6, the complete plate (without sub-plates) is formed first, and then the elements at the delamination are redefined with new node numbers. A new set of node numbers that shared the same coordinate values with the existing nodes across the surface of delamination sub-plate was defined. This created the layer of delamination between the surfaces of two elements. Then, the delamination borders were tied to the existing nodes using the TIE surface-based constraint. It was found during the study that any arbitrary shape or multi-level delamination can be implemented quite easily using this method. The arbitrary shape can be overlaid on the rectangular delamination area and nodes outside the shape can be tied, which leaves only the desired delamination shape. In future this could enable 3D simulations of real impact damage using the automated MATLAB program and ABAQUS, where the shape or image of the impact damage can be obtained from C-scans, X-ray or a CT scan.

For a comparison study with the rectangular-shaped delamination, a circular-shaped delamination with 20 mm diameter was created using the alternative method described above. Only one size is considered for this study, but the circular delamination was placed at four different depths (0.25 mm, 0.50 mm, 0.75 mm and 1 mm). Figure 4-7 shows the brief procedure, which involved three main steps. Firstly, a rectangular delamination surface was created at the required depth. Secondly, the circular shape was implemented by approximating the circular shape with the Cartesian grid. The final step was to use the Tie constraint, where the nodes outside the border of the circular shape (in

the rectangular delamination area) were tied to the other layer, making the elements in that area return back to non-defective elements.

For a systematic study on the guided wave scattering, only the rectangular-shaped delamination was considered. The initial 20 mm x 20 mm defect size was changed to 10 mm, 30 mm, 40 mm, 50 mm, and 60 mm (Figure 4-8) in order to investigate the influence of the delamination size on the wave scattering. The depth of the delamination was varied at 0.25 mm, 0.50 mm, 0.75 mm and 1 mm. The distance from the excitation to the center of the delamination was maintained at 100 mm. The delamination extent on the line scan varied with delamination size, as shown in Figure 4-8.

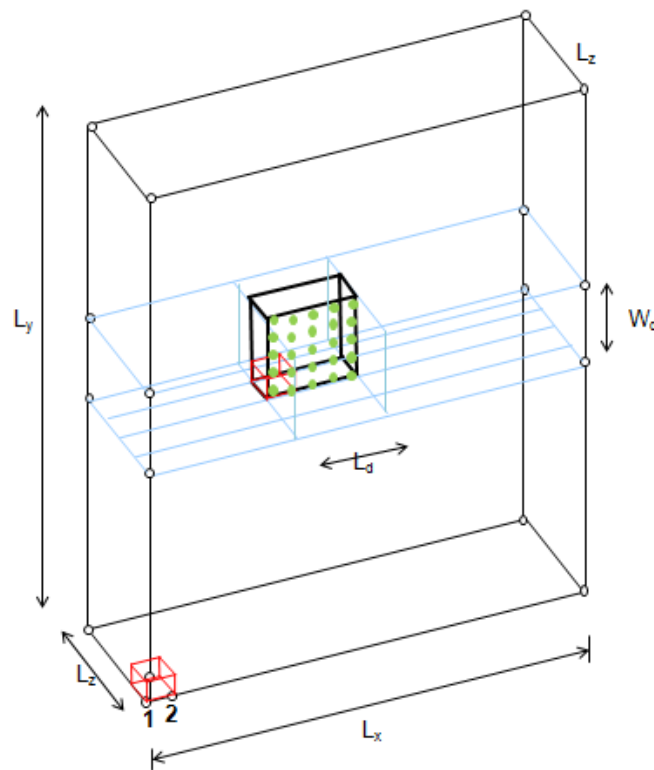


Figure 4-6: Layered plate with rectangular shaped delamination; set of nodes across delamination surface (in green color); two master elements were defined.

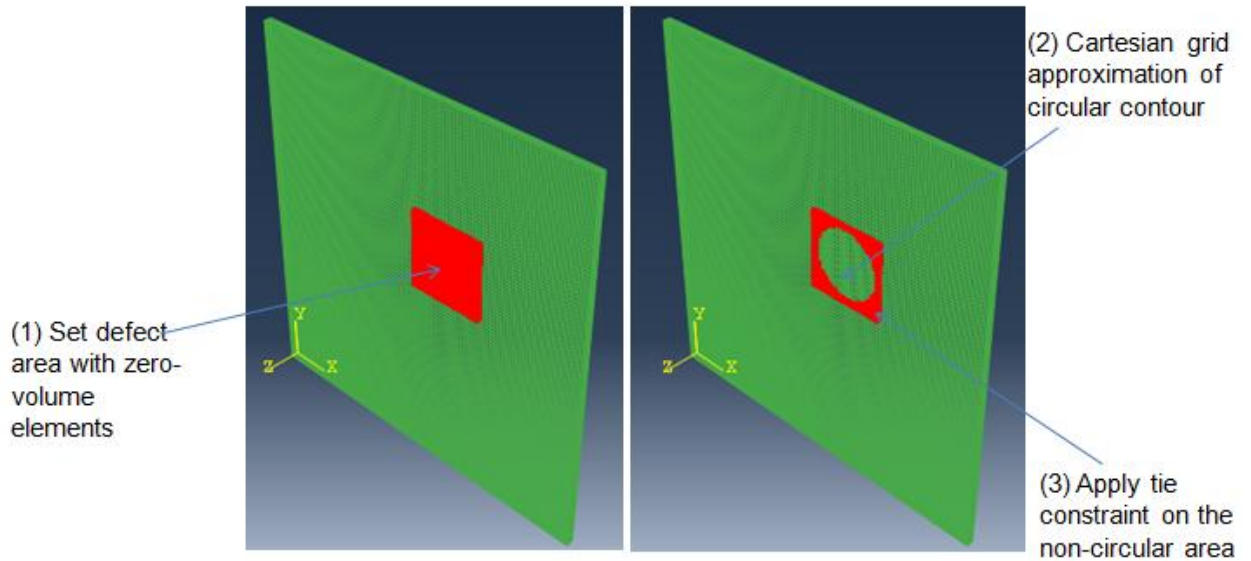


Figure 4-7: Modeling a circular delamination by approximating the circular shape with Cartesian grid.

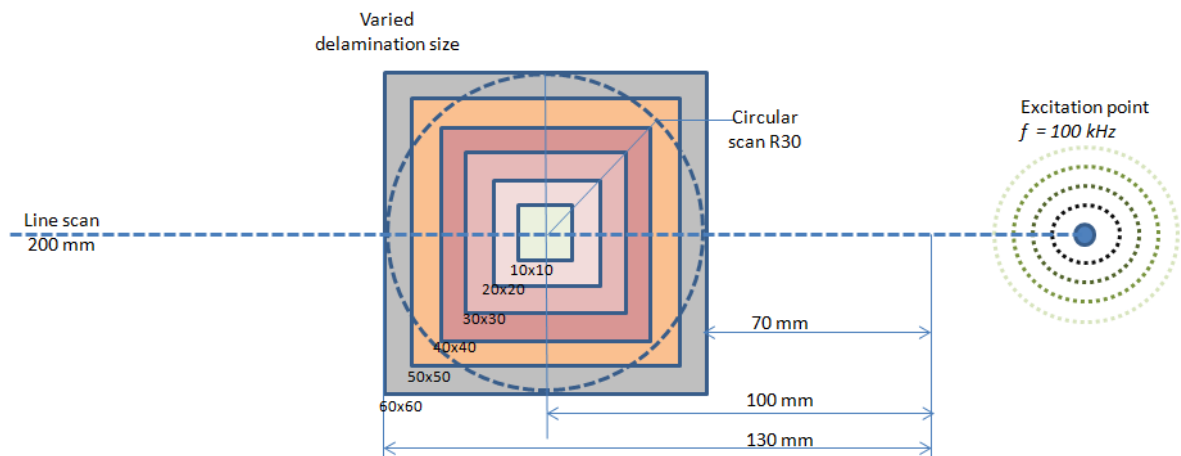


Figure 4-8: Various delamination sizes; distance between excitation point to the central delamination was 100 mm; 200 mm line scan in 0° direction; 30 mm radius circular scan around delamination.

4. 4. 3 Layered model with material degradation

In order to develop more realistic damage implementation, there is a need for accurate and practical modeling of impact damage in composite structures. In this study, the stiffness properties at the defective region were reduced. This was to represent the impact damage zone that was strongly micro-cracked. According to the literature review [4–7], cracks by low-velocity impact have been shown to lead to local decay in stiffness properties. A combination of material degradation with a delamination could represent the complex multiple defects in composites caused by low-velocity impact.

As can be seen in Figure 4-9, three different modeling approaches involving material degradation were performed. The pink-shaded area shows the designated elements with reduced stiffness properties. The first model was the 3D model with full thickness material degradation. Secondly, a combination of delamination and a layer of degraded element properties were modeled. The final model was also a combination of delamination and degraded properties, but with full-thickness properties degradation. These FE approaches give the possibility to simulate different material behavior and to replicate the complexity of composite damage mechanisms. The aim was to investigate the effect of material degradation and multiple defects on the guided wave scattering.

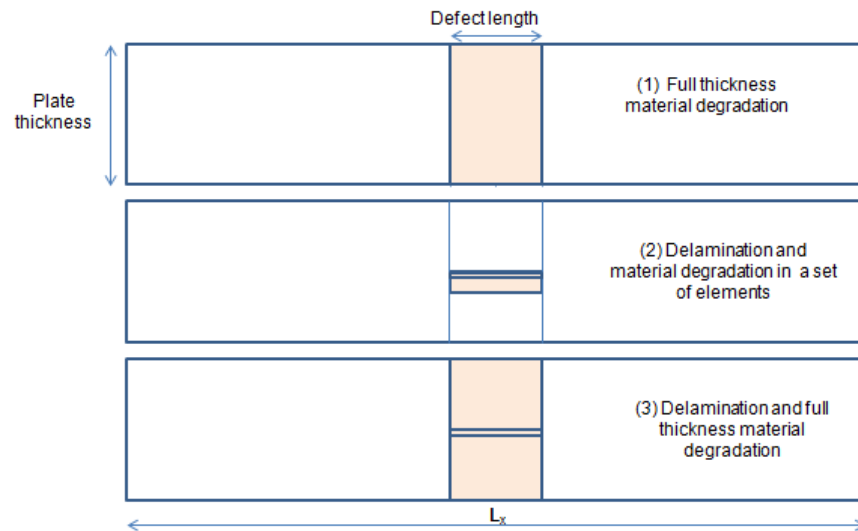


Figure 4-9: Modeling three types of defects with material degradation for the FE models.

Figure 4-9 show the first FE model was modeled with full thickness material degradation. A layered plate model as described in section 4.3.2 was applied. Then, rectangular areas of 20 mm x 20 mm were defined in every layer through the thickness at the desired location (pink-shaded area). The elements within these areas were then assigned with different, reduced material properties. The stiffness properties of the elements were reduced by 75%, 50% and 25% in order to investigate the effects of the reduction on the wave scattering. Rayleigh damping was also added to the material properties. The second model combined the delamination and a layer of elements with reduced material properties. The delamination layer was placed on the top of the elements with the reduced properties. A similar approach to model delamination in a layered model was used (refer section 4.3.2), and the stiffness properties were reduced similarly as for the first model. Only delamination at 1 mm depth was considered in this study as the standard case investigating symmetrically located delamination. As discussed in the literature, it is understood that the defect on the impacted surface normally begins with the matrix cracking and then gradually develops through the plate thickness, where delamination is expected to be present as well. Hence, the final model was a mix of a delamination and full thickness material degradation. This can be modeled by combining the existing program for the generation of full thickness material degradation and the single delamination in a layered model. The choice of similar percentage reduction of the material properties as above was maintained. This model was investigated for the symmetrically located delamination only.

4.5 Signal monitoring points and evaluation

Figure 4-10 shows the locations of the excitation and monitoring points for a standard delamination size of 20 mm x 20 mm (in red). The excitation location was placed 100 mm from the center of the delamination. The excitation frequency was 100 kHz, and the wavelength was approximately 16 mm. For each simulation with ABAQUS/Explicit, 200 mm line scan and 30 mm radius circular scans around the defect were conducted to

monitor the out-of plane displacement. The same excitation and monitoring points were assigned for the FE models without defect, except an additional circular scan around the excitation point was also performed.

The history output in term of the out-of-plane displacement time traces for each monitoring point was written to a report file. The file was then imported into MATLAB for signal processing and analysis. As described in Chapter 3, the signal envelopes (Hilbert) and frequency domain signals (FFT) were used for analyzing the signals. Wave characteristics such as velocities and attenuation were calculated and compared with the experimental results and DISPERSE predictions. To characterize the influence of a defect on the scattered field, two sets of simulations were made separately: (i) baseline data on an undamaged plate model and (ii) data on a model with defect. From the difference of the incident and scattered field, the characteristic of the scattered wave was obtained.

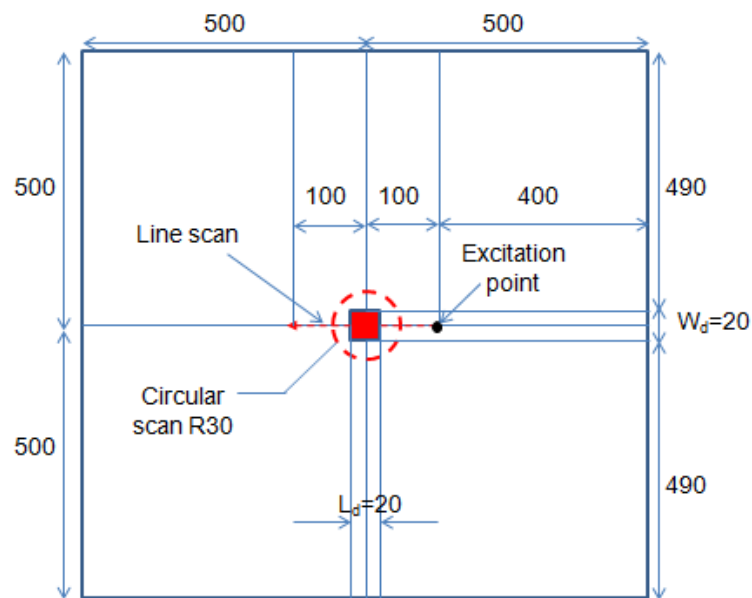


Figure 4-10: Typical plate geometry and monitoring scan locations; unit for dimension is mm.

4.6 Long delamination in 2D plate model

This section presents the 2D FE model used to investigate mode conversion phenomena. As mentioned in Chapter 2, mode conversion between different modes (A_0 to the S_0 mode, or vice versa) can be observed when the guided wave interacts with defects [45, 116]. The propagating mode splits when it arrives at the entrance of the delamination and then propagates independently in the top and lower sub-laminates of the delamination. Both sub-laminates were formed with different thicknesses depending on the position of the delamination. Figure 4-11 shows the two sub-laminates labeled with thicknesses of h_{top} and h_{low} respectively for the top and lower sub-laminates.

To efficiently detect the formation of the converted modes, especially the A_0 mode at layers that are not in the mid-plane, it is essential to place the monitoring nodes at the mid-plane of each sub-laminate (mp_2 and mp_3). Therefore, an even number of elements at each sub-laminate is required. 16 elements through the thickness (size of 0.125 mm in z-direction) were chosen in order to fulfill the above criteria. If the delamination is placed at 0.75 mm depth, the thicknesses and the element numbers for the top and low sub-laminates respectively are $h_{top} = 1.25$ mm (10 elements) and $h_{low} = 0.75$ mm (6 elements). Consequently, the A_0 mode can be monitored at the mid-plane of each sub-plate; mp_2 at 0.375 mm and mp_3 at 1.375 mm. The 16-elements through the thickness for a 1 m x 1m plate would lead to a large number of elements. Hence, it was decided to use a 2D model instead in order to avoid longer simulation times and to not look at the 3D effects.

To create this model, the existing MATLAB program for creating the full 3D layered model was modified. The number of elements in the x direction was kept the same as for the other 3D plates (1 mm element size, 1000 elements). Meanwhile, the element size in the y direction was modified to be 1 mm, one element wide. In order to obtain an infinitely large plate, a symmetric boundary condition in the y direction was applied (*BC, Type = Symmetry). Hence, the total number of generated elements was 16000. The material used in each layer had the properties of the unidirectional composite as used for

the layered models. The material properties were orientated based on the $[0/90]_{2s}$ layup arrangement. Damping was not considered in this study. The reason was to avoid any additional reduction in amplitudes of the converted modes.

The delamination was modeled similarly as the procedure explained in section 4.4.2. Figure 4-11: shows the FE models of the four different cases, where the depth of the delamination was varied from 1 mm to 0.25 mm. The length of the delamination was set to 200 mm. A longer delamination was used in order to avoid an overlap in time of wave reflections coming from both the entrance and exit of the delamination. As shown in the Figure 4-11, the orientation of the material properties in the layers adjacent to the delamination varied for each case.

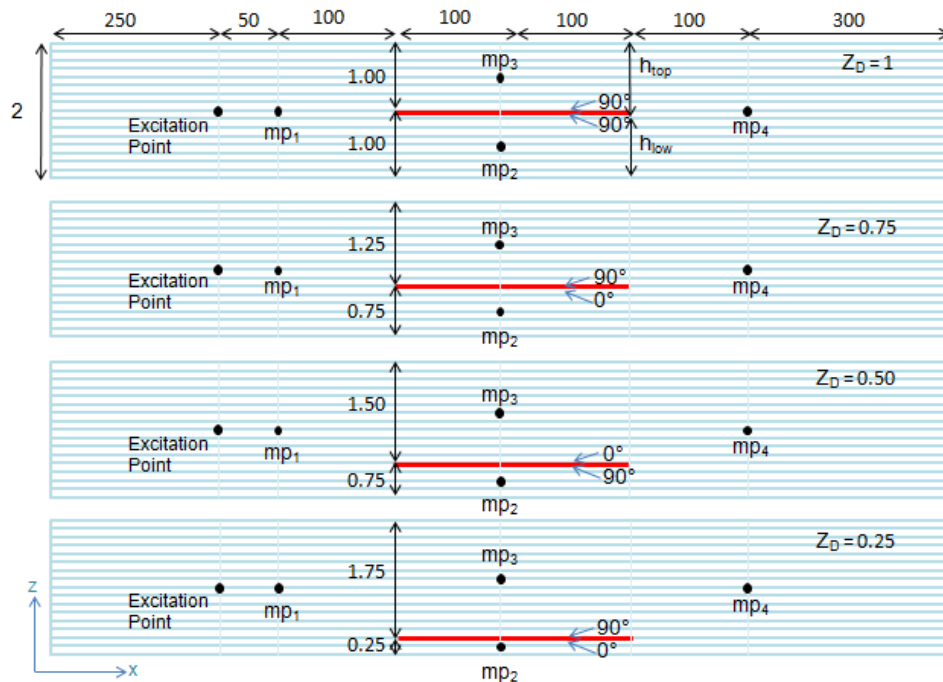


Figure 4-11: Configuration of the 2D model with delamination located at different depths; delamination length is 200 mm; four monitoring nodes were placed at different locations; sub-laminates with different thickness labeled; material orientation above and below delamination shown.

The locations of the excitation and monitoring points can be seen in Figure 4-11: . The excitation point was placed 150 mm from the entrance of the delamination. The frequency of excitation was 100 kHz. An out-of-plane force was applied in the z-direction in order to simulate the A_0 mode propagation. Four monitoring points were placed at different locations. The locations of the monitoring points were based on the aim to investigate wave reflection, transmission and mode conversion at locations before, through and behind the delamination. Two monitoring nodes were placed at the middle plane of the top and lower sub-laminates (mp_2 and mp_3); while the other two nodes were positioned 100 mm before (mp_1) and behind the delamination (mp_4). At each monitoring point, the in-plane (for S_0) and out-of-plane (for A_0) displacements were monitored.

4.7 Conclusions

This chapter presents the procedure for the finite element modeling of the composite plates used throughout the study. The generation of the 3D FE models using a MATLAB program file was described. The MATLAB program was designed to be fully automated and altered easily for parameter variations. Composite plates with and without defect were modelled either by using the homogenized [0/90] properties or individual layer properties. Delamination was introduced in both types of models. Various delamination shapes, sizes and depths were defined. The input file was also modified to combine delamination with several types of material degradation. In order to thoroughly investigate guided wave mode conversion, the 3D model was modified to model an infinitely wide 2D model with a longer delamination size. The use of modeling techniques presented here enables the achievement of an accurate and efficient FE composite model with defects. All results from the work described in this chapter are presented in Chapters 5, 6, and 7.

CHAPTER 5 A₀ MODE WAVE PROPAGATION IN UNDAMAGED COMPOSITE PLATES

This chapter presents the measurement and simulation results for the A₀ mode propagation in undamaged laminate composite plates. The propagation of the A₀ mode was measured using a non-contact laser interferometer and compared to the results of Finite Element (FE) simulations as well as to DISPERSE semi-analytical predictions. The aim of this work is to gain a better understanding of the propagation of the A₀ mode in anisotropic plates. Wave dispersion and attenuation of the A₀ mode and their angular dependency were investigated experimentally and validated. The first part of this chapter presents the verification of the FE modeling approaches to ensure the accuracy of the FE modeling used for this study. In the second part, the simulated and experimental wave characteristics for three different plates were compared and discussed. The final part of this chapter discusses the angular dependency of the A₀ mode wave propagation characteristics.

5.1 Accuracy of the FE modeling approaches

5.1.1 Comparison between homogenized and layered models

This section presents the investigation of different modeling approaches for the simulation of the A₀ mode propagation in composite plates. The possibility of modeling laminate composite plates using homogenized properties rather than individual layer properties was investigated. This could help to reduce the simulation time and computational cost.

As described in Chapter 3, three types of composite specimens were used in this study: (1) a 3.6 mm thick 24-ply cross ply [0/90]_{6s} composite plate, (2) two 2 mm thick 8-ply cross ply [0/90]_{2s} composite plate, and (3) a 3.6 mm thick 24-ply unidirectional (UD) composite plate. The dimensions of the specimens are provided in Table 3.1. The material properties are listed in Tables 3-2 and 3-3. As mentioned in Chapter 3, these properties were measured for the 3.6 mm thick cross-ply and 3.6 mm thick UD plates. For the FE simulations of the cross ply plates, two types of models were used: (1) a homogenized

model, assigned with the homogenized $[0^\circ/90^\circ]$ properties, and (2) a layered model, assigning each individual layer with the unidirectional $[0^\circ]$ properties. It is important to note that the material properties used for modeling the 8 layer cross-ply specimen were assumed to be similar to the properties listed in Tables 3-2 and 3-3, although the constituent materials in this plate were different to the other two plates. 24 elements were defined in the thickness direction to model the 3.6 mm cross-ply and 3.6 mm ply UD specimens. Meanwhile, 8 elements through the thickness were applied to model the 8-crossply specimen.

Figure 5-1 shows the predicted amplitude of the guided wave pulse propagating along a line (in 0° direction) and angular amplitude variation around the excitation point in the intact part of the three composite plates. Repeatable amplitude profiles from both types of models can be observed, especially from the line scans in the 0° direction. Comparable angular patterns were also achieved for the anisotropy influence on the directivity pattern which can be observed clearly. Higher amplitudes along the principal directions can be observed (in the 0° and 90° directions for the cross-ply models and in the 0° direction for the UD model).

Comparing both types of models, the amplitudes monitored in the 0° direction are reasonably matched for all types of plates. The amplitudes in the 0° and 90° directions for the homogenized models of cross-ply plates are about the same as expected. In contrast to the layered model of the cross-ply plates, the amplitudes in the 90° direction are lower than the amplitudes in the 0° direction. The difference can be observed to be about 4% and 15% respectively for the 3.6 mm thick and 2 mm thick cross-ply plates. This discrepancy is likely to be related to the lower bending stiffness because of symmetric outer layers of the cross-ply plates having the material orientation in the 0° direction.

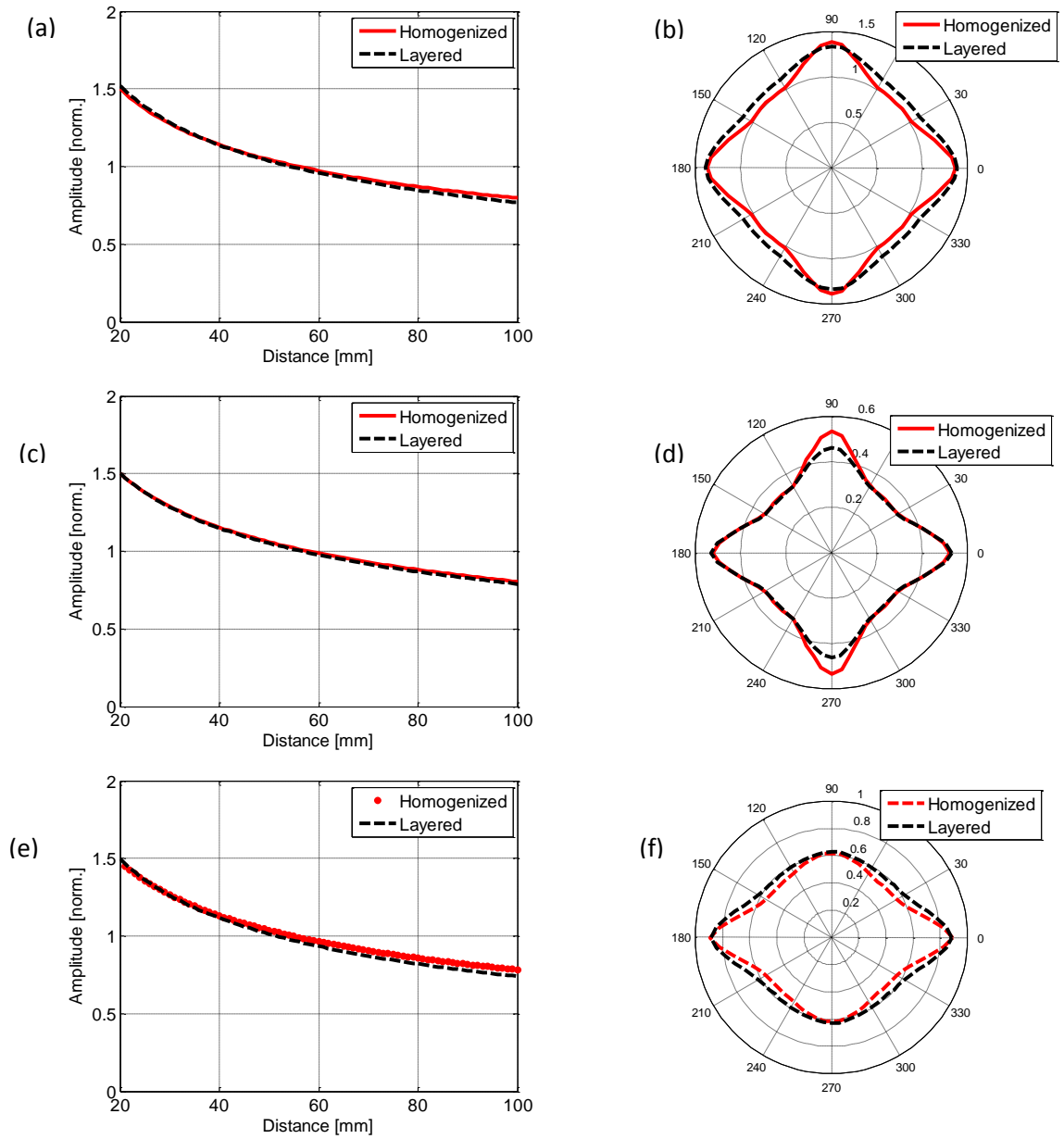


Figure 5-1: Maximum amplitude of signal envelope in intact composite plates; (a) and (b) for the 24-ply cross ply plate; (c) and (d) for the 8-ply cross ply plate; (e) and (f) for the 24-ply unidirectional composite plate; line scan measured every 1 mm step along line in 0° direction; polar plot of amplitude every 5° at 30 mm radius around excitation point; 100 kHz excitation frequency.

From the angular plots in Figure 5-1, both types of models for the 2 mm cross-ply plate show a comparable angular pattern between 15° to 75° directions. However, there are small discrepancies in the amplitudes in these directions for the 3.6 mm cross-ply and 3.6 mm UD plates. This could be related to the different definitions of the material anisotropy between the homogenized and layered model.

In another note, it can be observed that the shape of the angular pattern is not the same when comparing the two cross-ply plates (Figure 5-1b and Figure 5-1d), although both plates were assigned with the same material properties. A rhombus shaped angular pattern can be seen for the 3.6 mm cross-ply plate, while the 2 mm cross-ply plate has lower amplitude in directions between 15° to 75°. Reduced amplitude can be found in the 45° direction and the wave energy is being focused into the principal directions (0° and 90°). This could be due to their respective frequency–thickness product, where the fd product for the 2 mm plate ($fd = 200 \text{ kHz}\cdot\text{mm}$) is lower than for the 3.6 mm cross-ply plates ($fd = 360 \text{ kHz}\cdot\text{mm}$).

Although as expected there are small discrepancies between the models due to the experimental material properties used, the main characteristics of the guided wave amplitudes such as the anisotropy influence on the angular pattern can be observed. Both types of models are reasonably consistent, suggesting that in principle homogenized material properties could be employed to simulate the guided wave propagation in an undamaged composite plate. This would reduce the required simulation time for a laminate composite model, as it eliminates the need to model each layer individually. This reduces the required number of elements and increases their size, allowing a larger time step. Hence, the homogenized model was used for further investigations in this chapter.

5.1.2 Influence of element size in the thickness direction

This part investigates the influence of the element size in the thickness direction on the A_0 mode propagation using the homogenized model. This study was carried out to determine the appropriate number of elements through the thickness in order to ensure the accuracy of the A_0 guided wave propagation properties. 24, 8 and 4 elements through the thickness were used for the cross-ply homogenized model. The corresponding element sizes in the 3.6 mm thick plate were 0.15 mm, 0.45 mm and 0.90 mm. As mentioned in Chapter 4, an even element number through the thickness is required in order to separate the anti-symmetric and symmetric modes. There should be optimal sufficient number of elements across the thickness to closely represent the required mode shapes, which in this case was the out-of-plane displacement of the A_0 mode. Since the mode shapes are linked to the propagation properties, the predicted amplitude profile of the A_0 mode obtained from the three different cases were compared.

Figure 5-2 shows the comparison between the homogenized FE models with different numbers of elements in the thickness direction. From the figure, all models gave comparable amplitude profiles with less than 1% difference. The numerical stability was satisfied as the time increments ($0.01 \mu\text{s}$) were below the critical time step for each case; $\Delta t_{cr} = 0.05 \mu\text{s}$, $0.16 \mu\text{s}$ and $0.33 \mu\text{s}$, respectively for the 0.15 mm, 0.45 mm and 0.90 mm element sizes. The result shows that the higher numbers of elements through the thickness do not give any significant difference, except much longer simulation time. Hence, the smallest number (4 elements through thickness) was chosen to be used for the homogenized composite model.

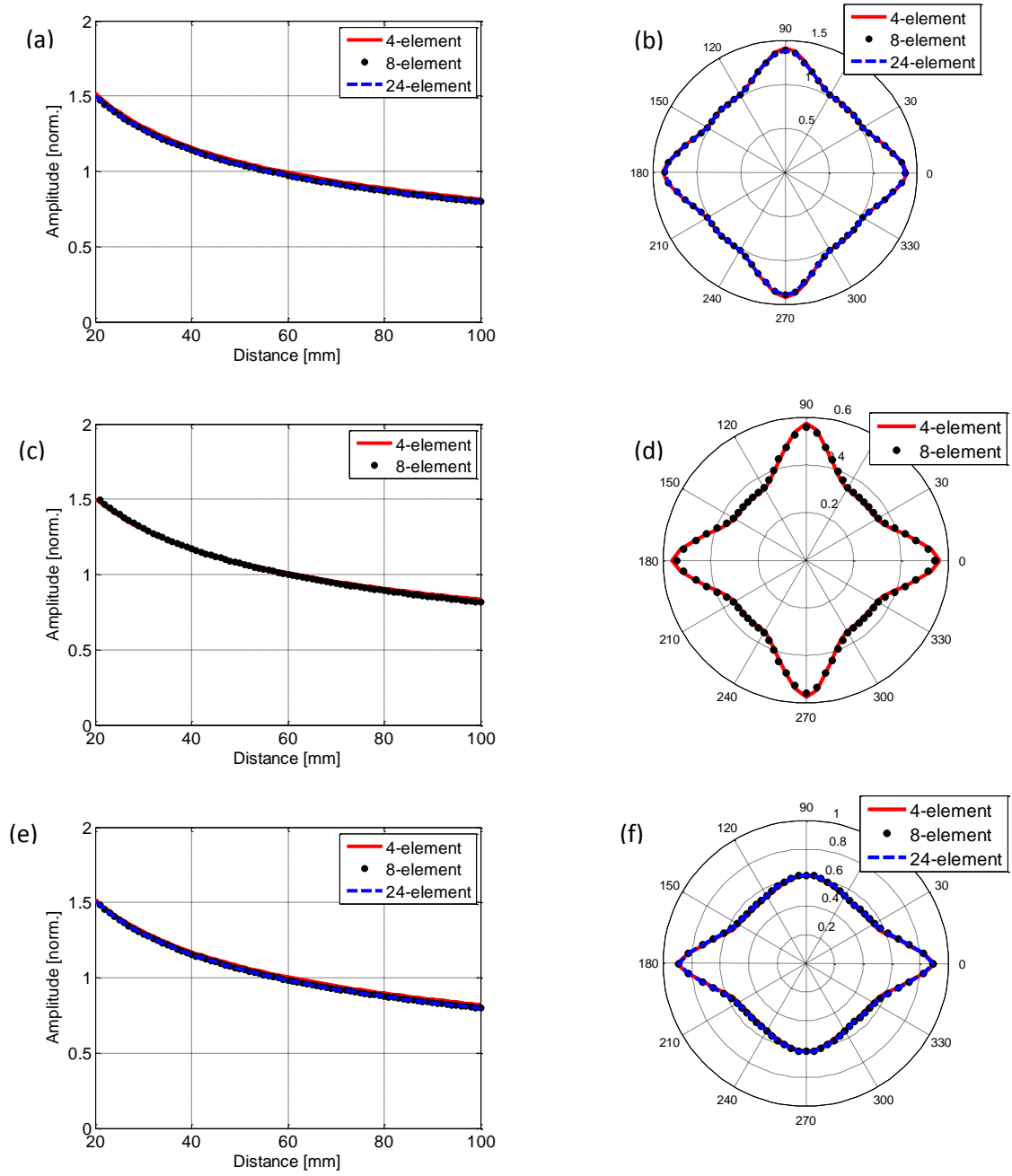


Figure 5-2: Maximum amplitude of signal envelope in intact composite plates; (a) and (b) for the 24-ply cross ply plate; (c) and (d) for the 8-ply cross ply plate (only 4 and 8 elements investigated); (e) and (f) for the 24-ply unidirectional composite plate; line scan measured every 1 mm step along line in 0° direction; polar plot of amplitude every 5° at 30 mm radius around excitation point; 100 kHz excitation frequency.

5.1.3 Estimation of damping influence on finite element model

The final check was to introduce material damping in the FE models. From the literature, it was found that many authors modeled guided wave propagation through composite media without considering the damping effect. However, if material damping is also incorporated in the FE model, then SHM techniques based on the change in amplitude can be understood better and implemented effectively. For this reason, the Rayleigh damping model has been used to compute the A_0 mode wave propagation in different types of composite plates.

Besides the guided wave dispersion, there are two other factors that influence the reduction in signal amplitude with propagation distance: (1) geometrical beam spreading, and (2) material damping. In the FE simulation without damping, the reduction in the signal amplitude is caused by the geometrical beam spreading ($1/\sqrt{r}$). Hence, the additional material damping has to be included in the FE model in order to match the wave profiles of the experimental results. Although the complex material properties were available (Table 3-2 and 3-3), it is not possible to define the imaginary part of the stiffness properties in Abaqus/Explicit. Therefore, the stiffness proportional damping (Rayleigh damping, $Beta \beta$), which is available in Abaqus/Explicit, was introduced in the composite model.

Based on the observed difference between the predicted (FE no damping) and the measured wave profiles (Exp.), appropriate Rayleigh damping values were introduced for each plate. For the 3.6 mm cross-ply plate, $Beta = 45, 60,$ and 75 ns were introduced in the material definition of the model (Figure 5-3a). $Beta = 10, 20,$ and 30 ns and $Beta = 20, 40,$ and 60 ns were applied for the 2 mm cross-ply (Figure 5-3c) and the 3.6 mm UD plate (Figure 5-3e) respectively. As can be seen from Figure 5-3, $Beta = 60$ ns matched quite well with the experimental data of the 3.6 cross-ply plate, while the other two $Beta$ values did not match. Comparing the second plate models (Figure 5-3c), it is observed that the FE simulations with $Beta = 30$ ns matched the experimental results. For the final UD plate

(Figure 5-3e), the simulation with Beta = 40 ns produced comparable results to the experimental measurement.

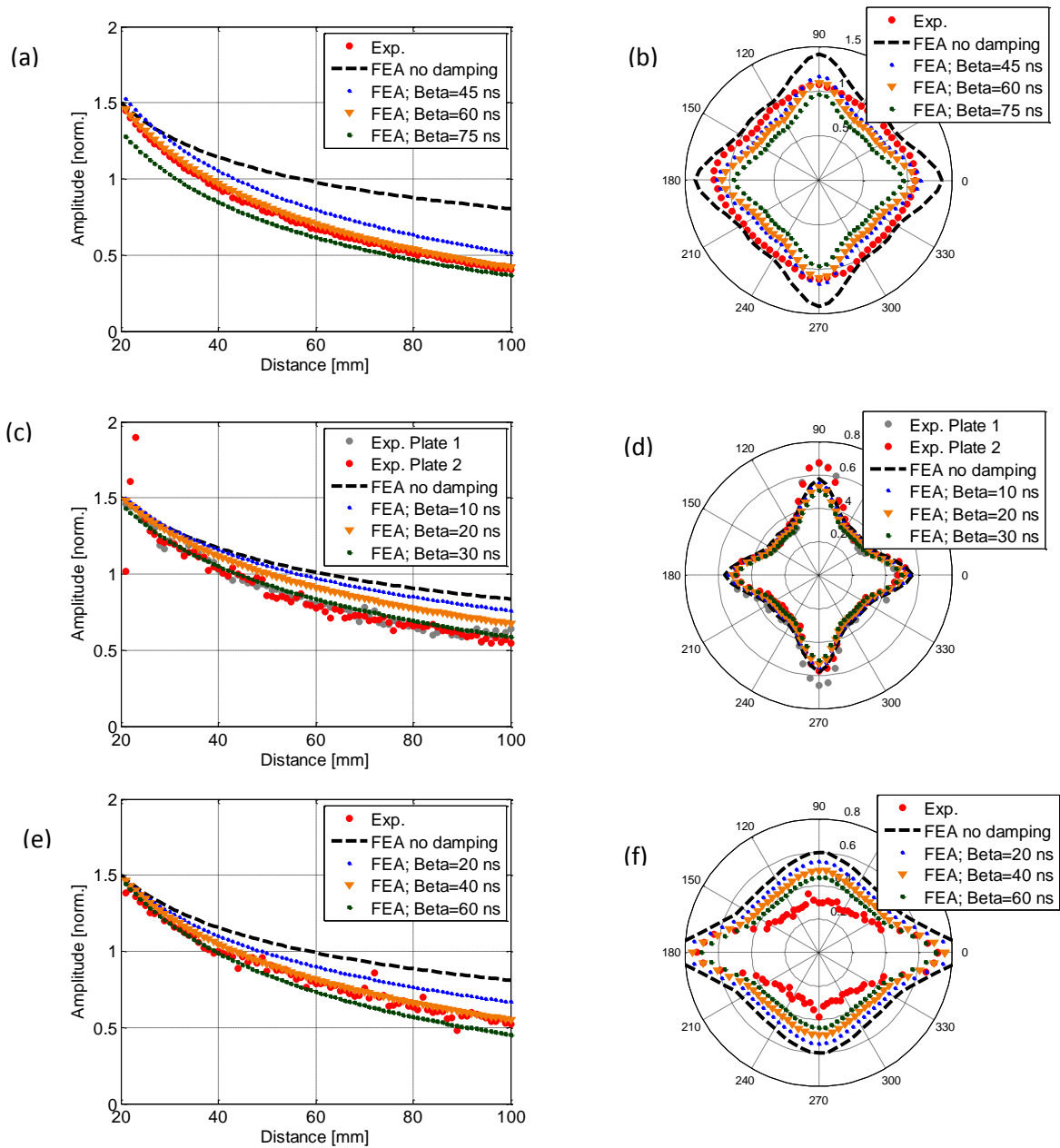


Figure 5-3: Comparison between FE models with different Rayleigh damping values; amplitude profiles (a) and (b) for the 3.6 mm cross-ply plate, (c) and (d) for the 2 mm cross-ply plate, and (e) and (f) for the 3.6 mm UD plate; 100 kHz; homogenized model.

However, the angular patterns around the excitation of the damped models (with an appropriate damping value) do not entirely match the experimental results, although their line scans are comparable. For the 3.6 mm cross-ply plate (Figure 5-3b), there is good agreement in the 0° and 90° directions between the damped model (Beta = 60 ns) and the experimental results except for amplitudes in the non-principal directions. The shape of the angular pattern can be observed to be different, where the FE results have lower amplitude. The uncertainty in the material properties remains a potential source of error for the FE simulation. In contrast, the shape of the angular pattern matched the experimental results for the 2 mm cross-ply plate (Figure 5-3d). Some difference between the damped FE model (Beta = 30 ns) and the experimental results can be seen in the 90° direction. This is due to the symmetric outer layers of the composite plates having the fibers arranged in the 90° direction, thus having higher bending stiffness in this direction.

From Figure 5-3f, the angular pattern of the UD plate matched quite well in the 0° direction. The shape of angular pattern of the damped FE model (Beta = 40 ns) is consistent with the shape observed on the experimental UD plate. Small differences can be seen in the directions between 30° to 150°, but the highest difference can be observed in the 90° direction. These differences could be due to the defined material properties (particularly in the non-principal directions), which their inaccuracy affecting the amplitude pattern in some directions. These results suggest that the damped FE models could approximately model the propagation of the A_0 mode in angular directions, matching reasonably well with the experimental results, especially in the 0° direction. Except for the small differences in certain directions, the agreement is good for the results obtained by the FE modeling for the three types of the composite plates. The angular dependency of the guided waves behavior can be observed to match quite well with the experimental results. This suggests that a correct amount of Beta of Rayleigh damping can be used to model the material damping in anisotropic composites plates. The accuracy of the FE modeling is shown to be improved at this stage.

5.2 Estimation of attenuation coefficient

This section presents the A_0 mode attenuation coefficient measured in the three different composite laminate plates. The attenuation values were estimated at a frequency range of 50 kHz to 150 kHz in order to observe the frequency-dependent behavior of the guided waves. Then, the measured frequency-dependent coefficients were compared to the theoretical values obtained by DISPERSE. In this study, FE analysis was not investigated, as it was demonstrated in the previous section 5.1.3 that the A_0 mode wave attenuation can be properly incorporated using appropriate Rayleigh damping. To validate the experimental results, DISPERSE [43] was used to theoretically predict the guided wave propagation characteristics based on the provided imaginary material properties [11, 59]. Two DISPERSE models were used to define the composite plates: homogenized and layered models, similar as defined in the FE model. Each model was defined using lossy orthotropic stiffness properties, where both real and imaginary stiffness properties were used as the input for the material properties. This type of material is normally used to represent material with high damping such as composites. As stated earlier in Chapter 3, the uncertainty of the imaginary properties is significantly larger than for the real constants. Thus, it is expected that the attenuation measurements are going to have larger errors than the velocity measurements.

From Figure 5-4, the amplitude decay pattern of the propagating A_0 pulses in the composite plates did not follow the geometric beam spreading relationship ($1/\sqrt{r}$) that is normally observed in metals. This shows that there was an additional mechanism for the wave energy to be lost during propagation, known to be affected by the damping in the composite materials. This damping refers to the capacity of the material to dissipate energy. In addition, the wave attenuation could be due to the wave dispersion as well. In order to obtain the wave attenuation affected by the material damping, the wave attenuation coefficient was corrected for the beam spreading effect first (refer Eq. 3.4). Then, the attenuation coefficient was obtained by fitting the amplitude curve with the theoretical curves (following Eq. 3-3).

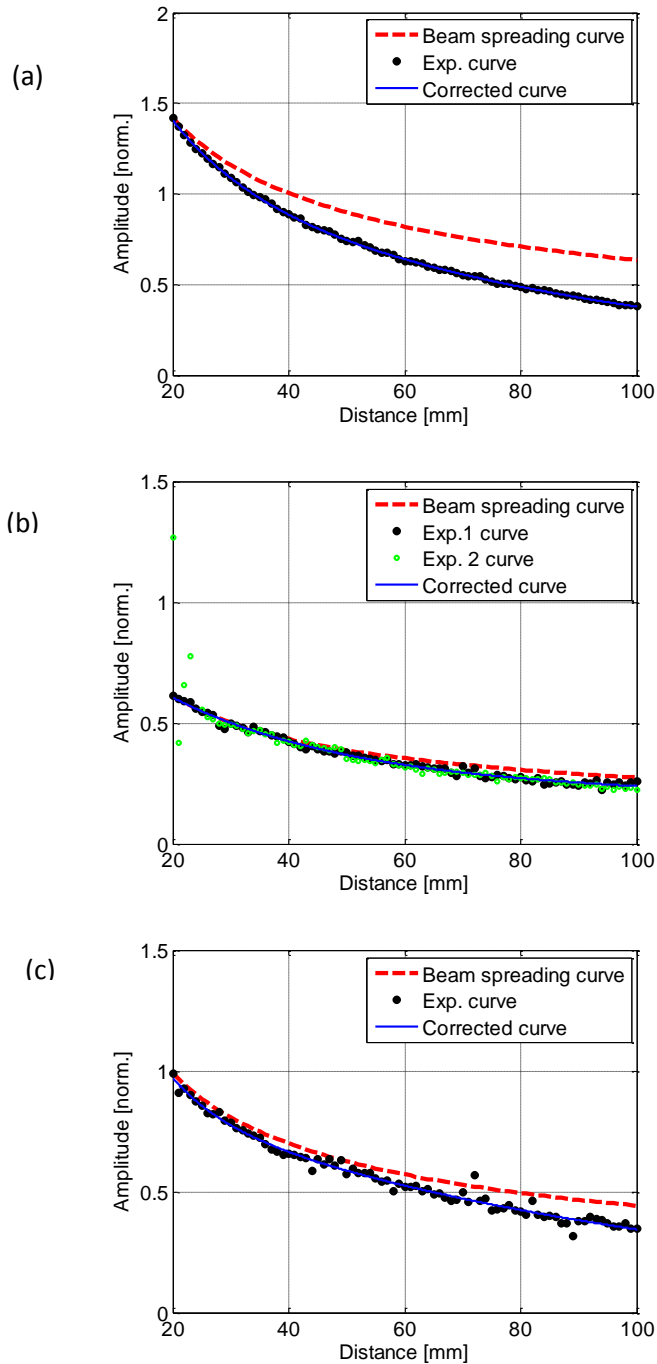


Figure 5-4: Geometrical beam spreading and the measured exponential reduction of the propagating A_0 mode amplitude in (a) 24-cross ply; (b) 8-cross ply; (c) 24-unidirectional composite plates; Blue dashed line corresponds to the corrected amplitude pattern due to material damping and beam spreading; 100 kHz excitation frequency.

Table 5-1: Attenuation coefficients of A_0 guided wave mode in different composite plates; excitation frequency 100 kHz; measured in 0° direction.

Plates	Corrected attenuation coefficients (dB/mm)	Predicted coefficient by DISPERSE homogenized model (dB/mm)	Predicted coefficient by DISPERSE layered model (dB/mm)
24 cross-ply	0.099	0.102	0.171
8 cross-ply	0.046	0.083	0.143
24 UD ply	0.088	0.09	0.09

Table 5-1 lists the attenuation coefficient calculated within the range of monitored distance (20 to 100 mm from the excitation point). The corresponding attenuation coefficients measured in the 0° direction at 100 kHz frequency are 0.099 dB/mm, 0.046 dB/mm, and 0.088 dB/mm, respectively for the 3.6 mm cross-ply, 2mm cross-ply, and 3.6 mm UD plates. Comparison between the 3.6 mm UD and the 3.6 mm cross-ply plates shows that the fiber arrangement (alternately arranged into the 0° and 90° directions) contributed to higher attenuation than the one with all fibers arranged in the 0° direction. Although both plates are made of the same number of plies and material properties, the wave attenuation differed by 13%. This could be due to the direction of measurements taken along the fiber direction (0°) of the UD plate, in which it has higher stiffness properties than in the cross-ply plate. In comparison to what has been published by other researchers, Ono and Gallego [121] measured attenuation coefficient (α) of the A_0 mode = 0.08 dB/mm in a 16 cross-ply composite plate and $\alpha = 0.06$ dB/mm in a 16-ply UD plate in 0° direction. Although the measurements were performed at 300 kHz, their result is qualitatively similar to the ones presented here, where the attenuation in the UD plate is lower than the cross-ply plate, although their number of plies and materials were the same.

From Table 5-1, it can be seen that the 2 mm plate ($\alpha = 0.046$ dB/mm) has lower wave attenuation than the 3.6 mm plate ($\alpha = 0.099$ dB/mm). Referring to literature for a qualitative comparison, Herrmann et al. [72, 122] also showed a similar behavior of the attenuation coefficient for the A_0 mode in 12-ply and 16-ply UD plates. The attenuation values were respectively = 0.025 dB/mm and 0.06 dB/mm (in the 0° direction). Two reasons seem to correlate to this behavior: the material thickness and differences in the materials used for their fiber-matrix system. Thicker materials generally show greater damping due to increased energy absorption. Various studies have shown that the wave absorption coefficient of a composite material is a function of thickness and porosity. Prosser [123] discussed the influence of plate thickness on wave attenuation. It was demonstrated that the thicker plate increased the wave attenuation. To relate to the second point, Biwa [71] has indicated that a major governing factor of wave attenuation is the viscoelastic absorption in the matrix. This results in an increase of the wave attenuation with increasing matrix content. These seem to support the finding presented here, where the 3.6 mm cross-ply plate has higher matrix content (40%) than the 2 mm cross-ply plate (35%). However, it should be noted that both types of plates were made of different fiber-matrix system, which could additionally contribute to the different wave attenuation of both plates.

From Table 5-1, the predicted attenuation coefficients for the DISPERSE homogenized and layered models were also presented. From the table, the homogenized model for the 3.6 mm cross-ply plate predicted a closer value to the measured attenuation at 100 kHz frequency, with less than 3% error. In contrast, nearly twice the measured value was predicted for the 2 mm cross ply plate. This could be due to the assigned material properties for the 2 mm plate that were merely relying on the available properties measured for the other two plates.

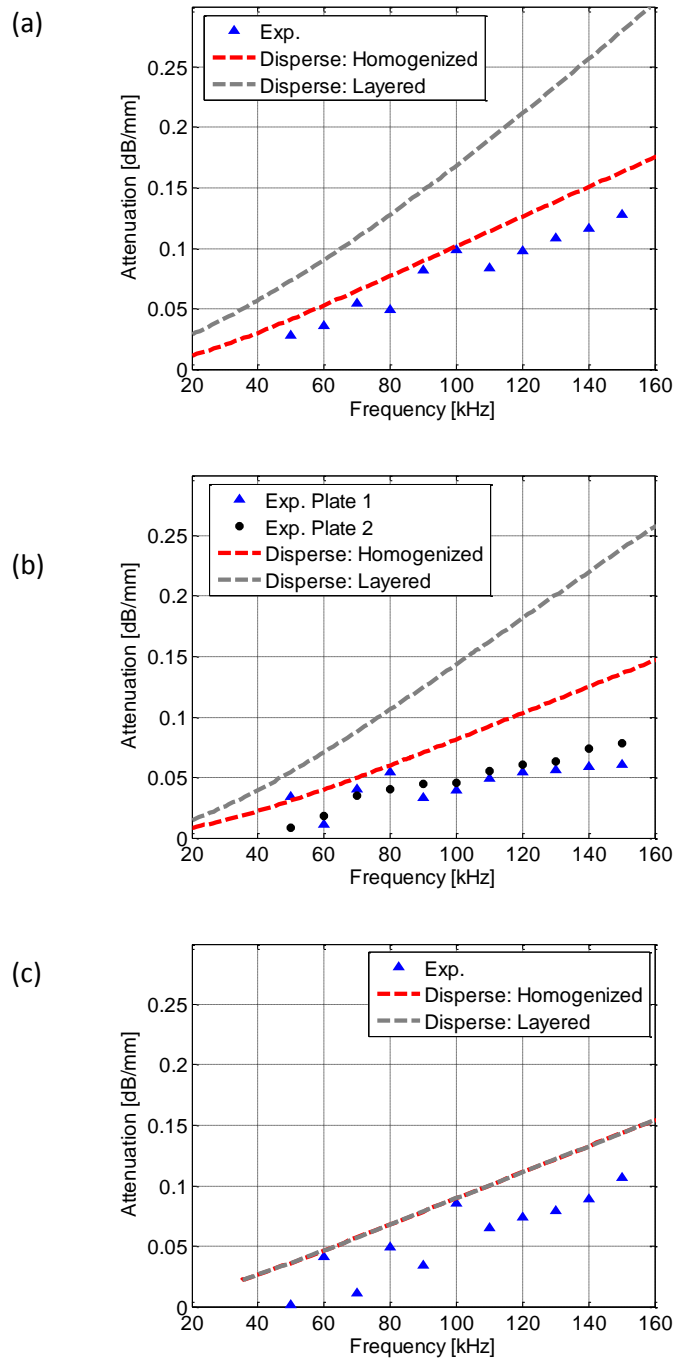


Figure 5-5: Measured frequency-dependent attenuation coefficient together with DISPERSE predictions; corrected for geometrical beam spreading; excitation frequency 50 – 150 kHz; measured in 0° direction; (a) 24-cross ply; (b) 8-cross ply; (c) 24-unidirectional composite plates.

Both DISPERSE models of the three types of plates were further analyzed to estimate the attenuation coefficient in the frequency range from 50 kHz to 150 kHz. Figure 5-5 shows the DISPERSE predictions together with the measured coefficients for comparison. It can be seen that the DISPERSE homogenized models are in good agreement to the measured coefficients for all types of plates. The overall trend is comparable to the experimental results, although it gives slightly higher values. The attenuation increased with frequency for all three types of composite plates, as expected for the A_0 mode. A small variation of the measured coefficients at frequencies below 100 kHz can be observed, which could be due to measurement errors. At frequencies above 100 kHz the values became more stable. For the 3.6 mm cross-ply plate (Figure 5-5a), the measured attenuation values increased from approximately 0.05 dB/mm at 50 kHz to 0.15 dB/mm at 150 kHz. This gives a rough estimation of about 0.10 dB/mm increment over the frequency range. The measured attenuation coefficients for the 2 mm cross-ply plate (Figure 5-5b) were consistently lower than those measured for the 3.6 mm cross-ply plate. As discussed previously, this is due to the thickness of the plate and the matrix content. Similarly, the attenuation coefficients for the 3.6 mm UD plate were measured as 0.001 dB/mm at 50 kHz and increased approximately to 0.11 dB/mm at 150 kHz, also lower than the 3.6 mm cross-ply plate. Since the experimental and DISPERSE homogenized results compare reasonably well, these attenuation values hold important information to determine how far the A_0 mode can travel at certain excitation frequencies and can be used for future reference. The increase in attenuation with frequency imposes an upper frequency limit on inspections.

Comparing the two types of DISPERSE models, the attenuation of the layered model is significantly higher than the attenuation of the homogenized model. This is in line with what has been reported by [124] that an overestimation of the attenuation coefficient is normally observed in the multi-layered model. It was also reported that the results for the homogenized model are close to the layered model within the low frequency range of the comparison. A possible explanation could be related to the

differences in the real and imaginary properties used to predict the wave attenuation in the composite system. Referring to the stiffness properties in Table 3-2 and Table 3-3, the homogenized material properties are consistently higher in most directions compared to the UD properties that have higher stiffness properties only in the principal directions. Since the wave attenuation is normally lower with higher imaginary stiffness properties, this could be why the attenuation of the homogenized model is lower than the layered model.

From these results, some difference between DISPERSE predictions and the measured attenuation values is expected given that the uncertainties of the imaginary stiffness values are large. Note that this shows the difficulty in estimating and predicting the attenuation coefficient. Nonetheless, the primary value of this work is that the attenuation of guided waves in three different composite plates has been successfully estimated, and is approximately comparable (but slightly lower) to the predictions by the DISPERSE homogenized model. The frequency-dependency of the A_0 mode wave attenuation has been shown and validated. Comparisons between the attenuation coefficients of the three different composite plates show the influence of plate thickness, fiber arrangements and material properties.

5.3 Estimation of wave velocities

This section reports the velocity dispersion characteristic of the A_0 guided wave mode in the three types of composite plates. This section focused on the measurements in the 0° direction. Figure 5-6 shows the comparisons of measured group and phase velocities together with predictions by DISPERSE and FE analysis. Both DISPERSE homogenized and layered models were used because it has been observed there is a large difference between the two models for the attenuation coefficient. For the FE analysis, only the homogenized model was used since both models showed comparable results, as discussed in section 5.1.1.

As can be seen from Figure 5-6, the main observation is the comparable results between both DISPERSE models in calculating the group and phase velocities for all different types of plates. Unlike the frequency-dependent attenuation, this means that both material models can be used to predict the velocity dispersion. It is also apparent that the FE predictions matched the DISPERSE results within 1% error. This is as expected because both simulations were using the same stiffness coefficients (real part), which determine the guided wave velocity in plates.

Comparing the predicted results to the experimental results (Figure 5-6), the measured phase velocities scattered around the predicted values reasonably well. Larger error can be observed at the higher frequency region with the largest (approximately less than 30% error) obtained from the 2 mm cross-ply plate. It can be seen that both 2 mm cross-ply specimens do not show repeatable results, which might be due to the uncertainty in the phase measurements as well as other inaccuracies from the experimental measurements.

Meanwhile, there appears to be a systematic offset between measured and predicted group velocities. The offset in the group velocity varies between plates by about 10% to 20%, with the maximum difference at the higher frequency range. However, these results are within a range of error band for the velocity measurements as reported in [124]. A major source of the differences remains from the uncertainties of the provided stiffness properties. To support this claim, it is evident that there is the largest error in the phase and group velocities of the 2 mm cross-ply plate. This is because the prediction for this plate was based on the assumed properties, which were originally measured for the other two plates. When the stiffness properties were modified to increase by 10%, it was observed that the predicted group and phase velocities increased by 7% and 4% respectively, and matched approximately the experimental value.

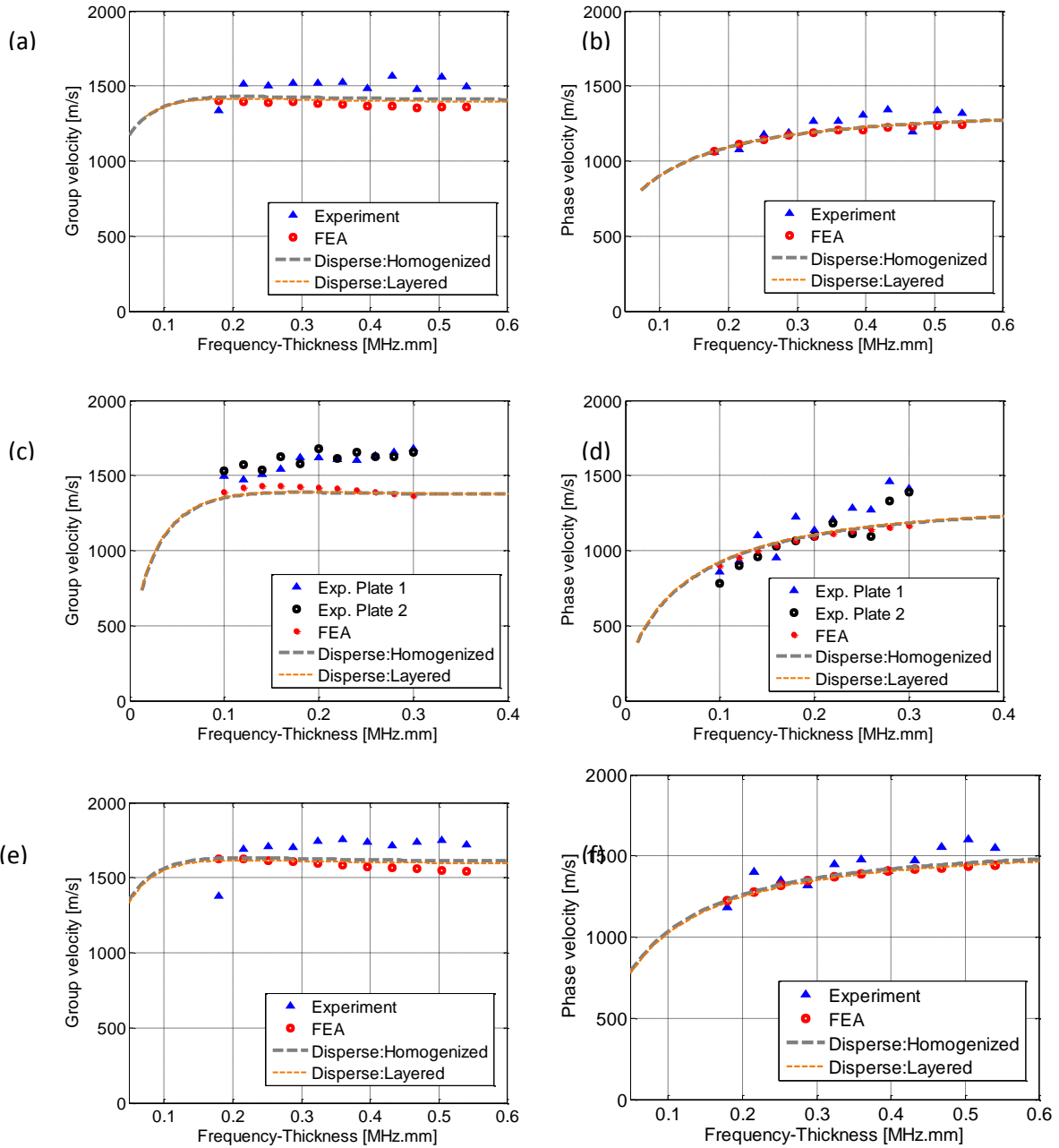


Figure 5-6: Measured and predicted velocities for the A_0 mode propagation in the composite plates; a) and (b) for the 3.6 mm cross-ply plate, (c) and (d) for the 2 mm cross-ply plate, and (e) and (f) for the 3.6 mm UD plate; 100 kHz; measured in 0° direction.

In term of velocity dispersion, it can be seen that the A_0 mode is highly dispersive in the frequency range below 50 kHz for all composite plates. On the contrary, the dispersion of the A_0 mode in all plates is smaller above 50 kHz. Since different frequency components in a wave packet travel at different speeds, the shape of the wave packet is expected to have small distortion while traveling due to the differences in the arrival times of each frequency component. Within the frequency range of the excited wave packet (50 kHz to 150 kHz), the differences in the arrival times are very small; hence, the wave packet retains its shape as it travels. This feature is desirable for the SHM of composites, and supports the decision to choose 100 kHz as the nominal excitation frequency.

Comparing the two cross-ply plates, the experimental results for the 2 mm cross-ply plate (Figure 5-6b) are higher than for the 3.6 mm cross-ply plate (Figure 5-6a). This is in contrast to the simulated results, which predicted higher velocities in the 3.6 mm cross-ply plate than for the 2 mm cross-ply plate as the velocity increases with the $f.d$ product. The differences in the experimental results, therefore, demonstrate the influence of the fiber properties on the guided wave velocity. The longitudinal and transverse moduli of the Tenax HTS fiber of the 2 mm cross-ply plate (140 GPa, 7 GPa respectively) are higher than the moduli of the HEC fiber of the 3.6 mm cross-ply plate (130 GPa, 1.57 GPa respectively). This could reasonably explain the differences between the two cross-ply plates.

Table 5-2 shows the comparison between the experimental and simulation results for the phase and group velocities. Due to the very small error between the DISPERSE and FE predictions, Table 5-2 shows their averaged group and phase velocities. By comparing results of all plates, it can be observed that the 3.6 mm UD plate has the highest phase and group velocities. As expected, this is because of the relationship between the velocity and the stiffness properties of the UD plate ($C_{33} = 109.9$ GPa in the 0° direction), which is higher than the properties for the cross-ply plate ($C_{33} = 64.24$ GPa, refer Table 3-2 and

Table 3-3). Overall, it can be seen that the trend and the values of the measured A_0 mode wave velocities are in good agreement with the predicted results.

From a separate study, Table 5-3 shows the DISPERSE prediction of group and phase velocity for varying plate thickness in a layered 2 mm cross-ply composite model. These values are shown here as a reference when dealing with damage detection in Chapter 6, knowing that the wave velocity is important in order to locate the damage. However, the main important point that needs to be addressed here is the variation in the velocities with the orientation of the plies, beside the effect from the frequency-thickness product. From a literature review, it is understood that the propagation speed of the A_0 mode increases with fd , and for the S_0 mode the propagation speed slightly decreases with fd . However, it can be observed from Table 5-3 that this relationship is not valid when a higher number of plies are arranged in the 90° direction, regardless of the plate thickness. For example, the group velocity of the A_0 mode for the 0.75 mm cross-ply composite [0/90/0; 1362 m/s] is higher than for the 1 mm cross-ply of [0/90/0/90; 1255 m/s]. It is apparent that there is a reduction in the velocity of the A_0 mode when the percentage of fibers orientated in the 90° direction is larger than the fibers orientated in the 0° direction. Referring to the DISPERSE predictions (Figure 5-6c and d for the 2 mm cross-ply plate), the velocity dispersion is quite high when $fd < 100$ kHz.mm. Hence, it should be noted that a combination of these factors will have a greater effect on the A_0 mode propagation.

Table 5-2: Group and phase velocities in three composite plates; comparison between the experimental results and DISPERSE / FE predictions; measured in the 0° direction; 100 kHz.

Plates	Experiments (m/s)		DISPERSE / FE (m/s)	
	C_p	C_g	C_p	C_g
3.6 mm cross-ply	1270	1510	1210	1400
2 mm cross-ply	1110	1650	1100	1390
3.6 mm UD plate	1480	1750	1380	1620

Table 5-3: DISPERSE predictions of the group and phase velocities in sub-laminates of 2 mm cross-ply composite plate with different thickness and laminate orientation; orthotropic-lossy materials; 0° direction; 100 kHz.

Plate's Thickness (mm)	fd (kHz.mm)	Layup orientation	A ₀ mode		S ₀ mode	
			C _g (m/s)	C _p (m/s)	C _g (m/s)	C _p (m/s)
0.25	25	0	1130	620	-	-
0.50	50	0/90	1064	600	6833	6855
0.75	75	0/90/0	1362	924	-	-
1.00	100	0/90/0/90	1255	866	6831	6854
1.25	125	90/90/0/90/0	1253	860	6124	6201
1.50	150	0/90/90/0/90/0	1385	1074	6824	6852
1.75	175	90/0/90/90/0/90/0	1366	1026	6356	6400
2.00	200	0/90/0/90/90/0/90/0	1388	1134	6819	6851

5.4 Angular dependency of the A₀ mode

The study of the wave velocities and attenuation in the previous sections was limited to the propagation in the 0° direction. In this final section of Chapter 5, the properties of the A₀ mode propagating in directions from 0° to 90° (with 15° step size) of the 3.6 cross-ply and 3.6 UD plates have been studied. In order to obtain information about the angular dependency characteristics, 100 mm line scans were performed in those directions, and the wave properties were extracted from the received signals. Measurement in non-principal directions on the 2 mm cross-ply plate cannot be performed due to the small width. Four characteristics of the wave propagation such as attenuation, group velocity, phase velocity and slowness are presented to analyze the angular dependency of the A₀ mode propagation.

The major objective of this study is to examine how these properties change in different directions. Several studies [42, 69, 125] have shown that the characteristic of beam steering may occur when guided waves propagate in non-principal directions. The wave packet travelling in a unidirectional plate, for example, tends to steer towards the fastest direction (in the fiber direction) [126]. From the literature review, it is understood that the wave properties would be different when they are measured along a principal direction (along or across the fibers) or in non-principal directions. When the waves propagate in a non-principal direction, the wave packet does not travel in the direction of the wave fronts (phase direction) but rather travels normal to the phase slowness surface. This imposes a challenge for an efficient NDE and SHM system of composites if the guided modes cannot propagate or be detected in certain directions. Therefore, it is crucial to be aware of the changes in the characteristics of the guided waves in other directions although this study is a more complex area of research.

5.4.1 Cross-ply composite plate

Figure 5-7a presents the experimental amplitude curves of the A_0 mode in the directions of 0° to 90° with 15° interval, together with the FE results (Figure 5-7b) for the 3.6 cross-ply composite plate. A similar level of amplitude concentration can be observed from both results, which indicates the accuracy of the numerical FE modeling. The amplitude curve measured in the 0° direction matched the amplitude curve in the 90° direction, with higher amplitudes compared to the other directions. This is due to the symmetrical fiber arrangement in the 0° and 90° directions. Comparable amplitude curves for the measurements in the 15° and 75° directions can also be observed. Meanwhile, the amplitude curves in the 30° , 45° and 60° directions shows a quite similar pattern, with amplitudes being the lowest. This shows that lower wave energy propagates in these directions, and indicates the beam steering towards the fiber directions. However, it is quite surprising to see that the FE results in the 15° and 75° directions predict higher amplitude especially at locations close to the excitation point. This is in contrast to the experimental measurements, where this behavior cannot be observed clearly due to the

closer amplitudes curves from measurements in the 30°, 45° and 60° directions. It is possible that the FE simulation results demonstrate that wave packets tend to steer towards the fiber direction, since the 15° and 75° directions are the closest directions to the principal directions. Another interesting observation is that the amplitudes started to decay similarly as obtained in the 30°, 45°, and 60° directions after propagating 60 mm from the excitation point. Hence, this indicates the higher energy loss within the near field region in the non-principal directions.

In order to investigate the angular dependency of the A_0 mode properties, Figure 5-8 presents the angular plots of corrected attenuation coefficients (Figure 5-8a), group velocities (Figure 5-8b), phase velocities (Figure 5-8c) and slowness profiles (Figure 5-8d). Since the guided waves radiate symmetrically from a point source, the full angular profiles were plotted for a better presentation, although the measurements and calculations were made in directions between 0° and 90°. Both experimental and FE results were also compared to the DISPERSE predictions. As expected for a cross-ply composite plate, DISPERSE predictions for the attenuation coefficient, group velocity, phase velocity and the slowness profile are relatively uniform in all directions. The attenuation coefficient in all directions is less than 0.1 dB/mm and the average group and phase velocity is about 1400 m/s and 1200 m/s respectively. Since the phase slowness is the inverse of the phase velocity, all directions are expected to have a uniform value as well.

Turning to the experimental results, it can be observed that the measured attenuation coefficients are scattered around the DISPERSE prediction (Figure 5-8a). The attenuation coefficient in the 30° direction is significantly higher, which could be due to measurements errors related to the laser monitoring in this direction. The FE results show slightly higher attenuation values in the 30°, 45° and 60° directions. Interestingly, these peaks have been observed in a similar manner by Asamene et al. [127]. They also found that the attenuation coefficients were lower in the 0° and 90° directions and were three times higher in the 30°, 45° and 60° directions. However, the problem with the

attenuation values in the 30°, 45° and 60° directions can be attributed to a numerical error from the location of the monitoring nodes.

As seen in Figure 5-8b, the agreement between the experiments, FE and DISPERSE results for the group velocity is excellent for all directions. Slightly higher group velocities were obtained experimentally. As was previously discussed in section 5.3, this could be due to the higher uncertainty in the material properties used for the predictions. Overall the group velocity of the A_0 mode in a cross-ply composite plate shows no angular dependency. For the phase velocity profile (Figure 5-8c), comparable results were obtained between the experimental and DISPERSE results, with consistently higher phase velocities from the experiments. All three results matched for the phase velocity in the 0° direction. The FE results in directions between 15° to 75° were obtained from four monitoring nodes placed at the intended monitoring location, and then the phase values of these signals were interpolated using the bilinear interpolation method. This method results in a reasonable consistency (as shown in Figure 5-8c) with the largest error can be observed in the 15° and 75° directions.

One of the ways to illustrate changes caused by the influence of anisotropy is by studying the slowness profiles. The slowness profile, as can be seen in Figure 5-8d, presents the reciprocal of the phase velocities in different directions. The slowness profile of the A_0 mode in a cross-ply composite plate shows a relatively uniform propagation in all directions and indicates only a small angular dependency on the phase front direction.

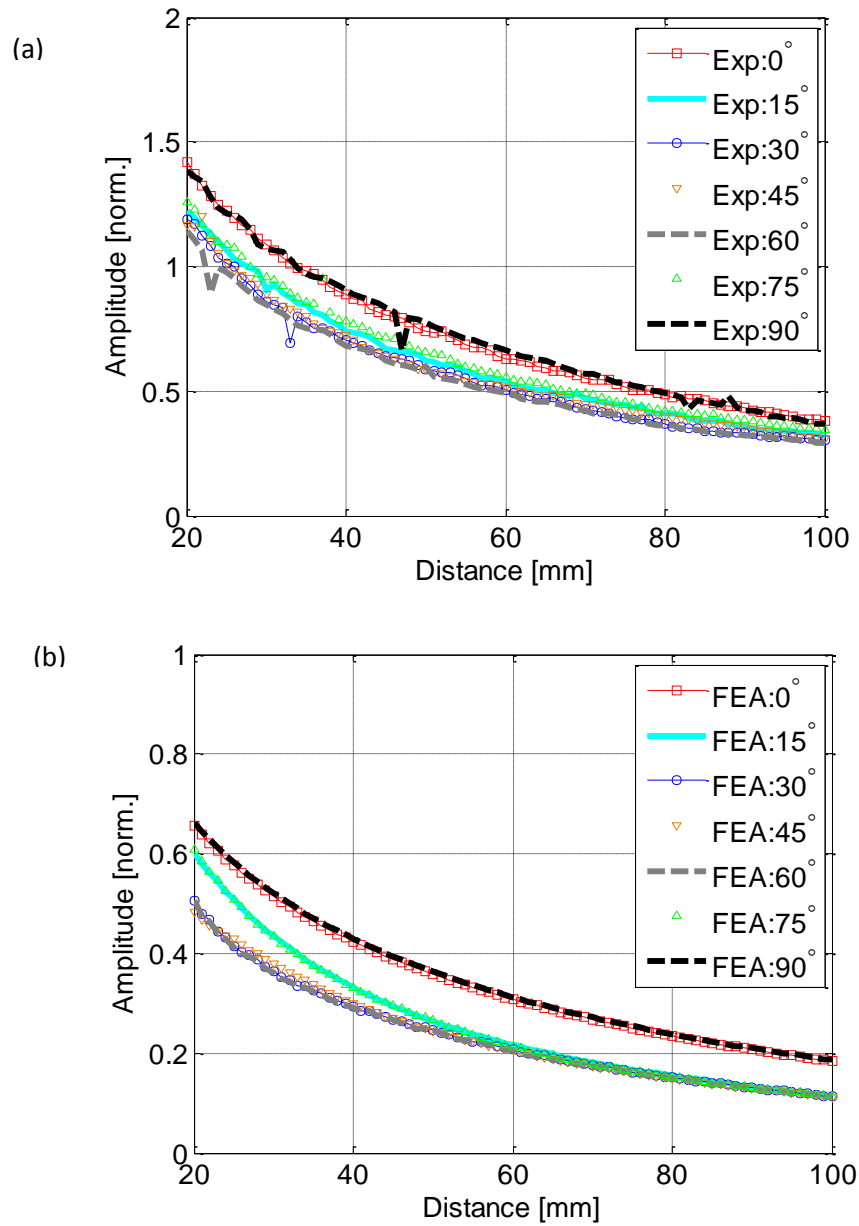


Figure 5-7: (a) Experimental measurement and (b) FE simulations of maximum amplitude of signal envelope (Hilbert transform) of propagating A_0 guided wave pulse in 24-crossply plate; measured every 1 mm step; every 15° in directions of 0° to 90° directions; 100 kHz.

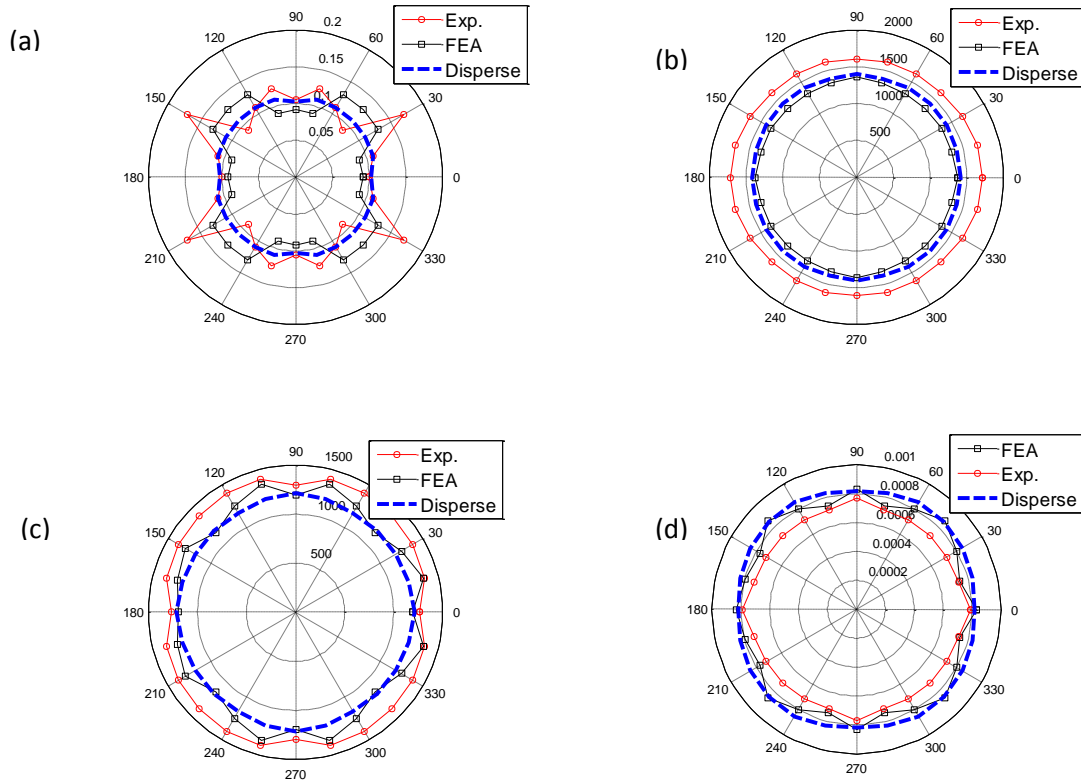


Figure 5-8: Experimental, FE and DISPERSE values for angular dependency of the A_0 guided wave properties in a 24-crossply plate; (a) attenuation coefficient, (b) group velocity, (c) phase velocity and (d) phase slowness; measured within 100 mm distance every 15° step.

5.4.2 Unidirectional plate

A similar study as in the previous section was conducted for the 3.6 mm UD plate.

Figure 5-9 presents the measured (Figure 5-9a) and simulated (Figure 5-9b) amplitudes of the A_0 mode propagating along radial lines. Similar amplitude patterns can be observed from both results, which indicate the accuracy in the FE modeling with added Rayleigh damping. The highest amplitude was in the 0° direction, and then followed by the amplitudes in the 15° direction. Nearly comparable curves were obtained from the amplitudes in the 30°, 45°, 60°, 75° and 90° directions, where the amplitudes were the lowest. Comparing to the FE results in the 15° direction particularly, it is quite interesting that the FE can produce a very distinctive and similar amplitude pattern compared to the

experimental curve. This contradicts the experimental and FE results shown for the cross-ply plate (Figure 5-7), where this effect cannot be clearly observed. A similar level of amplitude drop (reduction by half) within the 50 mm propagation distance can be observed. After propagating about 80 mm distance, the guided wave in the 15° direction started to behave similarly as in other directions in the 0° direction, which was higher. Thus, it can be seen that the beam steering tends to steer the wave packet towards the fiber direction (0° direction). This suggests that it may be quite difficult for the A_0 mode to be used efficiently for defect characterization in the non-principal directions.

The angular wave characteristics were calculated and plotted in a polar coordinate system. The measured angular patterns are displayed with comparison to the DISPERSE and FE simulations. Figure 5-10a shows the expected angular-dependent attenuation coefficients predicted by DISPERSE. The experimental and FE results show almost similar attenuation in all directions, while DISPERSE predicts much higher value in the 90° direction. The scattered FE result was due to the numerical error as explained previously in Section 5.4.1. From the calculation of the group velocity as a function of angular direction (Figure 5-10b), good agreement between the trends of the three results can be observed. The experimental measurements show slightly higher group velocities between the 0° and 30° directions. The FE predicted slightly lower group velocities than the DISPERSE result in the directions between 30° and 60°. According to the DISPERSE prediction, the highest group velocity is in the 0° direction (approximately 1500 m/s), and then slowly decreased by 25% when propagating in directions between 45° and 90° (approximately 1200 m/s). In a similar pattern, DISPERSE predicted the angular-dependent phase velocity. The phase velocity is highest in the 0° direction then reduced to more than 30% in the 90° direction. The experimental results are comparable to the DISPERSE prediction, but, the FE results show a slight variation in the phase velocities between directions of 15° to 75°. The FE result was extracted from interpolated signals of four neighboring nodes in order to reduce the numerical error. Overall the measurement results are consistent with data obtained from DISPERSE.

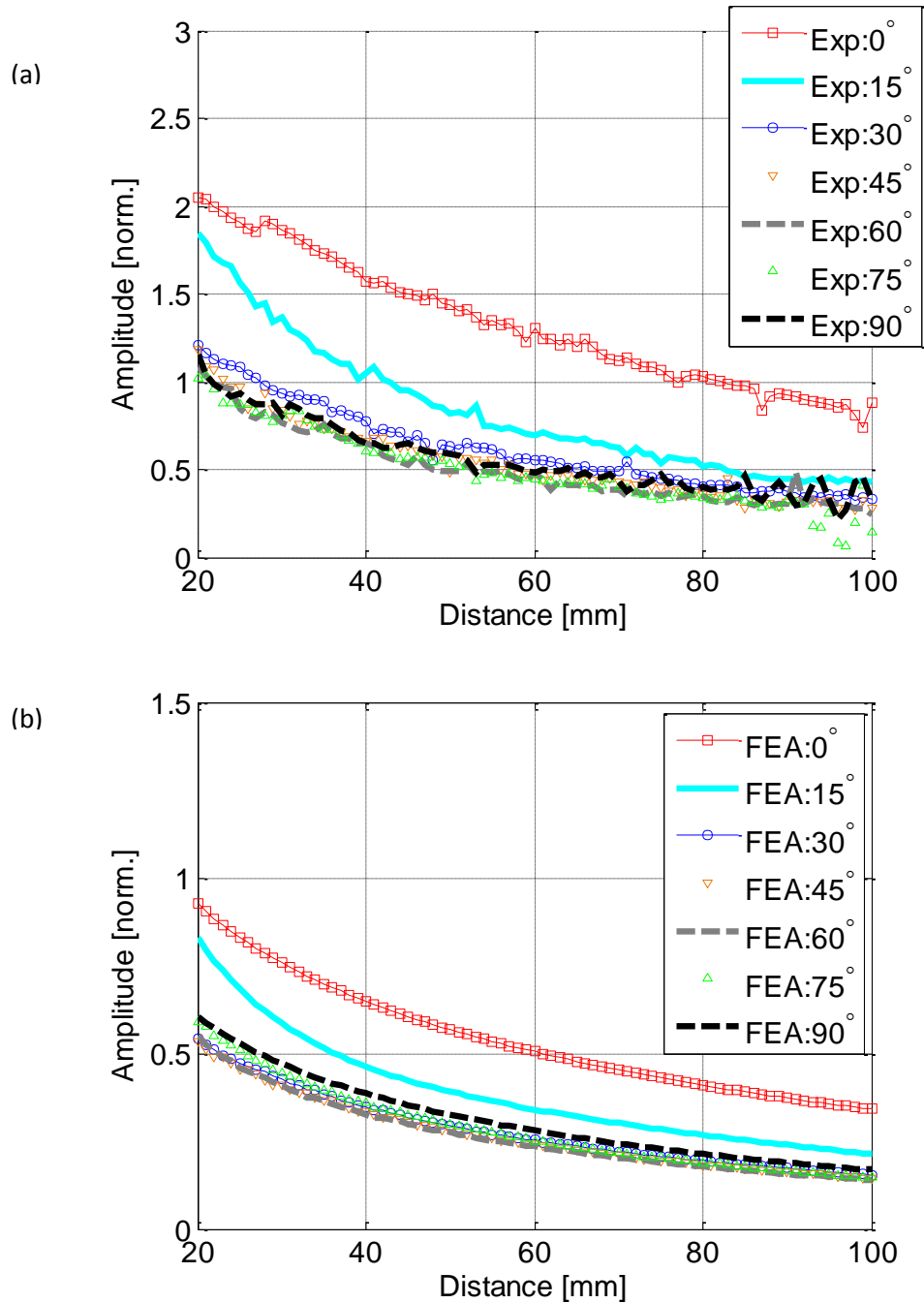


Figure 5-9: (a) Experimental measurement and (b) FE simulations of maximum amplitude of signal envelope (Hilbert transform) of propagating A_0 guided wave pulse in 3.6 mm UD plate; measured every 1 mm step; every 15° in directions of 0° to 90° directions.

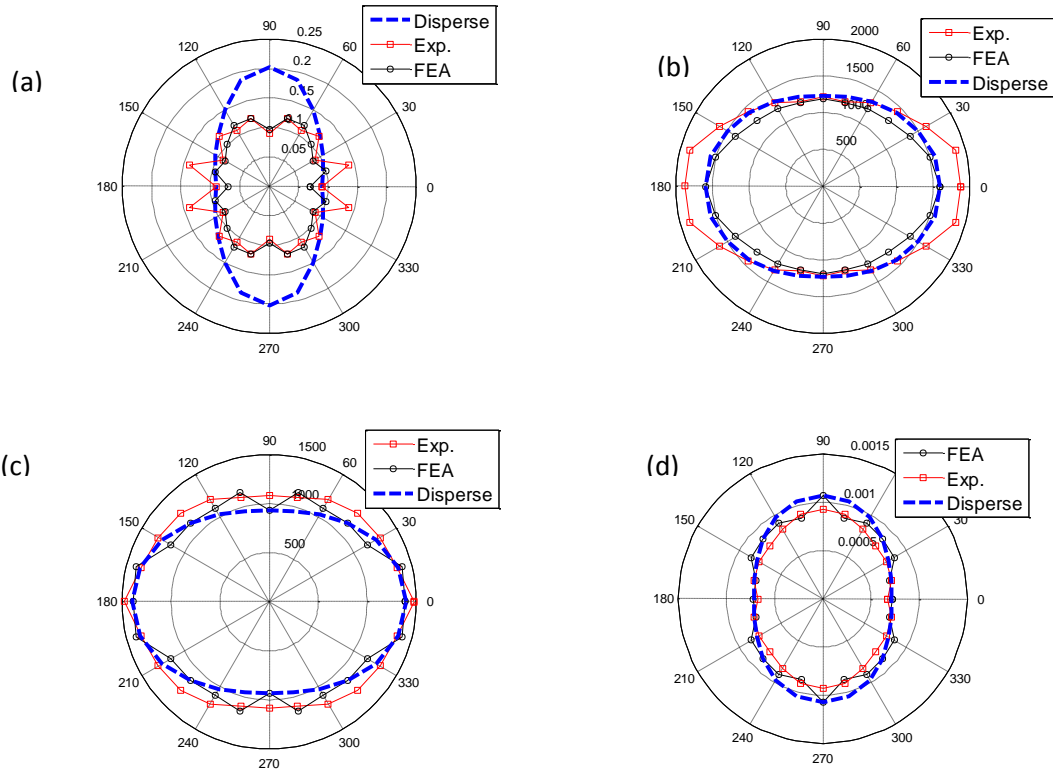


Figure 5-10: Experimental, FE and DISPERSE data of angular dependency of the A_0 guided wave properties in a 3.6 mm UD plate; (a) attenuation coefficient, (b) group velocity, (c) phase velocity, and (d) phase slowness; measured within 50 mm distance in every 15° step.

Figure 5-10d presents the slowness profile where the slowness is the inverse of the phase velocity. As for the phase velocity results, overall a good agreement between measurements and FE and DISPERSE predictions can be observed. Due to the higher angular dependency in the UD plate, significant guided wave steering perpendicular to the phase slowness curve, especially in the directions close to the fiber direction, can be predicted. In this context the attenuation guided waves plays an important part, since it determines how far waves can travel and be detected by a sensor. For example in the UD plate, the received signals of the A_0 mode will diminish quickly in the 90° direction due to the highest wave attenuation. With the FE models and the procedure presented in

Chapter 3 and 4, the A_0 mode wave properties in any propagation direction can be predicted, enabling the optimization of an efficient sensor network.

5.5 Conclusions

The results presented in this chapter provide the guided wave characteristics and properties for three types of composite plates. An approximation of the A_0 mode wave propagation simulation using the 3D FE approach was established and validated in section 5.1. Results from both homogenized and layered FE models are reasonably consistent, suggesting that in principle homogenized material properties could be employed to simulate the guided wave propagation in an undamaged composite plate. This would greatly reduce the required simulation time for thick layered composite specimens, as it eliminates the need to model each layer individually. Section 5.1.2 shows that increasing the number of element through the thickness will not give any significant difference; hence, a smaller number of elements in the thickness direction is adequate for simulating the A_0 mode wave propagation. In Section 5.1.3, it has been shown that Rayleigh damping could be used to correctly model the guided wave attenuation in the three types of composites plates. In Section 5.2, the attenuation coefficients of the guided wave in the three different composite plates have been successfully estimated and validated, although the consistency of the measurements is known to be difficult to obtain. Section 5.3 presents the estimation of the frequency dependent phase and group velocity of the A_0 mode in the fiber direction. The measured wave characteristics are reasonably in agreement with the predicted results. The angular characteristic of the guided wave properties arises from the directional dependence of the material properties and has been investigated in section 5.4. It has been shown that the properties of the A_0 mode in a unidirectional composite plate can have a significant directional dependency. These complications are crucial to be understood to improve the interpretation of received signals, particularly for defect characterization. The FE simulation tool has shown the capability to characterize the guided wave propagation in composites. This study improved the understanding of the guided waves behavior in different composites plates.

CHAPTER 6 FE ANALYSIS OF GUIDED WAVES INTERACTION WITH DEFECTS

The motivation of the work presented in this Chapter is the development of 3D FE modeling and the analysis of the first anti-symmetrical (A_0) guided wave mode scattering in damaged composite plates. The development of an accurate 3D model of guided wave interaction with realistic defects in composites can provide a practical way to optimize guided wave-based detection techniques for the fields of NDE and SHM. Limited publications were found for the analysis using the full 3D FE model, normally due to large computational demand. The main objective is to understand the scattering characteristics of the A_0 mode at a defect and to evaluate the defect characteristics. The primary goal is to compare to the experimental results (discussed in Chapter 7) where the accuracy of the modeling technique used to represent the impact damage in a composite plate can be verified.

The chapter begins with the verification of the composite plate models. The impact damage in the composite plate was initially modeled as a rectangular-shaped delamination. The first verification is to investigate the accuracy between two FE models assigned with different sets of material properties (homogenized and layered models). The wave scattering from these two models was compared in order to see whether both models could provide comparable results. Further verifications investigate the influence of additional damping in the FE models and comparison between two different delamination shapes.

The second part of this Chapter investigates the interaction of guided waves with large delamination using a 2D FE model. A larger delamination length was used to reduce any interference from the delamination boundaries. Using this model, a delamination was placed at different depths and the scattering and mode conversion of guided waves studied.

The third part of this Chapter discusses the influence of the delamination on the wave scattering. The delamination was placed at different depths and modelled with different sizes. This allows the determination of the relationship between the damage parameters and the scattered wave field. The results may provide the basis for the quantification of the damage detection using guided ultrasonic waves, as well as form a library of expected wave scattering patterns for a given plate and defect geometry.

In order to provide guidelines for extending the modeling of realistic multimode impact damage, the final section of this chapter discusses wave scattering by a mixed-mode defect in composite plates. Degradation in the stiffness properties was assigned together with delamination to represent the multi-mode impact damage. The predicted interaction of A_0 guided waves with the defects is presented. The important findings from the results and future improvements for a realistic composite model with impact damage will be discussed to conclude this chapter.

As described in Chapter 4, only one type of composite plate was used for this study, which was similar to the damaged specimen used for the experimental study. The plate thickness was set to 2 mm thickness (8 elements through the thickness). The plate dimensions were set to 1000 mm x 1000 mm. An 8-cross-ply laminate $[0^\circ/90^\circ]_{2s}$ was assigned with individual layup properties (Table 3.3). The orthotropic homogenized $[0^\circ/90^\circ]$ properties (Table 3.2) were assigned for the homogenized model. It is important to note that the material properties were assumed to be similar to the properties listed in Table 3-2 and 3-3, although these properties were originally measured for the other two composite plates (Chapter 5). The frequency of excitation used was a 100 kHz tone-burst, which was less than the cut-off frequencies for higher modes. Two monitoring types have been used to describe the scattering of the A_0 wave pulses: (1) a 200 mm line scan in the 0° direction monitored across the delamination region, and (2) a circular scan with 30 mm radius measured every 5° around the delamination area.

6.1 Verifications of the FE modeling approaches

6.1.1 Comparison between homogenized and layered models

A similar comparison analysis was discussed in Chapter 5 for the case of undamaged composite plates. It was revealed that both models provide comparable A_0 wave propagation in the undamaged composite plate. This is an important note knowing that the 3D homogenized model could reduce the simulation time and cost of the computational system. However, a similar verification process has to be performed once again because the FE models were then modeled with a delamination. This was an important decision before attempting to use the homogenized model with defect for further investigation.

Two FE models with different sets of material properties were assigned: (1) a solid single layer model of 2 mm thickness with 8 elements through the thickness, where the elements were assigned with homogenized $[0^\circ/90^\circ]$ material stiffness properties, and (2) a layered 8-ply model with 0.25 mm nominal ply thickness, where the elements at each layer were assigned with the unidirectional material stiffness properties and oriented at 0° and 90° alternately. The delamination area was 20 mm x 20 mm and was placed at different depths. The center of the delamination was located 100 mm away from the excitation point. Additional damping to represent the natural material absorption coefficient is not yet considered at this point. Details about the influence of delamination depth will be discussed later in another sub-Chapter.

Figure 6-1 shows the comparison of line scans between the homogenized and layered models, compared to their baseline data (simulated from composite models without defect). Three locations could be used to distinguish the amplitude patterns between both models: before the delamination (< 90 mm), within the delamination (from 90 mm to 110 mm) and after the delamination (> 110 mm). At locations before the delamination area, the amplitudes of the A_0 mode simulated in both types of models are comparable as is their baseline data. Comparing amplitudes at the delamination area, a

significant change and fluctuation in the signal amplitudes can be observed compared to those measured in the undamaged location. Although both models simulated at some depths look quite similar, it is obvious that both models show big differences for the case of 0.75 mm depth. The amplitudes of the A_0 mode propagating through the delamination region (from the layered model) show small amplitude peaks and increased significantly behind the delamination region. This is in contrast to the homogenized model, where higher peaks in the delamination area can be observed, as well as the sudden drop in the amplitude when the A_0 mode travelled past the delamination. In addition to the unexpected behaviour, all simulations at different depths reveal the inconsistency in the amplitude pattern at locations behind the delamination.

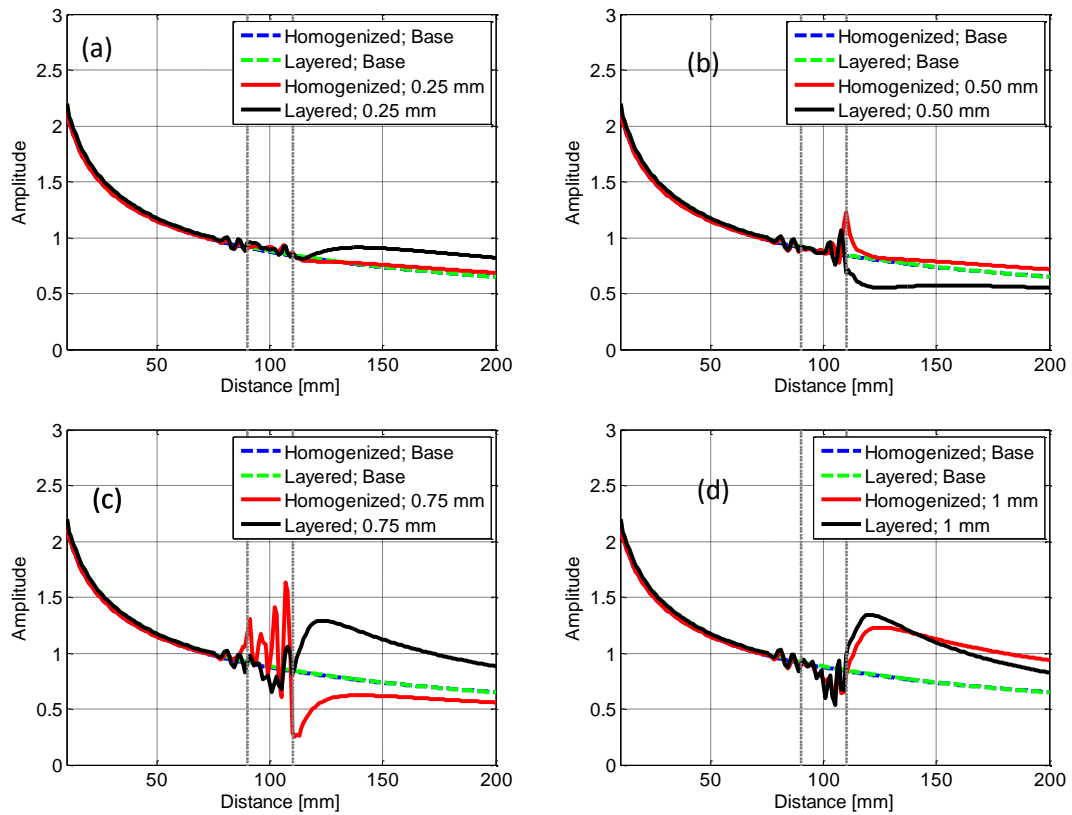


Figure 6-1: Amplitude of propagating guided wave over defective area of composite plate (0° direction) modeled using homogenized (black line) and layered material properties (red line); delamination was placed at different depth: (a) 0.25 mm, (b) 0.50 mm, (c) 0.75 mm and (d) 1 mm; blue and green dashed lines correspond to the baseline wave propagation over undamaged area.

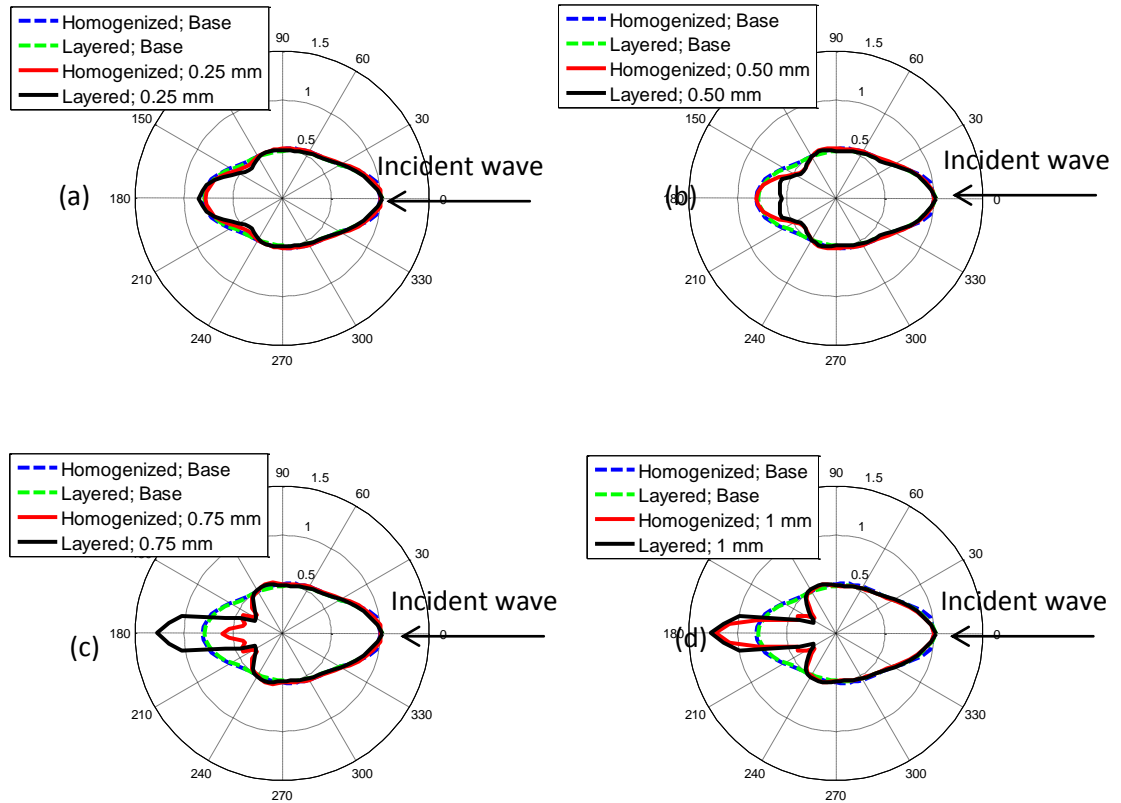


Figure 6-2: Plot of amplitude variation measured every 5 ° at 30 mm radius around center of the delamination; modeled using homogenized (black line) and layered material properties (red line); delamination was placed at different depth: (a) 0.25 mm, (b) 0.50 mm, (c) 0.75 mm and (d) 1 mm; blue and green dashed line correspond to the baseline wave propagation over undamaged area.

Figure 6-2 shows the wave scattering around a defect for both models in form of circular plots around the delamination (30 mm radius). In general, the back scattering matches fairly well with the baseline data. But, there are significant differences in the forward scattering pattern (between 150° to 240°) in both models except for the models with the delamination placed at 0.25 mm and 1 mm depth. Low scattered amplitudes at delamination $z_d = 0.25$ mm can be observed from the line scan as well (Figure 5-1a). As can be seen in Figure 6-2, there was a significant difference in the amplitude profiles between the two models for the cases where $z_d = 0.50$ mm and $z_d = 0.75$ mm. In contrast, quite a

good match was obtained from both homogenized and layered models when $z_d = 1$ mm, although their line scans do not exactly match at locations behind the delamination (Figure 5-1d). This can be explained by the matching homogenized [0/90] properties for the 4 layers above and below the delamination [0/90/0/90]. From these results, it seems that the wave scattering by delamination can be reasonably modelled using both types of models for symmetrically located delamination ($z_d = 1$ mm).

The reason for such differences in the amplitude patterns from both types of models may be related to the material properties defined in the models. With the delamination in the path of the propagating wave, the wave velocities vary since the plate is divided into two sub-plates (below and above the delamination). As has been shown in Section 5.3, the wave velocity is dependent on the frequency-thickness product and also on the material orientation. For the delamination at 0.75 mm for example, the sub-laminate below the delamination has a lay-up of [0/90/0] and significant different propagation velocities than what would be predicted from the homogenized model, leading to different interference of the wave pulses. This factor definitely influences the scattering behaviour, the signal amplitudes in particular. The illustration of the material orientations and depths of delamination can be found in Chapter 4 Figure 4-3.

6.1.2 Influence of additional damping

In the previous chapter it was noted that the incorporation of Rayleigh damping ($\beta = 30$ ns) in the FE model (2 mm cross-ply plate, Figure 5-3b) resulted in a good match with the experimental results for the wave propagation in intact plates. In order to model the accurate wave propagation behaviour in composite plates with defects, this Section deals with the influence of the Rayleigh damping in a layered model with a standard case delamination of size 20 mm x 20 mm, positioned at 1 mm depth (ply no. 4). Only one case study is shown here, for $z_d = 1$ mm, as the effects were found to be similar for all depth cases.

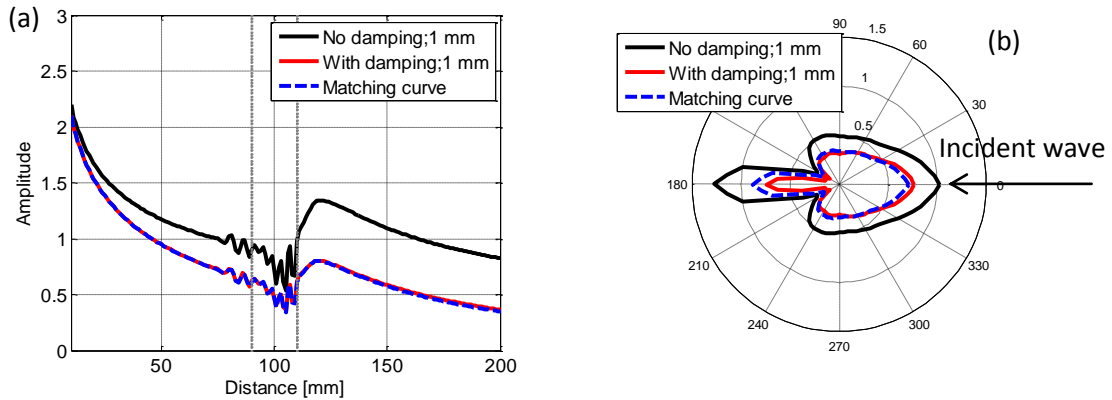


Figure 6-3: Comparison between layered models with and without additional damping; delamination at 1 mm: (a) 200 mm line scan (b) 30 mm radius circular scan.

As can be seen from Figure 6-3, the additional damping in the FE model resulted only in reduced amplitudes of the propagating A_0 pulses as expected for the additional wave attenuation. No changes in the relative amplitudes or the scattering pattern were observed. The amplitudes from the model without damping could be fitted with an exponential function with the appropriate damping coefficient, as shown in Figure 6-3a (blue dashed line). From the angular scattering (Figure 6-3b) overall same behaviour but small differences due to damping is fine and nicely points out some problems. These results suggest that the scattering at a defect could in principle be investigated without accurate knowledge of the material damping, as it has only a small influence on the scattered wave pattern. However, one should bear in mind that the reduction in the guided wave amplitudes due to material damping can be quite significant over longer propagation distances. For further investigations throughout this Chapter, all FE models were incorporated with Rayleigh damping ($\beta = 30$ ns).

6.1.3 Influence of delamination shape

In practice impact leads to irregularly shaped damage patterns, with delaminations often observed to have an approximately oval shape. However, many previous publications have used either the circular or the rectangular delamination shapes [74], [103], [128]. In this section it is considered whether a simple rectangular delamination shape can be used, which is straight-forward to implement in a FE model. Two regular shapes to represent a delamination are investigated: a rectangular-shaped delamination (dimensions: 20 mm x 20 mm) and a circular-shaped delamination (diameter: 20 mm).

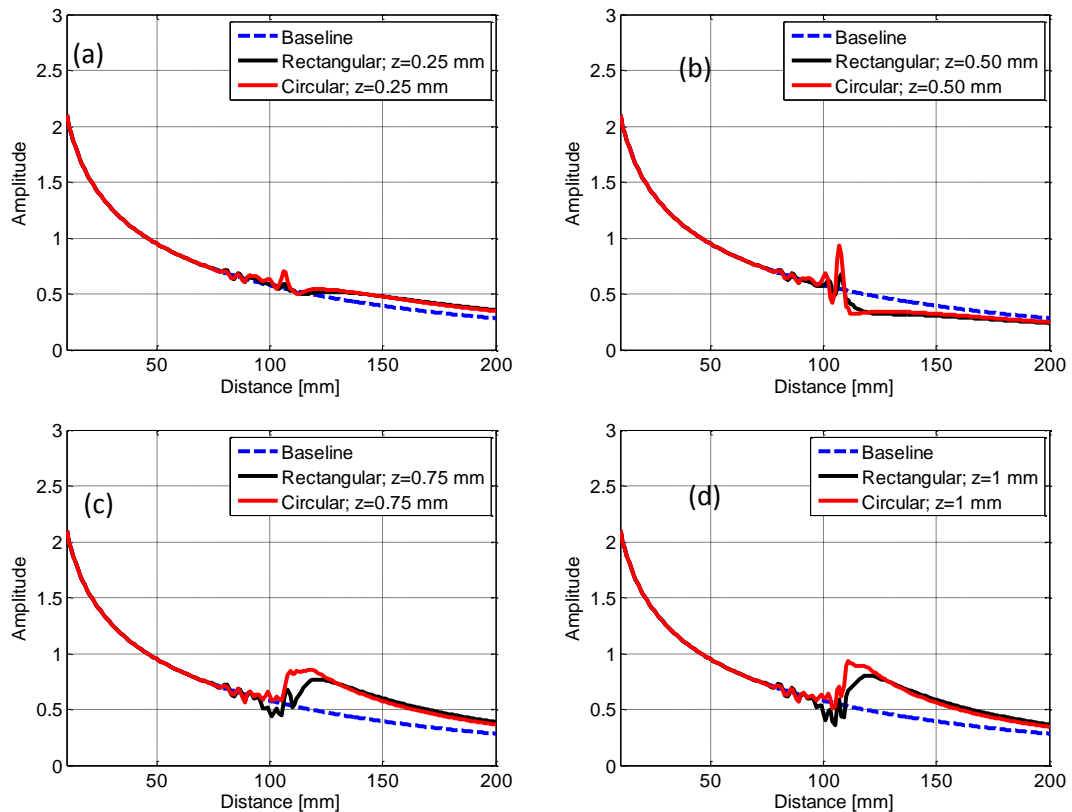


Figure 6-4: Line scans for a comparison between layered models with 20 mm x 20 mm rectangular-shaped and 20 mm diameter circular-shaped delamination; delamination depths: (a) 0.25 mm, (b) 0.50 mm, (c) 0.75 mm and (d) 1 mm.

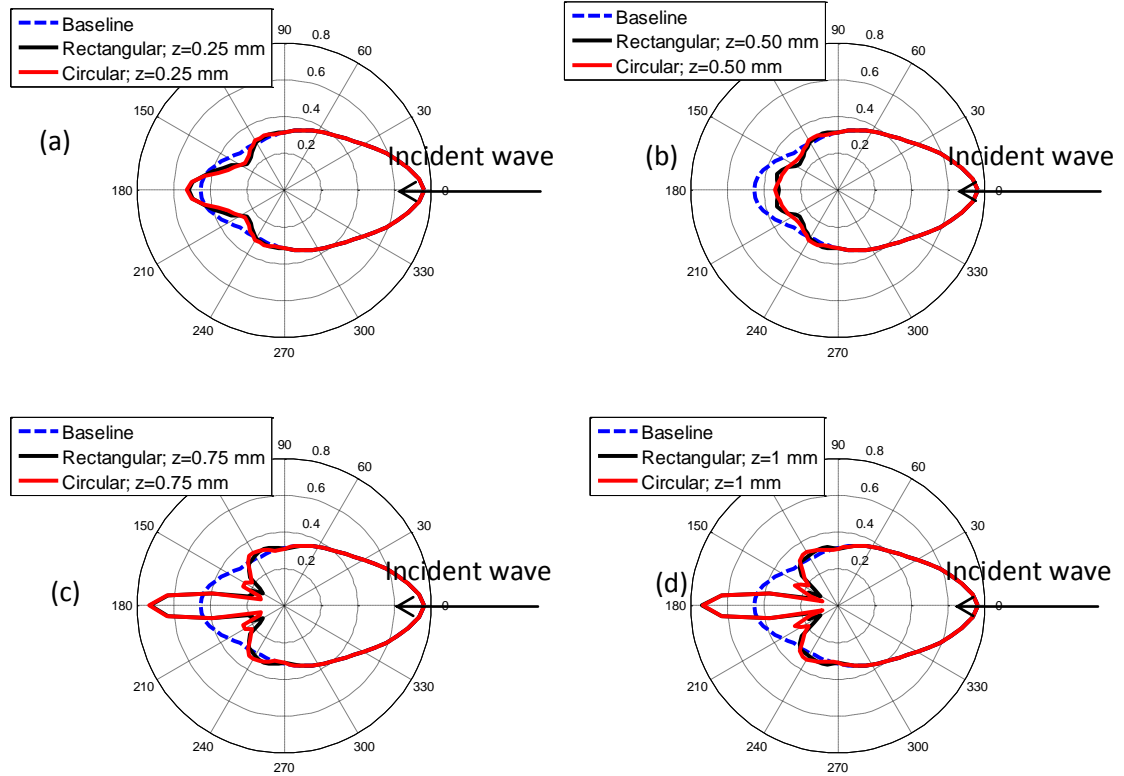


Figure 6-5: Circular scans for a comparison between layered models with 20 mm x 20 mm rectangular-shaped and 20 mm diameter circular-shaped delamination; delamination depths: (a) 0.25 mm, (b) 0.50 mm, (c) 0.75 mm and (d) 1 mm.

As can be seen from Figure 6-4 and Figure 6-5, both models resulted in comparable amplitudes pattern, especially for the forward propagating wave. The line scans (Fig. 6-4) show slightly higher peak amplitudes on top of the circular shaped delamination compared to the peaks from the square shaped delamination. Very small differences in the angular scattering pattern were observed (Fig. 6-5), particularly in the 150° and 210° directions. A possible explanation for this might be the different delamination extent in these directions. For the delamination size comparable to the wavelength it was observed that circular and rectangular shaped delaminations of the same maximum extent (diameter matching rectangle) resulted in overall very similar scattering patterns and amplitudes. Therefore, a simple and easy to implement rectangular shape was chosen for further FE modeling and analysis. However, these findings should be checked for

delamination sizes larger than the wavelength where the delamination shape could have a larger influence on the guided wave scattering.

6.2 Interaction of A_0 guided waves at large delamination

6.2.1 Guided waves propagation through delamination

A 3D FE simulation was carried out to investigate the A_0 mode scattered field at a large delamination size. Based on the findings obtained from the previous section, a layered FE model, added Rayleigh damping ($Beta = 30$ ns), and a square-shaped delamination was used. The delamination of 200 mm x 200 mm size was positioned at the symmetrical plane ($z_d = 1$ mm depth). A longer delamination was used for the purpose of studying guided waves interaction with defects without any overlapped reflections. For this case study, the excitation point was located 100 mm away from the delamination entrance.

Figure 6-6 presents snapshots of the stress fields at different time instants. Figure 6-6a shows the snapshot at 120 μ s as the incident A_0 mode has just propagated into the delamination area. Amplitudes of the propagating wave are seen to be higher in the 0° and 90° directions as expected for a cross-ply composite plate. Small entry reflection can be observed in Figure 6-6b. Also, two shadow areas began to appear approximately in the 150° and 210° directions. This happened as the wave was being reflected at the upper and lower boundary of the delamination. Figure 6-6 shows considerable waves transmitted across the delamination and advancing to the exit of delamination. A significant portion of the wave reflections inside the delamination area can also be observed from Figure 6-6d. Experimental observation by Pohl et al. [58] confirmed such multiple reflections taking place inside the delaminated area. These accumulate a large amount of wave energy trapped within the delamination area. From a practical NDE point of view, the area with high wave energy can serve as a good marker for localizing defects in composites. Similar trapped modes have also been discovered by Sohn et al. [33] using an experimental approach. Figure 6-6e reveals the wave transmitted across the exit of the delamination and the reverberations of the reflected waves from the exit of the delamination. These

reflected waves then again interfere with the main propagating waves, which in turn formed a large transmitted wave, as can be seen from the final Figure 6-6f.

Figure 6-7a shows typical FE time histories at locations 40 mm, 60 mm, and 80 mm from the excitation point, corresponding to 60 mm, 40 mm and 20 mm from the delamination entrance. This figure shows the A_0 mode pulses propagating towards the delamination. A single reflected wave was obtained for the signals monitored before the delamination area. There were actually two reflected pulses for the signal monitored at 40 mm, but this cannot be seen properly due to the small amplitudes compared to the amplitude of the incident wave. The amplitude of the reflected wave was about ten times lower than the amplitude of the incident waves. It can be observed that the amplitude of the reflected wave increased when distance between the monitoring point and delamination reduced.

By using the relationship between arrival time and group velocity, the distance between the defect and the monitoring point can be calculated. For example, at 40 mm (60 mm from delamination), the arrival time of the incident and reflected wave were respectively 30 μs and 125 μs , and the group velocity of the A_0 mode propagating in a 2 mm thick composite plate is approximately 1400 m/s. The distance between the delamination entrance and the monitoring point was estimated as approximately 65 mm. The error between the known defect location and the estimated one is just under 10%, and this is due to the uncertainties in determining the exact pulse arrival times.

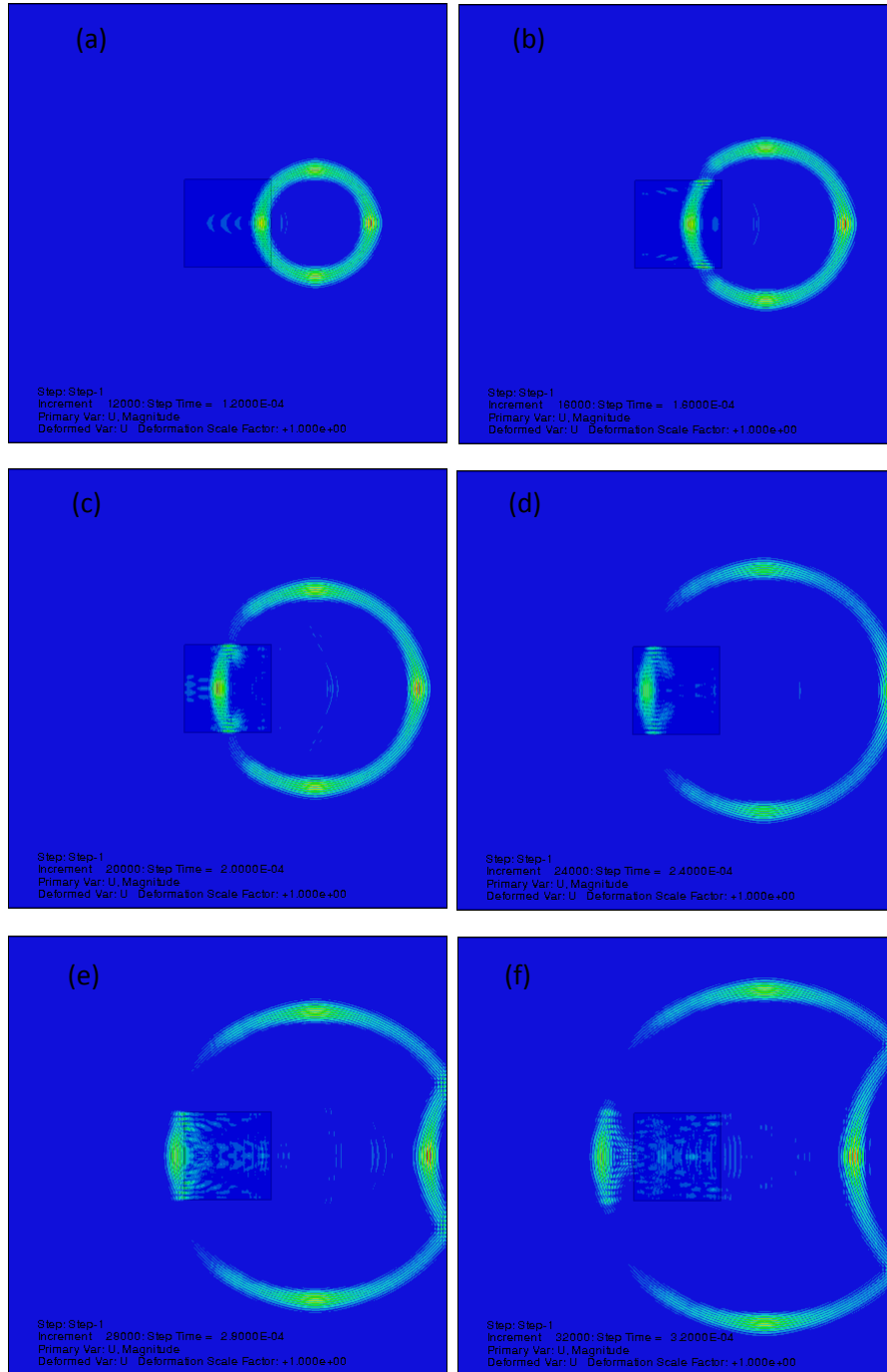


Figure 6-6: Exact stress fields at different time instants; (a) 120 μs , (b) 160 μs , (c) 200 μs , (d) 240 μs , (e) 280 μs , (f) 320 μs ; 200 mm x 200 mm rectangular delamination positioned at symmetrical layer (1 mm depth); excitation point at 100 mm from center of delamination.

Figure 6-7b shows the predicted time traces at locations of 320 mm, 340 mm and 360 mm. The signals were received 20 mm, 40 mm and 60 mm after the delamination exit. The amplitude of the transmitted wave was reduced by nearly half compared to the pulses monitored before the delamination. As discussed in Section 6.1 (line scan), the amplitude decay in damaged composite plates beyond the delamination area not necessarily follows the geometrical and material damping relationship. This demonstrates that the defect size based on the amplitude reduction cannot be easily estimated.

From the numerical simulation of the signal received at 340 mm (Figure 6-7b), the arrival time of the largest transmitted wave was found to be 270 μ s. Based on the velocity-distance relationship, the pulse corresponds to the main transmitted $A_0A_0A_0$ wave group. The $A_0A_0A_0$ pulse propagated as the A_0 mode in the undamaged plate before the delamination, through the delamination, and in the undamaged plate behind the delamination). The arrival of the $A_0S_0A_0$ wave group is observed earlier at 140 μ s, also matching to the theoretical prediction. The $A_0S_0A_0$ wave group represents a pulse that propagated across the delamination as an S_0 mode and as an A_0 mode in the undamaged plate before and behind the delamination. Multiple S_0 mode reflected pulses can also be observed between the $A_0S_0A_0$ and $A_0A_0A_0$ pulses, but with small amplitude. This wave group keeps reflecting at both delamination entrance and exit since the S_0 mode travels faster than the A_0 mode, and for the symmetrical delamination is confined only in the delamination area. From this study, small reflected waves and mode conversion were observed, which the next section discusses in more detail.

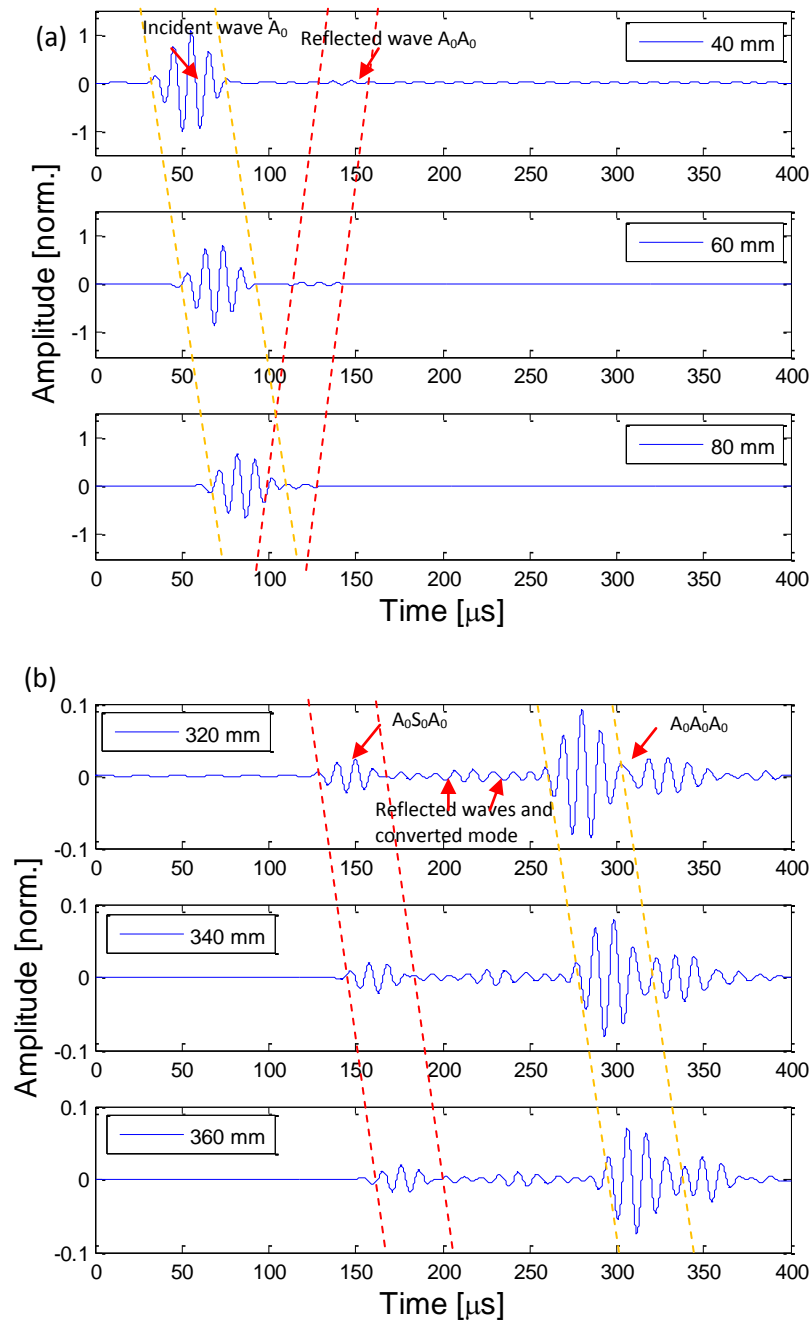


Figure 6-7: The predicted guided wave time signals for a 200 mm x 200 mm delamination; 1 mm depth; (a) points before delamination, (b) points behind delamination.

6.2.2 Mode conversion at delamination

This section investigates the mode conversion phenomena using a 2D FE model in order to understand better the mechanism of interaction between guided waves and defect. Four composite plate models were considered with a delamination length of 200 mm positioned at different depths of 0.25 mm, 0.50 mm, 0.75 mm and 1 mm. Additional Rayleigh damping was not considered in this model and the effect of the beam spreading ($1/vr$) was eliminated when using this 2D model. The 2D model was used because of the need of using 16 elements through the thickness for monitoring the A_0 and S_0 mode in layers at different depth. A detailed explanation can be found in Section 4.6 and the configuration of the models can be seen in Figure 4-11.

Figure 6-8 shows the snapshots of the displacement fields of the guided waves with the delamination placed at different depths, taken at a propagation time of 110 μ s. It can be observed that there are slower and faster wave modes propagating independently in the top and bottom sub-plates for the asymmetrical delamination cases ($z_d = 0.25, 0.50$ and 0.75 mm). In contrast, the displacement fields in the top and bottom sub-plates are the same for the symmetrical delamination ($z_d = 1$ mm). This figure illustrated that the wave travels with different speed depending on the thickness and lay-up of the sub-plates. With a delamination, it is assumed that the guided wave propagates via two sheets of material positioned above and below the delamination. This creates two sub-plates with different thicknesses and with different laminate orientations. In general, the wave velocity changes in the delamination area since the wave has to travel through two smaller sub-plates thicknesses (lower and upper) than the main plate thickness. The group and phase velocities vary according to the changes in the frequency-thickness (fh) product of the material. If the delamination is placed symmetrically at the mid plane, for example $z_d = 1$ mm, both sub-plates will have a same thickness (1 mm), and the wave velocity is expected to be the same. However, if the delamination is asymmetrically located, for example $z_d = 0.25$ mm, the lower sub-plate will have a smaller thickness (0.25 mm) than the upper sub-plate (1.75 mm). For the A_0 mode, a low fh product region produces a

reduction in the velocities, where the arrival time of the A_0 mode travelling within the delamination area is greater than in the same plate without delamination.

From Figure 6-8, it can be observed that the wave in the upper sub-plates is propagating faster than in the lower sub-plates for the case of $z_d = 0.25$ mm and 0.50 mm. This is consistent with the above explanation and what has been predicted through DISPERSE software (Table 5-3). But for the case of $z_d = 0.75$ mm, the wave in the upper sub-plate was propagating slightly slower ($C_g = 1250$ m/s) than the lower sub-plate ($C_g = 1360$ m/s), which was contrary to the known velocity- fh relationship ($C_g \propto fh$). As discussed in Section 5.3, this is due to the influence of ply orientation, which acts as an additional factor in varying the wave velocity. This topic has not been investigated in detail in this study. In order to have a complete view of the A_0 mode interaction with the delamination located at different depths, Figure 6-9, Figure 6-11 and Figure 6-12 present the time signals of the A_0 and S_0 pulses. As detailed in Figure 4-11, one monitoring point was placed at 100 mm before the delamination (undamaged area), two monitoring points at the mid-plane of the upper/ lower delamination sub-plates, and one monitoring point at 100 mm behind the delamination. The out-of-plane and in-plane displacements at each point were recorded, corresponding to the A_0 and S_0 modes respectively. By estimating the wave velocities of the incident and the reflected waves, information on the mode conversions and newly-formed wave group can be obtained.

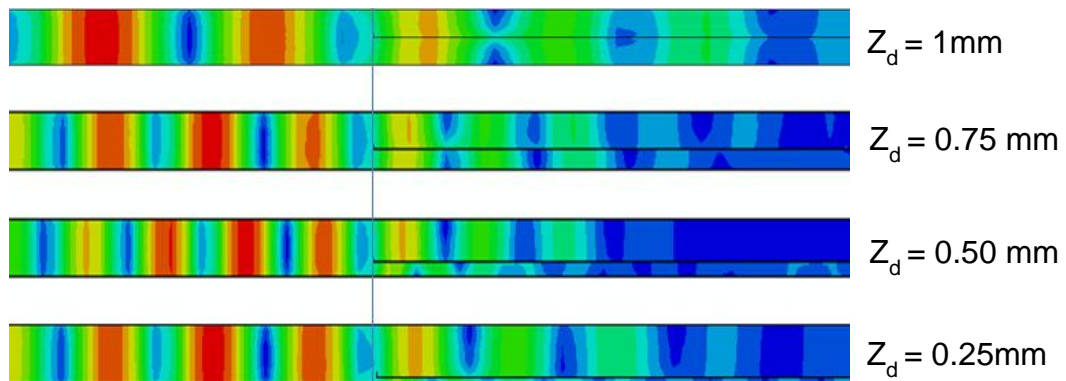


Figure 6-8: Snapshots of displacement fields at 110 μ s time instant; 200 mm long delamination positioned at different depth; 2D FE.

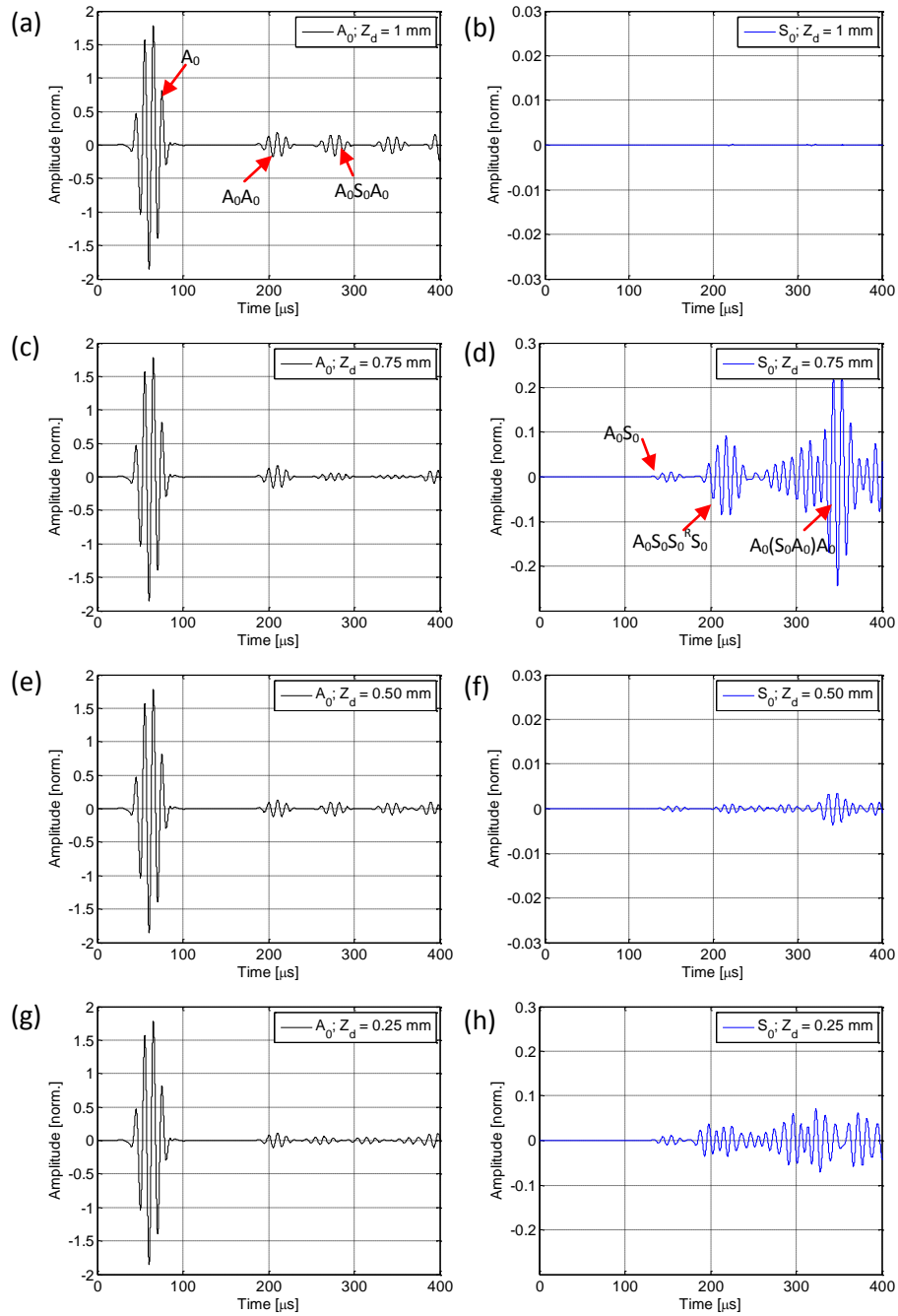


Figure 6-9: Received signals monitored at 100 mm before delamination; delamination depth is varied from 0.25 mm to 1 mm; left side corresponding to the A_0 mode signals; right side corresponding to S_0 mode signals.

Figure 6-9 shows the signals obtained at a location 100 mm before the delamination, which was 50 mm away from the excitation point. The signals on the left and right sides correspond to the A_0 and S_0 modes respectively. Referring to the A_0 signals, the arrival times of the incident A_0 mode wave for all case studies were exactly the same as expected, $t_{A_I} = 40 \mu\text{s}$. This matches to the calculation of the arrival time illustrated in Figure 6-10. Three reflected pulses can be observed, but only the first reflected pulse has higher signal amplitude, which was around 10% of the incident waves. This observation is consistent with these publications [82, 95, 129]. The arrival times of the first (A_{r1}) and second reflected (A_{r2}) waves were approximately about $180 \mu\text{s}$ and $250 \mu\text{s}$ respectively. Referring to Figure 6-10, the cumulative travel period of each possible mode propagating in the undamaged parts (before and behind the delamination) and delamination regions can be obtained. The corresponding wave group for the A_{r1} is the A_0A_0 , which is the pulse being reflected at the entrance of the delamination. An obvious trend of the first reflected pulse can be observed, where its amplitude reduced with decreasing delamination depth by approximately 25% for each depth. Meanwhile, the second reflected pulse corresponds to the $A_0S_0A_0$ wave group, which represents a pulse that propagated across the delamination as an S_0 mode and was reflected at the exit of the delamination.

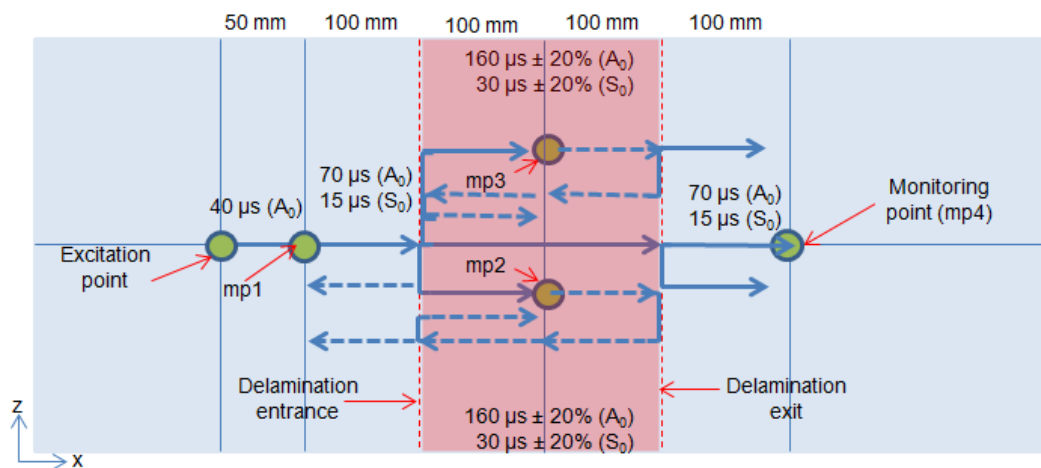


Figure 6-10: Illustration of the guided wave interaction with a delamination; possible mode conversion between the A_0 and S_0 mode reflected waves (dashed blue line); delamination located through the plate thickness (in pink area); travel times are included for each mode that travels in undamaged and damaged areas.

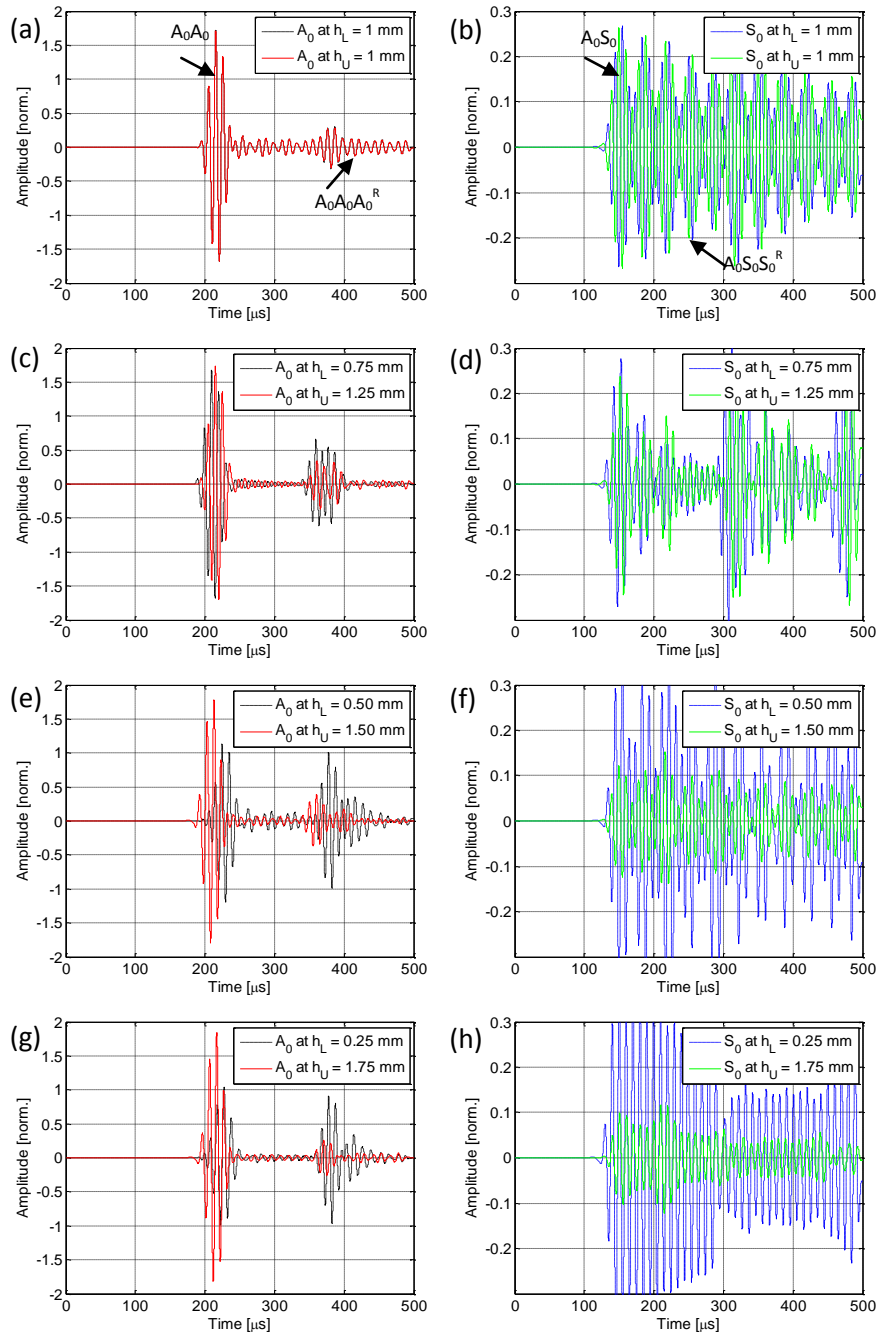


Figure 6-11: Received signals monitored at 100 mm within delamination; delamination depth is varied from 0.25 mm to 1 mm; left side corresponding to the A_0 mode signals; right side corresponding to S_0 mode signals.

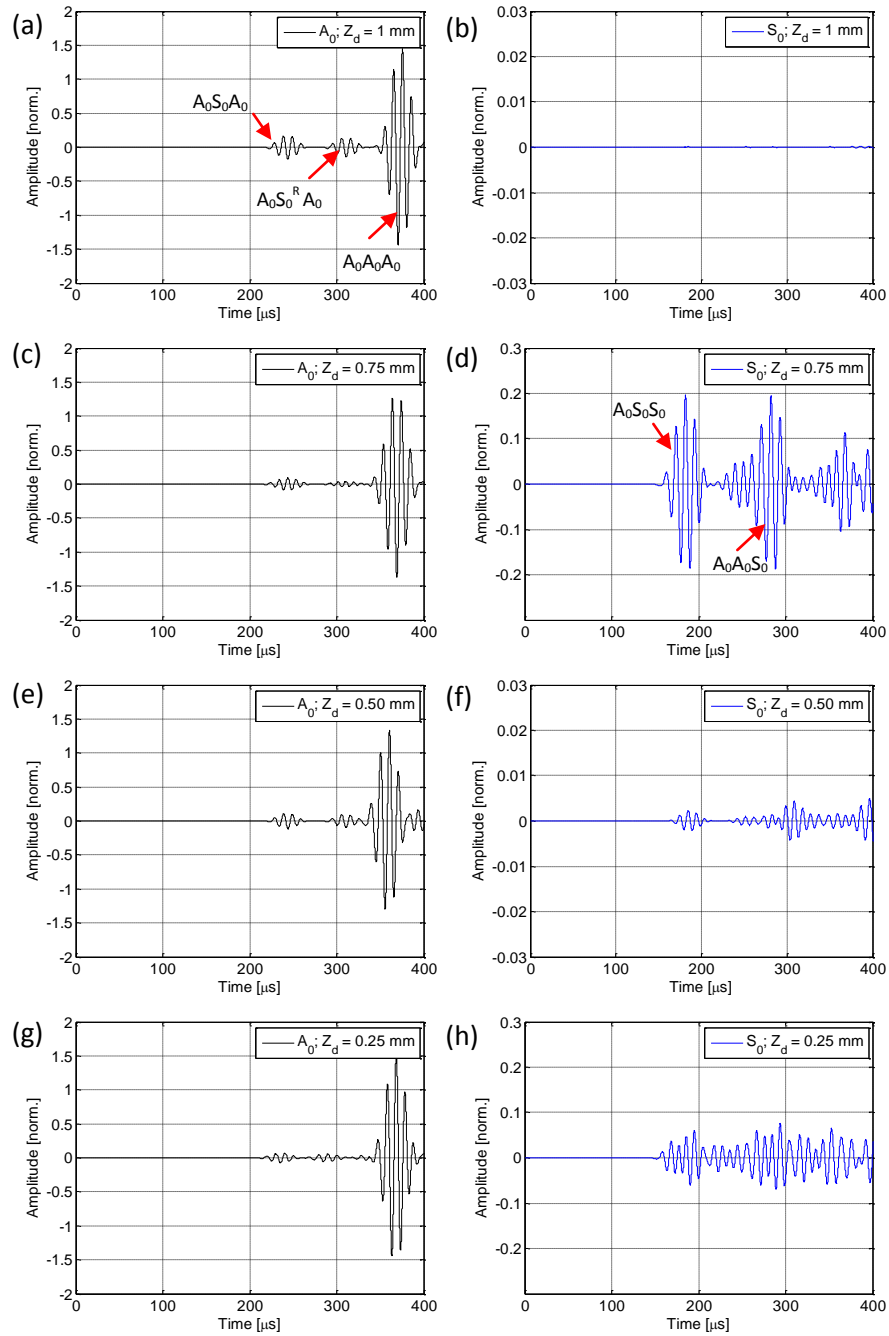


Figure 6-12: Received signals monitored at 100 mm behind delamination; delamination depth is varied from 0.25 mm to 1 mm; left side corresponding to the A_0 mode signals; right side corresponding to S_0 mode signals.

The S_0 mode pulses monitored before the delamination are shown in Figure 6-9 (right side). Referring to Figure 6-10, the arrival time of the first S_0 pulse matched to the arrival time of the A_0S_0 wave group (125 μs), reflected at the delamination entrance. Meanwhile, the second pulse corresponds to the $A_0S_0S_0^R$ wave group (185 μs), which indicates a reflection from the delamination exit. Superscript R is used in order to differentiate the reflected mode from the main propagating mode. By using a similar approach, other wave groups can also be determined. From Figure 6-9, no S_0 reflected pulse can be observed when the delamination is placed at the symmetrical plane ($z_d=1$ mm). In contrast, high amplitude of in-plane displacement can be observed only for the case of the delamination placed at 0.25 mm and 0.75 mm. Meanwhile, a very small S_0 amplitude was observed when $z_d=0.75$ mm. Guo and Cawley [46] have previously observed this phenomenon and concluded that the S_0 mode cannot detect delamination at any depth of the laminate. This is because the amplitude of the S_0 reflection is strongly dependent on the position of the delamination through the thickness of the laminate. In another publication, Ramadas et. al [79, 82] found that the mode converted S_0 mode was confined only in the delamination area if the delamination was placed symmetrically at the mid-plane of a composite plate. This can be related to the mode shape distribution across the thickness of the laminate (Figure 2-5) as the position of the zero shear stress (at mid-plane) at which the delamination has no effect on the S_0 mode propagation.

Another analysis has been performed to analyze both in-plane and out-of plane displacements at a location within the delamination. It is an interesting aspect to analyze the variation of the received signals with changes in the sub-plate thickness. Figure 6-11 presents the out-of plane and in-plane signals monitored at the lower and upper sub-plates. The wave groups can be identified using Figure 6-10. For the out-of-plane signals (Figure 6-11 left side), two wave groups can be seen to travel at different speeds in the upper and lower sub-plates for the asymmetrical delamination case studies (0.25 mm, 0.50 mm and 0.75 mm). The same arrival time in the symmetrical delamination case is expected as both lower and upper sub-plates have the same thickness. This is consistent

with what has been seen in the distribution of the stress field (Figure 6-8) and has been discussed in detail in Section 6.2.1. Meanwhile, for the in-plane signals of all case studies (6-12, right side), it can be seen that the arrival times of the two groups of modes are quite similar, which is due to the S_0 mode being less dispersive at this frequency-thickness, as shown in Table 5-3. These results show that the changes in the plate thickness caused to a significant influence on the wave velocities and wave displacements of the A_0 mode.

Comparing both modes (Figure 6-11), it can be observed that the S_0 mode can be observed to arrive earlier ($125 \mu\text{s}$) than the incident pulse of the A_0 mode ($190 \mu\text{s}$) as expected. This is due to its notably higher velocity than the velocity of the A_0 mode. Reflected S_0 mode pulses can be seen to come together very close. For the case of $z_d = 1 \text{ mm}$, very high oscillation of the S_0 mode pulses can be observed, which was due to the S_0 mode being trapped inside the delamination region, as has been observed in Section 6.2.1. This result confirmed the finding from [79] that for this case the S_0 mode is confined to the delamination area only and not transmitted to the outside of the delamination. This is due to the phase cancellation between the two symmetrical wave modes. Meanwhile, the higher and lower amplitudes for the different thicknesses of sub-plates can be related to the mode shape of both A_0 and S_0 modes at 100 kHz (refer Figure 2-5). The amplitude of the A_0 mode pulses can be observed to increase slightly when the sub-plate thickness increased. On the other hand for the S_0 mode pulses, the amplitude reduced when the sub-plate thickness increased. Table 6-1 summarizes the amplitude values at each sub-plates, extracted from Figure 6-11.

The final part of this section presents the A_0 and S_0 mode signals obtained at the monitoring point behind the delamination, shown in Figure 6-12. It is clear that both modes propagate in the undamaged region behind the delamination, except for the symmetrically located delamination. The transmitted $A_0A_0A_0$ mode pulse with the highest amplitude arrived at approximately $340 \mu\text{s}$. The earlier arrival of the $A_0S_0A_0$ mode can be seen at $210 \mu\text{s}$ and the other pulse seen at $280 \mu\text{s}$ belongs to the multiple reflections of

the $A_0S_0A_0$ wave group within the delamination region ($A_0S_0^RA_0$). A trend of the amplitude of the first transmitted wave can be seen to reduce with the depth of delamination. Figure 6-12 shows the S_0 pulses monitored behind the delamination. The transmitted S_0 pulses can be seen to arrive at 150 μs as the $A_0S_0S_0$ wave group. The second strong pulse arrived at 290 μs , matches to the calculation of the $A_0A_0S_0$ wave group. Similar observations as in Figure 6-9 (S_0 mode, undamaged region before delamination) can be seen in Figure 6-12 as well. The S_0 mode pulses cannot be found when the delamination was placed symmetrically at the mid-plane, but the S_0 mode signal can be detected at other delamination depth. The amplitude of the S_0 mode pulses is again very small when $z_d = 0.50$ mm. This again demonstrates that the S_0 mode cannot interrogate the delamination at certain depths. However, the amplitude of the reflected S_0 mode can be observed a slightly higher than the reflected A_0 mode, particularly for the case of $z_d = 0.75$ mm and 0.25 mm. Although the amplitude of the reflected A_0 mode is rather small for a practical NDE of composites, reflected A_0 mode can be detected for all delamination depths. It has been demonstrated that the visibility of these reflected waves and their arrival times is important for the defect characterization.

Table 6-1: Amplitudes of the A_0 and S_0 mode at different sub-plates thicknesses; 2D FE; 100 kHz

Thickness	A_0	S_0
Lower plate	Amplitude	Amplitude
1	1.71	0.25
0.75	1.67	0.28
0.5	1.13	0.32
0.25	1.00	0.36
Upper plate	Amplitude	Amplitude
1	1.71	0.25
1.25	1.73	0.24
1.5	1.79	0.12
1.75	1.83	0.10

6.3 Influence of delamination size on wave scattering

In this section the wave amplitude and directivity of the A_0 mode scattering for different sizes of delamination are investigated. The purpose was to investigate how these parameters influence the guided wave scattering and to provide the basis for the quantification of the damage sensitivity using guided ultrasonic waves. Six different sizes were considered: 10 mm, 20 mm, 30 mm, 40 mm, 50 mm and 60 mm (same length and width), with the delamination located at the mid plane (depth: 1 mm), as shown in Figure 4-12 (Chapter 4). The distance from the excitation point to the center of the rectangular-shaped delamination was 100 mm. The layered 3D FE model with added Rayleigh damping was used for the simulation and analysis.

Three distinctive regions can be clearly seen in Figure 6-13, as has been observed previously in Section 6.1. Amplitudes over the intact part of the model (before the delamination) were exactly the same as the baseline data. A small fluctuation in the amplitude profile for all case studies, about 7% compared to the baseline data, can be seen within 15 mm distance before the delamination entrance. This is due to the reflected waves interfering with the incident wave. Significant changes in the amplitudes levels can be observed in the defective area, for all case studies. The amplitude on the delamination can be higher or lower than the baseline amplitude. As has been discussed in Section 6.2, this could be due to the newly generated modes that travel with different speeds, as well as interferences between each group of new modes that are being reflected within the delamination sideways.

Behind the delamination, the amplitudes for all case studies started to show different patterns and much bigger discrepancies compared to the baseline data. This finding may support the previous observation on the analysis of the large defect wave fields, where a part of several group of waves with dissimilar wave speeds reflected at the delamination exit and transmitted out from the delamination. This event created different amplitude profiles compared to the baseline data even though the waves now travelled in

the area behind the delamination. No clear trend can be observed, except for the case studies of delamination sizes 10 mm and 20 mm. The amplitude of the A_0 mode leaving the delamination area behaved similarly as the baseline data but with higher amplitude. In contrast, the greater delamination sizes (30 mm and 40 mm) caused significant changes in the propagation characteristics. For delamination cases of 50 mm and 60 mm, two parts of amplitude fluctuations can be observed clearly at 75 mm and 125 mm, and 70 mm and 130 mm. These distances mark the location of the entrance and exit of delamination. This provides the information of length of delaminations which is crucially needed for the NDE of composites.

Having discussed how the size affected the wave propagation across the delamination, it is necessary to explain the wave scattering around the delamination. The angular pattern of the scattered amplitude around various delamination sizes can be seen in Figure 6-14. The backward scattered amplitudes show a regular pattern similarly to the baseline data, except in the directions between 60° to 90° and 270° to 300° . The effect of the bigger delamination size can be observed in these directions. Unique forward scattering patterns can be observed at angles between 120° and 240° . The forward scattering was divided to form several side lobes in certain directions. Increasing the delamination size caused the movement of the side lobe directions from the main forward scattering (at 180°). No clear trend can be observed on the amplitude of the main forward scattering lobe, as has been observed similarly in the line scan from Figure 6-13.

In order to investigate the influence of the size on the angular pattern, the amplitude of the scattered waves was isolated by subtracting the incident time traces from the baseline simulation. Shown in Figure 6-15 are the isolated amplitudes of the scattered waves. The formation of the side lobes and their movement into certain directions can be seen to have a systematic trend. The side lobes increased in size and moved about 20° to 30° as the delamination size increases. A slight variation can be observed for the case of a small delamination size (10 mm x 10 mm), but overall a similar

scattering pattern can be observed. From Figure 6-15, it can also be observed that the field of the scattered amplitude increases with the delamination size, except for the case of 60 mm x 60 mm, which is due to the highest backward scattering that consequently reduced the transmitted and scattered waves.

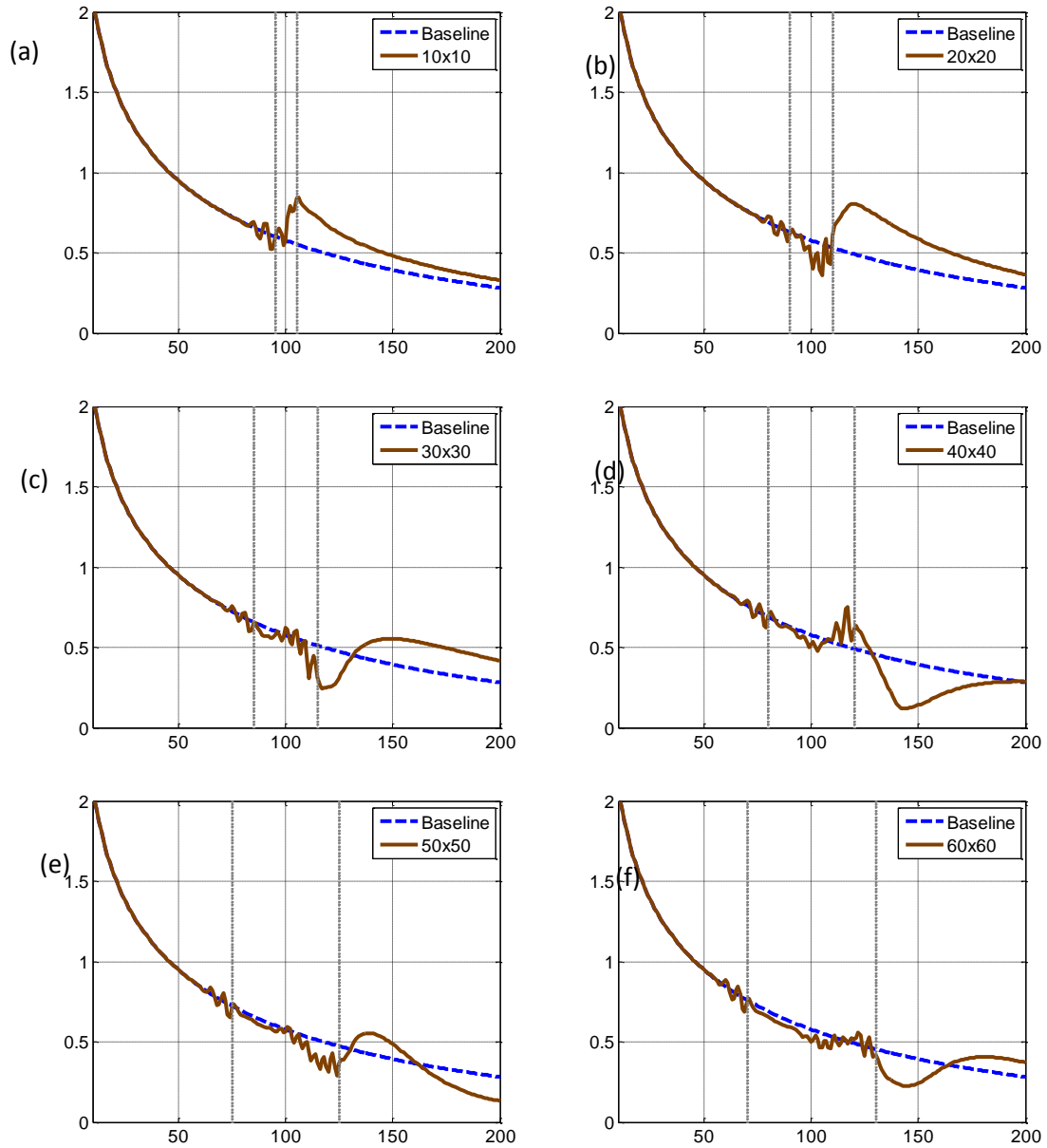


Figure 6-13: Maxima of signal envelope of guided wave for different delamination sizes; unit in mm; symmetric delamination ($z_d = 1$ mm); FE layered model of 2 mm cross-ply composite plate.

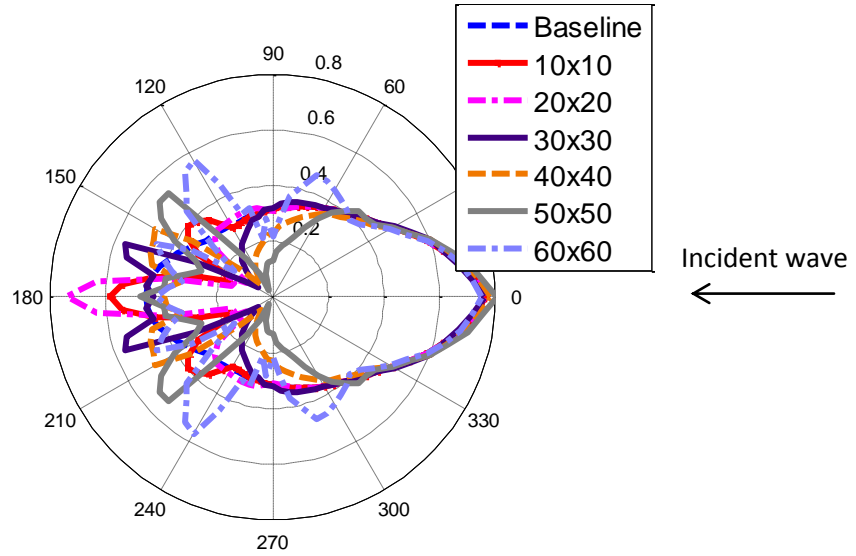


Figure 6-14: Maxima of signal envelope around various sizes of delamination; unit in mm; symmetric delamination ($z_d = 1$ mm); measured every 5° at 30 mm radius around center of the delamination; FE layered model of 2 mm cross-ply composite plate.

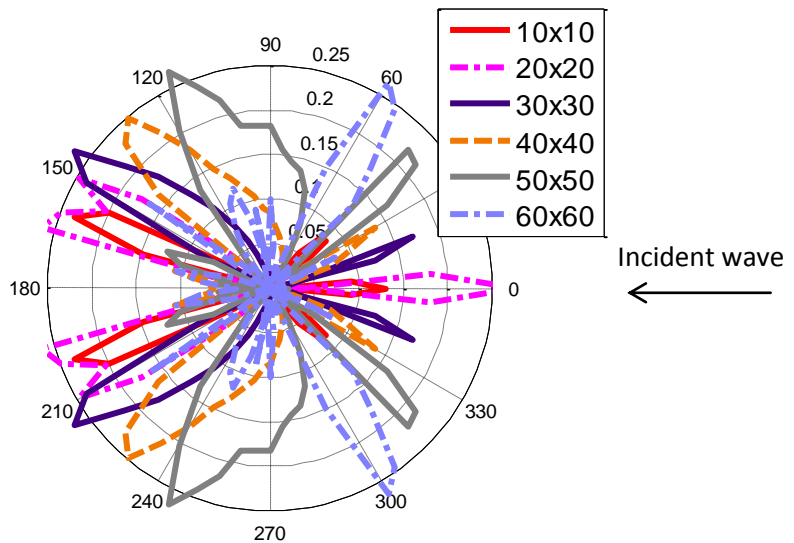


Figure 6-15: Scattered amplitude (using baseline subtraction method) around various sizes of delamination; unit in mm; symmetric delamination ($z_d = 1$ mm); measured every 5° at 30 mm radius around center of the delamination; FE layered model of 2 mm cross-ply composite plate.

This section so far focused only on the influence of the delamination size, which was assumed to be square. In order to separate the influence of the delamination length and width, two sets of simulations were performed and their baseline subtracted amplitudes were obtained for plotting the angular pattern. The first set consists of 3D FE models having the same delamination width (20 mm) but different lengths (varied from 10 to 60 mm) to investigate the influence of the delamination length. Then, the delamination widths were varied from 10 to 60 mm with a constant length (20 mm) for the second simulation set. Constant 20 mm length or width was chosen in order to avoid additional effects on the forward scattering (as has been seen for the case delamination size of 10 mm and 20 mm).

Results shown in Figure 6-16 and Figure 6-17 present the influence of the length and width respectively. It can be observed that both figures show the formation of the forward side lobes, but only Figure 6-17 shows the angular movement of the side lobes with increasing delamination width. It seems possible that the directivity of the side lobes is due to the wave being reflected at the sides of the delamination, as similarly observed in Figure 6-6. To illustrate this phenomenon, Figure 6-18 presents two examples of delamination size of 40 mm x 20 mm and 20 mm x 40 mm. From the figure, the shadowed area at the delamination sides matched the angular directivity seen in Figure 6-17 as well as in Figure 6-6. This angle of the forward scattering indicates the obstruction of the wave propagation path due to the larger width of the damaged area and energy trapping within the delamination.

Two further effects, which are an increase in the back scattering and a decrease in the forward scattering with increasing delamination width, can also be observed in Figure 6-16 and Figure 6-17. A wider delamination causes more guided wave to be reflected at the delamination entrance. Hence, this causes the reduction in the forward scattering in addition to the wave energy being trapped inside the delamination.

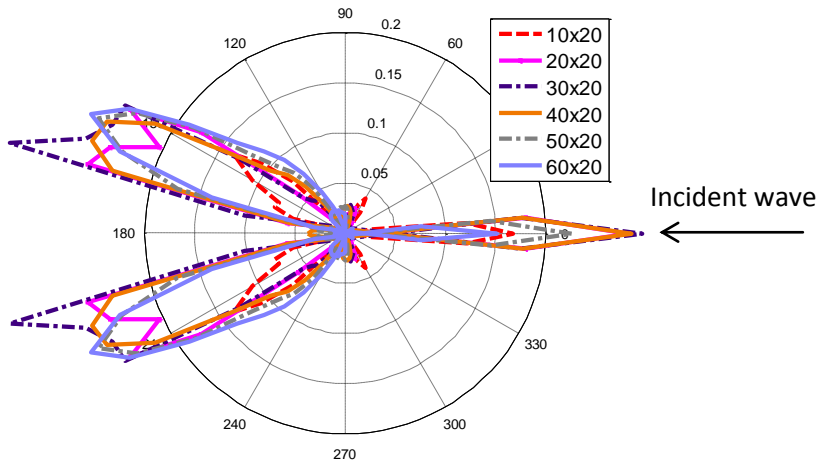


Figure 6-16: Scattered amplitudes (using baseline subtraction method) around delamination with different length; unit in mm; symmetric delamination ($z_d = 1$ mm); measured every 5° at 30 mm radius around center of the delamination; FE layered model of 2 mm cross-ply composite plate.

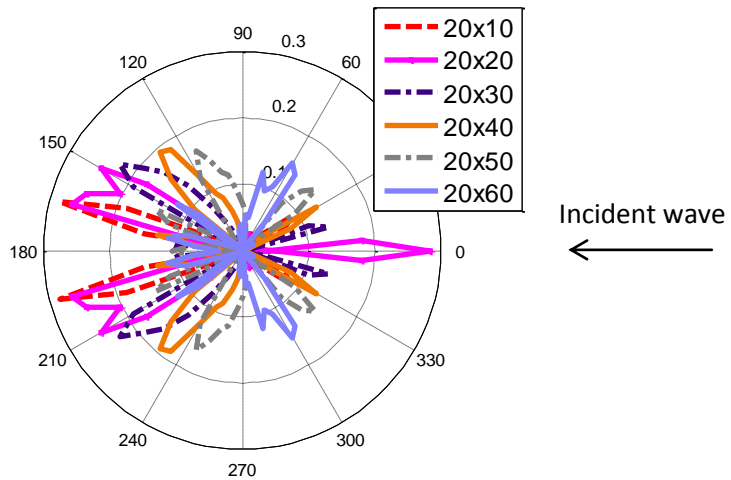


Figure 6-17: Scattered amplitudes (using baseline subtraction method) around delamination with different width; unit in mm; symmetric delamination ($z_d = 1$ mm); measured every 5° at 30 mm radius around center of the delamination; FE layered model of 2 mm cross-ply composite plate.

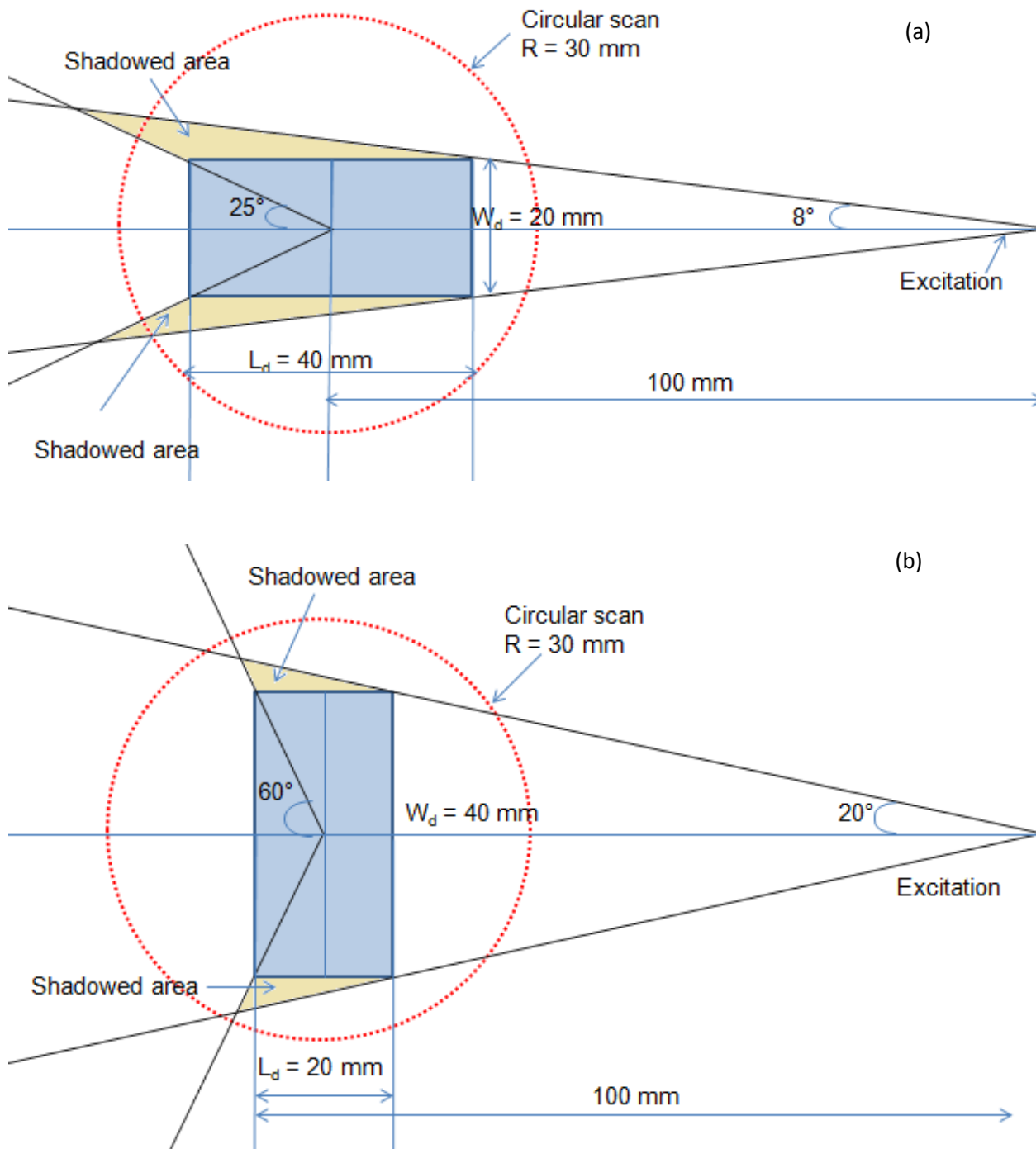


Figure 6-18: Schematic illustration of trapped wave energy in plate with delamination size of (a) 40 mm x 20 mm, and (b) 20 mm x 40 mm; excitation point to the center of delamination = 100 mm.

As shown in Figure 6-16 for the effect of the delamination length, the forward scattered wave field remains nearly consistent with only small changes in the scattering amplitude. The scattering pattern is almost independent of the delamination length. Interestingly, there is a small trend in the back scattering (0° direction) that reduces with the increasing delamination length. But this trend can be observed only for the case of the delamination length larger than 20 mm. This could be related to the interferences between reflections from the entrance and the exit of delamination, as has been observed in the case of a large delamination model (Section 6.2). The larger size contributes to a smaller reflection due to the increasing time delay between the pulses that are being reflected at the delamination entrance and exit. From the study of the effect of the size, length and the width of delamination, it can be concluded that each factor influenced the wave scattering pattern differently. The width of the delamination contributed to significant trends in the angular scattered amplitude pattern: (1) side lobes, (2) larger back scattering from a wider delamination, and (3) lower forward scattering with the increasing delamination width.

6.4 Influence of delamination depth on wave scattering

This section investigates the influence of delamination position through the plate thickness on the scattered waves. It was discussed in the Section 6.2 that the scattering pattern and the signal characteristics depend on the through-thickness location of the delamination, and also on the orientation of the material properties. The delamination causes local changes in the sub-plates thicknesses, which affects the guided wave to split and travel into two sub-plates above and below the delamination. A group of new modes is also generated as a result of mode conversion at the delamination entrance. In order to further study the relationship between the scattering pattern and delamination depth, FE simulations were performed for case studies of delamination with different sizes (10 mm to 60 mm) placed at different depths. Figure 6-19 presents a systematic study of the effect of delamination depths for six square delamination sizes (from 10 mm to 60 mm).

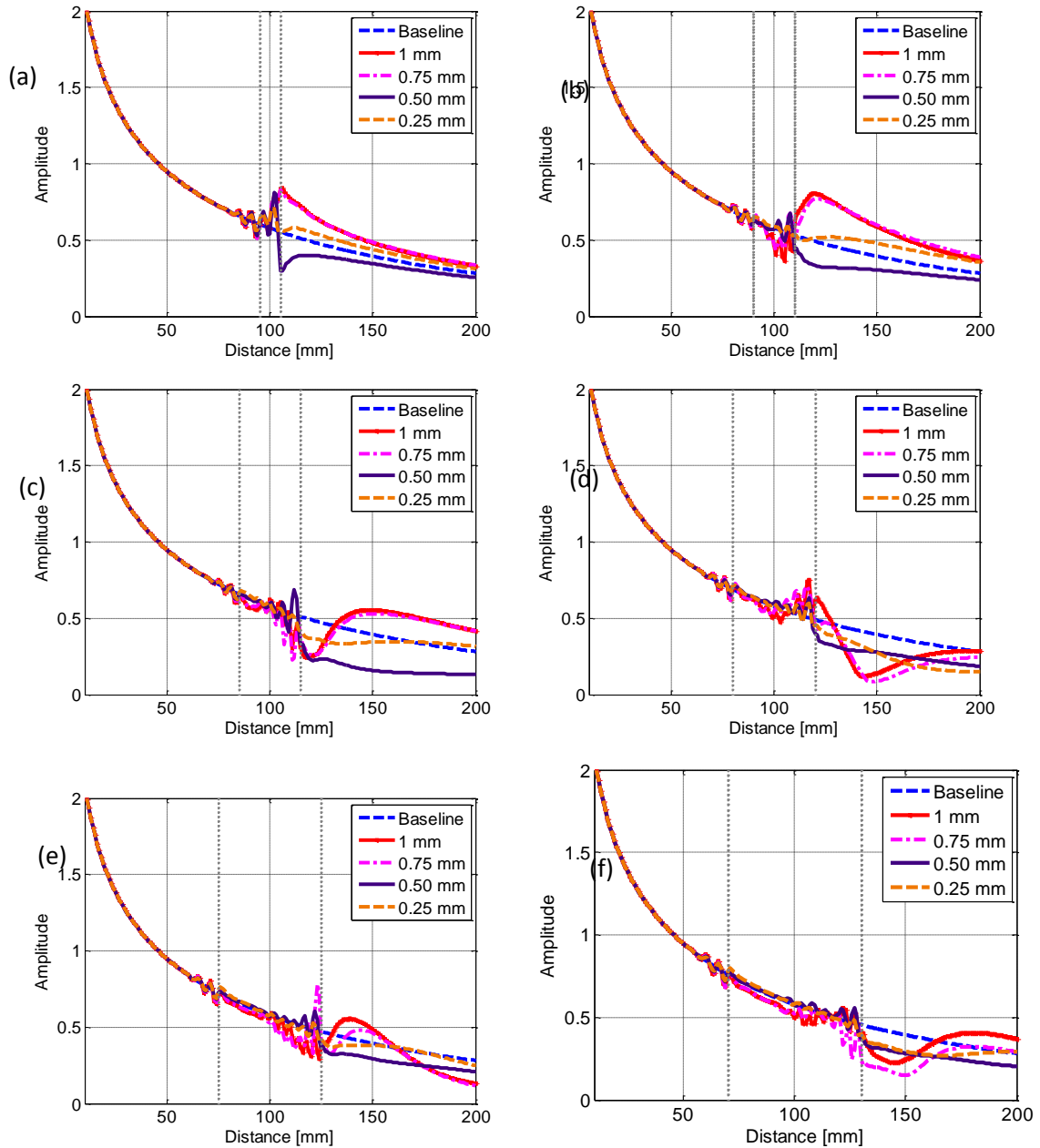


Figure 6-19: Maxima of signal envelope across various delamination sizes; (a) 10 mm x 10 mm, (b) 20 mm x 20 mm, (c) 30 mm x 30 mm, (d) 40 mm x 40 mm, (e) 50 mm x 50 mm and (f) 60 mm x 60 mm; at different delamination depths; FE layered model of 2 mm cross-ply composite plate.

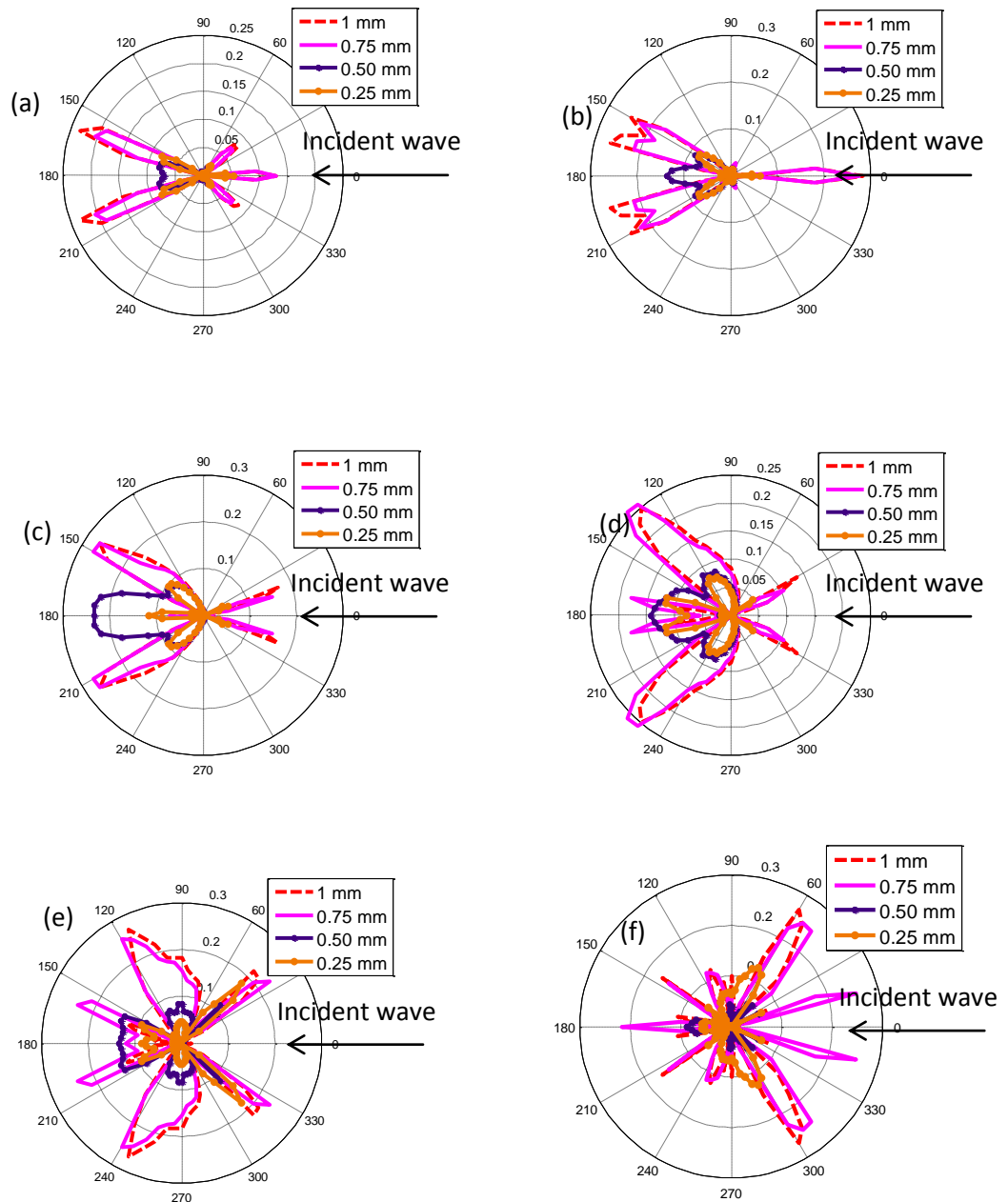


Figure 6-20: Scattered amplitudes (using baseline subtraction method) around various delamination sizes; (a) 10 mm x 10 mm, (b) 20 mm x 20 mm, (c) 30 mm x 30 mm, (d) 40 mm x 40 mm, (e) 50 mm x 50 mm and (f) 60 mm x 60 mm; at different delamination depths; measured every 5° at 30 mm radius around center of the delamination; FE layered model of 2 mm cross-ply composite plate.

As can be seen in Figure 6-19, the known three distinctive regions can be observed. No significant influence can be seen in the region before and on the delamination. Interestingly, the effect of the delamination depth can be observed at the amplitude patterns behind the delamination region. It is obvious that the signal amplitudes behaved differently behind the delaminations located at different depths. The amplitudes of transmitted guided wave pulses through the delaminations placed at 0.75 mm and 1 mm show almost similar trend in all cases of the six difference sizes. Referring back to the stress field shown in Figure 6-8 and wave speed at different thicknesses (Table 5-3), it can be observed that the wave in the lower and upper sub-plates travelled with a comparable speed (around 1260 m/s for sub-plates with thickness 1mm and 1.25 mm thickness and 1360 m/s for sub-plate with 0.75 mm thickness). From Figure 6-19, the amplitude drop behind the delamination region is quite similar for all case studies of delamination depth (z_d) placed at 0.50 mm. Meanwhile, when the delamination is placed close to the plate surface ($z_d = 0.25$ mm), the amplitude pattern can be seen to be nearly the same as the baseline data for the case of small delamination size ($< 2\lambda$). For larger delamination size, the amplitudes started to behave differently and this could be due to multiple parametric influences.

By using the baseline subtraction method, Figure 6-20 presents the angular pattern of the isolated wave scattering around various delamination sizes and depths. The scattering around delaminations placed at 0.75 mm and 1mm show very similar behaviour for all different cases, except for size 60 mm x 60 mm because the circular scan was measured on top of the 60 mm x 60 mm delamination. When the delamination was placed close to the mid-plane of the plate (1 mm and 0.75 mm), higher scattered amplitudes can be observed compared to other locations through the thickness. In contrast, the magnitude of the backward and forward scattering was very small for the case of the delamination placed very close to the surface, i.e., $z_d = 0.25$ mm. As explained before in Section 6.2, this is related to the mode shape of the A_0 mode. The different forward scattering pattern can also be observed from Figure 6-20 when the delamination is placed

at 0.50 mm, particularly in the 0° direction. Referring back to Figure 6-9, Figure 6-11 and Figure 6-12, the significant difference between wave speeds in the upper and lower sub-plates could contribute to the higher acoustic mismatch, thus introducing more reflections. More reflections in a smaller space (in this case, smaller delamination length) caused the higher scattered wave amplitude.

From Figure 6-20, the influence of delamination depth can be observed when delamination sizes were 30 mm, 40 mm and 50 mm. The magnitude of the forward side lobes reduced with the delamination depth. No obvious trend can be observed for the delamination sizes 10 mm, 20 mm and 60 mm. In general, many factors that are related to the through thickness location can affect the wave scattering. The mode shape of the propagating mode and the wave speed in sub-plates of different thicknesses are amongst the factors. From the investigation in this chapter, it has been shown so far that the scattering in composite plates is complicated as many factors can influence the scattering characteristics. By investigating those factors independently, individual trends can be observed and recognized. Unlike the S_0 mode, delaminations at any depth can be detected by the changes in the forward and backward scattering of the A_0 mode.

6.5 Influence of reduction in stiffness properties

In this section, the simulation results for FE models incorporating multiple defects are presented. A FE method for modelling multiple defects in a composite plate was proposed in order to represent realistic impact damage, as discussed in Section 4.4. From a simulation point of view, the impact damage can be modelled by de-merging FE element nodes, which represents the delaminations, and also can be modelled by degrading the stiffness properties. This normally represents the distributed macroscopic fibre breaking and matrix cracking in the layered composite plate. In literature [4, 5], low-velocity impact in composites is shown to lead to local decay in the stiffness properties. Hence, it is assumed that the stiffness properties at the impacted zone are significantly reduced. Since

the wave velocity is directly proportional to the stiffness properties, a change in the wave propagation velocity is expected, that will lead to an acoustic impedance mismatch.

In this study, the stiffness constants were reduced. The aim was to investigate the effect of material degradation on the guided wave scattering pattern. Three different modelling approaches involving stiffness properties degradation were performed. The models were a 3D FE model (1) with a full-thickness (2 mm) stiffness reduction in the elements located in an area of 20 mm x 20 mm without any delamination, (2) combined delamination and a 0.25 mm thick layer with reduced stiffness properties, and (3) combined delamination and reduced stiffness properties through the complete thickness. In each study, the stiffness properties were reduced by 25%, 50% and 75% to systematically investigate the effects of varying the stiffness properties on the wave scattering. In order to minimize the influence of depth on the scattered amplitude, only one delamination depth was considered in this study. The delamination was placed at 1 mm depth.

6.5.1 Reduced stiffness properties

Figure 6-21 compares the guided wave propagation in three composite models with dissimilar reduction of the stiffness constants. Delamination was not considered in this model. The typical three regions as can normally be seen in the composite plate with a delamination can also be observed here in Figure 6-21a. At the entrance of this defective region (where the properties were reduced), a systematic trend can be observed. The model with the highest property reduction (75%) has the highest amplitude fluctuation followed by the models with 50% and 25% property reduction. As has been discussed in the previous Sections, this is caused by the reflected waves at the entrance and exit of the defective region. This result shows that the increase of the reflected waves could indicate a stiffness property degradation in the composite plate. Changes in the amplitude within the region of the reduced properties clearly indicate the obstruction in this area. The

highest amplitude changes can be seen from the model with highest property reduction (75%), and the model with the lowest property reduction (25%) show a comparable amplitude pattern compared to the baseline data, except in the region past the defective area (propagation distance > 110 mm). No clear trend can be observed in the area behind the defective region.

Based on the wave velocity–material properties relationship, the velocity changed considerably when the stiffness of the materials was varied. When guided wave travels from a source and encounters an area of reduced stiffness properties, the velocity of the propagating wave reduces. Consequently, the acoustic impedance between the undamaged and defective regions changed. When the impedance mismatch is higher, it will result in higher wave reflections. In this study, the impedance mismatches between the region of undamaged and damaged could be approximated as 25%, 50% and 75% since the stiffness is proportional to the wave velocity. Therefore, it is expected that the model with the highest stiffness reduction will have the highest wave scattering due to the higher impedance mismatch.

Figure 6-21b shows the angular pattern of the scattered waves at 30 mm radius from the center of the defective area. The directivity of the wave scattering in each model can be seen to be approximately in similar directions. Large wave scattering can be found behind the defective area (forward scattering side lobes) for the FE models with 75% and 50% property reduction. The two main lobes between 150° to 170° directions and 190° to 210° directions matched the geometry of the defective area. No forward scattering can be found in the 180° direction (20 mm behind the delamination exit) for all three models. Comparing their backward scattering patterns, there was no significant trend. Therefore, it can be concluded that as the stiffness properties reduced, the extent of scattering increases in term of wave scattering (of the side lobes) in two main directions. This however depends on the geometry of the defect as well. Overall, the effect of material degradation can be observed.

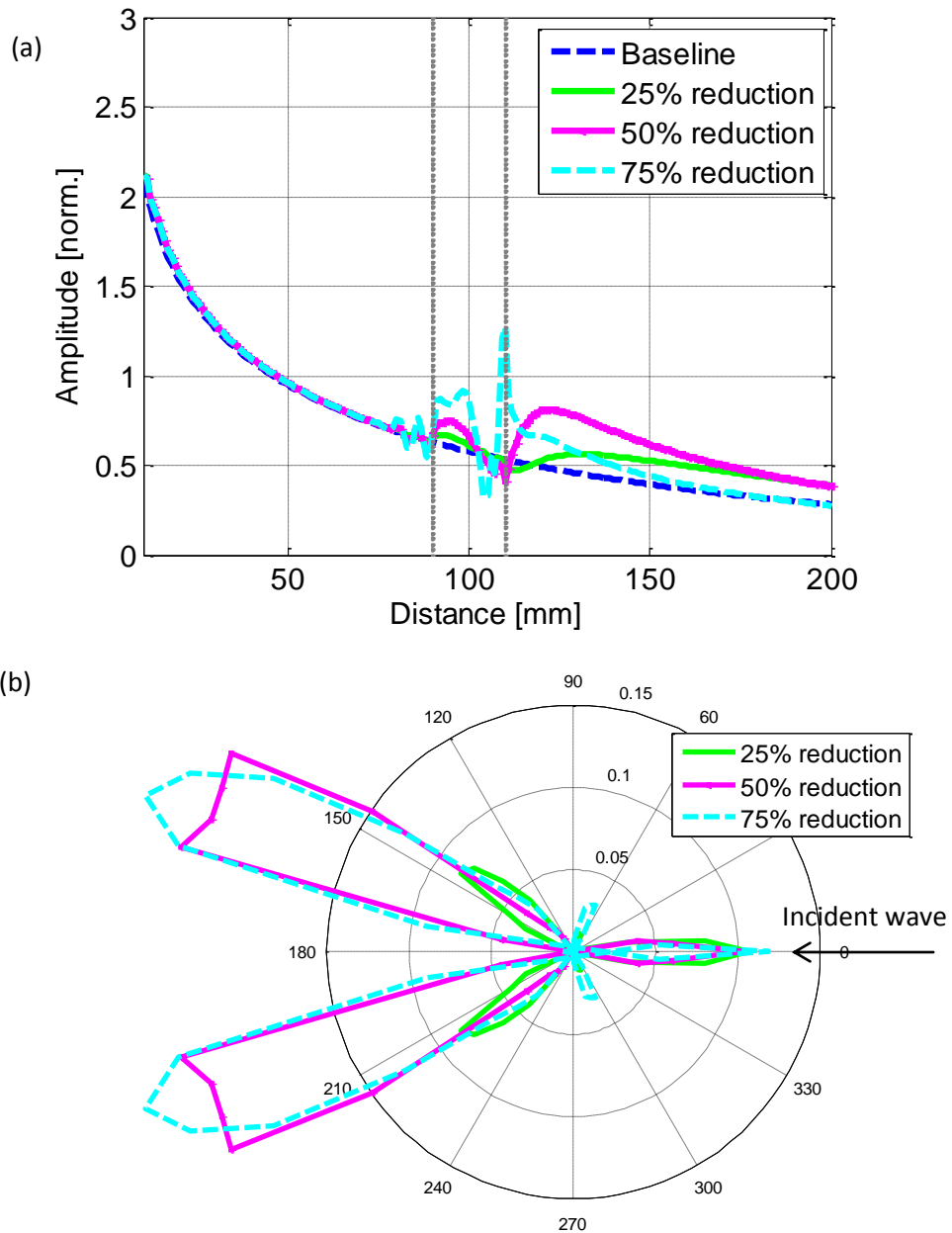


Figure 6-21: (a) Maximum amplitude of signal envelope propagating through and (b) 30 mm radius of scattered amplitudes (using baseline subtraction method) around region with reduced properties in cross-ply composite plate; stiffness properties reduced by 25%, 50% and 75%; baseline results correspond to the undamaged model; FE layered model of 2 mm cross-ply composite plate.

6.5.2 Delamination with reduced stiffness properties

This section discusses simulation results for the models with combined defects; a delamination and a 0.25 mm thick layer of elements with reduced stiffness properties. Figure 6-22 shows a comparison of three FE models with different degradation. Note that the result for no stiffness reduction corresponds to the results obtained in the FE model with a delamination of 20 mm x 20 mm, as shown previously in Figure 6-13b (Section 6.3). Overall, only a very small effect can be observed as only one layer of elements changed properties, which caused a small unsymmetrical defect through the thickness location. This result demonstrates that the additional defect (by reducing stiffness properties in a layer of elements at the delamination interface) has not shown any significant influence on the A_0 mode scattering, except for an increment of about 20% in the signal amplitude at the location within the defective region.

Figure 6-23 shows the simulation results for the models with combined defects of a delamination and through thickness stiffness reduction. It can be seen in Figure 6-23a that there are large amplitude peaks at the defective region for the three models. All case studies have amplitudes higher than the baseline data and also higher than the model with delamination only. No clear trend can be found in the region behind the defective area, with the lowest stiffness reduction (25%) having the largest amplitude drop upon leaving the defective area. Behind the defective region, the two models with 75% and 50% reduction can be seen to have a similar amplitude pattern. Comparing the models with reduced properties to the model with a delamination only, it can be observed that the amplitudes are significantly higher than the model with delamination only. In addition to the changes in the wave speed inside the plate, the reduction in stiffness properties produces more wave scattering within the defective region,

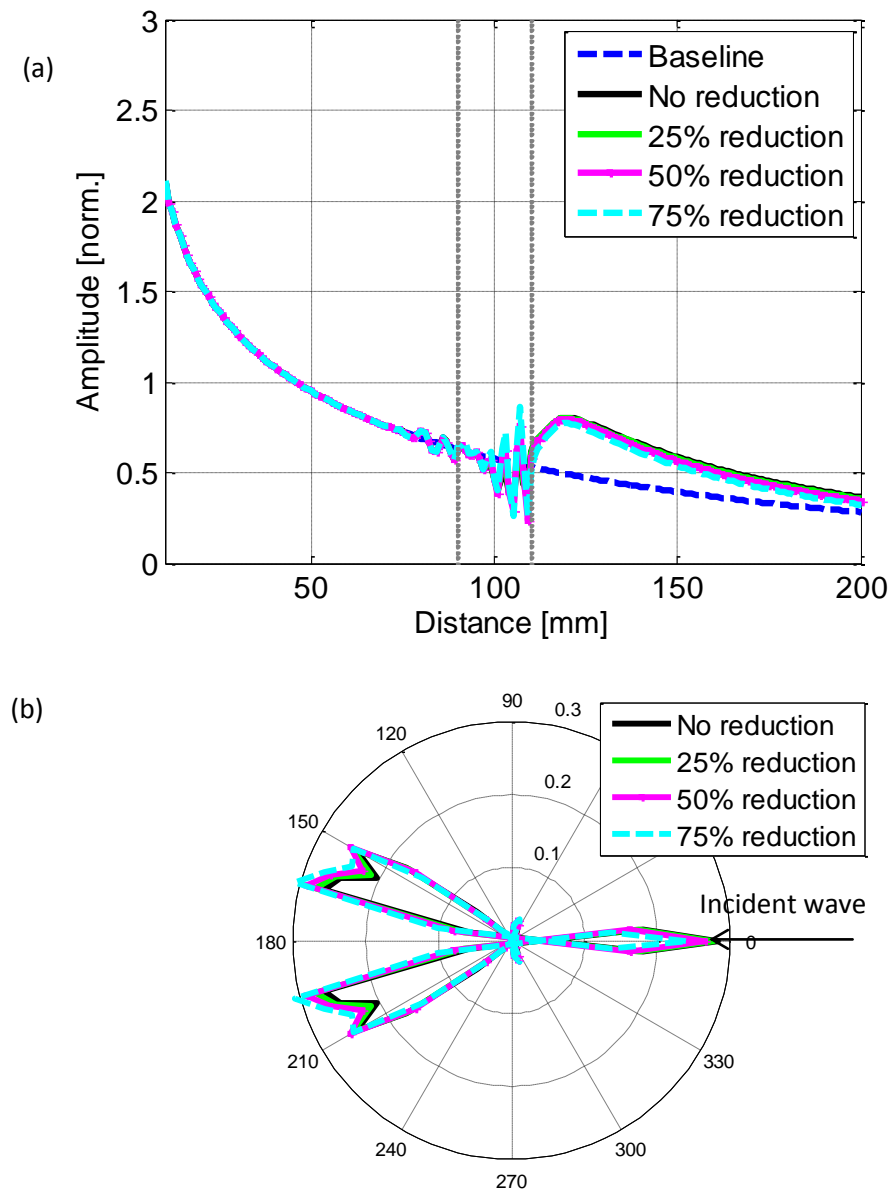


Figure 6-22: (a) Maximum amplitude of signal envelope propagating through and (b) 30 mm radius of scattered amplitudes (using baseline subtraction method) around multiple defects in cross-ply composite plate; stiffness properties reduced by 25%, 50% and 75%; no reduction results correspond to case of 20 mm x 20 mm delamination; monitoring points in mid-plane; FE layered model of 2 mm cross-ply composite plate.

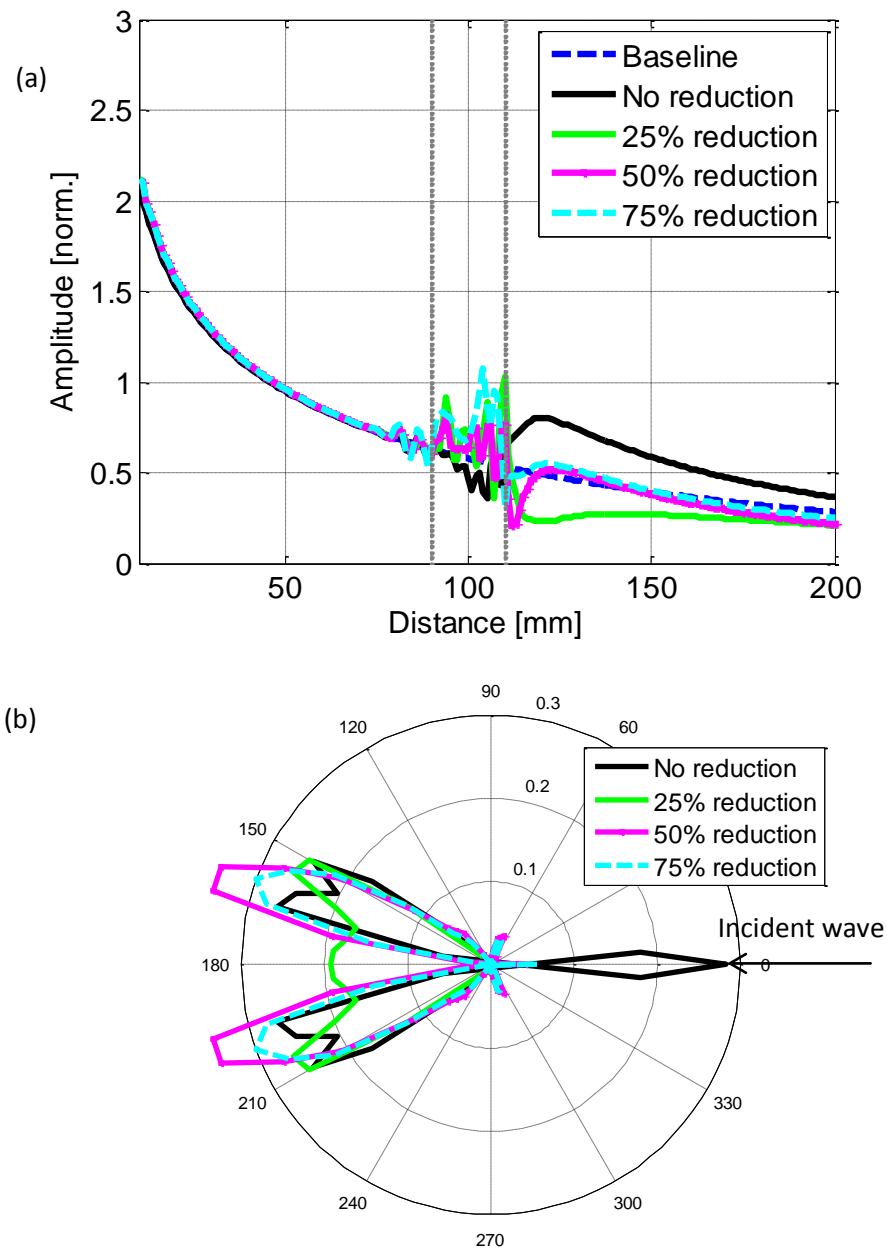


Figure 6-23: (a) Maximum amplitude of signal envelope propagating through and (b) 30 mm radius of scattered amplitudes (using baseline subtraction method) around multiple defects in cross-ply composite plate; stiffness properties are reduced by 25%, 50% and 75%; no reduction results correspond to case of 20 mm x 20 mm delamination; monitoring points in mid-plane; FE layered model of 2 mm cross-ply composite plate.

From the angular scattering pattern shown in Figure 6-23b, no clear trend in the forward side lobes can be found. However, the scattered wave magnitudes from the three models with reduced material properties were larger than for the model with the delamination only. The largest forward scattered wave in the 180° direction can be seen in the model with 25% property reduction. The reason for this could be related to the higher transmitted wave, where the A_0 mode propagated towards the exit of the defective area and progressed past the defective region. Small backward scattering for all models compared to the model with delamination only can be observed. No systematic trend can be observed from the composite model with multiple defects, which demonstrates the complexity of the guided wave scattering. However, the results from this section provide an improved understanding on the influence of the material degradation, although admittedly, the FE models are limited to a particular square-shaped delamination and elements with reduced material properties.

6.6 Conclusions

This chapter investigated the A_0 mode wave scattering characteristics at defects in a 2mm cross-ply composite plate $[0/90]_{2s}$. All simulations were performed at 100 kHz excitation frequency, corresponding to 14 mm wavelength. Section 6.1 showed that a layered FE model with individual layer material properties should be used instead of using homogenized material properties to analyse wave scattering by delaminations. This is contrary to what has been seen in Chapter 5 where both types of models produced comparable results for the undamaged composite model. The influence of damping was small as it only reduces the amplitudes. The square- and circular- shaped delaminations provide comparable results, which indicate that the same maximum extent (diameter matching rectangle) resulted in overall very similar scattering patterns and amplitudes. Section 6.2 reports the fundamental interaction of the A_0 mode at a delamination. The appearance of sideways energy trapping and various groups of modes that propagate independently in the upper and lower sub-plates can be observed from the 2D FE simulations. The study from Section 6.3 indicates the significant effect of the delamination

width and length on the guided wave scattering characteristics as well as on the reflected waves. It was found that due to increasing delamination length two scattering side lobes formed and that increasing delamination width caused changes of the scattering directions. The length of delamination can be estimated based on the arrival times of two reflection pulses. From Section 6.4, the findings suggest that the depth of the delamination influences the amplitude of the reflected pulses. The closer the delamination is located to the plate surface, the smaller will be the scattered amplitude. The largest forward scattering was obtained when the delamination was close to the mid plane of the plate. This can be related to the mode shapes of the A_0 and S_0 modes. From the final section, it can be concluded that as the stiffness properties are reduced due to impact damage, the extent of scattering gets larger. By modelling a square delamination combined with reduced material properties, an improved understanding of the guided wave scattering at single and multiple types of defects has been obtained.

CHAPTER 7 IMPACT DAMAGE CHARACTERIZATION IN COMPOSITE PLATES

Low-energy impact on composite specimens typically produces barely visible damage at the impacted surface. The internal defects can be complex, consisting of multimode damage such matrix cracks, delamination or fiber breakage. The extent of the impact damage normally spreads across the thickness under the impacted surface. Studies on the impact response of composites shown that delaminations occurred at the very bottom layer, resulting from matrix cracks and fiber failure at the point of impact [130, 131]. Studies of the low velocity impact highlighted that damage modes depend on the geometric shape of the impactor and laminate configuration of the composite structure [3, 5]. Choi et al. showed that a change of stacking sequence has a more significant influence of the impact damage than a change of thickness [5]. This means that the characterization of impact damage can be very complicated and varies for every different composite structure. Simulated FE results from Chapter 6 have shown the complexity of the scattered guided wave, influenced by various defect parameters. It is expected that the characterization of real impact damage will be more difficult. Hence, the evaluation of the impact damage requires experience and a good understanding of the composite as well as the knowledge of guided wave propagation and scattering in composite plates. Using information presented in Chapter 5 and Chapter 6, the qualitative assessment and quantitative characterization of the impact damage can be made, which in turn, can validate the accuracy of the 3D FE modeling technique that has been used throughout this study.

In this chapter, the characterization of impact damage in 2 mm thick 8-cross-ply composite panels using guided ultrasonic waves is presented. Two composite specimens (symmetric layup sequence of $[0/90]_{2s}$) with barely visible impact damage were used for this study, supplied by the Composite Systems Innovation Centre, University of Sheffield. The specimens had been subjected to a 7.4 J energy impact using a hemispherical 15 mm impactor head following standard drop weight procedures. The first part of this chapter describes the characterization of the impact damage in the composite plates using various

NDE methods such as X-rays and conventional ultrasonic C-scan imaging. The information obtained from these methods was compared to the measured guided wave displacements fields around the damage area. The final part compares the experimental wave scattering to the FE simulations results. The wave characteristics such as amplitude variations and scattering by the impact damage are discussed to validate the FE simulations results in Chapter 6. The comparison to the FE model developed based on the description of the impact damage was also discussed.

7.1 Impact damage detection in cross-ply composite plates

7.1.1 X-ray imaging

X-ray imaging is a known NDE method for characterizing defects in composites. This method generally is capable of inspecting materials with hidden flaws by using short-wavelength electromagnetic radiation to penetrate into various materials. Since the quantity of radiation transmitted through the material can be detected and measured, variations in the transmitted X-ray intensity are used to determine the thickness or composition of the object or flaws in the object. This section reports the findings performed by collaborators to characterize the impact damage on the composite plates.

Figure 7-1 show a conventional X-ray image of an impacted cross-ply composite plate, provided by collaborators from the Composite Systems Innovation Centre, University of Sheffield. It should be noted that the X-ray testing was performed on a different, but similar plate to the specimens. The oval shape and the marking out of the damage extremities can be clearly seen. The high black density region is significant compared to other regions, which identifies the location of the impactor head. This could correspond to a small degree of fiber fracture under the impactor head. The high contrast region marked the boundaries between the undamaged and damaged regions, which could be contributed to delamination and matrix cracks. The low contrast regions correspond to the undamaged regions, where no significant changes could be detected. Based on the report by the collaborator, the extended length beyond the impactor-

located damage area (15 mm in diameter) were estimated to be approximately 20 mm and 25 mm respectively on the left and right sides, making the total length of the defective region approximately 60 mm (in X- direction). Due to the oval shape, the widths (minor diameters) varied from 5 mm to 30 mm across the defective region. Unfortunately there was no scale provided on the image.

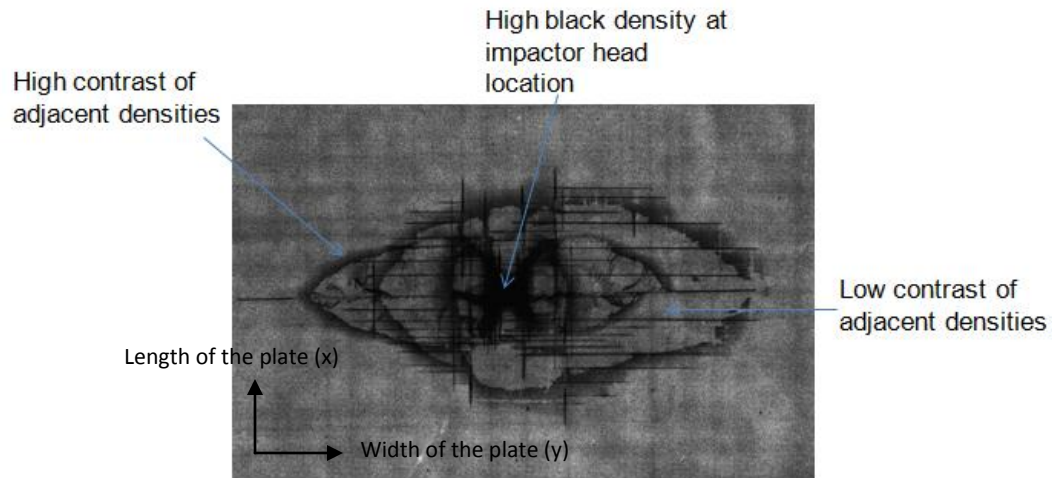


Figure 7-1: X-ray images of composite plate impacted at 7.4 J with impact damage; provided by collaborator in Composite Systems Innovation Centre, University of Sheffield.

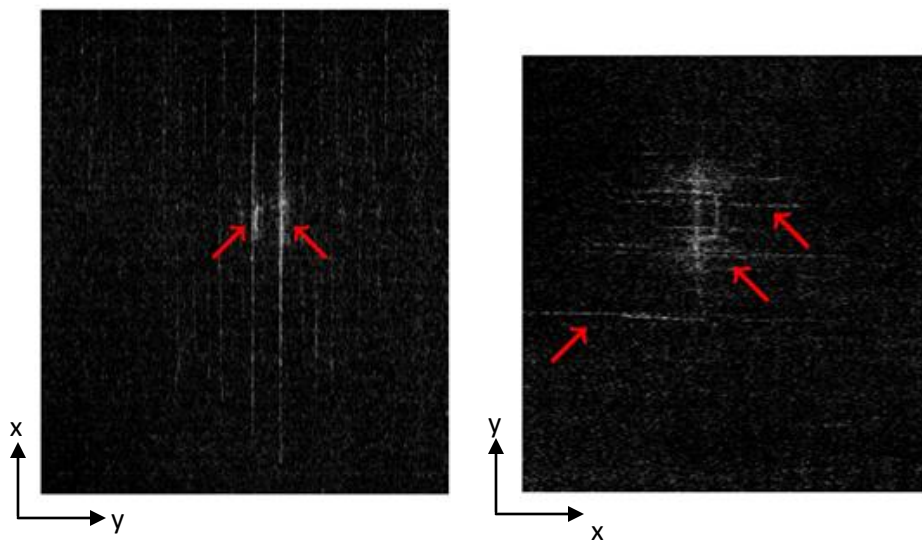


Figure 7-2: X-ray images of composite plate impacted at 7.4 J with impact damage; (a) vertical scattering (b) horizontal scattering; performed by collaborator in Department of Medical Physics and Biomedical Engineering, UCL.

Figure 6-21 presents the reconstructed X-ray images on one of the two tested composite plates that are based on the edge-illumination technique, performed in the Department of Medical Physics and Biomedical Engineering, University College London. The method enables dark-field imaging by using incoherent illumination and operates with broadband radiation [16]. The same composite panels were used in their studies and it is expected that these results could provide some extra information about the impact damage. As a preliminary demonstration, the extracted images show a strong differential contrast for the composite plate. The presence of the high contrast of adjacent densities can be clearly observed from both vertical and horizontal X-ray scattering, which reveal defects inside the plate. The bright lines could indicate local fiber debonding and the two small bright areas which nearly resemble the shape seen in Figure 7-1 could probably mark the area of matrix cracks in the plate. This bright area could be used to approximate the size of impact damage in the plate. However, no further information is obtained from the collaborator since this project is still under development. Overall, the damaged region, shape and the extent of the impact damages were observed from the X-ray analysis.

7.1.2 Ultrasonic C-scan

A conventional immersion ultrasonic C-scan based on the pulse-echo method for characterizing the impact damage was performed on the 2 mm thick 8-cross-ply composite panel. As described in Section 3.4, a 5 MHz focused transducer was used as both transmitter and receiver. The corresponding wavelength in the composite panel is 0.54 mm. The technique involves the detection of echoes that are produced when an ultrasonic pulse is reflected from a discontinuity or an interface in the test plate. The C-scan display records echoes from the internal portions of the test plate as a function of the position of each reflecting interface within a 40 mm x 40 mm area, with 1mm resolution in both the x- and y- direction. For the C-scan image representation, two different time gating settings were used as shown in Figure 3-12 (Chapter 3). The first time gate was set to capture the positive maximum of reflections from the surface. The second

time gate was set to capture the negative minimum amplitude that corresponds to the reflections within the plate.

Figure 7-3 presents typical received time traces measured from the front surface. The time traces were obtained at four locations, all located at $y = 20$ mm, but x positions were varied: 5 mm, 15 mm, 25 mm and 35 mm. The signal monitored at position ($x = 5$ mm, $y = 20$ mm) represents a signal collected at the undamaged area. The green dashed line ($x = 25$ mm, $y = 20$ mm) corresponds to the reflection from the dented and cracked area (caused by the impact). Measuring the time of flight from the front surface reflection and knowing the thickness and wave speed of the material (approximately 2700 m/s \pm 10%), one can determine the arrival time of the reflection from the back-wall surface. Since the front surface reflection (first echo) arrived at 98 μ s, the back-wall reflection was calculated to arrive at approximately 99.5 μ s \pm 10%. The time interval of echoes from every layer cannot be detected as the wavelength (0.54 mm) is larger than the nominal thickness of each layer (0.25 mm thick). Figure 7-3 shows three groups of reflections that can be observed based on their arrival times. These groups correspond to the reflections from (i) the surface, (ii) within the plate thickness and (iii) back-wall of the plate.

From Figure 7-3, it can be observed that the lowest reflected amplitude (0.2 V) was obtained from the signal measured at the center of the impacted area ($x = 25$ mm, $y = 20$ mm). The other three signals have higher amplitudes (0.6 V) of the surface reflection, which described the undamaged and smoother surface. For the second group of the reflections within the plate, multiple peaks of reflections occurred, which can be due to local higher scattering from within the plate. Again it can be observed that the lowest reflection amplitude (0.1 V) was obtained at the impacted area. This shows that the irregular surface (at the impactor location) greatly degraded the normal incident and reflected waves. Meanwhile, the other three signals have inconsistencies in their amplitudes. This may be related to the variations and changes in the interlaminar condition caused by the impact on the surface. What is interesting in this data is that the

assumed undamaged signal (based on visual inspection on the surface area) also produced multiple reflections as the other signals. The highest reflected amplitude was observed at $98.5 \mu\text{s}$. Briefly, the arrival time matches approximately to a quarter of the plate thickness. This could indicate the through-thickness location of the delamination as the delamination is normally located in-plane between plies, which produces high reflections. Turning now to the last reflected group (the back-wall reflections), it can be observed that the highest amplitude reflection was obtained from signal monitored at the undamaged area ($x = 5 \text{ mm}$, $y = 20 \text{ mm}$). This could be due to less wave attenuation and scattering between the plies. Meanwhile, the back-wall reflections from the damaged area are lower than that observed in the undamaged location, which relates to the scattering by the impact damage within the plate.

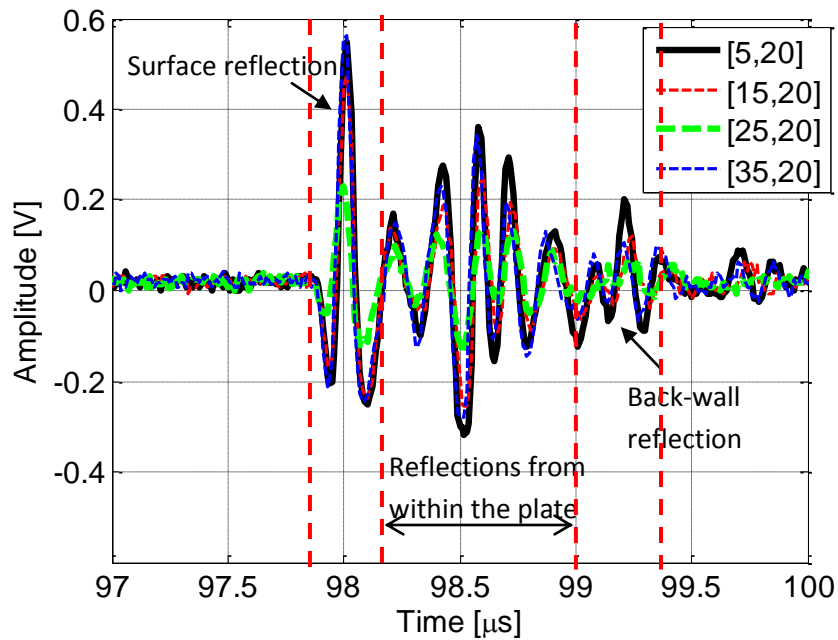


Figure 7-3: Comparison of response signals at various locations; signal at location $x=5 \text{ mm}$, $y = 20 \text{ mm}$ corresponds to the undamaged signal; pulse-echo mode; focused; 5 MHz frequency.

Figure 7-4 shows the C-scan image of the front surface of the test plate (that has a smoother surface compared to the back-wall surface). This image was generated using the maximum peak amplitude of the first reflection. Referring to Figure 7-3, the first reflection is mainly a reflection from the plate surface and therefore it is expected not to be sensitive to the internal defects. From Figure 7-4, the impact damage is located in the middle of the scanned area. The oval shape region reasonably matches the 15 mm diameter of the hemisphere shaped impactor head. The oval shaped section with lower amplitude region, ranging from 0.1 to 0.4 V, can be clearly observed with an approximate length of 10 mm (x-axis) and width of 15 mm (y-axis). This lower amplitude at the impacted area can be explained by the fact that the incident wave encounters the dented surface, which causes the wave to be reflected back at different angles and causes energy loss due to the scattering at the surface. Meanwhile, the rest of the area has a consistently higher and uniform reflected amplitude within a range of 0.5 to 0.6 V due to the smooth plate surface.

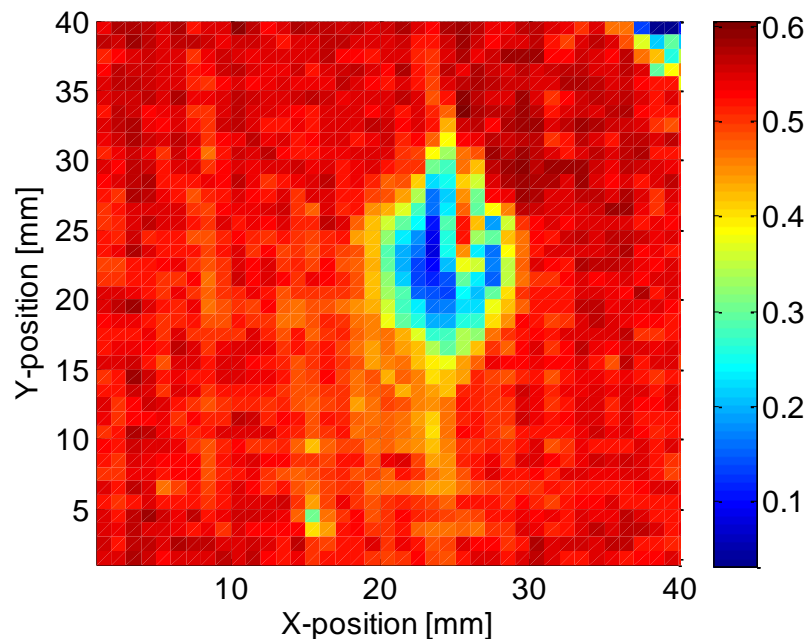


Figure 7-4: C-scan image of the front surface of the 2 mm cross-ply specimen; 40 mm x 40 mm scanned area; 5 MHz frequency; 76.2 mm transducer focal length.

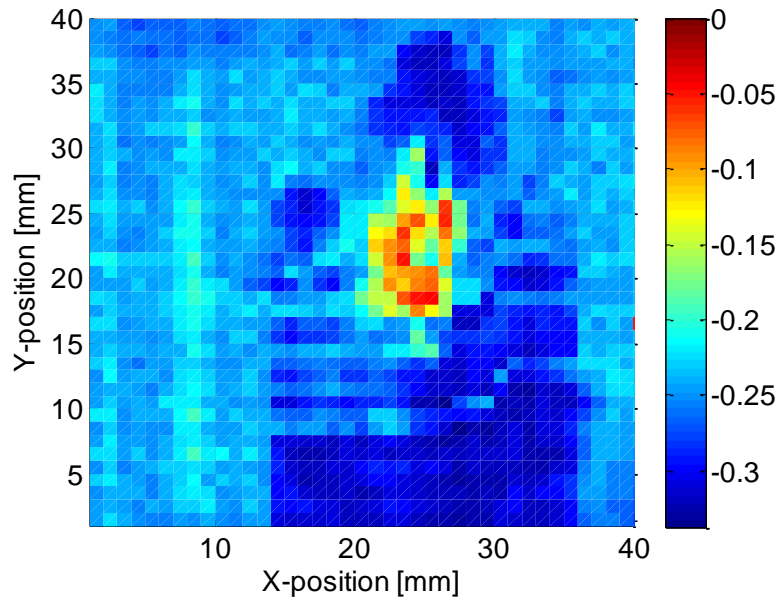


Figure 7-5: C-scan image of negative peak amplitude measured from the frontal surface of the 2 mm cross-ply panel; 40 mm x 40 mm scanned area; 5 MHz frequency; 76.2 mm transducer focal length.

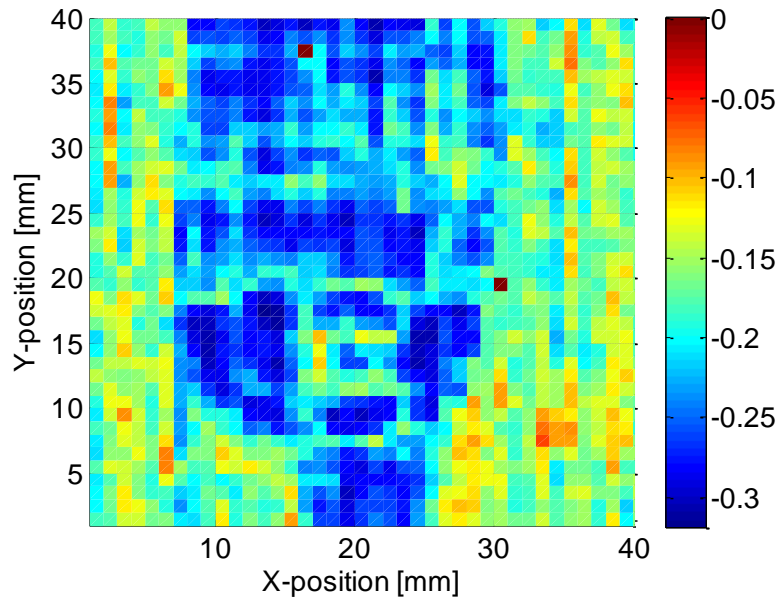


Figure 7-6: C-scan image of negative peak amplitude measured from the back-wall surface of the 2 mm cross-ply panel; 40 mm x 40 mm scanned area; 5 MHz frequency; 76.2 mm transducer focal length.

Figure 7-5 shows a C-scan image of the same section as Figure 7-4, but plotted using the minimum negative amplitude, time gated after the surface reflection. This image represents the internal reflections from within the plate. From the figure, the oval shape with relatively low minimum amplitude (0 – 0.2 V) as similarly obtained from Figure 7-4 can be seen. This shows that the surface indentation not only reduced the normal incident wave but also the reflected wave from within the plate. It also appears there is another large region (half oval shape) with the highest negative amplitude (0.2 – 0.3 V). This is not observed in Figure 7-4, which is time gated for the first surface reflection only.

The same time gating (after surface reflection; negative minimum amplitudes) was also used from the back wall surface (rougher surface compared to the front surface). Figure 7-6 shows an approximately similar pattern as obtained in Figure 7-5, although the sharp oval shape area (0 – 0.2 V) was not observed in this figure as the back surface was not dented. The extent of the impact damage (0.2 – 0.3 V) is reproducible although the surface of the back-wall is rougher. This time gated approach seems to be more sensitive to the extent of the impact damage in the composite laminate. The possible defective area is much larger, about 20 mm and 40 mm in the x- and y-axis respectively, and the damage level (indicated by different amplitude relative to the neighborhood area) is significant. However, the width of the damaged area could be larger than the scanned area, and may spread in a similar oval-shaped pattern. In relation to that point, Sohn et. al [33] have found that the impact response and damage states in flat composite panels is dependent on the diameter of the spherical impactor head. Although this result does not give full information about damage distribution through the thickness, it has provided an useful approximation of size and depth of the impact damage in the composite plate. It is worthwhile at this stage to use this information for the comparison between the numerical predictions and the experimental results of the guided wave scattering at impact damage.

7.1.3 Guided waves displacement fields

The propagation and scattering of the guided waves on the same composite plates was observed experimentally. The methodology is described in Section 3.3.2. A Cartesian raster scan of the 40 mm x 40 mm area containing the impact damage with a step size of 1 mm was performed. The A_0 guided wave mode was excited by a fixed piezoelectric transducer at 100 kHz frequency, located 50 mm from the impacted area. The out-of-plane velocity was measured for each point of the scanned area using a laser vibrometer fixed to a scanning rig and moved parallel to the specimen. From the scanned time signals, wave field images were reconstructed and processed to study the interaction of the guided wave with the impact damage.

Figure 7-7 presents the guided wave fields at various time snapshots, respectively for damaged composite plate 1 and 2. It can be seen that the incident wave interacts with the impact damage and causes scattering within the damaged region. Relatively weak scattering by the damage is present when the incident wave arrives (Figure 7-7a and Figure 7-7c), then a significant increase of the scattering is apparent when wave has travelled past the damaged area (Figure 7-7b and Figure 7-7d). Based on the FE study in Chapter 6, a significant portion of the waves is also reflected back from the exit of the impact damage. These reflected waves travel within the damaged region and keep reflecting back at both entrance and exit of the impact damage. As a consequence of these multiple reflections, a considerable amount of guided wave energy is trapped inside the impact damage area. This causes an increase in the amplitude of the wave in that region.

The amplitude of the transmitted waves diminished noticeably after passing through the impacted area. Similar wave behavior was also observed by Sohn et al. [33], where the measurement was performed on a quasi-isotropic composite plate. This finding however is contradictory to some of the FE simulation results (Section 6.2.1), where a large amount of transmitted wave can be observed. However, some FE results have

demonstrated the reduction in the amplitude past the delamination area. The FE simulations for the delamination placed at 0.50 mm depth (various sizes, Section 6.4) is in agreement with this experimental measurement. Comparing both specimens, which were impacted with same 7.4J impact energy, it can be seen that guided wave scattering in both plates are unique and such variations are expected due to the complexity in the failure mechanism of impact damage.

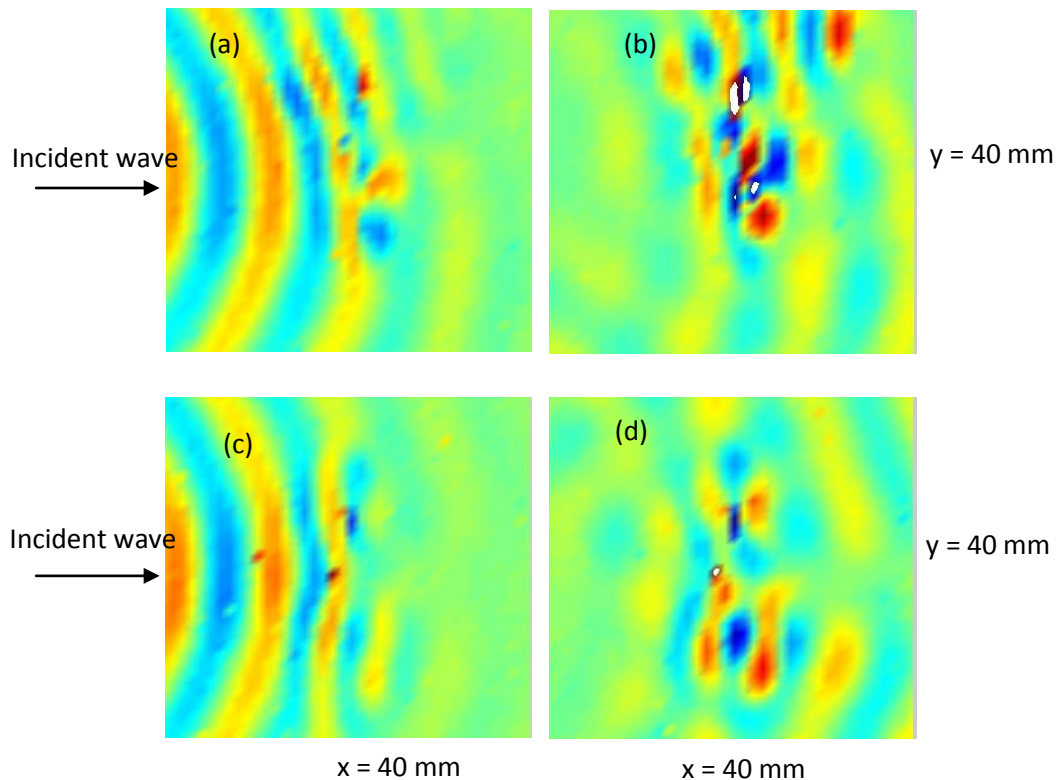


Figure 7-7: Guided wave displacement fields in two composite plates; Plate No. 1, snapshot time (a) 20 μ s and (b) 30 μ s; Plate No. 2, snapshot time (c) 20 μ s and (d) 30 μ s; 7.4 J impact; 40 mm x 40 mm scanned area.

Figure 7-8 presents the image of the maximum amplitude of the signal envelope over the damaged areas in both composite specimens. Areas of higher amplitudes can be seen, that occur close to the impact location center ($x = 20 \text{ mm}$, $y = 20 \text{ mm}$). This indicates the presence of severe damage such as a delamination or fiber and matrix cracking, and matched reasonably well with the visually observed size of the impact damage on the plates as well as the X-ray and C-scan images. Meanwhile, the undamaged area is represented by the low amplitude distribution. From the figure, three different zones can be observed and each zone has its own wave propagation behavior; (i) Zone 1: before the impact damage ($x < 15 \text{ mm}$), (ii) Zone 2: across the impact damage ($15 \text{ mm} < x < 25 \text{ mm}$), and (iii) Zone 3: behind the impact damage ($x > 25 \text{ mm}$).

The first zone (before damage) shows the incident waves propagating towards the impact damage location. It is also can be seen there were reflected waves propagating back towards the excitation source. Some periodical increase and decrease of the amplitude is visible in the region around $x = 15 \text{ mm}$, potentially indicating the interference between the incident and the reflected waves at the impact damage. In zone 2, high amplitudes of the A_0 mode signals are visible, which could indicate the multiple reflections and scattering events within the impact damage area. Meanwhile, in zone 3, the transmitted waves propagating out from the damaged area are seen to be blocked in certain direction with significantly reduced signal amplitudes. Considerable waves transmitted across the impact damage indicate that probably little mode conversion occurred as has been observed from the FE simulations. The cross-section of the impact damage in Plate no. 1 can be roughly approximated with length of 10 mm (x -axis) and width of 20 mm (y -axis), identified by the higher amplitude maxima. For Plate no. 2, the cross section area of the impact damage can be estimated to be about $10 \text{ mm} \times 25 \text{ mm}$.

Referring to the FE simulation results in Section 6.2, good agreement between the experimental and simulated result was achieved. Similar wave propagation behaviour before and within the impact damage can be observed from both results. The increase in

amplitudes identifies the localization of the impact damage in the measured area. There was a significant difference in the wave behavior behind the damage location, where many FE simulations did not predict a persistent amplitude drop compared to the experimental results.

It was mentioned in [132, 133] that damage in composites can also be characterized by the wave energy localization and concentration in certain restricted areas. Since the energy transported by a wave is directly proportional to the square of the amplitude of the wave, the wave energy around the impact damage was plotted to investigate the wave energy localization. Figure 7-9 presents the plots for both composite specimens. From the figure, the damage characteristics that create the highest wave energy at the potential defect location are taken to be those of the damage site. The concentration of energy trapped by the impact damage can also be observed at the damage location. In accordance with Figure 7-8, this Figure 7-9 also revealed areas with no energy propagation beyond the impact damage. Although the wave energy method efficiently localizes the impact location and improves the image results, it contains similar information as the image constructed using the maxima of the signal envelope (Hilbert transform). From this study, it is evident that the impact damage can be detected using the guided ultrasonic wave measurement. Details of the impact damage such as depth, exact length and width as well as its complex scattering are further investigated in the next section.

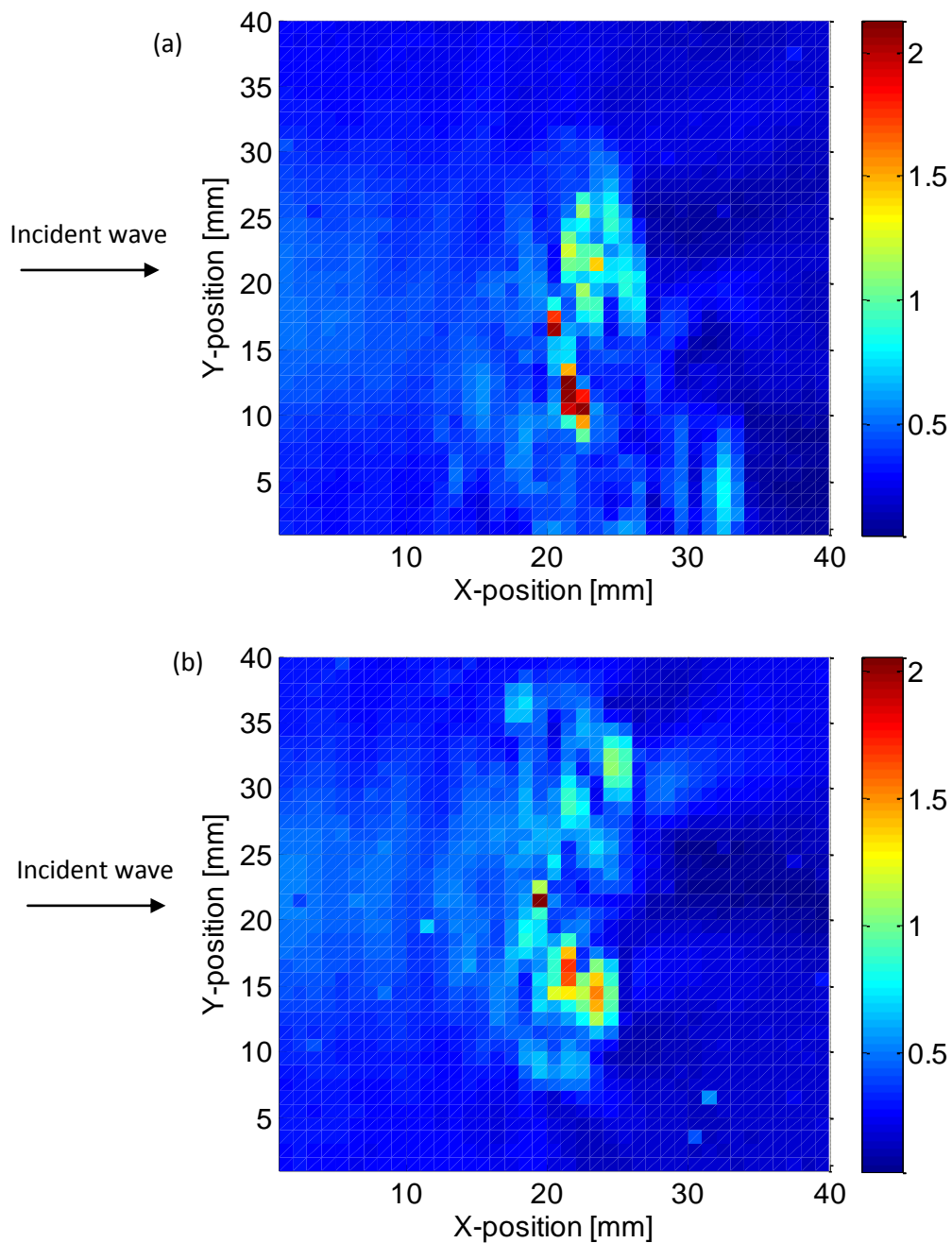


Figure 7-8: Maximum amplitudes of guided wave pulse across damaged area of composite plate: a) plate 1; b) plate 2; frequency 100 kHz; 40 mm x 40 mm area with impact location at center ($x = 20$ mm, $y = 20$ mm).

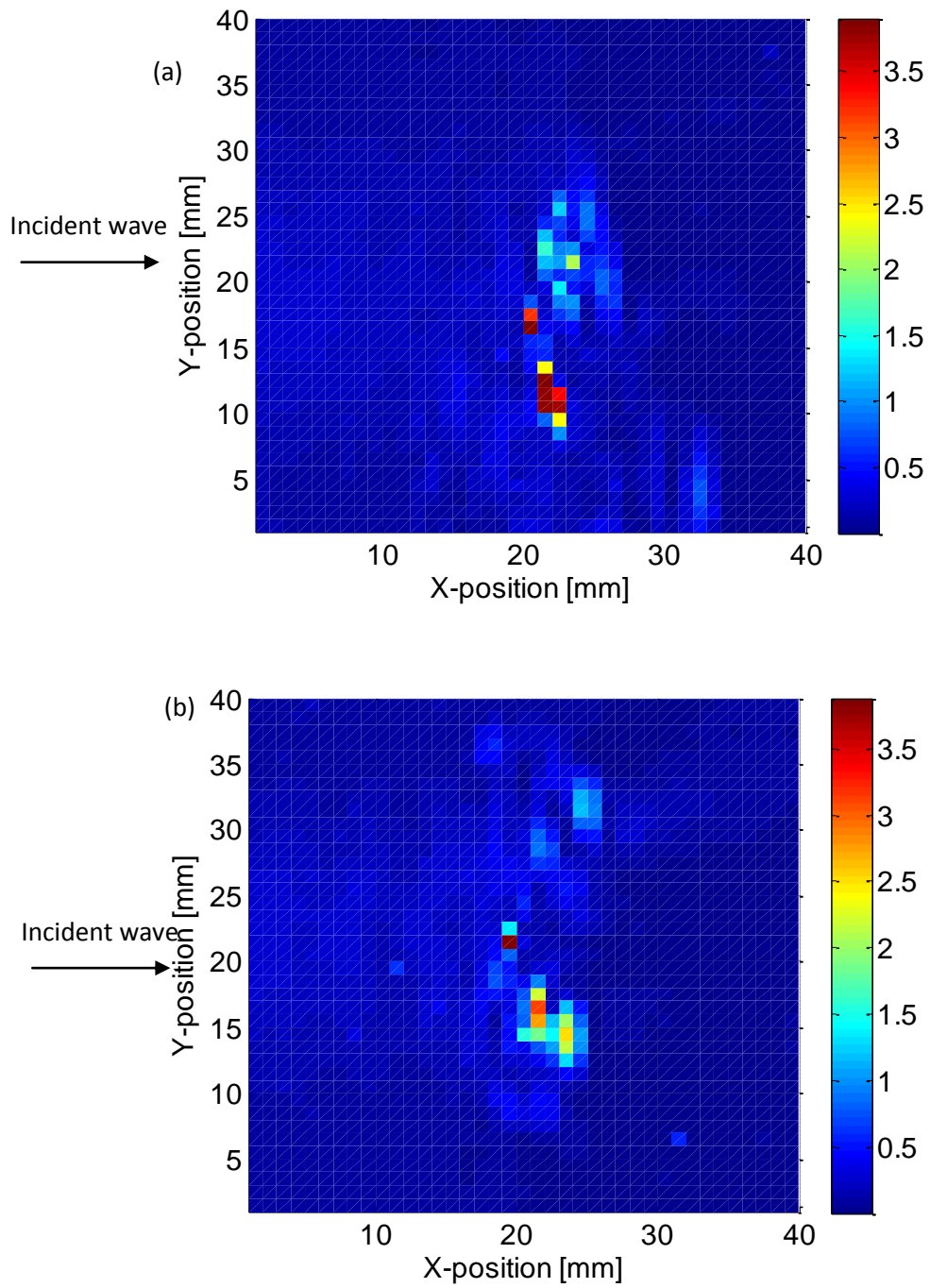


Figure 7-9: Wave energy distribution across damaged area of composite plate: a) plate 1; b) plate 2; frequency 100 kHz; 40 mm x 40 mm area with impact location at center ($x = 20$ mm, $y = 20$ mm).

7.2 Scattering of A_0 wave mode by impact damage

The scattering of the guided waves on the area containing the impact damage area was observed. Guided wave signals measured at locations between the excitation and damage (25 mm from transducer) and at the center of the impact damage (50 mm) are shown in Figure 7-10. Before the guided wave reaches the damaged area the incident wave pulse can be seen to match the prescribed excitation signal as a 5 cycle sinusoidal wave packet. Pulses arriving later in time consist of reflections at different parts of the specimens, but as the specimen geometry is rather narrow, no time separation is possible between reflections at the defect and plate edges. The reflected signal by the impact damage could be overlapped with the reflections from plate sides. If a bigger specimen would be used, the approximate damage location could be estimated with the knowledge of wave velocity and the arrival times of the reflected wave. Measuring the wave propagation on the area containing the impact damage, a significant change in signal shape and increase in amplitude can be observed. The amplitudes of the wave pulse measured at 50 mm (center of impact damage) are almost twice of those measured at the undamaged location. No clear and single wave pulse can be discerned; multiple reflections within the damaged area appeared to lead to a standing vibration.

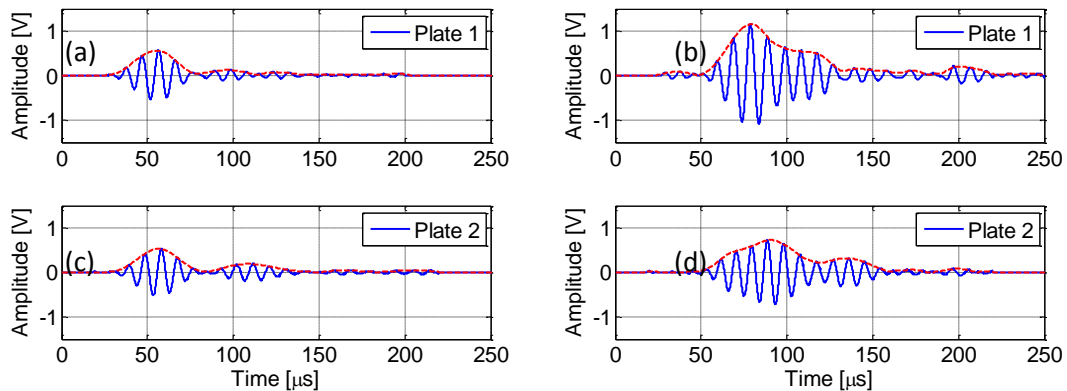


Figure 7-10: Experimental time traces monitored at 25 mm from transducer (undamaged area); a) plate 1; c) plate 2; and 50 mm (damaged area): b) plate 1; d) plate 2; excitation frequency 100 kHz, time trace (solid, blue), and envelope (dashed, red).

The guided wave propagation on the damaged part of the plates was monitored in 1 mm steps along a 200 mm line in the 0° direction, shown in Figure 7-11 and Figure 7-12, excited at different distances of 50 mm and 100 mm from the impact center respectively. For each measurement point the maximum amplitude of the wave pulse was extracted using the Hilbert transform. The figure shows that the amplitude of the guided wave pulse propagating in the intact part (before arriving at impact location) gives repeatable results similar to the baseline data. The amplitude decreases with propagation distance due to the geometric beam spreading as well as the influence from the material damping. The amplitude measurements on both plates give similar results. Some scattering of the amplitude values can be observed, either due to local inhomogeneities in the plates or due to measurement errors caused by insufficient reflection of the laser beam. High amplitudes can be observed around the center of the impact damage, respectively at 50 mm and 100 mm distance in both plates. The length of these high amplitudes region is about 8 mm. This indicates the presence of the damage, and reasonably matches the observed length of the impact damage in X-ray, C-scan and guided wave Cartesian scan (measured approximately 10 mm in x-direction, and 15 mm in y-direction). This could be due to a delamination or fiber and matrix cracking induced by the impact which could introduce multiple reflections within the damaged area and lead to standing waves. Small periodic variations of the signal amplitude can be seen about 20 mm before the impact damage location. These variations can be explained by the interference between the incident wave pulse and reflections at the impact damage that propagate back to the direction of excitation as similarly seen from the FE simulations. Behind the damage location, a significant reduction of the wave pulse can be observed as compared to the baseline data, reduced by more than 75%. This behavior is different to what have been observed from the FE simulations except for the case studies of the 0.50 mm delamination depth. It could also be possible that the amplitude reduction is affected by the irregular distribution of impact damage compared to the regular square delamination. However, this interesting finding might allow the detection of impact damage from monitoring the

amplitude of guided wave pulses between fixed sensors on a structure, as the amplitude reduction is quite similar for the two plate specimens with impact damage.

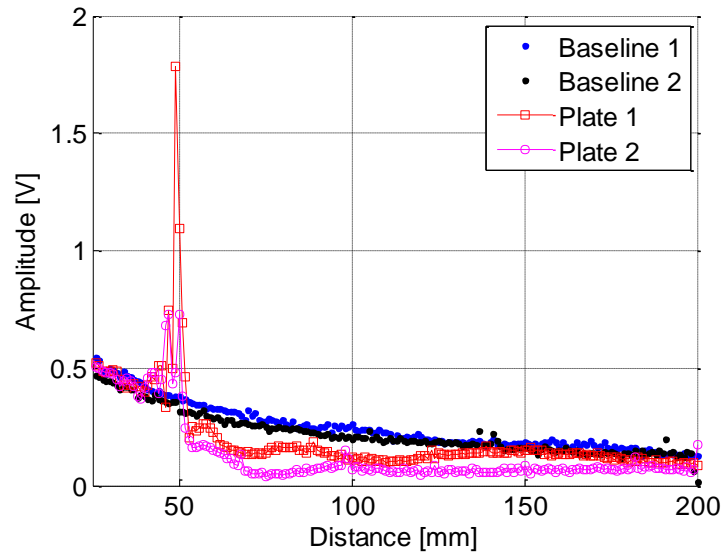


Figure 7-11: Amplitude of propagating guided wave pulse over damaged part; excitation frequency 100 kHz, transducer placed 50 mm from the impact damage area; measured every 1 mm step.

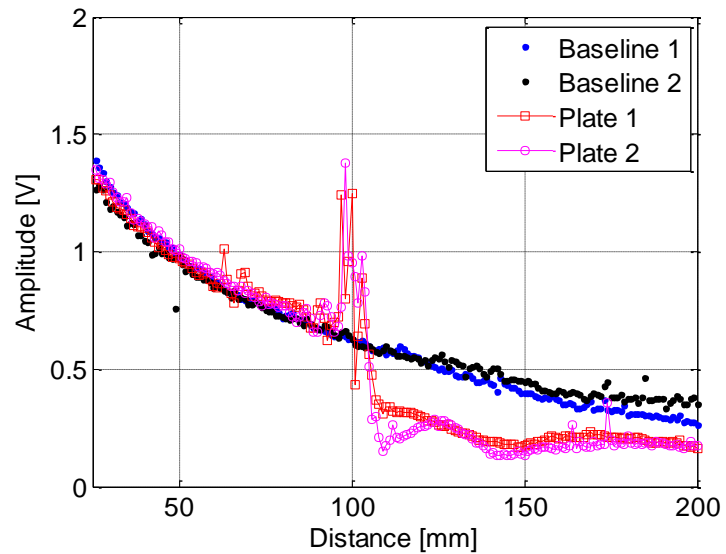


Figure 7-12: Amplitude of propagating guided wave pulse over damaged part; excitation frequency 100 kHz, transducer placed 100 mm from the impact damage area; measured every 1 mm step.

In order to understand the wave propagation and scattering around the impact damage, a circular scan was performed on each composite plate around the impact damage location (Figure 7-13a and Figure 7-14a). Another circular scan was performed at the symmetric location in the undamaged area as baseline data, shown in Figure 7-13b and Figure 7-14b. For the baseline measurement, one can observe a good agreement between the measurements on the two plates. The amplitude in the incident wave direction (180°) is about twice the amplitude in the 0° direction, similar to the amplitude decrease observed in the baseline data in Figure 7-11 and Figure 7-12. The amplitudes in the 90° and 270° directions are significantly lower than what would be expected in an isotropic plate due to the energy distribution along the fiber directions, leading to an oval shaped amplitude distribution. For the measurement around the damage location (Figure 7-13a and Figure 7-14a), the incident wave (0° direction) has a similar amplitude distribution as the baseline data (180° direction) and no significant back-scattered energy is observed. However, the amplitude of the guided wave propagating past the impact damage is significantly reduced for both specimens. Especially for plate 2 scattering approximately 45° relative to the wave propagation direction seems to occur, but for plate 1 the scattered field is not symmetric and almost no energy is scattered between 180° and 270° . Comparing both case studies (different distances from the excitation source), it can be observed that the amplitude pattern behind the impact damage, particularly in directions between 90° - 270° , is slightly different to each other. This could be due to the transducer proximity to the impact location, whereby more complex interference between the incident and the scattered waves occur when transducer is placed closer to the impact damage. As each impact damage is unique such variations are expected, but similarities in the scattered guided wave field for both specimens can be observed. The next section discusses the comparison between these experimental results and the FE simulations.

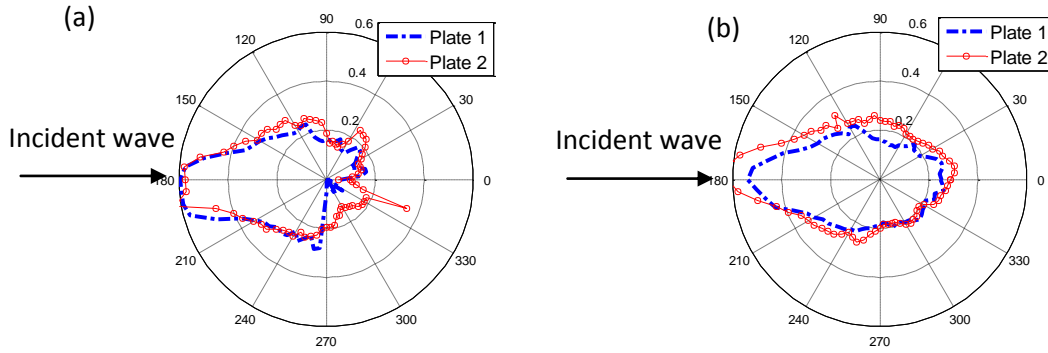


Figure 7-13: a) Plot of amplitude variation measured every 5° at 30 mm radius around (a) impact damage; b) undamaged plate, symmetric to damage location; 100 kHz; excitation 50 mm from impact damage.

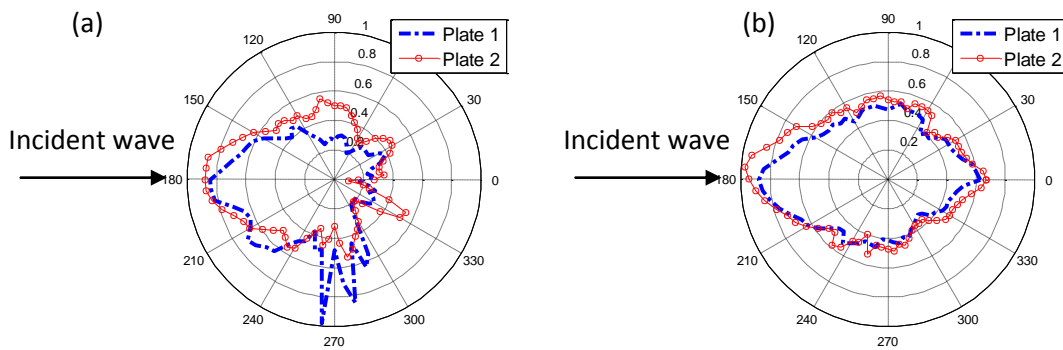


Figure 7-14: a) Plot of amplitude variation measured every 5° at 30 mm radius around (a) impact damage; b) undamaged plate, symmetric to damage location; 100 kHz; excitation 100 mm from impact damage.

7.3 Comparison with FE simulations

This section discusses the findings from the X-ray, C-scan and guided wave measurements in order to compare with the FE analysis. A new FE model will be developed based on the information obtained from all measurements and simulations, particularly the size and depth of the impact damage.

Firstly, the guided wave line scan measurement is compared to the X-ray and C-scan images. From Figure 7-11 and Figure 7-12, the experimental results show an increase in the amplitude of the area containing the impact damage, which is over 10 mm length. The observed length seems to match the description obtained from the C-scan image (surface reflections, Figure 7-4) and guided wave image (Figure 7-8). Meanwhile the X-ray image (Figure 7-1) estimated the 15 mm length that matches the impactor head, and stretched to more than 60 mm in total length. The damage extension that may have been seen partly in the C-scan image (reflections within plate thickness, Figure 7-5 and Figure 7-6) seems to match the X-ray description, but there was no clear correlation to the guided wave measurement results. Results obtained from the guided wave images show the length of the high energy localization is approximately 10 mm in the x-axis and 30 mm in the y-axis.

Using all these pieces of information, the experimental results were now compared independently to the FE results shown in Section 6.4 (case studies of the different delamination sizes at different depths). From Figure 6-20 (line scans), none of the case studies obtained significant high amplitude within the delamination area. In contrast, it is obvious that the experimental results (Figure 7-11 and Figure 7-12) show a significant increase in the amplitude over the damaged area. This may indicate an additional factor that has influenced the signals to behave in such way. The reason for this is not clear but it may relate to the material degradation at the impact damage. As has been shown in the literature [101, 118, 119], the material stiffness properties can be greatly affected during the impact event. According to the FE analysis on Section 6.5, the simulation results have shown that the increase in the amplitudes at the damaged area was significant when the stiffness properties were reduced by 75%. Hence, this suggests that the specimens may have a combination of defects at the impact damage locations: cracks, delamination and material degradation.

Comparing the amplitude pattern behind the delamination, the experimental results show a distinct pattern which is consistently lower amplitude compared to the baseline measurements. Meanwhile, the FE results show complex amplitude pattern, except for the case studies of 0.50 mm depth (for all sizes). A similar amplitude drop pattern behind the delamination area can be observed and this is in agreement with the line scan measurements. It is possible to hypothesize that the through-thickness location of the impact damage of the composite specimens were likely located at 0.50 mm depth, although it is understood that a multi-level delamination may occur in the specimen as well.

From the measured angular pattern (Figure 7-13 and Figure 7-14), a complex forward scattering pattern and formation of side lobes (left hemisphere) can be seen but it is difficult to conclude defect size from these measurements, except the information how the guided wave is scattered in the impact damage area. However, one thing can be observed that has also been seen from the FE simulation results. It is the formation of the side lobes of the forward scattering between 120° and 150° Directions. This description seems to match the prediction of angular scattering for delamination sizes of 30 mm and 40 mm in width, although the experimental results showed that the behavior of the scattering amplitude is generally more complicated than what has been predicted from the FE simulations.

In order to model a good FE representation of the composite specimen with impact damage, the length, width and the depth of the delamination model are needed. Building from the information gathered so far, it is suggested that the estimated defective area is approximately 10 mm to 60 mm by length and width up to 30 mm. It should be noted that the guided wave measurements estimated the length about 10 mm, and the extension up to 60 mm was shown by the X-ray image and partly by the C-scan internal reflection images. The depth of the impact damage seems to match to the 0.50 mm predictions from the FE simulation results. In addition, it is understood that the high

amplitude in the defective region could result from material degradation, and this triggered an investigation of a new FE model with combined defects (delamination and material degradation). The model with material degradation is needed in order to obtain a more realistic model of the impact damage, which is known to be complex and combine multiple types of defects. Hence, two new FE simulations were performed based on the characterization above. One of the simulations contained only delamination and the other one contained combined defects of delamination with the 75% full thickness material degradation. The size of the delamination was assigned to be 10 mm x 30 mm. Figure 7-15 and Figure 7-16 present the results.

From the line measurement over a 200 mm distance (Figure 7-15), the result of FE simulation for a delamination only defect (bright green line) shows a 20% higher amplitude peak only at the exit of the delamination (at 110 mm) and a subsequent amplitude drop (about 30%) behind the delamination region. Then the amplitudes about 10 mm behind the delamination increased again. The simulated amplitudes nearly matched the experimental results at distance close to 200 mm. From the FE simulation with material degradation (brown line), higher amplitude peaks can be seen in the defective region, increased to 50% higher than the baseline. Meanwhile, the amplitude behind the delamination shows about 60% reduction, and then increased back after 30 mm, which is double the measured amplitude. Turning now to the angular pattern around the damage location (Figure 7-16a), it can be observed that both FE simulations provide quite similar scattering pattern around the defects except for the amplitudes in directions of 150° and 210°. Both simulations predicted a significant increase in the amplitudes behind the damage position and small magnitude of the side lobes. These features are contradictory to the observed experimental angular pattern. From this comparison, it can be concluded that the new FE models do not provide a good match to the experimental results. Hence it was decided to compare the experimental results to the existing FE results presented in Chapter 6.

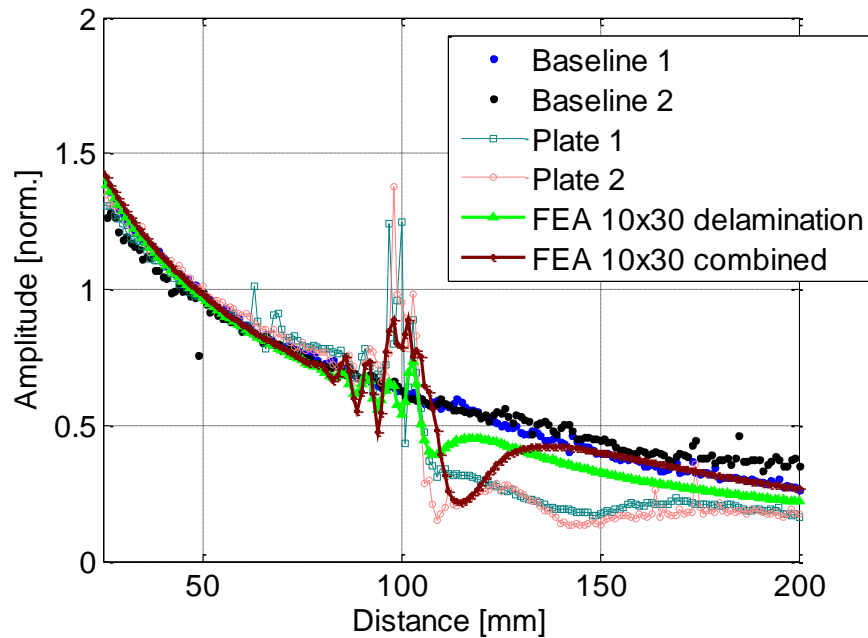


Figure 7-15: Comparison between experimental and FE simulations results for the amplitude of guided wave pulse over damaged area; FE delamination size 10 mm x 30 mm; FE combined delamination and full depth material degradation; excitation 100 mm from impact area; 100 kHz.

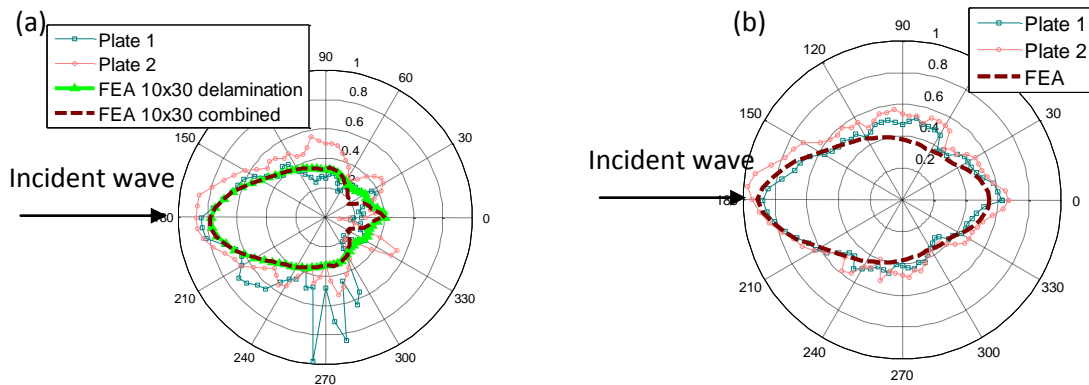


Figure 7-16: Comparison between experimental and FE simulations results of amplitude variation measured every 5° at 30 mm radius around (a) impact damage; b) undamaged plate (symmetric to damage location); excitation 100 mm from impact damage; 100 kHz.

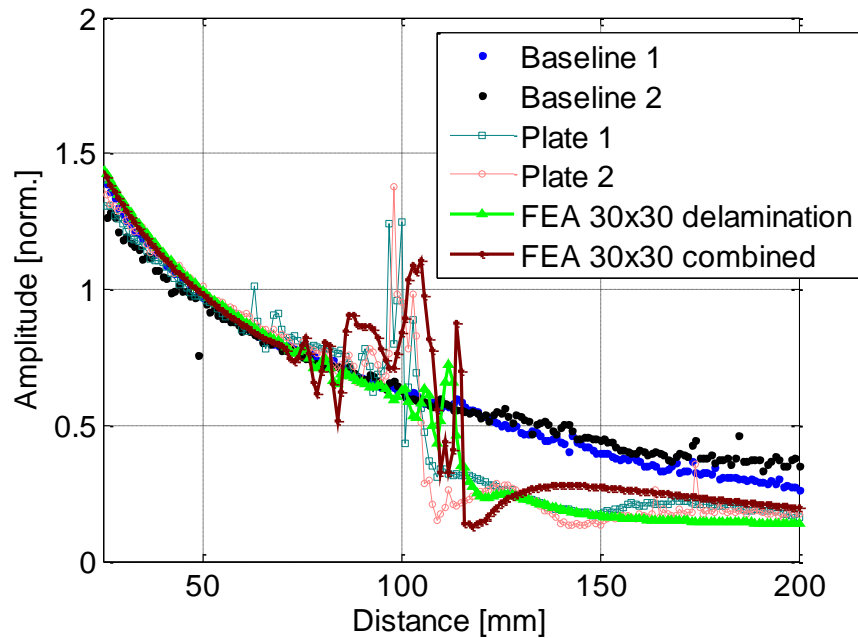


Figure 7-17: Comparison between experimental and FE simulations results for the amplitude of propagating guided wave pulse over damaged area; FE delamination size 30 mm x 30 mm; FE combined delamination (0.50 mm depth) and full depth material degradation (75%); transducer placed 100 mm from the impact area; 100 kHz.

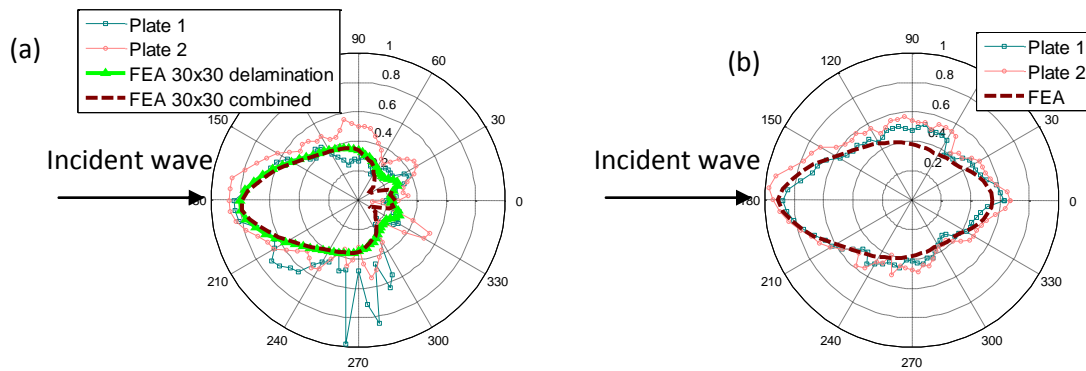


Figure 7-18: Comparison between experimental and FE simulations results of amplitude variation measured every 5° at 30 mm radius around (a) impact damage; b) undamaged plate (symmetric to damage location); excitation 100 mm from impact damage; 100 kHz.

Further comparison is made between the experimental and FE results with delamination size of 30 mm x 30 mm located at 0.50 mm depth with and without material degradation. Only two sizes were chosen according to earlier conclusions. Figure 7-17 and Figure 7-18 present the results. Comparing the line monitoring over 200 mm, a reasonable match between all amplitude profiles can be observed. Similar high amplitudes in the damaged region and a similar level of amplitude reduction behind the defective area can be observed. However, it is obvious that the FE result of the model with delamination only (bright green line) shows the lowest amplitudes within the damage region compared to the other FE model and the experimental results. As expected, the model with combined defects (brown line) provides higher amplitudes in the defective region reasonably matching the experimental peaks. The irregular rise and fall of the amplitudes before the guided wave pulses arrive at the defect location can also be observed to be closer to the experimental results than the model with delamination only. However, the length of the defect is obviously longer (30 mm) than the experimental measurements (approximately 10 mm).

For the comparison of the angular pattern at the symmetrical location to the defective area (Figure 7-18b), one can observe a good agreement between the baseline measurement and FE simulations. The amplitude in the incident wave direction (180°) is about twice the amplitude in the 0° direction, similar to the amplitude decrease observed from the line measurements. The amplitudes are higher along the fiber directions due to the larger stiffness. The incident wave (0° direction) has a similar amplitude distribution as the baseline data (Figure 7-18b; 180° direction) and no significant back-scattered energy is observed. Both FE simulations predicted a decrease in the amplitudes behind the damage position (180°), but the FE of delamination only predicted a smaller amount of scattered amplitudes compared to the FE of combined defects. For the measurement around the damage location (Figure 7-18a), it can be seen that both FE results provide a good prediction of the experimental observations. Low scattered amplitude can be observed

within the left hemisphere. Two side lobes of the forward scattering in 150° and 210° directions due to the 30 mm width reasonably match the experimental results.

From this comparison study, it can be concluded that the scattered waves from the FE simulations provide a regular pattern compared to the experimental results. This could be a result from defining the impact damage in the FE simulation as a rectangular delamination with layers of decreased stiffness, rather than the actual complex impact damage. Based on these independent characterizations, it would be safe to say that some of the FE predictions match reasonably well with the experimental results, particularly from the FE model with combined delamination (30 mm x 30 mm) with 75% reduction in the stiffness properties. The experimental results showed that the behavior of the scattered amplitude generally is more complicated than what has been predicted by the FE. However, this study has provided improved physical insights into the scattering phenomena at real impact damage which could be useful for the improvement of the FE modeling and performance of guided waves methods for in-situ NDE of large composite structures.

7.4 Conclusions

The first section of this chapter has demonstrated the characterization of impact damage using X-ray, ultrasonic C-scan and guided waves imaging methods. By using the X-ray and C-scan, the size and shape of the delamination can be roughly estimated and are useful for validating the guided wave measurements. The use of the A_0 guided ultrasonic wave mode excited at 100 kHz for the detection and characterization of impact damage in composite plates has been shown, with a view to employing this methodology for structural health monitoring (SHM). Scattering of the guided wave at the impact damage was observed experimentally, with increased amplitude at the impact location, and a repeatable scattering pattern with significant amplitude reduction of the guided wave propagating past the damage location. Good agreement between the experimental results and FE predictions was obtained. It has been shown that the FE model with combined defects (30

mm x 30 mm delamination size at 0.50 depth and 75% stiffness reduction) can reasonably produce a good match. This might allow the development of a system for the detection of impact damage by monitoring the amplitude of guided wave pulses between permanent sensors on a composite structure.

CHAPTER 8 CONCLUSIONS

This PhD thesis studied the potential of the first anti-symmetrical (A_0) guided waves mode for the monitoring and characterization of impact damage in laminate composite plates. Laminate composites, consisting of layers of polymer matrix reinforced with high strength carbon fibers, are increasingly employed for aerospace structures as they offer advantages for aerospace applications, such as good strength to weight ratio. However, impact during the operation and servicing of the aircraft can lead to barely visible and difficult-to-detect impact damage. Depending on the severity of the impact, fiber and matrix breakage or delaminations can occur, reducing the functionality of the structure. It is therefore essential that the effects of such impact can be detected and monitored by means of an appropriate structural health monitoring method.

Reliable structural health monitoring of composite panels can be achieved using guided ultrasonic waves. Low-frequency guided wave inspection offers the possibility of rapid damage detection in large structures. However, the behavior of the guided waves in composite structures is complicated due to the anisotropic material properties influencing the wave propagation characteristics. Therefore, the objective of this research was to investigate the interaction of guided ultrasonic waves with typical impact damage, such as delaminations and material degradation. This investigation was carried out with the aim to improve the understanding of the application of the A_0 Lamb wave mode for composite materials. Finite Element analysis and experimental results were compared.

8.1 Summary of findings

This thesis is divided into eight chapters. The first chapter presents the motivation to carry out this study and outlines the thesis structure. Chapter 2 presents an introduction to impact damage in composites and guided ultrasonic waves. Building on the literature review, the low-frequency first asymmetrical mode (A_0) has been chosen to be used rather than the first symmetrical mode (S_0). Although the attenuation of the A_0 wave mode is higher than the S_0 mode, the A_0 mode was selected because of the known detection

sensitivity for delaminations at any depth, and as the wave velocity has only a small angular direction dependency, particularly for cross-ply composite plates. Furthermore, limited studies of the A_0 mode interaction with real impact damage in composite plates were found, and this gave additional motivation to explore this field of study.

Chapter 3 describes the experimental methodology used throughout this study. The A_0 mode was excited using a piezoelectric transducer fixed to the specimens. The A_0 mode out-of-plane displacements were measured using a laser vibrometer, which allowed for non-contact, pointwise and automated measurements. The experimental measurements were performed on several undamaged composite plates first to obtain a better understanding of the influence of the anisotropic material on the propagation characteristics. Measurements were performed on composite plates with impact damage for the detection and characterization of impact damage. A conventional ultrasonic immersion C-scan to estimate size and shape of the impact damage was performed. Additionally, X-ray images were provided by collaborators for comparison.

Chapter 4 presents the methodology of the Finite Element simulations. 3D Finite Element simulations using ABAQUS Explicit were performed. A programme was developed in MATLAB which enables the fully automated generation of the ABAQUS input file for parameter variations. Using the Matlab program the orthotropic material properties for homogenized and layered (individual plies) composite models were assigned. Two types of defects were defined as a delamination with varying size and depth and stiffness property degradation. A quasi 2D FE model was used to investigate the influence of delamination depth on the guided wave mode conversion, reflection and transmission for a long delamination. The use of the modeling techniques presented in this chapter, subject to subsequent further improvements, could eventually lead to the ability to obtain an accurate and efficient FE model of composites with defects.

Chapter 5 presents the experimental and numerical results of the guided wave propagation characteristics on undamaged composite plates. Results from the verification study have shown that both the homogenized and layered FE models are reasonably consistent, suggesting that in principle homogenized material properties could be employed to simulate the guided wave propagation in an undamaged composite plate. This would reduce the required simulation time as it eliminates the need to model each layer individually. In Section 5.2 the frequency-dependent attenuation in three different composite plates has been successfully estimated and validated by DISPERSE predictions. The experimental amplitude curve was corrected for beam spreading and the attenuation due to the material damping was obtained by fitting the amplitude curve. The A_0 mode group and phase velocities obtained from the FE simulations were in agreement with the Disperse semi-analytical predictions.

Section 5.4 discusses the dependency of the A_0 wave properties on the direction of propagation. The group and phase velocities of the A_0 mode in a cross-ply plate were observed to be almost independent of the angular direction. Since the wave travels at the same velocity in any direction, this makes the development of an algorithm to locate and size the damage simpler. In contrast, the wave properties of the unidirectional plate show the expected angular dependency. There was a reasonable similarity between the experimental and FE results, where the wave behavior related to the beam steering can be clearly observed for both plates. An implication of this is the possibility of reduced detection sensitivity for damage located not in the main principal (fiber) directions. This information will help to improve future optimization strategies for the SHM of composites. Overall, this study has satisfactorily shown that the FE simulations can effectively model the angular characteristics of the A_0 mode wave propagation in anisotropic composite plates.

Chapter 6 discusses the A_0 mode wave scattering characteristics at defects in a cross-ply composite plate. Section 6.1 demonstrated that the presence of a delamination

made a significant difference between the results produced by the layered and homogenized material models. This is in contrast to Chapter 5, where both types of models gave comparable results when no defect was introduced. A study of different delamination shapes, square and circular, has shown comparable results. The rectangular delamination was chosen as it simplifies the modeling.

From the 2D FE simulations of guided wave interaction with large delaminations, it was found that the mode converted S_0 mode was generated when the A_0 mode encountered the delamination, but that the S_0 reflections could not be found outside the delamination region when the delamination was placed at a symmetrical depth. It was shown that the A_0 mode can detect delaminations at any depth, but that the reflected A_0 mode was rather small, about 10% of the incident wave amplitude. For the A_0 mode incidence, reflection and transmission at the delamination exit occur, which results in multiple reflections. Since the arrival times of the received multiple reflection signals correspond to the length of the delamination, analyzing these complex signals can in principle provide the information about the length of delaminations.

The study from Section 6.3 investigated the influence of the delamination width and length on the guided wave scattering characteristics. The delamination width had a strong influence on the scattering directivity. The angular dependency of the scattering indicates the obstruction of the wave propagation path due to the larger width of the damaged area and energy trapping within the delamination. Two further effects, which are an increase in the back scattering and a decrease in the forward scattering with increasing delamination width, can also be observed. These identified patterns are of great importance for the detectability of delaminations since the presence of a delamination becomes evident from scattered waves. For the effect of the delamination length, the forward scattered wave field is almost independent of the delamination length. This finding is important to note for the damage detection strategy. The data

processing algorithm must take into account that in some directions no (or only a limited) change in signal can be observed, even for a significant defect size.

From a study of the depth influence, the findings suggest that the depth of the delamination influences the generation of mode converted S_0 mode outside the delamination region. Unlike for the S_0 mode, delaminations at any depth can be detected by the changes in the forward and backward scattering of the A_0 mode. The smallest scattered amplitude was found when the delamination was close to the plate surface. The largest scattered wave was obtained when the delamination was placed at or close to the mid plane of the plate. From the final section, it can be concluded that scattered waves increase as the stiffness properties decrease. Introducing full-thickness stiffness reduction, the results have shown an increase of the scattered amplitude at the defective region. The FE model with combined defects has shown different characteristics compared to the FE model for a delamination only. In this work, the FE simulations of the wave interactions have been limited to particular types of damage. However, one can imagine forming a library of expected damage geometries for different types of composite materials and layups. This could serve as a future reference for the development of this NDE approach.

The final chapter of this PhD thesis presents the independent characterization of the impact damage using three different NDE methods: X-ray imaging, ultrasonic immersion C-scan and guided ultrasonic waves. Using those NDE methods, the size and shape of a delamination can be approximately estimated. The use of guided waves successfully demonstrated the ability to detect impact damage in composite plates. Reasonably good agreement between the experimental and FE results was obtained. Based on the independent characterizations, the FE model with a delamination (30 mm x 30 mm, placed at delamination depth 0.50 mm) combined with 75% reduction in the stiffness properties showed quite a good match to the experimental results. This suggests that the simplified and easy-to-implement FE model could be used to represent the complex impact damage in composite plates. Therefore, this could be useful for the

improvement of the FE modeling and performance of guided wave methods for the in-situ NDE of large composite structures.

8.2 Recommendation for future works

The findings from this PhD project are subjected to certain limitations. For instance, the 3D modeling of the guided wave scattering by defects was limited to circular and square shaped delaminations. Hence, it would be of particular interest to continue the present study by investigating more complex geometries and validating the simulation results by performing systematic experimental measurements. The validation of the investigated phenomenon may enable advances in the modelling of complex defects. The 3D modelling of the combined delamination with the material degradation has opened the perspective of studying any kind of defect using similar approaches. A microscopic investigation such as Scanning Electron Microscopic (SEM) or more sophisticated analysis such as Computed Tomography (CT) could also be performed on the impacted area in order to obtain more detailed images of the impacted and the surrounding area. This could improve the 3D modeling of the complex impact damage in composites. However, it should be noted that future work should not only include an improved damage model, but also needs to demonstrate how to improve the detection sensitivity and to quantify the damage severity.

8.3 Concluding remarks

The potential for the detection of impact damage in composite structures has been shown in this study, and a better understanding of the guided wave interaction with defects was achieved. It was demonstrated that the low frequency A_0 guided wave mode generated by a piezoelectric transducer can be successfully employed to monitor impact damage in composite plates. An embedded transducer attached permanently to the composite structure would be a great approach for an active SHM technique. However, low reflected pulse amplitude and wave attenuation need to be taken into consideration together with the anisotropy in composites. Both simulation and experimental results have shown that it

should be possible to characterize the impact damage, which can lead to an automated defect detection and online defect classification. However, this may be influenced by undesired changes of signals due to varying conditions of the composite material and the operational environment. Building on the knowledge gained from this PhD study, the non-destructive evaluation of large aerospace composites can be improved.

REFERENCES

- [1] B. D. Agarwal, L. J. Broutman, and K. Chandrashekhara, *Analysis and performance of fiber composites*. New Jersey: John Wiley & Sons, 2006.
- [2] W. J. Cantwell and J. Morton, "Comparison of the low and high velocity impact response of CFRP," *Composites*, vol. 20, no. 6, pp. 545–551, Nov. 1989.
- [3] M. O. W. Richardson and M. J. Wisheart, "Review of low-velocity impact properties of composite materials," *Compos. Part A Appl. Sci. Manuf.*, vol. 27, no. 12, pp. 1123–1131, Jan. 1996.
- [4] H. Y. Choi, H. T. Wu, and F. Chang, "A new approach toward understanding damage mechanisms and mechanics of laminated composites due to low-velocity impact: Part II--analysis," *J. Compos. Mater.*, vol. 25, no. 8, pp. 1012–1038, Aug. 1991.
- [5] W. J. Cantwell and J. Morton, "Geometrical effects in the low velocity impact response of CFRP," *Compos. Struct.*, vol. 12, no. 1, pp. 39–59, Jan. 1989.
- [6] W. J. Cantwell, "The influence of target geometry on the high velocity impact response of CFRP," *Compos. Struct.*, vol. 10, no. 3, pp. 247–265, Jan. 1988.
- [7] R. A. Kline, *Nondestructive characterization of composite media*. Pennsylvania: Technomic Publishing Company, 1992.
- [8] S. P. Joshi and C. T. Sun, "Impact induced fracture in a laminated composite," *J. Compos. Mater.*, vol. 19, no. 1, pp. 51–66, Jan. 1985.
- [9] M. Nishikawa, T. Okabe, and N. Takeda, "Numerical simulation of interlaminar damage propagation in CFRP cross-ply laminates under transverse loading," *Int. J. Solids Struct.*, vol. 44, no. 10, pp. 3101–3113, May 2007.
- [10] T.-W. Shyr and Y.-H. Pan, "Impact resistance and damage characteristics of composite laminates," *Compos. Struct.*, vol. 62, no. 2, pp. 193–203, Nov. 2003.
- [11] M. R. Wisnom, "The role of delamination in failure of fiber-reinforced composites," *Philos. Trans. R. Soc. A*, vol. 370, pp. 1850–1870, 2012.
- [12] A. N. Vorontsov, G. K. Murzakhanov, and V. N. Shchugorev, "Delamination failure of composite structures," *Mech. Compos. Mater.*, vol. 25, no. 6, pp. 723–737, 1990.
- [13] R. D. Adams and P. Cawley, "A review of defect types and nondestructive testing techniques for composites and bonded joints," *NDT Int.*, vol. 21, no. 4, pp. 208–222, Aug. 1988.

- [14] I. G. Scott and C. M. Scala, "A review of non-destructive testing of composite materials," *NDT Int.*, vol. 15, no. 2, pp. 75–86, Apr. 1982.
- [15] X. E. Gros, "An eddy current approach to the detection of damage caused by low-energy impacts on carbon fibre reinforced materials," *Mater. Des.*, vol. 16, no. 3, pp. 167–173, Jan. 1995.
- [16] M. Endrizzi, P. C. Diemoz, T. P. Millard, J. Louise Jones, R. D. Speller, I. K. Robinson, and A. Olivo, "Hard X-ray dark-field imaging with incoherent sample illumination," *Appl. Phys. Lett.*, vol. 104, no. 2, p. 024106, Jan. 2014.
- [17] W. N. Reynolds, "Nondestructive testing (NDT) of fibre-reinforced composite materials," *Mater. Des.*, vol. 5, no. 6, pp. 256–270, Dec. 1984.
- [18] M. Ajit, S. Frank, and B. Sauvik, "Acoustic emission waveforms in composite laminates under low velocity impact," *Proc. SPIE*, vol. 5047, pp. 1–12, Jul. 2003.
- [19] T. J. Swait, F. R. Jones, and S. A. Hayes, "A practical structural health monitoring system for carbon fibre reinforced composite based on electrical resistance," *Compos. Sci. Technol.*, vol. 72, no. 13, pp. 1515–1523, Aug. 2012.
- [20] N. Takeda, Y. Okabe, J. Kuwahara, S. Kojima, and T. Ogisu, "Development of smart composite structures with small-diameter fiber Bragg grating sensors for damage detection: Quantitative evaluation of delamination length in CFRP laminates using Lamb wave sensing," *Compos. Sci. Technol.*, vol. 65, no. 15–16, pp. 2575–2587, Dec. 2005.
- [21] A. Raghavan and C. E. S. Cesnik, "Review of guided-wave structural health monitoring," *Schock Vib. Dig.*, vol. 39, no. 2, pp. 91–114, 2007.
- [22] R. J. Freemantle, N. Hankinson, and C. J. Brotherhood, "Rapid phased array ultrasonic imaging of large area composite aerospace structures," *Insight*, vol. 47, no. 3, pp. 4–11, 2005.
- [23] T. R. Hay, R. L. Royer, H. Gao, X. Zhao, and J. L. Rose, "A comparison of embedded sensor Lamb wave ultrasonic tomography approaches for material loss detection," *Smart Mater. Struct.*, vol. 15, no. 4, pp. 946–951, Aug. 2006.
- [24] D. P. Jansen, D. A. Hutchins, and J. T. Mottram, "Lamb wave tomography of advanced composite laminates containing damage," *Ultrasonics*, vol. 32, no. 2, pp. 83–90, Mar. 1994.
- [25] K. Diamanti and C. Soutis, "Structural health monitoring techniques for aircraft composite structures," *Prog. Aerosp. Sci.*, vol. 46, no. 8, pp. 342–352, Nov. 2010.

- [26] J. L. Rose, "Ultrasonic guided waves in structural health monitoring," *Key Eng. Mater.*, vol. 270–273, pp. 14–21, 2004.
- [27] J. L. Rose, "A baseline and vision of ultrasonic guided wave inspection potential," *J. Press. Vessel Technol.*, vol. 124, pp. 273–282, 2002.
- [28] B. B. Djordjevic and G. Burnie, "Ultrasonic characterization of advanced composite materials," *Proc. Appl. Contemp. NDT Eng.*, pp. 47–57, 2009.
- [29] T. Wu and H. Liu, "On the measurement of anisotropic elastic constants of fiber-reinforced composite plate using ultrasonic bulk wave and laser generated Lamb wave," *Ultrasonics*, vol. 37, pp. 405–412, 1999.
- [30] P. Fromme and M. B. Sayir, "Detection of cracks at rivet holes using guided waves," *Ultrasonics*, vol. 40, no. 1–8, pp. 199–203, May 2002.
- [31] Y. Lu, L. Ye, Z. Su, and C. Yang, "Quantitative assessment of through-thickness crack size based on Lamb wave scattering in aluminium plates," *NDT E Int.*, vol. 41, no. 1, pp. 59–68, Jan. 2008.
- [32] P. Guy, Y. Jayet, and L. Goujon, "Guided wave interaction with complex delaminations. Application to damage detection in composite structures," *Proc. SPIE*, vol. 5047, pp. 25–33, Jul. 2003.
- [33] H. Sohn, D. Dutta, J. Y. Yang, H. J. Park, M. DeSimio, S. Olson, and E. Swenson, "Delamination detection in composites through guided wave field image processing," *Compos. Sci. Technol.*, vol. 71, no. 9, pp. 1250–1256, Jun. 2011.
- [34] H. Duflo, B. Morvan, and J. L. Izbicki, "Interaction of Lamb waves on bonded composite plates with defects," *Compos. Struct.*, vol. 79, no. 2, pp. 229–233, Jul. 2007.
- [35] T. Kundu, S. Das, S. A. Martin, and K. V. Jata, "Locating point of impact in anisotropic fiber reinforced composite plates," *Ultrasonics*, vol. 48, no. 3, pp. 193–201, Jul. 2008.
- [36] G. R. Liu and Z. C. Xi, *Elastic Waves in Anisotropic Laminates*. Boca Raton: CRC Press LLC, 2000.
- [37] J. D. Achenbach, *Wave propagation in elastic solids*. Amsterdam and New York: North-Holland Pub. Co., 1973.

- [38] P. Wilcox, M. Lowe, and P. Cawley, "The effect of dispersion on long-range inspection using ultrasonic guided waves," *NDT E Int.*, vol. 34, no. 1, pp. 1–9, Jan. 2001.
- [39] J. L. Rose, *Ultrasonic Waves in Solid Media*. Cambridge: Cambridge University Press, 2004.
- [40] W. H. Prosser, M. D. Seale, and B. T. Smith, "Time-frequency analysis of the dispersion of Lamb modes," *J. Acoust. Soc. Am.*, vol. 105, no. 5, pp. 2669–76, May 1999.
- [41] L. Wang and F. Yuan, "Group velocity and characteristic wave curves of Lamb waves in composites: Modeling and experiments," *Compos. Sci. Technol.*, vol. 67, no. 7–8, pp. 1370–1384, Jun. 2007.
- [42] M. J. S. Lowe, G. Neau, and M. Deschamps, "Properties of Guided Waves in Composite Plates, and Implications for NDE," *AIP Conf. Proc.*, vol. 700, no. 1, pp. 214–221, Feb. 2004.
- [43] B. Pavlakovic, M. Lowe, D. N. Alleyne, and P. Cawley, "DISPERSE: A general purpose program for creating dispersion curve," *Rev. Prog. QNDE*, vol. 16, pp. 185–192, 1997.
- [44] P. D. Wilcox, M. J. S. Lowe, and P. Cawley, "Mode and transducer selection for long range Lamb wave inspection," *J. Intell. Mater. Syst. Struct.*, vol. 12, no. 8, pp. 553–565, Aug. 2001.
- [45] D. N. Alleyne and P. Cawley, "Optimization of Lamb wave inspection techniques," *NDT E Int.*, vol. 25, no. 1, pp. 11–22, Jan. 1992.
- [46] N. Guo and P. Cawley, "The interaction of Lamb waves with delaminations in composite laminates," *J. Acoust. Soc. Am.*, vol. 94, no. 4, p. 2240, Oct. 1993.
- [47] J.-L. Shih, K.-T. Wu, C.-K. Jen, C.-H. Chiu, J.-C. Tzeng, and J.-W. Liaw, "Applications of flexible ultrasonic transducer array for defect detection at 150c," *Sensors*, vol. 13, no. 1, pp. 975–83, Jan. 2013.
- [48] S. Grondel, C. Paget, C. Delebarre, J. Assaad, and K. Levin, "Design of optimal configuration for generating A0 Lamb mode in a composite plate using piezoceramic transducers," *J. Acoust. Soc. Am.*, vol. 112, no. 1, pp. 84–90, Jul. 2002.
- [49] B. Lin and V. Giurgiutiu, "Modeling and testing of PZT and PVDF piezoelectric wafer active sensors," *Smart Mater. Struct.*, vol. 15, no. 4, pp. 1085–1093, Aug. 2006.

- [50] Z. Su, L. Ye, and Y. Lu, "Guided Lamb waves for identification of damage in composite structures: A review," *J. Sound Vib.*, vol. 295, no. 3–5, pp. 753–780, Aug. 2006.
- [51] L. P. Scudder and D. A. Hutchins, "Laser-generated ultrasonic guided waves in fiber-reinforced plates-theory and experiment," *IEEE Trans. Ultrason. Ferroelectr. Freq. Control*, vol. 43, no. 5, pp. 870–880, Sep. 1996.
- [52] H. Nakano and S. Nagai, "Laser generation of antisymmetric Lamb waves in thin plates," *Ultrasonics*, vol. 29, no. 3, pp. 230–234, May 1991.
- [53] H. Gao, S. Ali, and B. Lopez, "Efficient detection of delamination in multilayered structures using ultrasonic guided wave EMATs," *NDT E Int.*, vol. 43, no. 4, pp. 316–322, Jun. 2010.
- [54] R. Kazys, A. Demcenko, E. Zukauskas, and L. Mazeika, "Air-coupled ultrasonic investigation of multi-layered composite materials.," *Ultrasonics*, vol. 44, pp. 819–22, Dec. 2006.
- [55] O. Putkis, R. P. Dalton, and A. J. Croxford, "The anisotropic propagation of ultrasonic guided waves in composite materials and implications for practical applications.," in press, corrected proof, [doi:10.1016/j.ultras.2014.11.013](https://doi.org/10.1016/j.ultras.2014.11.013)
- [56] F.-K. Chang, J. F. C. Markmiller, J.-B. Ihn, and K. Y. Cheng, "A Potential Link from Damage Diagnostics to Health Prognostics of Composites through Built-in Sensors," *J. Vib. Acoust.*, vol. 129, no. 6, p. 718, Dec. 2007.
- [57] W. Gao, C. Glorieux, and J. Thoen, "Laser ultrasonic study of Lamb waves: determination of the thickness and velocities of a thin plate," *Int. J. Eng. Sci.*, vol. 41, no. 2, pp. 219–228, Jan. 2003.
- [58] J. Pohl and G. Mook, "Laser-vibrometric analysis of propagation and interaction of Lamb waves in CFRP-plates," *CEAS Aeronaut. J.*, vol. 4, no. 1, pp. 77–85, Jan. 2013.
- [59] P. Cawley, "The rapid non-destructive inspection of large composite structures," *Composites*, vol. 25, no. 5, pp. 351–357, May 1994.
- [60] B. Chapuis, N. Terrien, and D. Royer, "Excitation and focusing of Lamb waves in a multilayered anisotropic plate.," *J. Acoust. Soc. Am.*, vol. 127, no. 1, pp. 198–203, Jan. 2010.
- [61] V. Giurgiutiu, "Tuned Lamb wave excitation and detection with piezoelectric wafer active sensors for structural health monitoring," *J. Intell. Mater. Syst. Struct.*, vol. 16, no. 4, pp. 291–305, Apr. 2005.

- [62] S. V. Ende and R. Lammering, "Investigation on piezoelectrically induced Lamb wave generation and propagation," *Smart Mater. Struct.*, vol. 16, no. 5, pp. 1802–1809, Oct. 2007.
- [63] M. Tracy and F.-K. Chang, "Identifying Impacts in Composite Plates with Piezoelectric Strain Sensors, Part I: Theory," *J. Intell. Mater. Syst. Struct.*, vol. 9, no. 11, pp. 920–928, Nov. 1998.
- [64] G. R. Liu, K. Y. Lam, and H. M. Shang, "Scattering of waves by flaws in anisotropic laminated plates," *Compos. Part B Eng.*, vol. 27, no. 5, pp. 431–437, Jan. 1996.
- [65] T. H. Ju, S. K. Datta, and A. H. Shah, "Scattering of impact wave by a crack in composite plate," *J. Appl. Mech.*, vol. 59, no. 3, pp. 596–603, 1991.
- [66] M. Castaings and B. Hosten, "Guided waves propagating in sandwich structures made of anisotropic, viscoelastic, composite materials," *J. Acoust. Soc. Am.*, vol. 113, no. 5, p. 2622, May 2003.
- [67] S. K. Datta and A. H. Shah, *Elastic Waves in Composite Media and Structures: With Applications to Ultrasonic Nondestructive Evaluation*. Boca Raton: Taylor & Francis, 2008.
- [68] G. Neau, M. Deschamps, and M. J. S. Lowe, "Group velocity of Lamb waves in anisotropic plates: Comparison between theory and experiments," *AIP Conf. Proc.*, vol. 557, pp. 81–88, Apr. 2001.
- [69] G. Neau, M. J. S. Lowe, and M. Deschamps, "Propagation of Lamb waves in anisotropic and absorbing plates: Theoretical derivation and experiments," *AIP Conf. Proc.*, vol. 615, pp. 1062–1069, 2002.
- [70] E. Glushkov, N. Glushkova, A. Eremin, R. Lammering, and M. Neumann, "Frequency dependent directivity of guided waves excited by circular transducers in anisotropic composite plates," *J. Acoust. Soc. Am.*, vol. 132, no. 2, pp. 119–24, Aug. 2012.
- [71] S. Biwa, Y. Watanabe, and N. Ohno, "Analysis of wave attenuation in unidirectional viscoelastic composites by a differential scheme," *Compos. Sci. Technol.*, vol. 63, no. 2, pp. 237–247, Feb. 2003.
- [72] K. J. Schubert and A. S. Herrmann, "On attenuation and measurement of Lamb waves in viscoelastic composites," *Compos. Struct.*, vol. 94, no. 1, pp. 177–185, Jul. 2011.

- [73] W. M. Karunasena, A. H. Shah, and S. K. Datta, "Plane-strain-shear scattering by cracks in laminated composite plates," *J. Eng. Mech.*, vol. 117, pp. 1738–1754, Aug. 1991.
- [74] C.-T. Ng and M. Veidt, "Scattering of the fundamental anti-symmetric Lamb wave at delaminations in composite laminates," *J. Acoust. Soc. Am.*, vol. 129, no. 3, p. 1288, Mar. 2011.
- [75] W. M. Karunasena, A. H. Shah, and S. K. Datta, "Plane strain wave scattering by cracks in laminated composite plates," *J. Eng. Mech.*, Oct. 2007.
- [76] Q. Deng and Z. Yang, "Scattering of S0 Lamb mode in plate with multiple damage," *Appl. Math. Model.*, vol. 35, no. 1, pp. 550–562, Jan. 2011.
- [77] W. N. Reynolds, L. P. Scudder, and H. Pressman, "The use of ultrasonic wave attenuation to monitor polymer and composite quality," *Polym. Test.*, vol. 6, no. 5, pp. 325–336, Jan. 1986.
- [78] C. Willberg, S. Koch, G. Mook, J. Pohl, and U. Gabbert, "Continuous mode conversion of Lamb waves in CFRP plates," *Smart Mater. Struct.*, vol. 21, no. 7, p. 075022, Jul. 2012.
- [79] C. Ramadas, K. Balasubramaniam, M. Joshi, and C. V Krishnamurthy, "Interaction of the primary anti-symmetric Lamb mode (A0) with symmetric delaminations: numerical and experimental studies," *Smart Mater. Struct.*, vol. 18, no. 8, p. 085011, Aug. 2009.
- [80] Z. Liu, H. Yu, C. He, and B. Wu, "Delamination damage detection of laminated composite beams using air-coupled ultrasonic transducers," *Sci. China Physics, Mech. Astron.*, vol. 56, no. 7, pp. 1269–1279, May 2013.
- [81] C. Yang, L. Ye, Z. Su, and M. Bannister, "Some aspects of numerical simulation for Lamb wave propagation in composite laminates," *Compos. Struct.*, vol. 75, no. 1–4, pp. 267–275, Sep. 2006.
- [82] C. Ramadas, K. Balasubramaniam, M. Joshi, and C. V Krishnamurthy, "Interaction of guided Lamb waves with an asymmetrically located delamination in a laminated composite plate," *Smart Mater. Struct.*, vol. 19, no. 6, pp. 1–11, Jun. 2010.
- [83] C. A. C. Leckey, M. D. Rogge, and F. Raymond Parker, "Guided waves in anisotropic and quasi-isotropic aerospace composites: three-dimensional simulation and experiment," *Ultrasonics*, vol. 54, no. 1, pp. 385–94, Jan. 2014.

- [84] D. Singh, M. Bentahar, and R. El Guerjouma, "Interaction of fundamental Lamb modes with a point impact damaged zone in composite plates," *Acoust. 2012*, pp. 2423–2428, 2012.
- [85] G. Perillo, N. Vedivik, and A. Echtermeyer, "Damage development in stitch bonded GFRP composite plates under low velocity impact: Experimental and numerical results," *J. Compos. Mater.*, vol. 0, pp. 1–15, Feb. 2014.
- [86] M. Castaings, D. Singh, and P. Viot, "Sizing of impact damages in composite materials using ultrasonic guided waves," *NDT E Int.*, vol. 46, pp. 22–31, Mar. 2012.
- [87] R. Bratton and S. Datta, "Scattering of Lamb waves in a composite plate," *Rev. Prog. QNDE*, vol. 10B, pp. 1507–1514, 1991.
- [88] G. R. Liu and K. Y. Lam, "Characterization of a horizontal crack in anisotropic laminated plates," *Int. J. Solids Struct.*, vol. 31, no. 21, pp. 2965–2977, Nov. 1994.
- [89] N. Toyama, J. Noda, and T. Okabe, "Quantitative damage detection in cross-ply laminates using Lamb wave method," *Compos. Sci. Technol.*, vol. 63, no. 10, pp. 1473–1479, Aug. 2003.
- [90] N. Toyama and J. Takatsubo, "Lamb wave method for quick inspection of impact-induced delamination in composite laminates," *Compos. Sci. Technol.*, vol. 64, no. 9, pp. 1293–1300, Jul. 2004.
- [91] C. H. Wang and L. R. F. Rose, "Wave reflection and transmission in beams containing delamination and inhomogeneity," *J. Sound Vib.*, vol. 264, no. 4, pp. 851–872, Jul. 2003.
- [92] S. A. Meguid and X. D. Wang, "Wave scattering from cracks and imperfectly bonded inhomogeneities in advanced materials," *Mech. Mater.*, vol. 31, no. 3, pp. 187–195, Mar. 1999.
- [93] B. I. S. Murat, P. Khalili, and P. Fromme, "Impact damage detection in composite panels using guided ultrasonic waves," *AIP Conf. Proc.*, vol. 1581, no. 1, pp. 286–293, Feb. 2014.
- [94] B. I. S. Murat, P. Khalili, and P. Fromme, "Guided ultrasonic waves for impact damage detection in composite panels," *Proc. SPIE*, vol. 9064, pp. 1–7, Mar. 2014.
- [95] Z. Liu, H. Yu, C. He, and B. Wu, "Delamination detection in composite beams using pure Lamb mode generated by air-coupled ultrasonic transducer," *J. Intell. Mater. Syst. Struct.*, vol. 25, no. 5, pp. 541–550, Jul. 2013.

- [96] K. Kang, H. Chun, J. Son, J. Byun, M. Um, and S. Lee, "Quantitative Accessibility of Delamination in Composite Using Lamb Wave by Experiments and FEA," *Adv. Compos. Mater.*, vol. 20, pp. 361–373, 2011.
- [97] S. I. Ishak, G. R. Liu, S. P. Lim, and H. M. Shang, "Characterization of delamination in beams using flexural wave scattering analysis," *J. Vib. Acoust. Trans. ASME*, vol. 123, no. 4, pp. 421–427, 2001.
- [98] N. Hu, J. Li, Y. Cai, C. Yan, Y. Zhang, J. Qiu, K. Sakai, Y. Liu, X. Peng, and B. Yan, "Locating delamination in compositelaminated beams using the A0 Lamb mode," *Mech. Adv. Mater. Struct.*, vol. 19, no. 6, pp. 431–440, 2012.
- [99] S. Mustapha, L. Ye, D. Wang, and Y. Lu, "Assessment of debonding in sandwich CF/EP composite beams using A0 Lamb wave at low frequency," *Compos. Struct.*, vol. 93, no. 2, pp. 483–491, Jan. 2011.
- [100] C. Ramadas, M. Janardhan Padiyar, K. Balasubramaniam, M. Joshi, and C. V. Krishnamurthy, "Delamination Size Detection using Time of Flight of Anti-symmetric (A0) and Mode Converted Ao mode of Guided Lamb Waves," *J. Intell. Mater. Syst. Struct.*, vol. 21, no. 8, pp. 817–825, May 2010.
- [101] H. Yu, W. Xingguo, and L. Zhengneng, "Property degradation of anisotropic composite laminates with matrix cracking (I)— Constitutive relation developing for (θ m /90 n), cracked laminates by stiffness partition," *Appl. Math. Mech.*, vol. 19, no. 3, pp. 279–287, Mar. 1998.
- [102] C. Ramadas, K. Balasubramaniam, M. Joshi, and C. V Krishnamurthy, "Numerical and experimental studies on propagation of A0 mode in a composite plate containing semi-infinite delamination: Observation of turning modes," *Compos. Struct.*, vol. 93, no. 7, pp. 1929–1938, 2011.
- [103] K. Hayat and S. K. Ha, "Low-velocity impact-induced delamination detection by use of the S0 guided wave mode in cross-ply composite plates: A numerical study," *J. Mech. Sci. Technol.*, vol. 28, no. 2, pp. 445–455, Feb. 2014.
- [104] K. S. Tan, N. Guo, and B. S. Wong, "Experimental evaluation of delaminations in composite plates by the use of Lamb waves," *Compos. Sci. Technol.*, vol. 53, pp. 77–84, 1995.
- [105] D. Wang, L. Ye, Z. Su, and Y. Lu, "Quantitative identification of multiple damage in laminated composite beams using A0 Lamb mode," *J. Compos. Mater.*, vol. 45, no. 20, pp. 2061–2069, Jun. 2011.

- [106] C. Ramadas, K. Balasubramaniam, M. Joshi, and C. V. Krishnamurthy, "Characterisation of rectangular type delaminations in composite laminates through B- and D-scan images generated using Lamb waves," *NDT E Int.*, vol. 44, no. 3, pp. 281–289, May 2011.
- [107] K. Diamanti, J. M. Hodgkinson, and C. Soutis, "Detection of low-velocity impact damage in composite plates using Lamb waves," *Struct. Heal. Monit.*, vol. 3, no. 1, pp. 33–41, Mar. 2004.
- [108] W. J. Cantwell and J. Morton, "Geometrical effects in the low velocity impact response of CFRP," *Compos. Struct.*, vol. 12, no. 1, pp. 39–59, Jan. 1989.
- [109] H. Kaczmarek, "Lamb wave interaction with impact-induced damage in aircraft composite: Use of A0 mode excited by air-coupled transducer," *J. Compos. Mater.*, vol. 37, no. 3, pp. 217–232, 2003.
- [110] B. I. S. Murat and P. Fromme, "Detection of impact damage in composite panels using guided ultrasonic waves," *Proc. SPIE*, vol. 8695, pp. 1–8, Apr. 2013.
- [111] B. Hosten, D. A. Hutchins, and D. W. Schindel, "Measurement of elastic constants in composite materials using air-coupled ultrasonic bulk waves," *J. Acoust. Soc. Am.*, vol. 99, no. 4, p. 2116, Apr. 1996.
- [112] P. Fromme, P. D. Wilcox, M. J. S. Lowe, and P. Cawley, "On the development and testing of a guided ultrasonic wave array for structural integrity monitoring.," *IEEE Trans. Ultrason. Ferroelectr. Freq. Control*, vol. 53, no. 4, pp. 777–85, Apr. 2006.
- [113] D. W. Schindel, D. A. Hutchins, and M. Sayer, "The design and characterization of micromachined air-coupled capacitance transducers," *IEEE Trans. Ultrason. Ferroelectr. Freq. Control*, vol. 42, no. 1, pp. 42–50, Jan. 1995.
- [114] A. Bernard, M. J. S. Lowe, and M. Deschamps, "Guided waves energy velocity in absorbing and non-absorbing plates," *J. Acoust. Soc. Am.*, vol. 110, no. 1, p. 186, Jul. 2001.
- [115] Dassault Systemes, *ABAQUS Documentation*. Providence, RI, USA, 2011.
- [116] M. Castaings and M. Lowe, "Finite element model for waves guided along solid systems of arbitrary section coupled to infinite solid media.," *J. Acoust. Soc. Am.*, vol. 123, no. 2, pp. 696–708, Feb. 2008.
- [117] Robert Watson, *Modelling of guided ultrasonic wave scattering at defects*, MSc Thesis. Dept. of Mech. Eng., UCL, 2007.

- [118] A. Tounsi, K. H. Amara, A. Benzair, and A. Megueni, "On the transverse cracking and stiffness degradation of aged angle-ply laminates," *Mater. Lett.*, vol. 60, no. 21–22, pp. 2561–2564, Sep. 2006.
- [119] X. Duan, "Multi-directional stiffness degradation induced by matrix cracking in composite laminates," *Int. J. Fatigue*, vol. 24, no. 2–4, pp. 119–125, Apr. 2002.
- [120] T. E. Tay, "Element-Failure: An Alternative to Material Property Degradation Method for Progressive Damage in Composite Structures," *J. Compos. Mater.*, vol. 39, no. 18, pp. 1659–1675, Sep. 2005.
- [121] K. Ono and A. Gallego, "Attenuation of Lamb Waves in CFRP plates," *J. Acoust. Emiss.*, vol. 30, pp. 109–123, 2012.
- [122] M. Calomfirescu and A. S. Herrmann, "On the propagation of Lamb Waves in Viscoelastic Composites for SHM Applications," in *Key Engineering Materials*, 2007, vol. 347, pp. 543–548.
- [123] W. H. Prosser, "Advanced AE techniques in composite materials research," *J. Acoust. Emiss.*, vol. 14, no. 3–4, pp. 1–11, 1996.
- [124] P. Cawley, M. Lowe, and G. Neau, "Understanding attenuative Lamb wave propagation in composites," London, 2001.
- [125] P. Rajagopal and M. J. S. Lowe, "Angular influence on the scattering of fundamental shear horizontal guided waves by a through-thickness crack in an isotropic plate.," *J. Acoust. Soc. Am.*, vol. 124, no. 4, pp. 2021–30, Oct. 2008.
- [126] G. Neau, "Propagation of Lamb waves in anisotropic and absorbing plates: Theoretical derivation and experiments," *AIP Conf. Proc.*, vol. 615, no. 1, pp. 1062–1069, May 2002.
- [127] K. Asamene, L. Hudson, and M. Sundaresan, "Influence of attenuation on acoustic emission signals in carbon fiber reinforced polymer panels," *Ultrasonics*, vol. 59, pp. 86–93, Feb. 2015.
- [128] C. T. Ng, M. Veidt, L. R. F. Rose, and C. H. Wang, "Analytical and finite element prediction of Lamb wave scattering at delaminations in quasi-isotropic composite laminates," *J. Sound Vib.*, vol. 331, no. 22, pp. 4870–4883, Oct. 2012.
- [129] T. Hayashi and K. Kawashima, "Multiple reflections of Lamb waves at a delamination," *Ultrasonics*, vol. 40, no. 1–8, pp. 193–197, May 2002.

- [130] M. Aktaş, C. Atas, B. M. İçten, and R. Karakuzu, "An experimental investigation of the impact response of composite laminates," *Compos. Struct.*, vol. 87, no. 4, pp. 307–313, Feb. 2009.
- [131] P. O. Sjoblom, J. T. Hartness, and T. M. Cordell, "On low-velocity impact testing of composite materials," *J. Compos. Mater.*, vol. 22, no. 1, pp. 30–52, Jan. 1988.
- [132] E. Glushkov, N. Glushkova, M. V Golub, J. Moll, and C.-P. Fritzen, "Wave energy trapping and localization in a plate with a delamination," *Smart Mater. Struct.*, vol. 21, no. 12, p. 125001, Dec. 2012.
- [133] T. E. Michaels, J. E. Michaels, and M. Ruzzene, "Damage detection in plate structures using sparse ultrasonic transducer arrays and acoustic wavefield imaging," *Rev. Prog. QNDE*, vol. 24, pp. 938–945, 2005.